SCUOLA DI DOTTORATO
UNIVERSITÀ DEGLI STUDI DI MILANO-BICOCCA

Department of

Materials Science

PhD program Materials Science and Nanotechnology Cycle XXXI

Curriculumin Materials Science

Surface decoration of inorganic nanoparticles for novel polymer-based nanocomposite materials

Surname Tawfilas Name Massimo

Registration number 721649

Tutor: prof. Roberto Simonutti

Coordinator: prof. Marco Bernasconi

ACADEMIC YEAR 2017/2018

Table of Contents

Chapter 1. Introduction to polymer-based nanocomposite materials

Polymer nanocomposites contain a continuous polymer matrix and a homogeneously dispersed inorganic filler. Depending on the dimension of the filler, polymer nanocomposites may be divided into three categories. In the first category, all three dimensions (length, width and thickness) of the nanomaterials are in the nanometer range (1–100 nm). In the second category, two dimensions of the nanomaterials are in the nanometer range (the third dimension being much larger in size). In the third category, only one dimension is in the nanometer range. Examples of these categories of nanomaterials are as follows: spherical metals and silica nanoparticles are in the first category, carbon nanotubes, metal nanorods and cellulose nanofibres are in the second category, and layer silicates, platelet nanoclays and layer double hydroxides are in the third category. The field of polymer nanocomposites has been at the forefront of research in the polymer community for the past few decades. Exfoliated clay-based nanocomposites have dominated the polymer literature, but in the last years a large number of other significant areas of current and emerging interest are growing. The main idea is to combine the advantageous features of inorganic materials, i.e. optical, mechanical and physical properties, with the unique characteristics of polymer matrices like low cost and easy processability. The biggest contribute is given by the transition from microparticles to nanoparticles, that yields dramatic changes in physical properties to

inorganic systems. Nanoscale materials have a large surface area for a given volume. Since many important chemical and physical interactions are governed by surfaces and surface properties, a nanostructured material can have substantially different properties from a larger-dimensional material of the same composition[1].

Polymer grafted nanoparticles (PGNs)

Many challenges were taken by the scientific community to comprehend and produce new class of materials. The quest was to understand *how* to drive the nanoparticles dispersion in a controlled fashion, that represents the key factor that oversees the properties of polymer-based nanocomposite materials. This is possible if we are able to handle the thermodynamics behind this process. Different actors play a role in the plot described by the balance between entropic and enthalpic contribution. The potential of nanocomposite systems in many scientific fields pushes many groups to produce materials with well-defined properties. The problem that every scientist has to face is the compatibilization between the inorganic and the organic component. The issue of nano-sized objects is the high surface energy that they possess. This high energy resultsthermodyna to a phase separation in an organic polymer matrix[2,3]. In order to express the intrinsic properties of the NCs they must be well dispersed and distributed in the space[4]. The introduction of a thin polymeric layer on the surface of the inorganic nanoparticles (NPs) and nanocrystals (NCs) enables their good dispersion in solvents and matrixes, in which, otherwise, bare particles aggregate and precipitate[5–7]. These phenomena are thermodynamically driven and will be deeply discussed in the next chapters. Moreover,

through surface modification it can be introduced additional functionalities to the NPs, providing new properties for a wide number of applications[8]. The two main synthetic routes followed to create PGNs are the *grafting-to* and *grafting-from* approach (Figure 1).

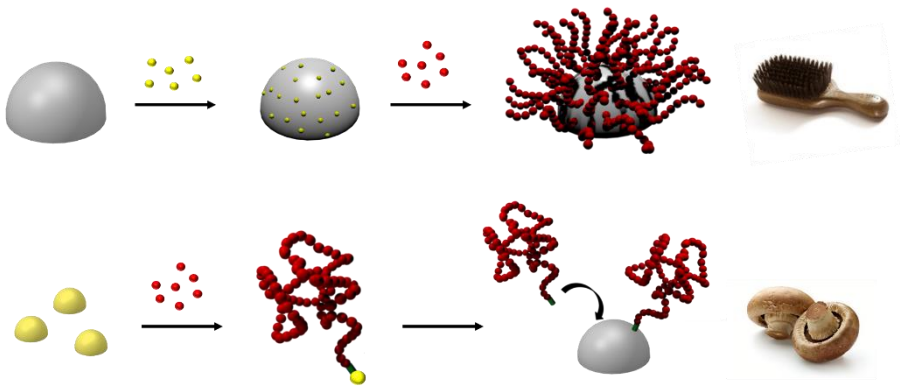

Figure 1 Schematic representation of the grafting-from (top) and the grafting-to approach (bottom). Yellow dots represent the initiator of the polymerization, while the red dots represent as generic monomer. In general, grafting-form method provides brush-like polymers grafted on the NPs, while the grafting-to method provides a mushroom-like polymer.

In the *grafting-to* method, a preformed and end functionalized polymer is attached to the surface. The *grafting-to* method has the advantage to be a simpler method but there are some drawbacks. Steric repulsion between polymer chains already attached and a chain diffusing to the surface limits the available graft density[9]. Moreover, the inorganic surface reactivity to end-functionalized polymer and their interaction with the solvent in which the reaction take place, drives the grafting-to process. In general, are obtained PGNc with a mushroom-like polymer conformation. The *grafting-from* method is a surface-initiated polymerization started with an initiator or chain transfer agent. The diffusion of a relatively small monomer to the surface does not suffer from the same steric repulsion as a diffusing polymer chain creating a

brush-like polymer tethered on the surface but leads to a less homogenous polymer layer. Makoto Asai et al.[10] observed that the *grafting-to* strategy leads to a more uniform polymer coverage of the NCs surface at a given grafting density. Both systems produce extremely defined, if controlled polymerizations techniques are exploited. the discovery and development of controlled radical polymerization (CRP) methods (atom transfer radical polymerization (ATRP)[11], reversible addition−fragmentation chain transfer (RAFT)[12], macromolecular design via reversible addition−fragmentation chain transfer (RAFT)/xanthates, and nitroxide-mediated polymerization (NMP)[13] were quickly adapted to take control over polymers tethers to NP surfaces[4]. The first reported use of ATRP for the modification of surfaces was in 1997 by Huang and Wirth[14]. These authors were able to effectively graft poly(acrylamide) brushes from benzyl chloride-functionalized silica particles. While the application was analytical in nature, the results glimmered ATRP to become extensively used for the creation of polymer brushes. Matyjaszewski et al. have made significant contributions to the expansion and refinement of ATRP in solution and on surfaces[15–17]. Russell and Hawker reported the earliest work with NMP on surfaces using silicon substrates[18]. Although these techniques have been used for a variety of monomer and substrate combinations, the versatility of monomer choice, lack of catalyst, and mild reaction conditions of RAFT have allowed for its rapid use in the past decade. Its first reported use for graft polymerization was in 2001[19], and since then it has been used for the modification of various surfaces using multiple approaches[20]. Taking control over the polymer chain grafting process leads to overwhelm the conformation of the chains tethered on

the surface. Thus, provide the production of materials able to self-assemble in a controlled fashion[21]. This control over the spatial distribution leads to the fabrication of nanocomposite materials with specific properties (optical, permeation etc..). NCs can be decorated with polymers with different molecular weight distribution forming a double layer that offers even better NCs dispersion in matrix[22–24]

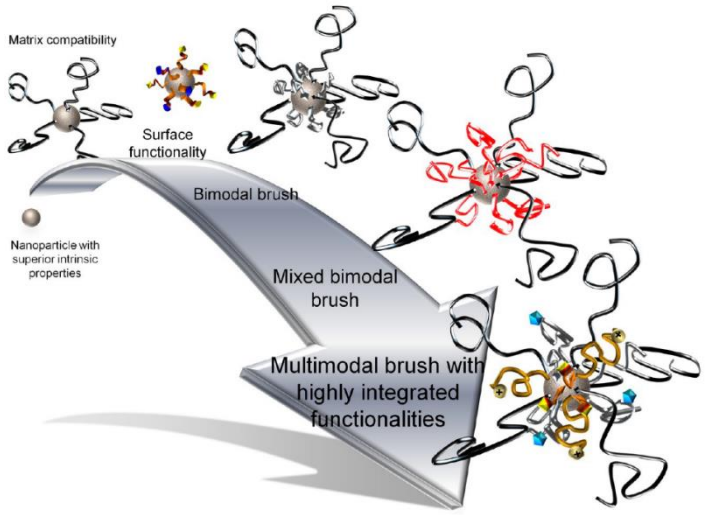

Figure 2 Surface ligand engineering going from the simplest to the most complex modifications (lab on a particle). Reproduced from Li, Ying Krentz, Timothy M. Wang, Lei Benicewicz, Brian C. Schadler, Linda S. Appl. Mater. Interfaces 2014, 6, 6005−6021.[8]

Additionally, it is possible to attach polymers with different chemical structures forming a *mixed* double layer. This interesting approach can combine the properties of different polymers increasing the functionalities of the final material. In this perspective it was developed the concept of the *"lab on a particle"* borrowed by the *"lab on a chip"* idea. In fact, inorganic surfaces can be modified adding small organic molecules with specific activity, like photoactive molecule for example, leading to the fabrication of a multifunctional nanosystems (Figure 2).

This PhD thesis found its place in this enthusiastic environment, since we believe that the birth of new materials starts from the combination and the sum of multi-functional elements. Thus, to complete the picture depicted by the scientific community we started from the bottom line, i.e. the synthesis of the inorganic substrate and the polymer chain. The fabrication of PGNs occurs in solution, either in the *grafting-from* or the *grafting-to* approach, meaning that we have to deal with a three-component system: the NCs, the polymer and the solvent. At first, we analyzed the behavior of TiO_2 nanocrystals in water. This solvent strongly binds the anatase surfaces in a way that make it a probe able to identify the titanium dioxide crystalline phase. Since the aim of this thesis was to create and develop nanocomposite materials, we further investigate the *grafting-to* of end-chain functionalized polyethylene oxide, producing a synthetic protocol to create well defined PGNs. In these conditions we were able to realize that, since we are dealing with complex system, taking control over the polymer-solvent interaction, the polymer-surface reactivity and the solvent-surface interaction allows to tune the density of the tethered polymer chains and thus, the conformation. The ability to control PGNs characteristics through experimental conditions, encouraged us to develop a polymer-based nanocomposite material starting from a mixed bimodal layer grafted nanoparticle. This system provided a dispersion of NCs in polymer matrix such that we were able to produce a material with a high loading of anatase NCs, maintaining the transparency of the final material. Plus, we obtained a material with improved optical properties and higher elastic modulus. Lastly, the fine tuning of PGNs characteristics contribute to dominate spatial distribution in polymer matrix, that arises

in enhanced gas permeability properties. The definition of the density and the length of polymer chains tethered to spherical NPs offer the ability to take advantage on the free volume formation in a nanocomposite material. Thus, we were able to fabricate a new membrane exploiting this property, by using a *smarter* polymer. It was selected and developed a monomer with a preferred selectivity to CO_2 inspired by polyaniline membranes. This monomer was designed to be polymerized via RAFT polymerization using the *grafting-from* approach. With this method it was prepared a PGNs membrane with enhanced gas permeability and selectivity to CO_2, a threat and a resource.

PGNs-based nanocomposite: synthesis

Generally, three ways have been applied to disperse PGNs in polymers. The first is direct mixing or blending of the polymer and the NPs as discrete phases (known as melt mixing). The second is the mixture of the inorganic filler dispersion with the polymer in solution (known as solvent casting). The third is the dispersion of the nanopowder in the monomer followed by in situ polymerization of the polymeric nanocomposite.

Melt mixing

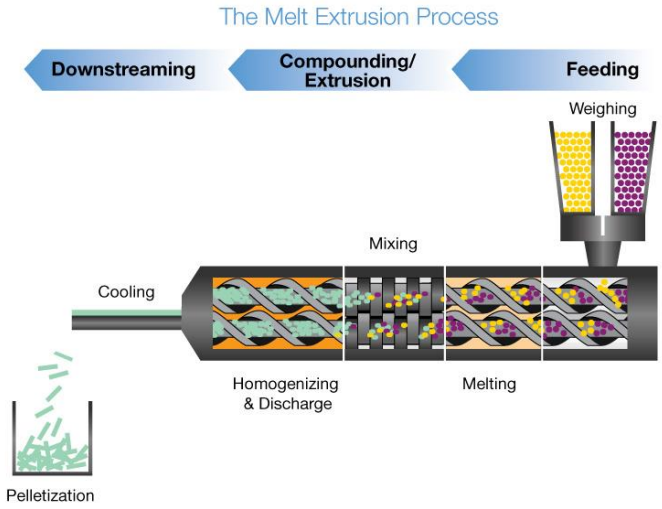

Figure 3 Example of melt mixing extrusion process with a twin-screw extruder. Nanopowder (yellow spheres) and polymer (purple spheres) are mixed to prepare a nanocomposite material in form of pellets.

Melt mixing is the fastest method for introducing new nanocomposites from thermoplastic polymer to market since it can take full advantage of well-built polymer processing equipments including extruders or injectors. For example, nanoscale silica or $CaCO_3$ filled Nylon composites have successfully been produced by using high velocity oxy-fuel (HVOF) combustion spray process. Hong and coworkers also reported that nano-ZnO and low-density polyethylene (PE) were melt compound in a high-shear mixer to prepare nanocomposites with an increase in the resistance to thermal degradation[25], while Zhao et al.[26] prepared by extrusion polypropylene (PP) composites in which ZnO nanoparticles modified with an organo- silane agent were good

dispersed. Although being successful in many cases, melt mixing method has several drawbacks. First, this process only builds up relatively weak interaction force between the polymer and the nanopowder. Nanopowders have a very strong tendency to aggregate and even if the surface modification is applied, breaking aggregates during melt processing is often difficult. Second, for some polymers, this processing method may be limited due to rapid increase of the viscosity with the addition of a few volume fractions of nanopowder. Moreover, the high temperature processing of this method limits its use.

Solvent casting

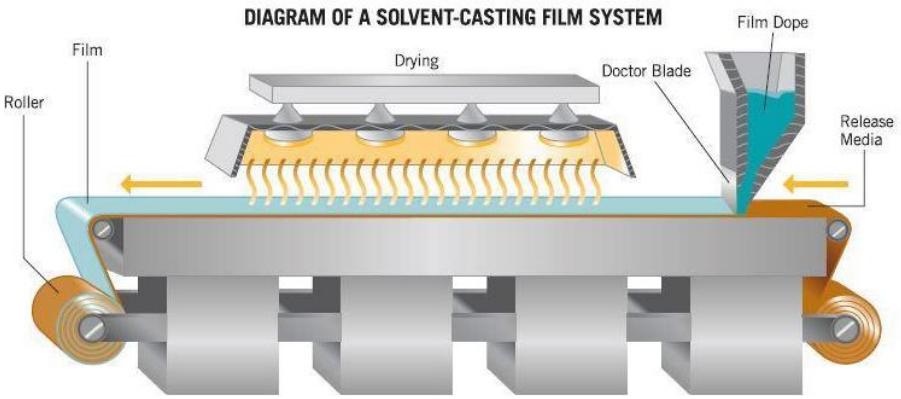

Figure 4 Diagram of industrial solvent casting process

Another approach for the preparation of nanocomposites is the dispersion of nanoparticles in the polymer solution. The mixture may be cast in containers or coated on substrates. Films or sheets are obtained by evaporation of the solvent. The major requirement in order to get homogeneous materials is the good solubility of polymer and

dispersibility of the nanoparticles in the solvent. It is possible to use different solvent to disperse nanoparticles and dissolve the polymer, but they have to be compatible. Due to its simplicity the film casting method is widely used mainly for the preparation of films of about 1-100 μm in thickness. They are prepared by spin coating or casting through a blade. Since the polymer synthesis can be separated from nanoparticles synthesis and the nanocomposite fabrication, from simpler to more complex polymer architectures can be used. For example, Ying Li and coworkers[22] successfully prepared brush-grafted TiO_2 and they finely dispersed the NCs in (PDMS), obtaining optically clear films.

In situ polymerization

Another method is the graft polymerization, where nanopowders are dispersed in the monomer, and the resulting mixture is polymerized by standard polymerization methods. Since the viscosity of monomer is quite low and the polymerization process can last some days, while the nanoparticles sedimentation can proceed quite quickly, the main challenge of this approach is to obtain stable dispersions of nanoparticles in the monomer. In order to get over this drawback, nanoparticles surface has to be modified in order to reduce the interfacial tension between the nanoparticles and the monomer, that would induce the formation of aggregates. Three types of modification are reported in literature. The first approach (called *ad-polymerization*) consist in the absorption of amphiphilic molecules, such as long chains acids, alcohols or amines, on the particles surface. The surfactant molecules interact with the surface by ionic attractions, hydrogen or

coordinative bonding building a sort of hydrophobic shell that avoid the nanoparticles aggregation. The surfactant molecules do not participate directly on the polymerization but permit a good dispersion of the nanoparticles in the monomer and, in a second step, in the polymer. Avella et al. have used $CaCO_3$ particles covered by stearic acid for in situ polymerization of the PMMA nanocomposite[27]. This is the approach used in our project in the fabrication of TiO_2-PMMA sheets, in which nanoparticles were functionalized with some amphiphilic molecules in order to disperse them in MMA. The dispersion stability was verified for a month because the bulk polymerization of the material lasts several days.

PGNs-based nanocomposite: properties and applications

Reinforcement agents: This is probably the oldest and well-established technology in which nanosystems are employed. The incorporation of NCs into polymer matrices was firstly noted thanks to the enhancement of rubbery material's mechanical properties. Clays are the mostly used inorganic filler used for this kind of application thanks to their abundance, low costs and facile integration in polymeric matrices with exfoliation process[28,29]. Properly dispersed and aligned clay platelets have proven to be very effective for increasing stiffness. Generally, the addition of inorganic fillers in a polymeric material arises in an enhancement of Young's modulus. This phenomenon is related to two main factors: the presence of a rigid object inside the polymer matrix, that leads to stiffer materials, moreover, the polymer grafted on the NCs

is able to make a higher number of entanglements with polymer matrix resulting in a tougher material[1].

Optoelectronic applications: In the simplest case, taking advantage of the intrinsic properties of the fillers (such as nanoscale size to limit light scattering and suitable crystalline phase for high refractive index) and polymer matrices (such as flexibility, good processability, and transparency) it is possible to produce a flexible polymeric material with enhanced refractive index[30–34]. The introduction of organic functional ligands or chromophores onto the nanoparticle surface can play an important role not only in the stability of these particles, but also in the tailoring of the optical and electronic properties of nanoparticles through energy transfer or charge transfer, leading to the production of photoactive nanoparticles embodied in polymer matrices[35]. These materials can be used as photo responsive sensors, or in the case of colloidal quantum dots they are suitable as fluorophores in luminescent solar concentrators. These systems consist of plastic optical waveguides doped with fluorophores, or glass slabs coated with active layers of emissive materials. Direct and diffused sunlight is absorbed by the fluorophores and re-emitted at longer wavelengths. The luminescence, guided by total internal reflection, propagates towards a photovoltaic cell placed at the edge of the waveguide, where it is converted into electricity[36–39]. The fine distribution of active nanoparticles is needed in order to achieve transparent materials able to absorb all the sun light and effectively deliver it to the edges of the luminescent solar concentrator.

Nanodielectric systems: High performance dielectrics are crucial to components for nowadays common technologies, ranging from gate dielectrics in transistors to high-voltage insulation and capacitors in power electronics. Polymer dielectrics afford a unique combination of processability with tunability of resistance, permittivity, dielectric loss, DC dielectric breakdown strength, and gradual failure mechanisms[40]. Different inorganic platforms provide a specific improvement; for example, for high voltage (HV) insulation, the use of inorganic fillers and coatings, e.g. boron nitride (BN), silica (SiO_2), alumina (Al_2O_3) titania (TiO_2), and silicon carbide (SiC), has been a staple for applications requiring higher temperatures and electrical stress. An optimized polymer−inorganic formulation improves electrical characteristics key to reliability and lifetime. The controlled incorporation provides the ability to tune the permittivity of nanocomposite materials. The origin of the high dielectric constant can be ascribed to the assembling of nanoparticles in controlled aggregates, where a number of core–shell crystals share their faces and form capacitive microstructures. These aggregates separated by a thin layer of polymer allow the high increase of avoiding the formation of the continuous network responsible for enhancement of the electrical characteristics[41].

References

(1) Kumar, S. K.; Benicewicz, B. C.; Vaia, R. A.; Winey, K. I. 50th Anniversary Perspective: Are Polymer Nanocomposites Practical for Applications? *Macromolecules* **2017**, *50* (3), 714–731.

(2) Khare, H. S.; Burris, D. L. A Quantitative Method for Measuring Nanocomposite Dispersion. *Polymer (Guildf).* **2010**, *51* (3), 719–729.

(3) Schaefer, D. W.; Justice, R. S. How Nano Are Nanocomposites? *Macromolecules* **2007**, *40* (24), 8501–8517.

(4) Kumar, S. K.; Jouault, N.; Benicewicz, B.; Neely, T. Nanocomposites with Polymer Grafted Nanoparticles. *Macromolecules* **2013**, *46* (9), 3199–3214.

(5) Lenart, W. R.; Hore, M. J. A. Structure-Property Relationships of Polymer-Grafted Nanospheres for Designing Advanced Nanocomposites. *Nano-Structures and Nano-Objects* **2017**.

(6) Li, Y.; Huang, Y.; Krentz, T.; Natarajan, B.; Neely, T.; Schadler, L. S. Polymer Nanocomposite Interfaces: The Hidden Lever for Optimizing Performance in Spherical Nanofilled Polymers. *Interface/Interphase Polym. Nanocomposites* **2016**, 1–69.

(7) Srivastava, S.; Schaefer, J. L.; Yang, Z.; Tu, Z.; Archer, L. A. 25th Anniversary Article: Polymer-Particle Composites: Phase Stability and Applications in Electrochemical Energy Storage. *Adv. Mater.* **2014**, *26* (2), 201–234.

(8) Li, Y.; Krentz, T. M.; Wang, L.; Benicewicz, B. C.; Schadler, L. S. Ligand Engineering of Polymer Nanocomposites: From the Simple to the Complex. *ACS Appl. Mater. Interfaces* **2014**, *6* (9), 6005–6021.

(9) Ligoure, C.; Leibler, L. Thermodynamics and Kinetics of Grafting End-Functionalized Polymers to an Interface. *J. Phys.* **1990**, *51* (12), 1313–1328.

(10) Asai, M.; Zhao, D.; Kumar, S. K. Role of Grafting Mechanism on the Polymer Coverage and Self-Assembly of Hairy Nanoparticles. *ACS Nano* **2017**, *11* (7), 7028–7035.

(11) Matyjaszewski, K. Atom Transfer Radical Polymerization (ATRP): Current Status and Future Perspectives. *Macromolecules* **2012**, *45* (10), 4015–4039.

(12) Moad, G.; Chong, Y. K.; Postma, A.; Rizzardo, E.; Thang, S. H. Advances in RAFT Polymerization : The Synthesis of Polymers with Defined End-Groups. 2005.

(13) Chauvin, F.; Dufils, P.-E.; Gigmes, D.; Guillaneuf, Y.; Marque, S. R. A.; Tordo, P.; Bertin, D. Nitroxide-Mediated Polymerization: The Pivotal Role of the k_d Value of the Initiating Alkoxyamine and the Importance of the Experimental Conditions. *Macromolecules* **2006**, *39* (16), 5238–5250.

(14) Huang, X.; Wirth, M. J. Surface-Initiated Radical Polymerization on Porous Silica. *Anal. Chem.* **1997**, *69* (22), 4577–4580.

(15) Pyun, J.; Matyjaszewski, K.; Kowalewski, T.; Savin, D.; Patterson, G.; Kickelbick, G.; Huesing, N. Synthesis of Well-Defined Block Copolymers Tethered to Polysilsesquioxane Nanoparticles and Their Nanoscale Morphology on Surfaces [2]. *J. Am. Chem. Soc.* **2001**, *123* (38), 9445–9446.

(16) Pyun, J.; Jia, S.; Kowalewski, T.; Patterson, G. D.; Matyjaszewski, K. Synthesis and Characterization of Organic/Inorganic Hybrid Nanoparticles: Kinetics of Surface-Initiated Atom Transfer Radical Polymerization and Morphology of Hybrid Nanoparticle Ultrathin Films. *Macromolecules* **2003**, *36* (14), 5094–5104.

(17) Matyjaszewski, K.; Miller, P. J.; Shukla, N.; Immaraporn, B.; Gelman, A.; Luokala, B. B.; Siclovan, T. M.; Kickelbick, G.; Valiant, T.; Hoffmann, H.; et al. Polymers at Interfaces: Using Atom Transfer Radical Polymerization in the Controlled Growth of Homopolymers and Block Copolymers from Silicon Surfaces in the Absence of Untethered Sacrificial Initiator. *Macromolecules* **1999**, *32* (26), 8716–8724.

(18) Husseman, M.; Malmström, E. E.; McNamara, M.; Mate, M.; Mecerreyes, D.; Benoit, D. G.; Hedrick, J. L.; Mansky, P.; Huang, E.; Russell, T. P.; et al. Controlled Synthesis of Polymer Brushes by "Living" Free Radical Polymerization Techniques. *Macromolecules*

1999, *32* (5), 1424–1431.

(19) Tsujii, Y.; Ejaz, M.; Sato, K.; Goto, A.; Fukuda, T. Mechanism and Kinetics of RAFT-Mediated Graft Polymerization of Styrene on a Solid Surface. 1. Experimental Evidence of Surface Radical Migration. *Macromolecules* **2001**, *34* (26), 8872–8878.

(20) Li, Y.; Schadler, L. S.; Benicewicz, B. C. Surface and Particle Modification via the RAFT Process: Approach and Properties. In *Handbook of RAFT Polymerization*; Wiley-VCH Verlag GmbH & Co. KGaA: Weinheim, Germany, 2008; pp 423–453.

(21) Akcora, P.; Liu, H.; Kumar, S. K.; Moll, J.; Li, Y.; Benicewicz, B. C.; Schadler, L. S.; Acehan, D.; Panagiotopoulos, A. Z.; Pryamitsyn, V.; et al. Anisotropic Self-Assembly of Spherical Polymer-Grafted Nanoparticles. *Nat. Mater.* **2009**, *8* (4), 354–359.

(22) Li, Y.; Tao, P.; Viswanath, A.; Benicewicz, B. C.; Schadler, L. S. Bimodal Surface Ligand Engineering: The Key to Tunable Nanocomposites. *Langmuir* **2013**, *29* (4), 1211–1220.

(23) Rungta, A.; Natarajan, B.; Neely, T.; Dukes, D.; Schadler, L. S.; Benicewicz, B. C. Grafting Bimodal Polymer Brushes on Nanoparticles Using Controlled Radical Polymerization. *Macromolecules* **2012**, *45* (23), 9303–9311.

(24) Natarajan, B.; Neely, T.; Rungta, A.; Benicewicz, B. C.; Schadler, L. S. Thermomechanical Properties of Bimodal Brush Modified Nanoparticle Composites. *Macromolecules* **2013**, *46* (12), 4909–4918.

(25) Hong, J. I.; Cho, K. S.; Chung, C. I.; Schadler, L. S.; Siegel, R. W. Retarded Cross-Linking in ZnO-Low-Density Polyethylene Nanocomposites. *J. Mater. Res.* **2002**, *17* (05), 940–943.

(26) Zhao, H.; Li, R. K. Y. A Study on the Photo-Degradation of Zinc Oxide (ZnO) Filled Polypropylene Nanocomposites. *Polymer (Guildf).* **2006**, *47* (9), 3207–3217.

(27) Avella, M.; Errico, M. E.; Martuscelli, E. Novel PMMA/$CaCO_3$

Nanocomposites Abrasion Resistant Prepared by an in Situ Polymerization Process. *Nano Lett.* **2001**, *1* (4), 213–217.

(28) Alexandre, M.; Dubois, P. Polymer-Layered Silicate Nanocomposites: Preparation, Properties and Uses of a New Class of Materials. *Mater. Sci. Eng. R Reports* **2000**, *28* (1), 1–63.

(29) Giannelis, E. P. Polymer Layered Silicate Nanocomposites. *Adv. Mater.* **1996**, *8* (1), 29–35.

(30) Fujita, M.; Idota, N.; Matsukawa, K.; Sugahara, Y. Preparation of Oleyl Phosphate-Modified TiO 2 / Poly (Methyl Methacrylate) Hybrid Thin Films for Investigation of Their Optical Properties. *J. ofNanomaterials* **2015**, *2015*, 1–7.

(31) Colombo, A.; Tassone, F.; Mauri, M.; Salerno, D.; Delaney, J. K.; Palmer, M. R.; Rie, R. D. La; Simonutti, R. Highly Transparent Nanocomposite Films from Water-Based Poly(2-Ethyl-2-Oxazoline)/TiO2 Dispersions. *RSC Adv.* **2012**, *2* (16), 6628.

(32) Nussbaumer, R. J.; Caseri, W. R.; Smith, P.; Tervoort, T. Polymer-TiO2 Nanocomposites: A Route towards Visually Transparent Broadband UV Filters and High Refractive Index Materials. *Macromol. Mater. Eng.* **2003**, *288* (1), 44–49.

(33) Tao, P.; Viswanath, A.; Li, Y.; Siegel, R. W.; Benicewicz, B. C.; Schadler, L. S. Bulk Transparent Epoxy Nanocomposites Filled with Poly(Glycidyl Methacrylate) Brush-Grafted TiO2 Nanoparticles. *Polym. (United Kingdom)* **2013**, *54* (6), 1639–1646.

(34) Tao, P.; Li, Y.; Rungta, A.; Viswanath, A.; Gao, J.; Benicewicz, B. C.; Siegel, R. W.; Schadler, L. S. TiO2 Nanocomposites with High Refractive Index and Transparency. *J. Mater. Chem.* **2011**, *21* (46), 18623.

(35) Gao, J.; Lü, C.; Lü, X.; Du, Y. APhen-Functionalized Nanoparticles–polymer Fluorescent Nanocomposites via Ligand Exchange and in Situ Bulk Polymerization. *J. Mater. Chem.* **2007**, *17* (43), 4591.

(36) Meinardi, F.; Colombo, A.; Velizhanin, K. A.; Simonutti, R.; Lorenzon, M.; Beverina, L.; Viswanatha, R.; Klimov, V. I.; Brovelli, S. Large-Area Luminescent Solar Concentrators Based on Stokes-Shift-Engineered Nanocrystals in a Mass-Polymerized PMMA Matrix. *Nat. Photonics* **2014**, *8* (5), 392–399.

(37) Meinardi, F.; McDaniel, H.; Carulli, F.; Colombo, A.; Velizhanin, K. A.; Makarov, N. S.; Simonutti, R.; Klimov, V. I.; Brovelli, S. Highly Efficient Large-Area Colourless Luminescent Solar Concentrators Using Heavy-Metal-Free Colloidal Quantum Dots. *Nat. Nanotechnol.* **2015**, *10* (10), 878–885.

(38) Monguzzi, A.; Bianchi, F.; Bianchi, A.; Mauri, M.; Simonutti, R.; Ruffo, R.; Tubino, R.; Meinardi, F. High Efficiency Up-Converting Single Phase Elastomers for Photon Managing Applications. *Adv. Energy Mater.* **2013**, *3* (5), 680–686.

(39) Monguzzi, A.; Mauri, M.; Bianchi, A.; Dibbanti, M. K.; Simonutti, R.; Meinardi, F. Solid-State Sensitized Upconversion in Polyacrylate Elastomers. *J. Phys. Chem. C* **2016**, *120* (5), 2609–2614.

(40) Prateek; Thakur, V. K.; Gupta, R. K. Recent Progress on Ferroelectric Polymer-Based Nanocomposites for High Energy Density Capacitors: Synthesis, Dielectric Properties, and Future Aspects. *Chem. Rev.* **2016**, *116* (7), 4260–4317.

(41) Crippa, M.; Bianchi, A.; Cristofori, D.; D'Arienzo, M.; Merletti, F.; Morazzoni, F.; Scotti, R.; Simonutti, R. High Dielectric Constant Rutile-Polystyrene Composite with Enhanced Percolative Threshold. *J. Mater. Chem. C* **2013**, *1* (3), 484–492.

Chapter 2. Surface Characterization of TiO_2 Polymorphic Nanocrystals through ^{1}H-TD-NMR

Introduction

Nanocrystals often display interesting properties, different from those of bulk materials of similar composition. In ferromagnetic NCs smaller than the bulk magnetic domain size, the phenomenon of superparamagnetism appears[1] which can be exploited for biomedical applications such as the improvement of magnetic resonance imaging[2, 3] or hyperthermal treatment of cancer cells.[4] Size reduction can also bring significant quantomechanical properties such as the quantized conductivity of nanowires or the enhanced luminescence of Si quantum dots.[5] Bioactivity is also influenced by crystal size and shape,[6] both at cellular and systemic level; for example silver NCs are effective bactericides[7], while renal clearance of non-biodegradable particles is limited to few nm CdSe/ZnS quantum dots.[8] At the nanoscale, the surface to volume ratio of materials becomes preponderant and the surface effects play a major role in determining the properties of the NC.[9] In many cases a proper surface modification of NCs is strongly required in order to avoid segregation[10] and thus produce viable nancomposites. Surface decoration is the main strategy to ensure optimal mixing of graphene,[11] silica,[12] or clays[13] within polymer matrices, producing materials with optimized properties. Interaction

with cells, including internalization and cytotoxicity, is also influenced by surface functionality even more than size.[14] TiO_2 in the form of NCs is routinely used in dye-sensitized solar cells[15] or dispersed in a solid polymer matrix, endowing it with enhanced mechanical[16], optical[17] or electrical[18] properties. Different properties are associated with the different phases of titanium dioxide, for example rutile is distinguished for its higher permittivity constant compared to anatase,[19] and thus significant efforts were made to synthesize phase pure TiO_2 NCs[20]. Toxicity can also depend on the polymorph,[21] a relevant issue considering the amount used in food.[22] In this work, we explore the application of time domain NMR (TD-NMR) to characterize the surface of TiO_2 nanoparticles, adding a new point of view to the wide diversity of methods commonly employed in the field of NCs characterization. To date, dynamic light scattering (DLS) is the most used technique for measuring the size distribution of NCs in solution,[23] often coupled with the z-potential surface charge measurement. Scanning and transmission electron microscopies (SEM, TEM) and x-rays diffraction (XRD) are widely used for determining the morphology (size and shape) and the crystal structure of NCs. The Brunauer-Emmett-Teller (BET) analysis allows quantifying the specific NCs' surface area, while Fourier transform infrared spectroscopy (FTIR)[24], high field nuclear magnetic resonance (NMR)[25], X-ray photoelectron spectroscopy (XPS) and elemental analysis can be used for characterizing the nature and the binding modes of surface ligands. Time Domain (TD) NMR, a technique based on the same principles as modern (pulsed) NMR but involves direct study of the free induction decay signal without Fourier transform. Interestingly by TD NMR it is possible to measure the effect

on the proton transverse relaxation times, ^{1}H T_2, of water exerted by the dispersed NCs, as function of the total accessible surface.

In this work we demonstrate for the first time that ^{1}H-TD-NMR is able to differentiate the surface of TiO_2 NCs of the three different polymorphic crystal structures: anatase, brookite and rutile. We selected TiO_2 as the subject of our study as this material can be synthesized at the nanoscale with high control over the size, shape and crystal structure. Rutile, anatase and brookite TiO_2 NCs were either synthesized or acquired and fully characterized via DLS, XRD, TEM and BET analyses.

^{1}H T_2 Relaxation of nanocrystal dispersions

Relaxation of nuclear spin magnetization of solvents in presence of paramagnetic iron or manganese NCs has been studied in depth due to important applications as contrast agent for magnetic resonance imaging (MRI).[2] Where the disperse phase contains protons, as in the case of emulsions, mobility contrast is often present and methods based on pulsed field gradient (PFG) are applicable to decouple local motions from the translational motion of the particles, thus determining their size.[26] Time Domain NMR can also be applied to directly determine the internal dynamic state of the disperse phase.[27]

Even in absence of the strong and long range relaxing effect due to the local magnetic field gradient generated by paramagnetic domains, short range interaction with the NCs leads to relaxation. Namely, the solvent molecules interacting with the NCs surface have a restricted mobility compared to the not-interacting one, and dipolar interactions with surface groups or with other adsorbed particles can bring a rapid

decrease of the transverse magnetization. Comprehensive models describing the relaxation of interacting and not interacting solvents have been proposed in the literature, and also used to estimate the size of diamagnetic inorganic particles such as silica, and the interaction between NCs and polymers, including qualitative and quantitative measurements of absorption of polymers on the surface.[28, 2] This concept has growing applications in the characterization of cements[30] and carbon fillers[31] and has recently been refined to include study of particle shape[32] or the coverage.[33]

Even though the mechanisms that induce NMR relaxation are still debated,[34] with possibly complementary effects due to dipolar interaction and motional constraint, most interpretative models describe solvent as a two phase system, composed by a population of molecules bound to the particle surface, and a population of bulk solvent, as depicted in Figure 5.

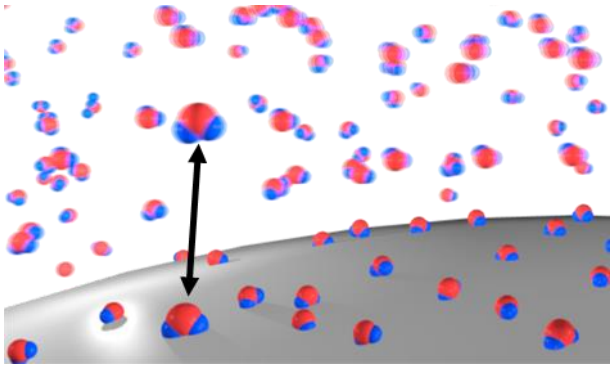

Figure 5: Representation of the interaction between water molecule and a generic nanocrystal. The arrows indicate the dynamic exchange between the bound phase and the free solvent. Free water molecules are represented blurred to indicate their high mobility.

For analytical treatment of the resulting NMR relaxation, we define P_b, and P_f as the probabilities to find a proton in the interacting (bound)

and not-interacting (free) phase at a given time, v_b and v_f the rates at which a solvent molecule leaves the two phases, and R_b and R_f the NMR relaxation rates of the two phases, respectively. At equilibrium, $v_b = v_f$ and the relaxation curve can be analytically determined according to the fast ($v_b \gg R_b$ and $v_f \gg R_f$) or slow exchange model ($v_b \ll R_b$ and $v_f \ll R_f$). In the first case, a single exponential decay is observed and the relaxation rate R is given by the average of the relaxation rates, weighted by the probability of occupying each phase:

$$R = P_b R_b + (1 - P_b) R_f \quad (1)$$

While in the slow exchange regime, the predicted relaxation curve is bimodal, and constituted by the summation of separate contributions from the free and bound protons

$$I(t) = I_0\left(P_b e^{-R_b t} + P_f e^{-R_f t}\right). \quad (2)$$

This simple expression, where I_0 and $I(t)$ represent the intensity at t=0 and at the time t, respectively, is substituted by a multimodal curve or even a continuous distribution in case different populations of particles or environments are present, as in nanoporous silica or natural rocks.[35] Relaxation curves acquired for water dispersions containing TiO_2 NCs this work are well fitted by a single exponential, so the equations will be expressed within the framework of the fast exchange regime. Since the probability P_b is the ratio between the number of solvent molecules interacting with the surface and the total number of solvent molecules, it can be defined by

$$P_b = C_M \sigma_p \frac{m_s}{N_0} \mu \quad (3)$$

where C_M is the NC mass fraction, σ_p their specific surface, m_s the solvent molar mass, N_0 the Avogadro's constant, and μ the number of solvent molecules bound to the surface, per unit surface. For water dispersions, the T_2 is in the range of seconds and thus the relaxation rate of the free solvent is significantly smaller than the bound solvent relaxation rate, and a linear relation between the nanocrystal concentration and the NMR measurable relaxation rate can be easily obtained:

$$R = \frac{\sigma_p m_s \mu R_b}{N_0} C_M + R_f \quad (4)$$

Some previous works[33, 36] postulates that each particle binds a layer with a thickness L independent from particle size and that the only relevant variable is R_b. We propose an even weaker assumption: the amount of particles per surface unit and the relaxation rate of the same cannot be disentangled. Thus, product μR_b defines the surface-solvent interaction as a whole. The most straightforward application is that, after a calibration of this parameter for a given system we can obtain an unknown specific surface area from a known concentration of NCs and vice versa. This basic application can be helpful in evaluating the amount of NCs after a centrifugation or dialysis step. More interestingly, if the specific surface σ can be determined independently from another technique, μR_b provides a measure of the solvent surface interaction, a predictive factor of its catalytic of biological activity. For example, it was shown that silica, alumina and polystyrene particles possess different specific relaxivity after surface normalization.[37] Unsurprisingly, hydrophobic polystyrene surfaces have an almost negligible interaction with water, as compared with silica.

Materials and methods

Titanium (IV) butoxide (TB, 97%), titanium (IV) chloride ($TiCl_4$, >99%), oleic acid (OLAC, 90%), oleyl amine (OLAM, 70%), 1-octadecene (ODE, 90%), Ammonium hydroxide solution (NH_4OH, 28%), Absolute ethanol (≥ 99.8%), hexane (≥ 95%), dimethylformamide (DMF, ≥ 99.9%), Water and toluene (≥ 99.9%) were purchased from Sigma Aldrich. Nitrosoniumtetrafluoroborate ($NOBF_4$, 98%) was purchased from Alfa Aesar. Rutile NCs were purchased and used as received or hydroxylated as described below. Two different samples were acquired, with different sizes and specific surface area: Rut50 was purchased from Sigma Aldrich (<100 nm diameter, nominal surface area 50 m^2g^{-1}) and Rut20 was purchased by NanoAmor (<50 nm diameter, nominal surface area 160 m^2g^{-1}).

Synthetic Methods

Synthesis of anatase TiO_2 NCs

The synthesis of TiO_2 NCs is accomplished using a solvothermal method.[38] Typically, TB (10 mmol) is added to a mixture of 60 mmol of OLAC, 40 mmol of OLAM and 11.7 mL of absolute ethanol. The mixture is poured in a 40 mL Teflon beaker and stirred for 15 min before being transferred into a 400 mL Teflon-lined stainless-steel autoclave containing 40 mL of a solution of ethanol and water (96% ethanol). The system is then heated to 180 °C for 18 h. The crude product is then centrifuged, precipitating a white powder constituted by titania NCs covered by oleic acid whose polar terminal group is bound to the

surface. The aliphatic portion of oleic acid allows easy dispersal in hexane, an apolar solvent. The particles are precipitated several times in ethanol to remove excess ligands and eventually dispersed in hexane. *Synthesis of brookite TiO_2 NCs*. TiO_2brookite NCs were synthesized following the procedure reported by Buonsanti et al.[39] In a typical synthesis a solution of ODE (0.24 mol, 60.6 g), OLAM (0.26mol, 69.6 g) and OLAC (0.02 mol. 5.65 g) are loaded into a three-neck flask and degassed at 120 °C for 90 min, after which the mixture is cooled down to 50 °C in N_2 ambient. $TiCl_4$ (0.02 mol, 3.8 g) is slowly added to the solution and the flask is heated up to 290 °C. The reaction is halted after 30 min and cooled down using an ice bath. The solution is dispersed in hexane and then precipitated several times in 2-propanol and then kept in hexane.

Ligand stripping procedure

A dispersion of TiO_2 particles in hexane is added to a solution of $NOBF_4$ and DMF. The resulting biphasic mixture is stirred to maximize the interface where the ligand exchange takes place. As the ligand is substituted by BF_4^-, the surface polarity changes and NCs are transferred from the non-polar (hexane) to the (DMF) phase, typically within 60 min.[40]. The surface modified NCs are then purified by precipitation with the addition of toluene, that is miscible with DMF, then the precipitated NCs are dispersed in water. In order to increase the hydroxyl groups on the NCs surface and to have a ligand free surface, the as prepared particles are treated with a solution of ammonium hydroxide and stirred for 24 hours at 70°C.[41]After that process the particles are purified by centrifugation with water till the solution reaches pH 7-9. This process

was applied to all TiO_2 samples in order to avoid different behaviors related to the sample preparation.

Characterization methods

The hydrodynamic diameter and size distributions of the particles were determined by Dynamic Light Scattering (DLS) in deionized water (0.1 mg mL-1). The measures were recorded at 25 °C, on a Malvern Zetasizer equipped with a continuous wave 1 mW He-Ne laser operating at 632.8 nm and an avalanche photodiode detector, Q.E. > 50% at 633 nm, placed at 173° with respect to the incident beam. Reported data is the average of at least three different measurements of the size distribution as function of the intensity. Colloid stability was evaluated with ζ-Potential was measured at 25 °C in deionized water, with a sample concentration of 0.1 mg mL-1 and using a Malvern Zetasizer instrument. Nitrogen adsorption-desorption isotherms were measured at liquid nitrogen temperature using an ASAP 2010 analyzer (Micrometrics). The samples were outgassed for 12h at 473K. Surface area was calculated using the Brunauer, Emmet, and Teller (BET) model.42 For X-ray characterization: a D8 Advance powder diffractometer (Bruker) was used, with CuKα1 radiation (λ=1.5418Å) and secondary-beam monochromator. The powder is added on a quartz sample holder and measured. Micro-Raman measurements were carried out at room temperature by a confocal LABRAM (JobinYvon) spectrometer, operating in backscattering configuration. Measurements were performed on the samples in dry powder form. A helium–neon laser (wavelength 632.8 nm, nominal power 17 mW) was used as

exciting source with spectral resolution of about 2 cm−1. The scattered light was detected by a CCD (Sincerity, JobinYvon). A microscope (Olympus BX40) was used to focus the excitation on the samples and to collect the scattered radiation with a 20x objective with a numerical aperture of 0.40. Spectra are presented after baseline subtraction of broad luminescence signals. The powder is added on a quartz sample holder and measured. Amount and definition of tethered ligand on the NCs surface has been verified with Attenuated Total Reflection (ATR)-FTIR and Thermogravimetric analysis (TGA). Fourier transform infrared characterization was performed using a Perkin Elmer Spectrum 100 instrument scanning from 650 to 4000 cm-1 with a resolution of 4 cm-1 for 64 scans. The sample, in form of powder, is added on the sample holder and directly analyzed over the Si crystal with the Universal ATR (UATR). Thermogravimetric analysis was carried out with TA Q500 analyzer (TA Instruments) by heating the samples powders from room temperature to 1073 K at 10 K/min in air. Bright field TEM (BF-TEM) imaging was performed on a JEOL JEM-1011 microscope equipped with a thermionic gun operating at 100 kV accelerating voltage. For these analyses the samples were prepared by dropping dilute suspensions of NCs onto carbon coated 200 mesh copper grids. All TD-NMR relaxation experiments were performed at 303K using a 0.5T (19.9MHz proton Larmor frequency) Bruker Minispec mq20 NMR spectrometer equipped with a BVT3000 temperature control system working with nitrogen gas. The temperature was calibrated using an external thermometer with an accuracy of 1 K. The precision is 0.1 K and the temperature is stable within that range during the measurements. All nanoparticles were studied at different

concentrations by preparing a stock dispersion at high concentration and then performing separate dilutions. For each concentration, we inserted 0.15 mL of water dispersion in a 10 mm NMR tube and sonicated it prior to measurement. For the measurement of the transverse relaxation curve of water protons the Carr-Purcell-Meiboom-Gill (CPMG) pulse sequence was used, acquiring 3000 points with a spacing of 4ms between successive echoes with full phase cycle and averaging with at least 16 scans. Trace element analysis was performed on the dry powder by Energy dispersive X-ray fluorescence analysis.

Results and discussions

Since size and shape potentially affect nanocrystal surface energy and interaction with the surrounding environment, NCs endowed with different shape and dimension have been synthetized for testing. Commercial TiO_2 rutile samples, purchased from two different suppliers, anatase and brookite TiO_2 NCs, synthesized by colloidal and solvothermal approaches, were fully characterized by means of TEM, DLS, XRD, Z-Potential and BET after being stripped by their capping agents. The resulting characteristics are listed in Table 1.

Table 1 Crystal dimensions derived from XRD for Ana10 calculated at (101) peak, Bro40 at (120), Rut20 and Rut50 at (110) reported with their standard deviation, TEM reported with their standard deviation and DLS measurements in water reported with their PDI. BET Specific surface areas as well as an estimate of surface area based on TEM size presented in the supporting information are reported with their standard deviation. Z-potential measured on water dispersions are reported with their standard deviation.

Sample	XRD	TEM (larger dimension first)		DLS	PDI	SSA_{BET}	$SSA_{predicted}$	ζ-Potential
	nm	nm				(m^2/g)	(m^2/g)	(mV)
Ana10	5.9±0.4	7.6±1.1		16	0.191	174±7	197.4±28.6	-27.8±6.5
Rut20	4.6±0.2	21.9±3.3	4.0±0.5	115	0.141	164±7	141.1±38.9	-31.0±4.8
Bro40	5.6±0.4	42.3±7.5	3.5±0.6	110	0.220	174±7	154.2±53.8	-29.3±5.2
Rut50	13.3±0.2	65.1±7.8	30.0±2.8	150	0.285	26±7	20.4±6.2	-17.7±7.9

A direct investigation of stripped crystals size distribution and morphology is provided by TEM microscopy: representative images of the assemblies detected by sampling dispersions are presented in Figure 6.

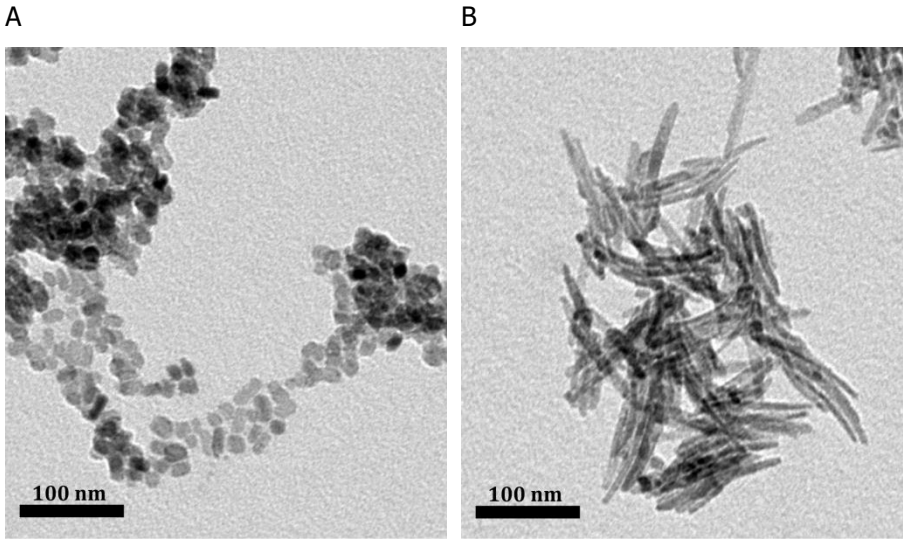

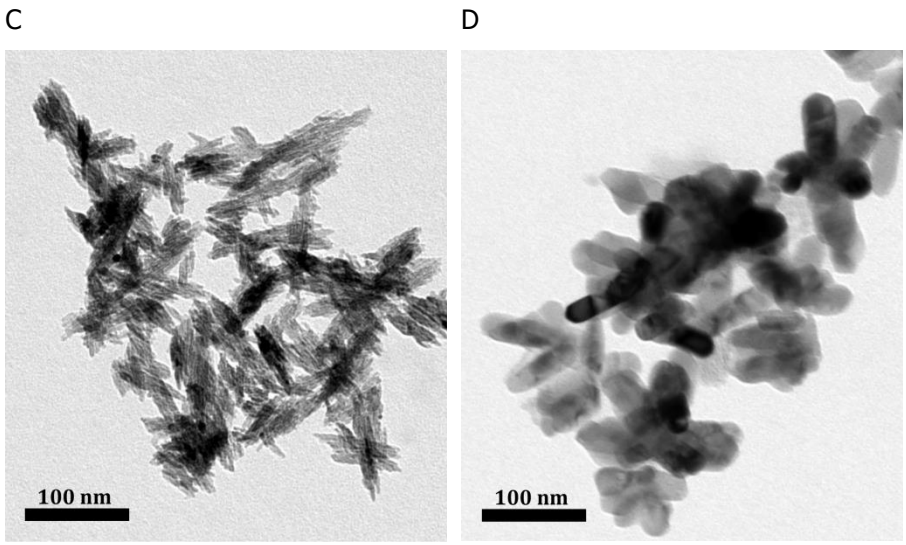

Figure 6: From top to bottom TEM images of A) Ana10, B) Bro40, C) Rut20, D) Rut50. All images were performed starting from highly dilute dispersions, indicating the extent of aggregation in the wet systems.

TEM micrographs show that both the commercial rutile (Figure 6, C - D) and brookite (Figure 6, B) NCs have a rod-like morphology, while anatase (Figure 6, A) has a quasi-spherical structure. Starting from the images it is possible to define height and width of the crystals and with this information, using simple geometrical models, it is calculated the specific surface area for all samples. The analysis of the pictures carried out with ImageJ software, in particular with the particle analyzer plug-in, it has been possible to determine the size of the particles Figure 7.

A

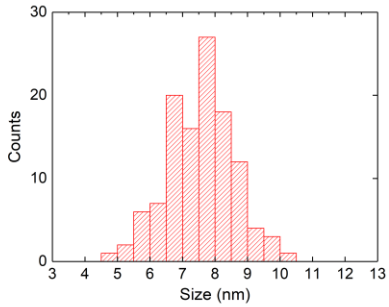
Counts
Size (nm)

B1

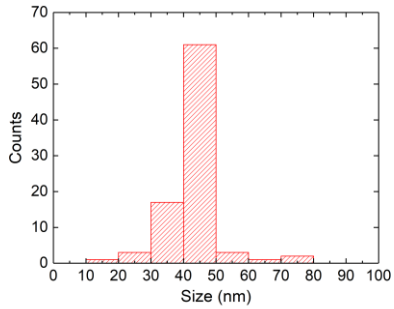
Counts
Size (nm)

B2

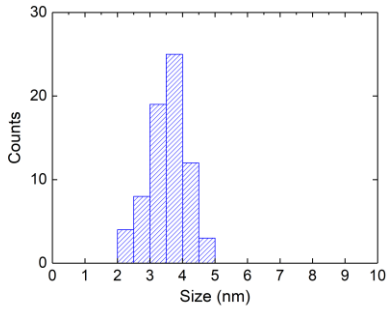
Counts
Size (nm)

C1

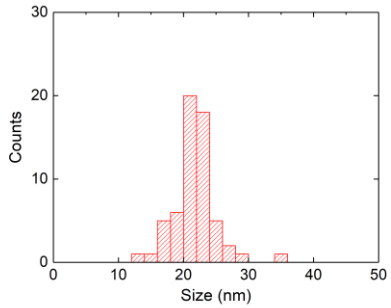
Counts
Size (nm)

C2

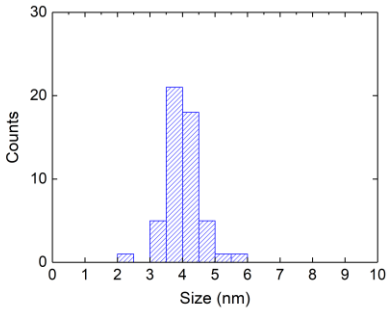
Counts
Size (nm)

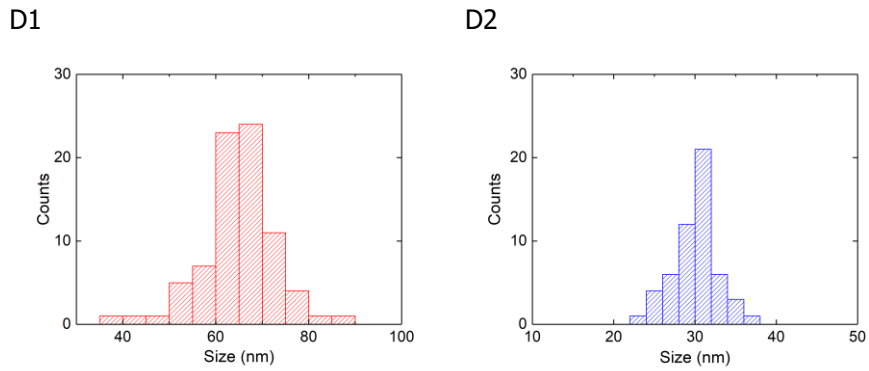

Figure 7 Histograms of the NCs size distribution from TEM micrographs: A size of the Ana10 (red); B1 length of the Bro40 (red); B2 width of the Bro40 (blue); C1 length of the Rut20 (red); C2 width of the Rut20 (blue); D1 length of the Rut50 (red); D2 width of the Rut50 (blue)

Rod-like NCs specific surface areas are calculated using a simple geometric model. The NC shape is simplified into a cylinder capped with two semi spheres Figure 8 surface area of the two components has been calculated using eq.5 and eq.6.

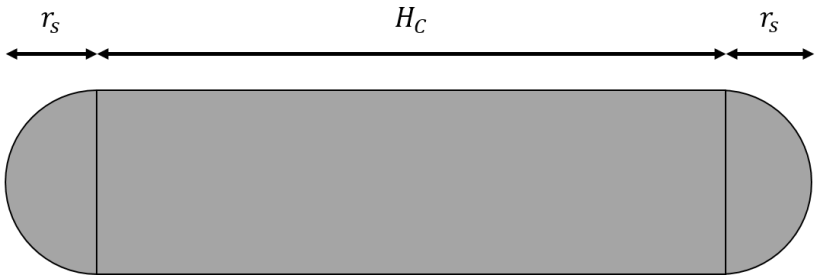

Figure 8 Representative picture of a simplified rod like NC

$$S_C = 2\pi\, r_S\, H_C \quad (5)$$

$$S_S = 4\pi\, r_S^2 \quad (6)$$

Where S_c represents the surface area of the cylinder, r_s represents the radius of the semi sphere, which corresponds to the radius of the cylinder, H_c represents the cylinder height and Ss that represents the surface area of the two semi spheres.

It is then calculated the mass of a single NC using eq.10

$$V_{NC} = V_s + V_c \quad (7)$$

$$V_s = \frac{4}{3}\pi r_s^3 \quad (8)$$

$$V_c = 2\pi r_s^2 H_C$$

(9)de gennes

$$m_{NC} = \frac{V_{NC}}{\rho_{TiO_2}} \quad (10)$$

Where V_{NC} is the sum of the spheres volume and the cylinders volume, ρ_{TiO2} represents the titanium dioxide density. At the end the specific surface area σ_p is obtained simply dividing the S_{NC} by the m_{NC} eq. 11.

$$\sigma_p = \frac{S_{NC}}{m_{NC}} \quad (11)$$

In order to get a complete picture of the NCs surface the calculated specific surface areas are compared with the values obtained performing N_2 adsorption (Table 1, BET) showing good agreement. All NCs synthesized with OLAC as capping agent were stripped with a ligand exchange process and substituted with BF^{4-} counter ions, followed by a hydroxylation reaction with NH_4OH. By removing OA, the surface becomes hydrophilic enabling transfer of NCs to water without affecting their size and shape, a fundamental aspect of our research. The DLS of the NCs in the 3 different stripping stages and the TEM pictures of the as synthesized NCs and the stripped ones show that the size and shape are not affected by the ligand exchange process (Figure 12). The effective replacement of organic ligands by inorganic BF_4^- anions is established by TGA and FTIR. In the IR spectra of the capped particle, Figure 9, the peaks associated to the aliphatic chain (3000-2750 cm^{-1}) and the peaks of the antisymmetric and symmetric stretching of the carboxylate group (1520 cm^{-1} and 1410 cm^{-1}) are evident. The

difference between the latter (~110 cm^{-1}) is indicative of a chelating bidentate attachment of oleic acid on the surface.[24] In the stripped NCs spectra the peaks related to the oleic acid aliphatic chain disappear, while the DMF peak appears (1640 cm^{-1}) due to the fact that DMF acts as a NCs stabilizer and is weakly bonded to the titania surface [40].This effect is immediately visible by comparing in Figure 9.

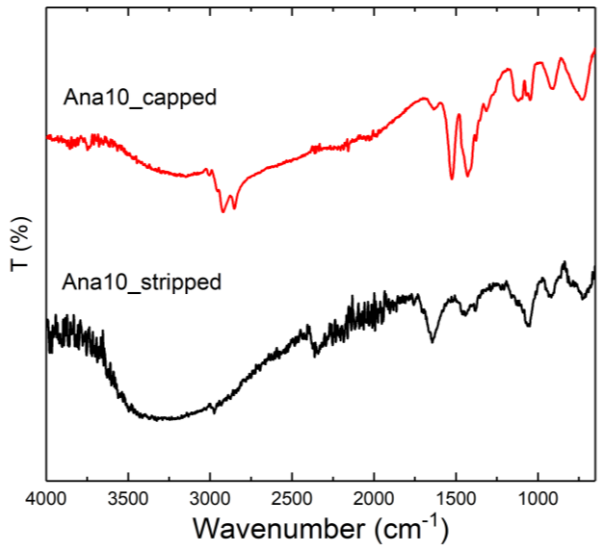

Figure 9 FTIR of capped (top, red) and stripped (bottom, black) anatase NCs. The lack of all adsorptions associated to the oleic acid molecules in the bottom spectrum indicates full stripping of the NP.

The TGA of the stripped NCs (Figure 10) shows that between 150 to 600 °C there is no more than 1% of organic material, indicating a fundamentally bare surface except for some absorbed residues that IR identifies as DMF.[40]

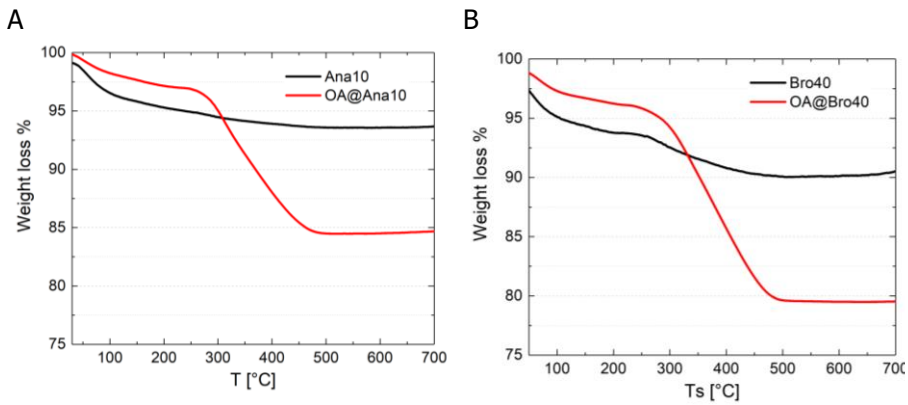

Figure 10 TGA graph A) Anatase NCs covered (OA@Ana10, red line) and stripped (Ana10, black line) by oleic acid capping agent; B) Brookite NCs covered (OA@Bro40, red line) and stripped (Bro40, black line) by oleic acid capping agent

Then, the crystallographic nature of the considered NCs has been verified by XRD as reported in Figure 11. All reflections of the rutile commercial samples correspond to the ones of the bulk structure.

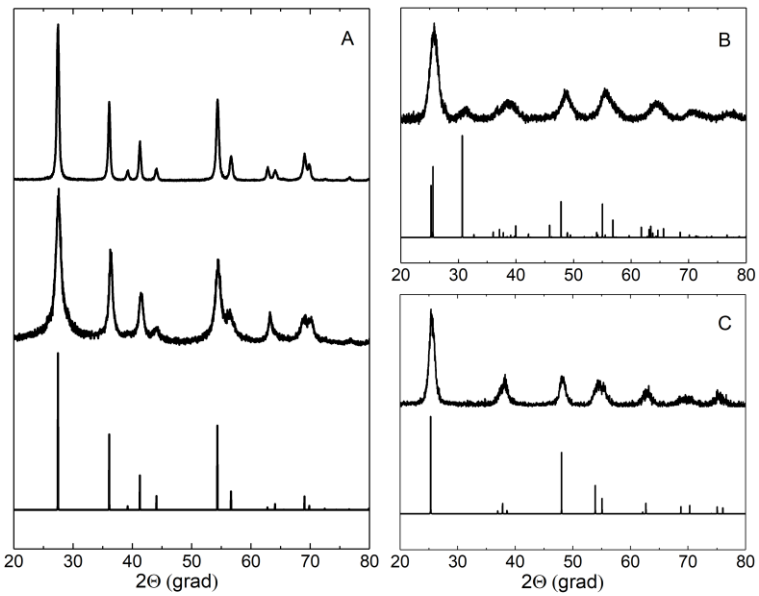

Figure 11 XRD diffractograms: A) Rutile, from top to down Rut50. Rut20 and rutile microcrystaline standard; B) Brookite, from top to down Bro40 and

brookite microcrystalline standard; C) Anatase, from top to down Ana10 and anatase microcrystalline standard.

Diffractograms of NCs are also influenced by crystal size that causes a broadening in the diffraction lines: the broadening is inversely proportional to crystal size. By analyzing the XRD data, indeed, it is possible to estimate the crystal dimensions using the Sherrer's formula

$$D = \frac{K\lambda}{Bcos\theta} \quad (12)$$

Where K is the shape factor, λ is the x ray wavelength, B is the line broadening at half the maximum intensity and Θ represents the Bragg angle of the considered peak. Eq. 5 was used to calculate the NCs dimensions as reported in table 1. The broadening due to the size effect is clear in the case of the Rut50 compared to the Rut20, the XRD pattern of the smaller rutile NCs appears broader than the larger one (Figure 11, A). The XRD pattern of the Ana10 corresponds to the standard one confirming the purity of the crystal phase (Figure 11, B). The shape of the synthesized quasi-spherical anatase is confirmed by the XRD sizes analysis of the nanocrystal. A full calculation of the crystallite size along the different crystallographic directions has been done showing homogenous sizes along the different directions (Figure 12).

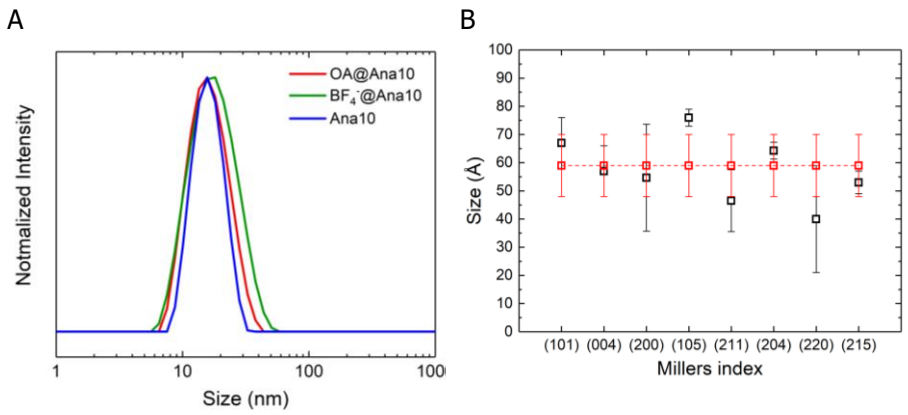

Figure 12 A) DLS graphs of the Anatase NCs of the covered NCs (red); Ana10 covered with BF4- (green); NCs stripped by capping agents (blue); B) Crystallite size of the Ana10 information optained by XRD analysis: red square represents the mean size with its standard; black square represents the crystallite size along the different crystallographic directions

The brookite TiO_2 crystal phase is instead characterized by a more complex XRD pattern. Here, the presence of significant broadening reduces the discriminating power of XRD: the main (101) diffraction peak of anatase at $2\theta = 25.3°$ cannot be distinguished from the (120) and (111) peaks of brookite at $2\theta = 25.3°$ and 25.7°, respectively. The only reliable indicator of the presence of brookite in the XRD patterns is the (121) peak at $2\theta = 30.8°$. To fully confirm the composition of the brookite sample, as suggested by Buonsanti et al.[39], a Raman analysis was also performed. According with its greater crystal symmetry, the anatase vibrational spectrum is simpler if compared to the brookite spectrum. The overall spectral profile of brookite reported in literature is characterized by a very strong band at 158cm^{-1} and a grouping of weaker bands at higher wavenumber. The most important distinction is around 400 cm^{-1}. In this region, the brookite displays a peak at 421 cm^{-1}, distinguishable from the anatase peak at 401 cm^{-1}.

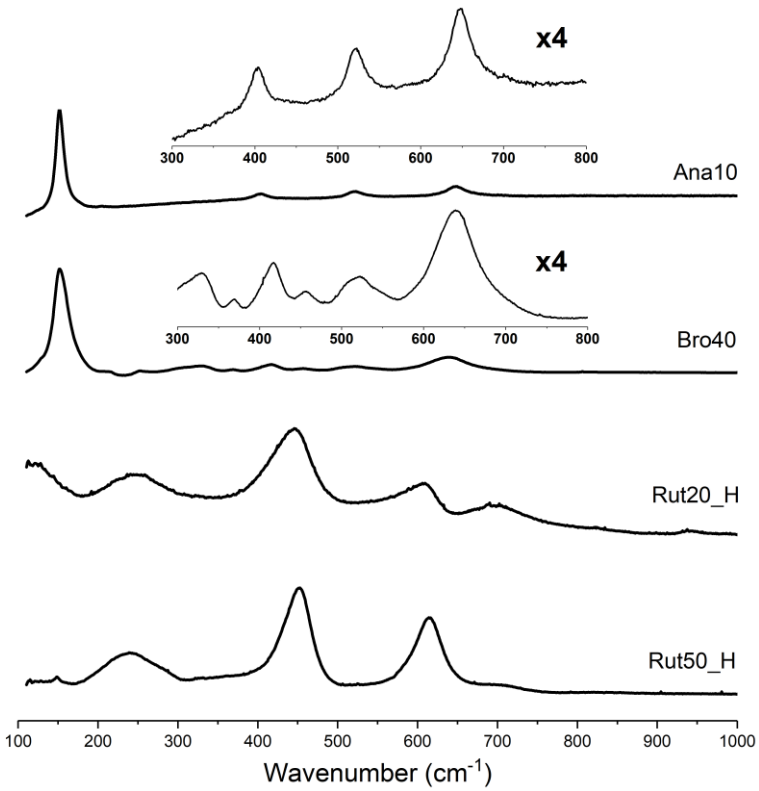

Figure 13 Raman spectra of TiO2 NCs. The rutile form is clearly distinguishable. The detected peaks at short wavenumber present in brookite and absent in anatase indicate the purity of the two samples.

The spectra, presented in Figure 13, fully agree with literature examples. The insets in the figure shows that peaks at 399 and 419 cm^{-1} are present in the anatase and brookite respectively, thus confirming the morphology of the samples. In order to understand the behavior of the as prepared NCs in solution, an evaluation of the NCs size in water dispersion is performed by DLS. The detected distributions of hydrodynamic diameters are presented in Figure 14 for all the samples: they all indicate rather low polydispersity index (PDI). The average hydrodynamic diameter values are reported in Table 1 and span from 16

to 140 nm, much larger than what is calculated from XRD probably due to the presence of aggregates.

The spherical approximations used in DLS tends to assign an apparent diameter close to the length of the longest axis to elongated nanoparticles. Since differences between the DLS size and the expected single particles values are in excess of an order of magnitude, this factor alone is insufficient to justify the differences. A possible contribution to DLS hydrodynamic radius is particle aggregation: aggregates diffuse coherently and are revealed by the scattered light as single larger particles. This a frequent phenomenon in case of small particles with high surface energy thus we checked its possible relevance by measuring the z-potential of all NCs.

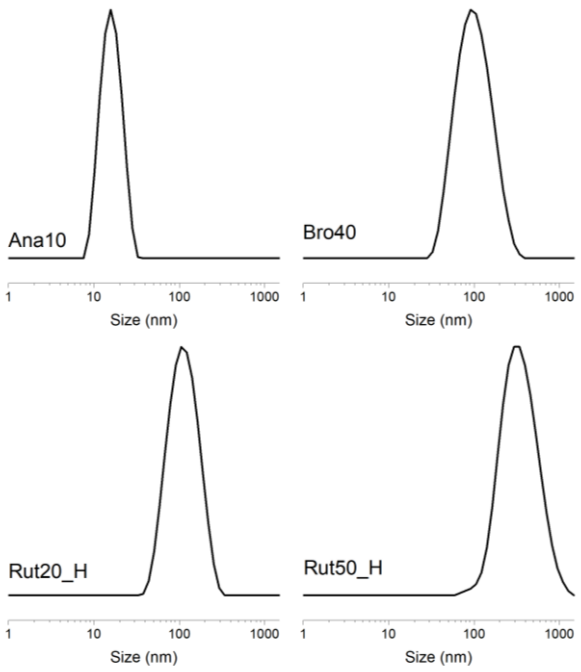

Figure 14 DLS graphs of the Ana10 (top left), Bro40 (top right), Rut20_H (bottom left) and Rut50_H (bottom right)

All the smaller particles, also reported in Table 1, provide results around -30 mV indicating stable colloidal dispersion, instead the larger Rut50 particles display a smaller value of -17.7 mV. Such Z-potential values indicate a good stability of the NCs in water and thus suggest that the bonding between NCs within an aggregation is rather loose. The specific surface area calculated by BET, Table 1, on the basis of N_2 adsorption on the centrifuged and dried NCs, is compatible with the theoretical specific surface area based on TEM sizes. In other words, our assumption is that the entire NC surface is accessible by water when in dispersion.

The study of the surface properties through ^{1}H-TD-NMR T_2 relaxation has been performed using water as solvent. Since TiO_2 NCs are known to be diamagnetic and thus does not cause NMR relaxation at long range, the theory for the NMR relaxation of protons of water molecules interacting with particle surfaces, described above, should hold as long as the solvent molecules bound to NCs surface are in fast exchange with the free ones.

In order to exclude the presence of metal traces that could be associated to paramagnetic centers in the surface, EDXRF analysis was carried on each sample. As reported in Table 2, the metal content has broad variations between the different NCs but is in general below 0.1% weight. Since there is no TEM evidence of internal structuration of the NCs, it is expected that these amounts are dispersed within the sample and do not give rise to paramagnetic effects.

Table 2 Metal trace concentrations (ppm in weight) resulting from EDXRF analysis.

Sample	Rut 20_H	Rut 50_H	Ana10	Bro40
Ca	126±24	33±15	233±30	590±57
Fe	82±13	6±2	8±3	24±5
Zn	204±92	389±89	873±141	222±85
Hf	81±59	582±107	<20 (BdL)	142±60

As described in the experimental section, TD-NMR data were acquired with the CPMG sequence which acquires a signal intensity I(t) as function of echo time.[3] All curves, regardless of the particle type and concentration, could be well fitted with single exponential function $I(t) = I(0)e^{-\frac{t}{T_2}}$ easily extracting the T_2 relaxation time (Figure 7). This validates the fast exchange model assumption and demonstrates the high accessibility of the surface. The presence of dense aggregates of NCs would generate a second population of water molecules with a different relaxation. No such population was detected

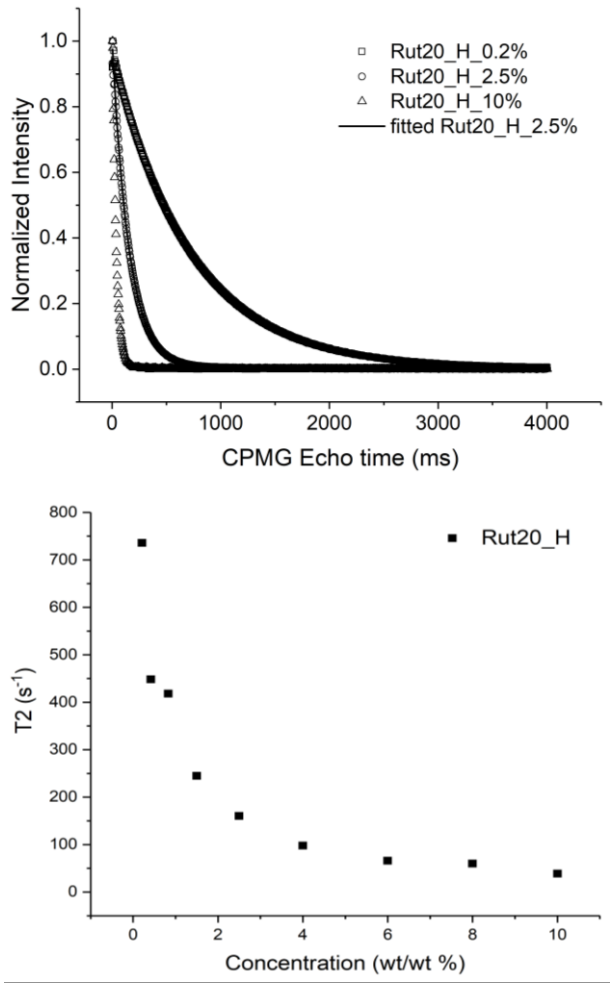

Figure 15 Left, example of monomodal fitting of selected dispersions of Rut20 with different concentration. Fitting lines are practically superimposed with the experimental data. On the right, the T2 values extracted from the CPMG experiments are plotted against NP concentration

For each NCs, relaxivity (R) values equal to $1/T_2$ were obtained at several dilutions and plotted against the product of concentration and specific surface ($\sigma_p C_M$). Figure 8 shows evolution of relaxivity for water-dispersed rutile NCs, including the as acquired commercial samples and their hydroxylated counterparts. All samples were stable in

water up to 6% w/w, allowing immediate measurement of relaxivity over an ample range of concentrations. All data are fitted by linear functions with good correlation ($r^2 \sim 0.99$), with slopes reported in Table 3. This indicates the particles are well dispersed, without tight aggregation phenomena that would modify the available surface as function of the concentration thus resulting in a nonlinear relaxivity function. Following eq. 4, the slope of the relaxivity is $\frac{m_s \mu R_b}{N_0}$ and is then a measure of the interaction of water with the surface.

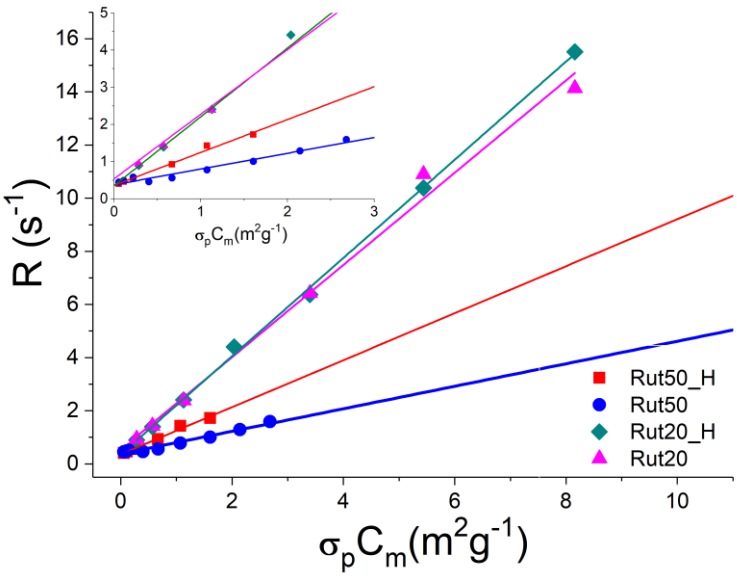

Figure 16 Relaxivity of particles with and without the hydroxylation treatment, indicated with the suffix _H. Relaxivity is expressed as function of available surface per gram of solution: Rut50_H red square (■); Rut50 blue circle (●); Rut20_H green diamond (◆) and Rut20 pink triangle (▲). Inset graph show a much more detailed picture of the region at low σpCM

It is immediately apparent that slopes for smaller Rut20 particles are much steeper than for Rut50, even after normalization against the specific surface measured by BET. This normalization removes the obvious relaxivity increase at fixed weight concentration due to

increased surface to volume ratio of smaller nanoparticles. The slope after this correction is instead representative of the surface interaction. Surface hydroxylation is expected to equalize the surface chemistry, and in fact it brings the samples closer in terms of relaxation behavior: as reported in the table 3 slope of sample Rut20 is only marginally affected, while the effect of Rut50 on water relaxation is enhanced by about a factor 2. Even after this modification, the Rut20 sample composed by smaller particles still has a much higher specific relaxivity, a first indication of the detailed insight that can be provided by the study of the water-particle interaction. The hydroxylated rutile samples are replotted in Figure 17 together with anatase and brookite whose surfaces are already hydroxylated due to our ligand stripping process.

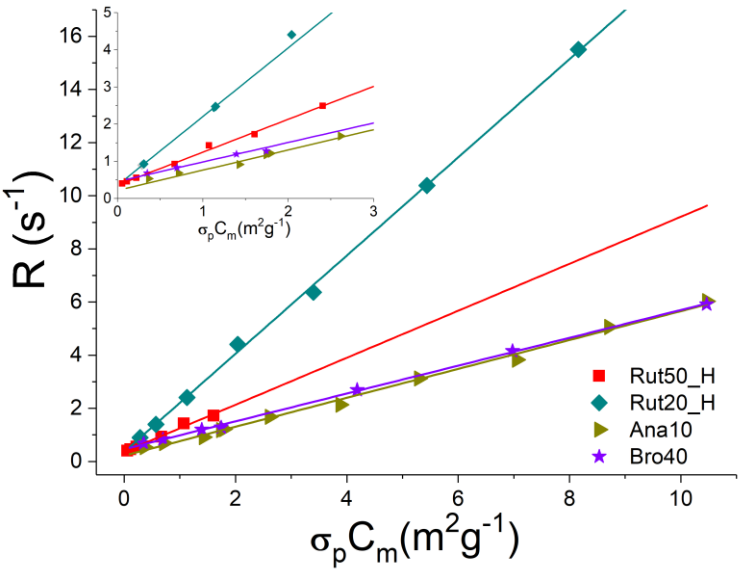

Figure 17 Comparison between the relaxivities of rutile phase rapresented by Rut50_H red square (■); Rut20_H green diamond (◆), anatase Ana10 acid green triangle (▶) and brookite Bro40 purple star (★). Inset graph show a much detailed picture of the region at low σpCM

Also here, for all kinds of NCs, the relaxivity data fit with the linear model proposed. The most striking feature of this plot is that anatase and brookite display a very similar slope, much lower than even the larger rutile particles. Particularly, Rut50 has a slope of 0.88±0.05 g/m^{2}s and is remarkably different from both anatase and brookite. Anatase and brookite, instead, present similar behavior: their slopes are 0.51±0.01 g/m^{2}s and 0.54±0.01 g/m^{2}s respectively. All three polymorphs of TiO_2 are therefore different from each other in terms of surface-water interaction, even though anatase and brookite are very close, making ^{1}H-TD-NMR an informative tool for titania NCs characterization. In the framework of the equations presented above, the different particles are then distinguished by the factor μR_b. The fact that the surface is clean from residual oleic acid allows us to relate the NMR relaxation behavior only to the NCs surface interaction with water.

Table 3: Slopes of the relaxivity as function of normalized surface for all nanocrystals

Sample	Slope	Slope hydroxylated
Ana10	0.51 ± 0.01	
Rut20	1.74 ±0.08	1.85 ± 0.02
Bro40	0.54± 0.01	
Rut50	0.42 ± 0.03	0.88 ± 0.05

As mentioned in the discussion, it is difficult to single out whether the higher relaxivity is due to higher relaxivity of the bound phase or by the greater number of binding sites per surface unit, especially considering that this investigation is based on exchange phenomena that average the interaction with the entire particle, a complementary approach to recent solid-state NMR investigations that focus on single facets.[44] Still, a

correlation can be traced with the recently described interplay between surface energy, relative stability of the various polymorphs and affinity with bound water.[45, 46] Navrotsky A. et al. present surface energy as function of particle size for all three polymorphs. It turns out that the functions for surface energies in the range of specific surface of our particles are in the same order as the μR_b measured by us: brookite is slightly more energetic than anatase, and rutile more than both. Even more interestingly, rutile has a very steep surface energy dependence from the surface area, this agrees with the increased interaction upon decrease of rutile particle size (rut50 to rut20), even after normalization for specific surface and after chemical equalization of the surface hydroxylation. These findings are yet qualitative but provide a basis for immediate applications in the characterization of the fine differences between particles of commercial origin or produced from different methods, and further investigation of the mechanisms of water-surface interaction in the various polymorphs of titania.

Conclusions

Time domain NMR has been performed on water dispersions of NCs representing the three titanium dioxide crystal phases in order to quantitatively understand the interaction that occurs between their surfaces and water molecules. From the preliminary information given by XRD, Raman, and EDXRF analysis, the crystal phase and purity of each sample was verified. By combining the DLS, z-potential, TEM images, and BET data we defined the size and shape of all particles, while evaluating their reciprocal interactions we verified the state of loose aggregation that they maintain in water. Thus, we could assume

an equivalence between the amount of wet surface, the one actually interacting with water in dispersion, and the surface probed by nitrogen adsorption. Finally, we verified the full stripping and hydroxylation of titania surfaces and described the water ^{1}H T_2 relaxation times only in terms of interaction between water and the different nanocrystal phases. By normalizing against the BET surface, we found a general agreement between NMR specific relaxivity and surface energy as presented for example by Ranade[47], since the values of brookite and anatase are very similar to each other and much smaller than rutile of similar specific surface. Relaxivity of rutile was also shown to increase with reduction of particle size, again in parallel with the evolution of surface energy as function of rutile particle size. Finally, the NMR technique is also sensitive to surface treatment such as hydroxylation. Thus, along with other established and increasingly widespread methods for the shape and functionality determination by solvent relaxation, we have shown that with TD-NMR technique is it possible to use water as a probe to identify different phases of the same oxide and crystals with different specific surface area, and to obtain detailed information on the surface treatment.

Reference

(1) Issa, B.; Obaidat, I.; Albiss, B.; Haik, Y., Magnetic Nanoparticles: Surface Effects and Properties Related to Biomedicine Applications. *Int. J. Mol. Sci.* **2013,** 14, (11), 21266.

(2) Laurent, S.; Forge, D.; Port, M.; Roch, A.; Robic, C.; Vander Elst, L.; Muller, R. N., Magnetic Iron Oxide Nanoparticles: Synthesis,

Stabilization, Vectorization, Physicochemical Characterizations, and Biological Applications. *Chem. Rev.* **2008,** 108, (6), 2064-2110.

(3) Vismara, E.; Bongio, C.; Coletti, A.; Edelman, R.; Serafini, A.; Mauri, M.; Simonutti, R.; Bertini, S.; Urso, E.; Assaraf, Y.; Livney, Y., Albumin and Hyaluronic Acid-Coated Superparamagnetic Iron Oxide Nanoparticles Loaded with Paclitaxel for Biomedical Applications. *Molecules* **2017,** 22, (7), 1030.

(4) Silva, A. C.; Oliveira, T. R.; Mamani, J. B.; Malheiros, S. M.; Malavolta, L.; Pavon, L. F.; Sibov, T. T.; Amaro, E., Jr.; Tannus, A.; Vidoto, E. L.; Martins, M. J.; Santos, R. S.; Gamarra, L. F., Application of hyperthermia induced by superparamagnetic iron oxide nanoparticles in glioma treatment. *Int J Nanomed.* **2011,** 6, 591-603.

(5) Lee, B. G.; Luo, J.-W.; Neale, N. R.; Beard, M. C.; Hiller, D.; Zacharias, M.; Stradins, P.; Zunger, A., Quasi-Direct Optical Transitions in Silicon Nanocrystals with Intensity Exceeding the Bulk. *Nano Letters* **2016,** 16, (3), 1583-1589.

(6) Champion, J. A.; Katare, Y. K.; Mitragotri, S., Particle shape: A new design parameter for micro- and nanoscale drug delivery carriers. *J. Control. Release* **2007,** 121, (1–2), 3-9.

(7) Kim, J. S.; Kuk, E.; Yu, K. N.; Kim, J.-H.; Park, S. J.; Lee, H. J.; Kim, S. H.; Park, Y. K.; Park, Y. H.; Hwang, C.-Y.; Kim, Y.-K.; Lee, Y.-S.; Jeong, D. H.; Cho, M.-H., Antimicrobial effects of silver nanoparticles. *Nanomedicine* **2007,** 3, (1), 95-101.

(8) Choi, H. S.; Liu, W.; Misra, P.; Tanaka, E.; Zimmer, J. P.; Itty Ipe, B.; Bawendi, M. G.; Frangioni, J. V., Renal clearance of quantum dots. *Nat. Biotechnol.* **2007,** 25, (10), 1165-70.

(9) Pan, J.; Liu, G.; Lu, G. Q.; Cheng, H.-M., On the True Photoreactivity Order of {001}, {010}, and {101} Facets of Anatase TiO_2 Crystals. *Angew. Chem. Int. Ed.* **2011,** 50, (9), 2133-2137.

(10) Li, Y.; Krentz, T. M.; Wang, L.; Benicewicz, B. C.; Schadler, L. S., Ligand engineering of polymer nanocomposites: from the simple to the complex. *ACS Appl. Mater. Interfaces* **2014,** 6, (9), 6005-21.

(11) Salice, P.; Mauri, M.; Castellino, M.; De Marco, M.; Bianchi, A.; Virga, A.; Tagliaferro, A.; Simonutti, R.; Menna, E., Synthesis and characterisation of a trithiocarbonate for the decoration of carbon nanostructures. *Chem. Comm.* **2013,** 49, (73), 8048-8050.

(12) Kumar, S. K.; Jouault, N.; Benicewicz, B.; Neely, T., Nanocomposites with Polymer Grafted Nanoparticles. *Macromolecules* **2013,** 46, (9), 3199-3214.

(13) Alexandre, M.; Dubois, P., Polymer-layered silicate nanocomposites: preparation, properties and uses of a new class of materials. *Mater. Sci. Eng. R Rep.* **2000,** 28, (1–2), 1-63.

(14) Clift, M. J.; Rothen-Rutishauser, B.; Brown, D. M.; Duffin, R.; Donaldson, K.; Proudfoot, L.; Guy, K.; Stone, V., The impact of different nanoparticle surface chemistry and size on uptake and toxicity in a murine macrophage cell line. *Toxicol. Appl. Pharmacol.* **2008,** 232, (3), 418-27.

(15) O'Regan, B.; Grätzel, M., A low-cost, high-efficiency solar cell based on dye-sensitized colloidal TiO2 films. *Nature* **1991,** 353, 737.

(16) Esthappan, S. K.; Kuttappan, S. K.; Joseph, R., Thermal and mechanical properties of polypropylene/titanium dioxide nanocomposite fibers. *Mater. Des.* **2012,** 37, 537-542.

(17) Colombo, A.; Tassone, F.; Mauri, M.; Salerno, D.; Delaney, J. K.; Palmer, M. R.; Rie, R. D. L.; Simonutti, R., Highly transparent nanocomposite films from water-based poly(2-ethyl-2-oxazoline)/TiO2 dispersions. *RSC Advances* **2012,** 2, (16), 6628-6636.

(18) Crippa, M.; Bianchi, A.; Cristofori, D.; D'Arienzo, M.; Merletti, F.; Morazzoni, F.; Scotti, R.; Simonutti, R., High dielectric constant rutile-

polystyrene composite with enhanced percolative threshold. *J. Mat. Chem. C* **2013,** 1, (3), 484-492.

(19) Berberich, L. J.; Bell, M. E., The Dielectric Properties of the Rutile Form of TiO2. *J. Appl. Phys.* **1940,** 11, (10), 681-692.

(20) Reyes-Coronado, D.; Rodríguez-Gattorno, G.; Espinosa-Pesqueira, M. E.; Cab, C.; Coss, R. d.; Oskam, G., Phase-pure TiO_2 nanoparticles: anatase, brookite and rutile. *Nanotechnology* **2008,** 19, (14), 145605.

(21) Uboldi, C.; Urbán, P.; Gilliland, D.; Bajak, E.; Valsami-Jones, E.; Ponti, J.; Rossi, F., Role of the crystalline form of titanium dioxide nanoparticles: Rutile, and not anatase, induces toxic effects in Balb/3T3 mouse fibroblasts. *Toxicol. in Vitro* **2016,** 31, 137-145.

(22) Weir, A.; Westerhoff, P.; Fabricius, L.; Hristovski, K.; von Goetz, N., Titanium Dioxide Nanoparticles in Food and Personal Care Products. *Environ. Sci. Technol.* **2012,** 46, (4), 2242-2250.

(23) Berne, B. J.; Pecora, R., *Dynamic Light Scattering: With Applications to Chemistry, Biology, and Physics*. Dover Publications: 2000.

(24) Thistlethwaite, P. J.; Hook, M. S., Diffuse Reflectance Fourier Transform Infrared Study of the Adsorption of Oleate/Oleic Acid onto Titania. *Langmuir* **2000,** 16, (11), 4993-4998.

(25) Wisser, F. M.; Abele, M.; Gasthauer, M.; Muller, K.; Moszner, N.; Kickelbick, G., Detection of surface silanol groups on pristine and functionalized silica mixed oxides and zirconia. *J. Colloid Interface Sci.* **2012,** 374, (1), 77-82.

(26) Johns, M. L.; Hollingsworth, K. G., Characterisation of emulsion systems using NMR and MRI. *Prog. Nucl. Magn. Reson. Spectrosc.* **2007,** 50, (2–3), 51-70.

(27) Bonetti, S.; Farina, M.; Mauri, M.; Koynov, K.; Butt, H. J.; Kappl, M.; Simonutti, R., Core@shell Poly(n-butylacrylate)@polystyrene Nanoparticles: Baroplastic Force-Responsiveness in Presence of Strong Phase Separation. *Macromol Rapid Commun* **2016,** 37, (7), 584-9.

(28) Mears, S. J.; Cosgrove, T.; Thompson, L.; Howell, I., Solvent Relaxation NMR Measurements on Polymer, Particle, Surfactant Systems. *Langmuir* **1998,** 14, (5), 997-1001.

(29) Cosgrove, T.; Griffiths, P. C.; Lloyd, P. M., Polymer Adsorption. The Effect of the Relative Sizes of Polymer and Particle. *Langmuir* **1995,** 11, (5), 1457-1463.

(30) Letellier, M.; Tinet, D.; Maggion, R.; Fripiat, J., Study of relaxation mechanisms in clay/water systems. Determination of the surface area. Application to cements. *Magn. Reson. Imaging* **1991,** 9, (5), 709-716.

(31) Fairhurst, D.; Cosgrove, T.; Prescott, S. W., Relaxation NMR as a tool to study the dispersion and formulation behavior of nanostructured carbon materials. *Magn. Reson. Chem.* **2016,** 54, (6), 521-526.

(32) Karpovich, A. L.; Vlasova, M. F.; Sapronova, N. I.; Sukharev, V. S.; Ivanov, V. V., Determination of dimensions of exfoliating materials in aqueous suspensions. *MethodsX* **2016,** 3, 19-24.

(33) Yuan, L.; Chen, L.; Chen, X.; Liu, R.; Ge, G., In Situ Measurement of Surface Functional Groups on Silica Nanoparticles Using Solvent Relaxation Nuclear Magnetic Resonance. *Langmuir* **2017,** 33, (35), 8724-8729.

(34) Gillis, P.; Peto, S.; Muller, R. N., Bound water in heterogeneous system relaxometry: An ill-defined concept. *Magn. Reson. Imaging* **1991,** 9, (5), 703-708.

(35) Valckenborg, R. M. E.; Pel, L.; Kopinga, K., Combined NMR cryoporometry and relaxometry. *J.Phys.D* **2002,** 35, (3), 249.

(36) Fairhurst, D.; Prescott, S., The use of nuclear magnetic resonance as an analytical tool in the characterisation of dispersion behaviour. *Spectrosc. Eur* **2011,** 23, (4), 13-16.

(37) Cosgrove, T.; Jack, K. S.; Green, N.; Obey, T. M.; Wood, M., NMR Solvent Relaxation Studies on Concentrated Particulate Dispersions. In

Supramolecular Structure in Confined Geometries, American Chemical Society: 1999; Vol. 736, pp 153-168.

(38) Dinh, C. T.; Nguyen, T. D.; Kleitz, F.; Do, T. O., Shape-controlled synthesis of highly crystalline titania nanocrystals. *ACS Nano* **2009,** 3, (11), 3737-43.

(39) Buonsanti, R.; Grillo, V.; Carlino, E.; Giannini, C.; Kipp, T.; Cingolani, R.; Cozzoli, P. D., Nonhydrolytic synthesis of high-quality anisotropically shaped brookite TiO_2 nanocrystals. *J. Am. Chem. Soc.* **2008,** 130, (33), 11223-33.

(40) Dong, A.; Ye, X.; Chen, J.; Kang, Y.; Gordon, T.; Kikkawa, J. M.; Murray, C. B., A generalized ligand-exchange strategy enabling sequential surface functionalization of colloidal nanocrystals. *J. Am. Chem. Soc.* **2011,** 133, (4), 998-1006.

(41) Jang, I.; Song, K.; Park, J. H.; Oh, S. G., Enhancement of dye adsorption on TiO_2 surface through hydroxylation process for Dye-sensitized solar cells. *Bulletin of the Korean Chemical Society* **2013,** 34, (10), 2883-2888.

(42) Dollimore, D.; Spooner, P.; Turner, A., The bet method of analysis of gas adsorption data and its relevance to the calculation of surface areas. *Suface. Technol.* **1976,** 4, (2), 121-160.

(43) Pearce, N. J. G.; Perkins, W. T.; Westgate, J. A.; Gorton, M. P.; Jackson, S. E.; Neal, C. R.; Chenery, S. P., A Compilation of New and Published Major and Trace Element Data for NIST SRM 610 and NIST SRM 612 Glass Reference Materials. *Geostandards Newsletter* **1997,** 21, (1), 115-144.

(44) Li, Y.; Wu, X.-P.; Jiang, N.; Lin, M.; Shen, L.; Sun, H.; Wang, Y.; Wang, M.; Ke, X.; Yu, Z.; Gao, F.; Dong, L.; Guo, X.; Hou, W.; Ding, W.; Gong, X.-Q.; Grey, C. P.; Peng, L., Distinguishing faceted oxide nanocrystals with ^{17}O solid-state NMR spectroscopy. *Nat. Commun.* **2017,** 8, (1), 581.

(45) Levchenko, A. A.; Li, G.; Boerio-Goates, J.; Woodfield, B. F.; Navrotsky, A., TiO2 Stability Landscape: Polymorphism, Surface Energy, and Bound Water Energetics. *Chem. Mater*. **2006,** 18, (26), 6324-6332.

(46) Navrotsky, A., Energetics of nanoparticle oxides: interplay between surface energy and polymorphism. *Geochemical Transactions* **2003,** 4, (6), 34-37.

(47) Ranade, M. R.; Navrotsky, A.; Zhang, H. Z.; Banfield, J. F.; Elder, S. H.; Zaban, A.; Borse, P. H.; Kulkarni, S. K.; Doran, G. S.; Whitfield, H. J., Energetics of Nanocrystalline TiO_2. *Proc. Natl. Acad. Sci. U.S.A.* **2002,** 99, (9), 6476-6481.

Chapter 3. Grafting-to of polyethylene oxide monomethyl ether on spherical anatase

Introduction

During the last decades relevant efforts had been devoted to healthcare and the treatment of human diseases, determining significant improvements in the adopted technologies with more sophisticated and accurate techniques. The application of nanotechnology in this field, nanomedicine, plays a key role in the development of new materials, tailored with specific functionalities, like drug delivery systems, optimized scaffolds for tissue regeneration[1], fluorescent moieties for optical detection, stimuli responsive ligands (pH, temperature) and specific targets for biological recognition [2–4]. All these properties can be applied together in the case of nanoparticles thanks to fine surface ligand design that provides a multilevel material able to face multiple issues[5]. The application of inorganic nanocrystals (NC) in diagnosis and therapy has become a critical component in the targeted treatment of diseases[6]. This kind of systems can add more functionalities to the final material; for example, magnetic NCs, like iron oxide, or quantum dots can be employed as contrast agents for bio imaging[6,7]. Titanium dioxide (TiO_2) NCs found a wide range of applications in biomedical field thanks to their stability and low toxicity characteristics in vitro and in vivo[8,9], which indicates their great potential of the applications in life sciences. TiO_2 has the property of killing bacteria, viruses, fungi, and

even cancer cells[10]. The TiO_2 is widely used in paint, pharmaceutical, and cosmetics industries. An additional advantage of TiO_2 is its radio-opacity, and titanium dioxide nanoparticles can potentially be used as labels for X-ray bioimaging applications[10]. Surface modification of inorganic oxides is important to provide diversity in size, shape, solubility, long-term stability, and attachment of selective functional groups. For example, the introduction of a thin polymeric layer enables a good dispersion of the inorganic nanocrystals in solvents, like blood or physiological environment, and matrices in which bare particles aggregate and precipitate due to the low dimensions and the high specific surface area[11]. Thanks to the control over graft density (chains per surface area, σ) and the molecular weight of the grafted chains (N) it is possible to control the morphology of the tethered polymer[12]. Moreover, it is possible to control the behavior of the NCs inside the cellular environment. In fact the surface of an inorganic nano-sized object must be "*protected*" since NCs are rapidly removed from circulation and accumulate mainly in the liver and spleen due to opsonization and recognition by the mononuclear phagocyte system (MPS)[13]. Is well known that the reduction in toxicity of TiO_2 nanoparticles is strictly related to the surface decoration with a polymer[9,14–16]. A wide range of biocompatible and biodegradable polymers can be selected as a shell for NCs: polysaccharides, polyacrylamide, poly(vinyl alcohol), poly(N-vinyl-2-pyrrolidone), poly(ethylene oxide) (PEO), and PEO-containing copolymers, have been used to coat the surface of NPs for additional stability, water solubility, and modification of surface charges. PEO's high hydrophilicity, low toxicity, low immunogenicity and capability of

preventing opsonization of nanoparticles, allowing for improved pharmacokinetics, have rendered it the go-to polymeric coating of choice for all kinds of pharmaceuticals, a strategy that is commonly known as PEGylation. This polymer, once grafted on a surface, (i) shields the charged surface and increases in hydrophilicity leading to reduced interaction and identification by opsonin proteins; (ii) decreases the interfacial free energy of the NCs in fluid media minimizing the interaction with proteins; (iii) generates repulsive forces through the compression of flexible PEO chains on the surface of NPs when encroached by proteins; (iv) thanks to the its high molecular mobility it can minimize the interaction time with the proteins to prevent any specific binding leading to a longer circulating time into human body; (v) if high surface density of PEO chains is achieved, no space is offered to opsonin proteins for binding and thus uptake by reticulo endothelial system (RES) is avoided[6,17]. Once the NCs are precisely decorated and fully compatibilized with the biological environment, it is possible to add more properties to the particles, for example, using a stimuli responsive polymer. It is well known that the conformation affects the thermal properties, in fact polymer systems that have larger conformational freedom are usually characterized by a low glass transition temperature (T_g) while more constrained polymers tend to have a higher T_g. There is growing interest on the effect that the chain conformation of a polymer grafted nanocrystal (PGNC), on flat or spherical substrates, can bring[18]. In fact, depending on the architecture and chemical composition of the attached polymer chains, the conformation and structure of a polymer can be manipulated using a variety of external stimuli. These responsive properties potentially

provide the basis for the development of "smart" surfaces influenced by solvent, temperature, pH, and ions[19,20]. The conformational behavior of surface-grafted polymers, derived from the theories initially proposed by Alexander[21] and de Gennes[22] suggest the existence of a variety of conformations, ranging from mushroom conformation, a nearly unperturbed random coil deployed on the nanoparticle surface, to brush conformation where coil is stretched, and the macromolecular chain describes a more elongated shape. De Gennes, in his theory[22], correlating grafting density with preferred conformations, suggested that a mushroom conformation exists at a low grafting density while at high grafting density the polymer chain adopts a brush conformation. We have to consider that de Gennes' model was developed for flat surfaces, in the case of polymer-grafted nanospheres, more conformations can be adopted by the polymer chain, and several studies have sought to characterize the structure of the chain on grafted nanospheres. A first attempt made by Daoud and Cotton[23], extended the phenomenological scaling arguments of Alexander and de Gennes to star-like polymers. This model assumes that all chains are bonded to a central point and that the free ends extend with an identical distance away from the center. Ohno et al[24]. extended this model to treat chains grafted to a nanoparticle of radius, r_0. They postulate the existence of a critical radius r_c, which is derived from the "star-polymer" treatment of Daoud and Cotton, that describes the threshold between the concentrated polymer brush region (CPB), where the chains are more stretched, and the semidilute polymer brush region (SDPB), where the polymer experiences more conformational freedom.

In general, it is accepted that at low enough molecular weight or at low enough graft density, the distance between the polymer chains is larger than the size of the random coil. Individual chains do not interact with adjacent chains, and thus they assume mushroom-like conformations on the grafting surface. In this case the size of the polymer coil, proportional to the radius of gyration (R_g) of the chain, scales with the degree of polymerization as $R_g \sim N^{\nu}$, where the excluded volume parameter (Flory exponent, ν) is between $\nu = 0.5$ and 0.6. Consequently, the measured brush height in this regime is approximately $h \approx 2R_g$, this parameter it is an indicator of the polymer conformation through its dimensions. Only when these mushroom-like structures would begin to overlap, the chains begin to behave as brushes. The presence of two regimes of polymer conformation is due to the geometry of the system, on a sphere, as the distance from the center increases the accessible volume for a polymer chain also increases resulting in a high concentration of strongly confined chains near the NP surface (concentrated polymer brush region, CPB) that become less confined as the distance from the nanoparticle surface increases (semidilute polymer brush region, SDPB).

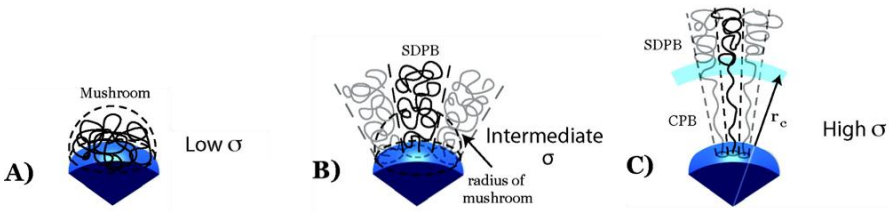

Figure 18 Schematic representation of the varied conformational behaviors of polymer brushes attached to spherical interfaces. At low values of σ the polymer chain assumes a mushroom conformation; at intermediate values of σ there is a change from the mushroom regime to the brush regime; at high σ it is possible to

define a CPB and a SDPB region. Copyright © 2010 American Chemical Society, image adopted by ref. 28.

The change in polymer conformation, as function of the distance from the NP core, is expected to be continuous and does not change sharply at the CPB/SDPB interface[24–27]. Thus, the two conformations observed in the CPB and SDPB regions are delimited by the r_c, which represents the buffer area between a mushroom like and a brush like regime (Figure 18)[28]. It is possible to get a complete picture of the polymer conformation using sophisticated analysis and techniques like Small Angle X-Ray and neutron scattering (SAXS, SANS), TEM micrographs, AFM etc. Many authors proposed a simplified model where it is assumed that a single grafted chain acts as a non-interacting rigid sphere tethered on the surface in a single point. Calculating that each chain normally spans the Flory radius (R_F, eq.8), and considering an experimental mean distance (Dm), deducted by TGA and BET analysis, it is possible to define a brush regime when $Dm < R_F$, vice versa when $Dm \geq R_F$ the mushroom regime is described[29–31].

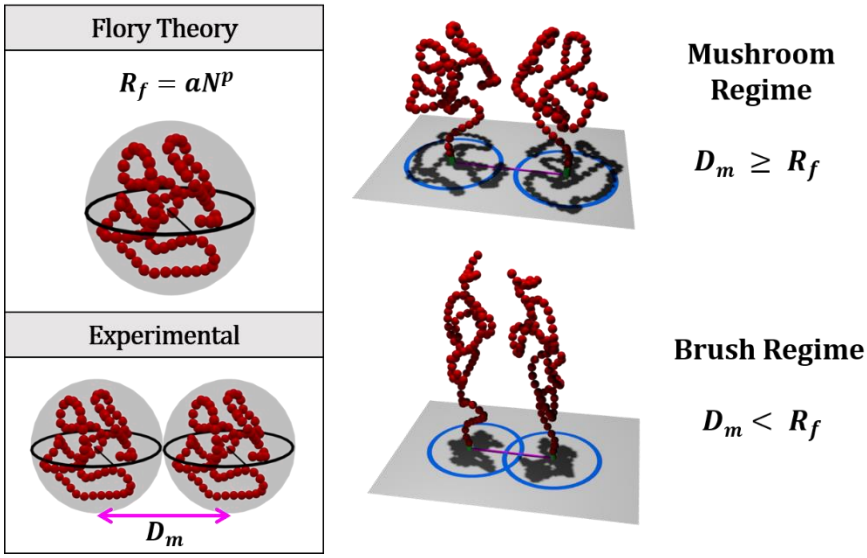

Figure 19 Model used in our work where R_F represent the radius of gyration defined by Flory and Dm represents the experimental mean distance. In this case we describe brush regime when $D_m < R_F$, vice versa when $D_m \geq R_F$ the mushroom regime is described.

The other aspect that we must consider when we speak about polymer grafted nanocrystals is the interaction of the polymer chain with the surrounding environment, especially solvents if we are dealing with drug delivery systems that should be stable in human blood conditions. The behavior of a free chain in a solvent has been deeply studied during the years and multiple models and theories have been developed. The model widely accepted nowadays stems from the work of P.J.Flory, Nobel laureate in Chemistry. Starting from the regular solution theory introduced by Joel Henry Hildebrand[32], Flory developed a thermodynamic model for polymer solutions that considers two main effect the variation of entropy, compared to the bulk polymer, when the polymer is dissolved in the polymer, and the enthalpy of mixing that is governed by the interaction parameter χ [33]. Considering that the variation of entropy can be considered, as a first approximation,

independent from the type of solvent used, the main term affecting polymer solubility is the interaction parameter χ . This parameter can determined experimentally or, is experimental data do not exist, it can be calculated from Hildebrand solubility parameters. However since Hildebrand parameters are not suitable for use outside their original area which was non-polar, non-hydrogen-bonding solvents we are going to use Hansen solubility parameters[31]. These parameters can be used to estimate the Flory-Huggins interaction parameters, χ between a polymer and a selected solvent using eq.1:

$$\chi_{12} = \frac{V_m}{RT}\left[\left(\delta_{D.2} - \delta_{D,1}\right)^2 + 0.25\left(\delta_{P,2} - \delta_{P,1}\right)^2 + 0.25\left(\delta_{H,2} - \delta_{H,1}\right)^2\right] \quad (1)$$

Where δ_D, δ_P and δ_H are the contributions of dispersion forces, polar interactions and hydrogen bonds to solubility, respectively, V_m is the molar volume of the solvent, T is temperature and R is the gas constant. In our contribution we explored the grafting-to approach of polyethylene oxide monomethylether (mPEO) chains on anatase NCs (diameter <10nm), synthesized via solvothermal technique and fully characterized. The polymers used in this study range over different molecular weights ($M\overline{w}$, 10^1-10^4 $gmol^{-1}$), functionalized with three anchoring groups: hydroxyl, carboxylic and phosphate end group. The grafting reactions have been made using two different solvents, water and dichloromethane (DCM), in order to manage the grafting process in which the polymer and the NCs surface reacts. With this systematic approach we developed a protocol to finely tune the polymer graft density and the conformation over titanium dioxide NCs thanks to the control over the binding group, the solvent and the molecular weight and the experimental conditions.

Materials and methods

Iodine (I_2), Triethyl phosphite ($PO(Et)_3$, 98%), pyiridine (99.8%), paraformaldehyde, dimethyl phosphite (98%), thionyl chloride ($SOCl_2$ >99.9%) oxalyl chloride (OxCl >99%), 1,4-Dibromobutane (99%), 2,6-lutidine (98%), sodium hydride (60% dispersion in mineral oil), succinic anhydride (95%), glutaric anhydride (95%), potassium carbonate (K_2CO_3), Sodium Sulfate (NaSO3, 99.9%), 4-dimethylaminopyridine (DMAP), triethylamine (TEA), Titanium (IV) butoxide (TB, 97%), oleic acid (OLAC, 90%), oleyl amine (OLAM, 70%), Ammonium hydroxide solution (NH_4OH, 28%), absolute ethanol (≥ 99.8%), hexane (≥ 95%), absolute methanol (>99.9%) dimethylformamide (DMF, ≥ 99.9%), phosphoryl chloride ($POCl_3$ >98%) freshly distilled before reactions, tetrahydrofuran (THF >99%) dried with sodium wire and benzophenone and distilled before the reactions start. Chloroform ($CHCl_3$), diethylether and toluene (≥ 99.9) are eventually dried over calcium chloride and distilled over activated molecular sieves. 2-methoxyethanol (98%) and polyethylene oxide monomethyl ether polymers purchased from Sigma Aldrich ($M\bar{w}$= 500, 2000, 5000, 10000, 20000 $gmol^{-1}$) were precipitated twice from ethanol, dried by azeotropic distillation from toluene, and stored in a dry nitrogen atmosphere. All chemicals were purchased from Sigma Aldrich except for Nitrosoniumtetrafluoroborate (NOBF4, 98%) that was purchased from Alfa Aesar.

Synthetic methods

Synthesis of anatase TiO_2 NCs

The synthesis of TiO_2 NCs is carried out with a solvothermal method[34]. In a typical reaction, a mixture of 60 mmol of OLAC, 40 mmol of OLAM and 11.7 mL of absolute ethanol are stirred for 15 minutes, then 10 mmol of TB are added dropwise. The mixture is poured in a 40 mL Teflon beaker and stirred for 15 min before being transferred into a 400 mL Teflon-lined stainless-steel autoclave containing 40 mL of a solution of ethanol and water (96% ethanol). The system is then heated to 180 °C for 18 h. The crude product is then centrifuged, precipitating a white powder constituted by titania NCs covered by oleic acid whose polar terminal group is bound to the surface. The aliphatic portion of oleic acid allows easy dispersal in hexane, an apolar solvent. The particles are precipitated several times in ethanol to remove excess ligands and eventually dispersed in hexane, chloroform or DCM.

Ligand stripping procedure[35]:

A dispersion of TiO_2 particles in hexane is added to a solution of $NOBF_4$ and DMF. The amount of $NOBF_4$ used for the experiment is calculated starting from the OLAC content estimated with TGA. The resulting biphasic mixture is stirred to maximize the interface where the ligand exchange takes place. As the ligand is substituted by BF_4-, the surface polarity changes and NCs are transferred from the non-polar (hexane) to the (DMF) phase, typically within 60 min.40. The surface modified NCs are then purified by precipitation with the addition of toluene, that is miscible with DMF, then the precipitated NCs are dispersed in water. In order to increase the hydroxyl groups on the NCs surface and to have

a ligand free surface, the as prepared particles are treated with a solution of ammonium hydroxide and stirred for 24 hours at 70°C. After that process the particles are purified by centrifugation with water till the solution reaches pH 7-9. This process was applied to all TiO_2 samples in order to avoid different behaviors related to the sample preparation.

Synthesis of functionalized mPEO derivatives:

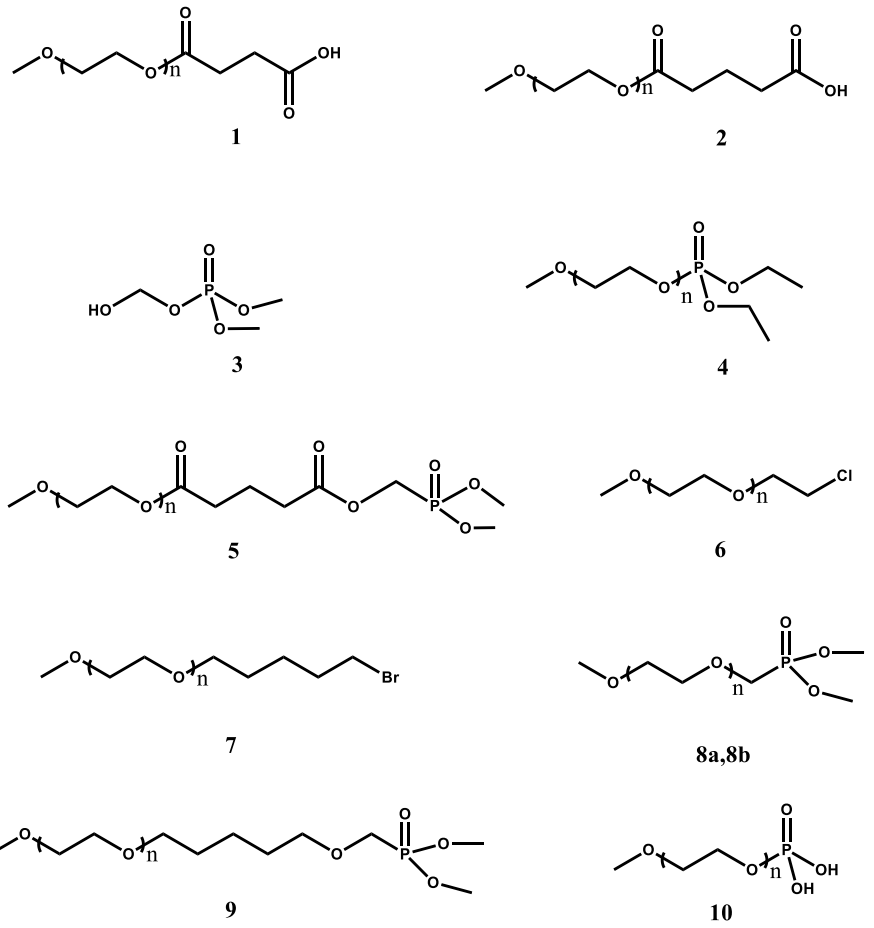

Figure 20 Representations of the functionalized polymers. Polymer 1, 2, 10 have been synthesized with mPEO n = 11, 44, 455, 909, 1818; products 3, 6, 7, 8a, 8b, 9 with mPEO n=455, product 4 with mPEO n = 11 and polymer 5 with mPEO n = 909

mPEO-succinic acid (1)

mPEO of different molecular weights are modified with the same procedure[36], we report an example with the mPEO 5000. Typically, 0.5 mmol of mPEO is added and dissolved in dioxane anhydrous along with

triethylamine (TEA) in a round bottom flask. A solution of 4-Dimethylaminopyridine (DMAP, 1 eq.) and succinic anhydride (1.2 eq.) in dioxane is slowly added to the mPEO solution. Then the reaction is stirred for 24 hours at room temperature and in controlled N_2 atmosphere. The solvent is dried in vacuum and the crude product is precipitated three times in diethyl ether and three times in ethanol (yield 81%). 1H NMR (500 MHz, $CDCl_3$): δ 4.27-4.24 ppm (t, 2H, -$CH_2C\mathbf{H_2}OCO$), δ 3.9-3.3 ppm (m, 4H, -$C\mathbf{H_2}C\mathbf{H_2}$- PEO chain) δ 3.37 ppm (s, 3H, -$OC\mathbf{H_3}$), δ 2.7-2.5 ppm (m, 4H, -$C\mathbf{H_2}C\mathbf{H_2}$-CO(OH))

mPEO-glutaric acid (2)

mPEO of different molecular weights are modified with a modified version of the previously reported procedure[36], an example is reported with the mPEO 5000. Typically, 0.5 mmol of mPEO is added and dissolved in dioxane anhydrous along with triethylamine (TEA) in a round bottom flask. A solution of 4-Dimethylaminopyridine (DMAP, 1 eq.) and butyr anhydride (1.2 eq.) in dioxane is slowly added to the mPEO solution. Then the reaction is stirred for 24 hours at room temperature and in controlled N_2 atmosphere. The solvent is dried in vacuum and the crude product is precipitated three times in diethyl ether and three times in ethanol (yield 84%). ^{1}H NMR (500 MHz, $CDCl_3$): δ 4.20-4.18 ppm (t, 2H, -$CH_2C\mathbf{H_2}OCO$), δ 3.9-3.3 ppm (m, 4H, -$C\mathbf{H_2}C\mathbf{H_2}$-PEO chain), δ 3.37 ppm (s, 3H, -$OC\mathbf{H_3}$), δ 2.7-2.5 ppm (m, 4H, -$C\mathbf{H_2}CH_2C\mathbf{H_2}$), δ 2.06-2.13 ppm (m, 2H, - $CH_2C\mathbf{H_2}CH_2$-).

Dimethyl (hydroxymethyl)phosphonate (3)

In a general procedure 1 eq. of paraformaldehyde (0.72 mol) and 0.5 eq of potassium carbonate are added and dissolved in 160 ml of methanol in a round bottom flask equipped with a condenser. Then 1 eq. of dimethyl phosphite is slowly added to the mixture. The reaction is stirred and kept at room temperature for 24 hours. The solvent is evaporated and the crude product is purified through silica gel chromatography (DCM:hexane 7:3) giving a colorless oil (yield >95%). ^{1}H NMR (500 MHz, $CDCl_3$): δ 3.94-3.93 ppm (d, 2H, OH-C**H$_2$**-P), δ 3.81-3.79 ppm (d, 6H, P(OC**H$_3$**)$_2$). ^{31}P NMR (500 MHz, CDCl3): δ 18 ppm (s, 1P, O**P**(OCH$_3$)$_2$).

mPEO-diethyl phosphonate (4)

Here is reported the procedure adopted for mPEO 500. In a round bottom flask equipped with a condenser and kept at 0°C, are dissolved 10 mmol of mPEO (1 eq.) and 1.5 eq. of triethyl phosphite in 15 ml of dry DCM. Then are slowly added 40 ml of 0.1 mM I2 in dry DCM. The reaction mixture is left in ice bath for 10 minutes and then brought to 80°C, left for 24 h and in controlled N_2 atmosphere. The DCM and the unreacted $PO(Et)_3$ are distilled with a Claisen apparatus. The crude product is then precipitated three times in cold diethyl ether, filtered and dried in vacuum. No product obtained with this synthetic route.

mPEO- dimethyl ethyl phosphonate glutarate (5)

The as prepared **2** (2.5 mmol, 1 eq.) is added in a pre-thermally heated round bottom flask and left under vacuum for 1 hour at 50°C. Then 30

ml of dry DCM are added in controlled N_2 atmosphere, once the polymer is dissolved dry DMF (0.1 eq) is added and the reaction mixture is put in an ice bath. OxCl (3 eq.) is slowly added dropwise in 10 minutes and then slowly brought at room temperature. The reaction mixture is stirred in controlled atmosphere for 24h. The unreacted OxCl is evaporated at reduced pressure and low temperature, the obtained solid is dissolved in 20 mL of dry DCM and left in an ice bath till it thermally stabilizes at 0°C. A solution of 2,6-lutidine (3 eq.) and dimethyl (hydroxymethyl)phosphonate (1.25 eq.) dissolved in 20 mL of dry DCM is added dropwise in 30 minutes to the reaction mixture. After 24 hours the solvent is evaporated at reduced pressure and low temperature. The crude product is then precipitated three times in cold diethyl ether, filtered and dried in vacuum. (yield 7%). ^{1}H NMR (500 MHz, $CDCl_3$): δ 4.47-4.44 ppm (d, 2H, O-C**H₂**-P), δ 4.20-4.18 ppm (t, 2H, -CH_2C**H₂**OCO), δ 3.9-3.3 ppm (m, 4H, -C**H₂**C**H₂**- PEO chain), δ 3.47-3.45 ppm (d, 6H, P(OC**H₃**)$_2$), δ 3.37 ppm (s, 3H, -OC**H₃**), δ 2.7-2.5 ppm (m, 4H, - C**H₂**CH_2C**H₂**), δ 2.06-2.13 ppm (m, 2H, - CH_2C**H₂**CH_2-). ^{31}P NMR (500 MHz, CDCl3): δ 18 ppm (s, 1P, O**P**(OCH_3)$_2$).

mPEO-chloride (6)

mPEO 2000 (5 mmol, 1 eq.) was dissolved in toluene (50 ml) alongside with dry pyridine (1 eq.) was added and thionyl chloride (4 eq., freshly distilled from quinolone), was added dropwise during 30 minutes under reflux. The mixture was heated for 4 hour, cooled to room temperature, filtered from pyridine hydrochloride and the toluene was evaporated in vacuo. The residue was dissolved in DCM, dried over anhydrous K_2CO_3

and filtered. The filtrate was treated with alumina (50 g) and precipitated by cold ether. The polymer was recrystallized from DCM/Diethyl ether (yield 94%). *(ATR)-FTIR* 1110 cm-1 (CH2-O-CH2), 663 cm-1 (C-Cl), no absorption for OH at 3300–3500 cm-1.

mPEO-bromide (7)

In an N_2 atmosphere, 20 mmol NaH was reacted with mPEO 2000 (20 mmol) in 50 mL anhydrous THF. After 2 hours, the mixture was dropwise added to a 20 mL THF solution of 1,4-di-bromobutane (3M) and a white precipitate of NaBr appeared after few minutes. The mixture was stirred for 8 h at 60 °C. After filtration and removal of the solvent, the crude product was extracted three times with CHCl3 (150 mL) and H2O (200 mL). The solvent was evaporated in vacuum and dried overnight in vacuum oven at 50°C to give a colorless liquid (49% yield). *(ATR)-FTIR* 1110 cm-1 (CH2-O-CH2), 755 cm-1 (C-Cl), no absorption for OH at 3300–3500 cm-1.

mPEO-dimethyl ethyl phosphonate (8a)

In a controlled atmosphere of N2 are added in a round bottom flask 3 mmol of compound **3** alongside with 20 mL of dry DCM. Once the solution appears clear 2,6-Lutidine (3 mmol) is added dropwise and stirred for 2 hours. Then the reaction mixture is put in ice bath and 20 mL of a solution 0.075M of compound **6** in dry DCM is added dropwise in 20 minutes. The mixture is carefully brought to room temperature and stirred overnight. The solid is filtered giving a pale-yellow solution, the solvent and the unreacted 2,6-lutidine are then evaporated in vacuum

and the solid is dissolved in DCM (100ml) and extracted with brine (3x100 mL). The organic layer is dried over sodium sulfate and after 2 hours filtered. The solvent is evaporated in vacuum and dried overnight in vacuum oven at 50°C (yield 8%). ^{1}H NMR (500 MHz, $CDCl_3$): δ 3.87 ppm (d, 2H, O-C**H**$_2$-P), δ 3.59 ppm (t, 2H, C**H**$_2$-O-CH_2-P), δ 3.54 ppm (m, 44H, -C**H**$_2$C**H**$_2$- PEO chain), δ 3.50-3.48 ppm (d, 6H, P(OC**H**$_3$)$_2$), δ 3.33 ppm (s, 3H, -OC**H**$_3$). ^{31}P NMR (500 MHz, CDCl3): δ 22 ppm (s, 1P, O**P**(OCH_3)$_2$).

mPEO-dimethyl ethyl phosphonate (8b)

In a controlled atmosphere of N2 are dispersed 3 times in a pre-thermally heated round bottom flask 80.3 mmol of NaH mmol in hexane in order to get rid of the mineral oil. Once the hexane is dried 60 mL of dry THF are added nad the solution I s cooled in an ice bath. Then are slowly added dropwise 73 mmol of compound **3,** the solution is stirred at 0°C for 1 hour. 20 mL of a solution 0.075M of compound **6** in dry THF is added dropwise in 20 minutes. The mixture is carefully brought to 40°C and stirred for 20 hours. 10 ml of deionized water is slowly added to the mixture in order to quench the reaction. The solvent is then evaporated in vacuum and the solid is dissolved in DCM (100ml) and extracted with brine (3x100 mL). The organic layer is dried over sodium sulfate and after 2 hours filtered. The polymer is further precipitated in cold diethyl ether 3 times, the solvent is evaporated in vacuum and dried overnight in vacuum oven at 50°C (yield 14%). ^{1}H NMR (500 MHz, $CDCl_3$): δ 3.87 ppm (d, 2H, O-C**H**$_2$-P), δ 3.59 ppm (t, 2H, C**H**$_2$-O-CH_2-P), δ 3.54 ppm (m, 44H, -C**H**$_2$C**H**$_2$- PEO chain), δ 3.50-3.48 ppm (d,

6H, P(OC**H**$_3$)$_2$), δ 3.33 ppm (s, 3H, -OC**H**$_3$). ^{31}P NMR (500 MHz, CDCl3): δ 22 ppm (s, 1P, O**P**(OCH$_3$)$_2$).

mPEO-dimethyl ethyl phosphonate (9)

In a controlled atmosphere of N2 are dispersed 3 times in a pre-thermally heated round bottom flask 11 mmol of NaH mmol in hexane in order to get rid of the mineral oil. Once the hexane is dried 60 mL of dry THF are added and the solution is cooled in an ice bath. Then are slowly added dropwise 8.8 mmol of compound **3,** the solution is stirred at 0°C for 1 hour. 20 mL of a solution 0.2M of compound **7** in dry THF is added dropwise in 20 minutes. The mixture is carefully brought to room temperature and stirred for 20 hours. 10 ml of deionized water is slowly added to the mixture in order to quench the reaction. The solvent is then evaporated in vacuum and the solid is dissolved in DCM (100ml) and extracted with brine (3x100 mL). The organic layer is dried over sodium sulfate and after 2 hours filtered. The polymer is further precipitated in cold diethyl ether 3 times, the solvent is evaporated in vacuum and dried overnight in vacuum oven at 50°C (yield 11%). ^{1}H NMR (500 MHz, $CDCl_3$): 3.88 ppm (d, 2H, O-C**H**$_2$-P), δ 3.5 ppm (m, 44H, -C**H**$_2$C**H**$_2$- PEO chain), δ 3.48 ppm (d, 6H, P(OC**H**$_3$)$_2$), δ 3.34 ppm (s, 3H, -OC**H**$_3$), δ 3.41 ppm (t, 2H, O-C**H**$_2$$CH_2CH_2CH_2CH_2$-O), δ 3.36 ppm (t, 2H, $CH_2CH_2CH_2CH_2$C**H**$_2$-O), δ 3.34 ppm (s, 3H, -OC**H**$_3$), δ 1.51 ppm (m, 4H, CH_2C**H**$_2$$CH_2$C**H**$_2$$CH_2$-O), δ 1.31 ppm (m, 2H, CH_2CH_2C**H**$_2$$CH_2CH_2$-O). ^{31}P NMR (500 MHz, CDCl3): δ 22 ppm (s, 1P, O**P**(OCH$_3$)$_2$).

mPEO-phosphate (10)

mPEO of different molecular weights are modified with the same procedure[37], we report an example with the mPEO 500. Typically, 0.5 mmol of mPEO is dissolved in dry DCM and added dropwise to a solution of phosphoryl chloride ($POCl_3$, 1.2 eq.) and TEA (2.4 eq.) in ice bath. The reaction is slowly brought to room temperature and the stirred for 24 hours. Then 5 mL of deionized water is slowly added to the mixture and left react for 1 hour. The solvent is removed in vacuum and the crude product is dissolved in DCM and extracted with acidic water (HCl 0.2 mM) and then extracted three times with saturated brine. The organic phase is collected and dried over $MgSO_3$, filtered and precipitated three times in diethyl ether. ^{1}H NMR (500 MHz, $CDCl_3$): 4.12 ppm (m, 2H, $CH_2C\mathbf{H_2}$-O-P), δ 3.62 ppm (m, 454H, -C$\mathbf{H_2}$C$\mathbf{H_2}$- PEO chain), δ 3.34 ppm (s, 3H, -OC$\mathbf{H_3}$), ^{31}P NMR (500 MHz, CDCl3): δ 2.01 ppm (s, 1P, O**P**$(OH)_2$).

Grafting-to approach of mPEO derivatives on TiO_2 nanocrystals

The decoration of the NCs is done is with a grafting-to approach using functionalized mPEO **1** and **10** of different molecular weights ($M\overline{w}$, 44, 500, 2000, 5000,10000 and 20000 $gmol^{-1}$). A precise amount of the as prepared mPEO functionalized polymer is dissolved in a selected solvent (DCM, water) and diluted till the solution reaches a molar concentration of 4 mM. Typically the moles of polymer is equal to the moles of OA grafted on the anatase NCs. The stripped anatase NCs, in form of powder, are added in the solution and the mixture is sonicated for 10 minutes. Once the dispersion became homogenous, the solution

is stirred for in different experimental conditions. The product is then purified by centrifugation for three times with DCM and dried in vacuum at 60°C overnight.

Characterization methods

The hydrodynamic diameter and size distributions of the particles were determined by *Dynamic Light Scattering* (DLS) in deionized water and DCM (0.1 mg mL^{-1}). The measures were recorded at 25 °C on a Malvern Zetasizer equipped with a continuous wave 1 mW He−Ne laser operating at 632.8 nm and an avalanche photodiode detector, Q.E. > 50% at 633 nm, placed at 173° with respect to the incident beam. Reported data are the average of at least three different measurements of the size distribution as the function of the intensity. Colloid stability was evaluated with *ζ-Potential* analysis; the measure was taken at 25 °C in deionized water, with a sample concentration of 0.1 mg mL−1 and using a Malvern Zetasizer instrument. *Nitrogen adsorption−desorption isotherms* were measured at liquid nitrogen temperature using an ASAP 2010 analyzer (Micro- metrics). The samples were outgassed for 12 h at 473 K. The surface area was calculated using the *Brunauer−Emmet−Teller* (BET) model[38]. For *X-ray* characterization, a D8 Advance powder diffractometer (Bruker) was used with Cu $K\alpha_1$ radiation (λ = 1.5418 Å) and secondary-beam monochromator. The powder is added on a quartz sample holder and measured. Amount and definition of tethered ligand on the NCs surface has been verified with *Attenuated Total Reflection (ATR)-FTIR and Thermogravimetric analysis* (TGA). Fourier transform infrared characterization was

performed using a PerkinElmer Spectrum 100 instrument scanning from 650 to 4000 cm−1 with a resolution of 4 cm−1 for 64 scans. The sample, in the form of powder, is added on the sample holder and directly analyzed over the Si crystal with the Universal ATR (UATR).TGA analysis was carried out with a Mettler Toledo TGA/DSC1 STARe System, at a constant gas flow (50 cm^3 min^1). The thermal profile was the following: 25° C 5 min (air); 25–800° C with a rate 10 C min^{-1} (air). *Bright field Transmission electron microscopy* (BF-TEM) imaging was performed on a JEOL JEM-1011 microscope equipped with a thermionic gun operating at 100 kV accelerating voltage. For these analyses, the samples were prepared by dropping dilute suspensions of NCs onto carbon-coated 200 mesh copper grids. ^1H, ^{31}P NMR spectra were recorded using a Bruker AMX-500 spectrometer operating at 500 MHz. Thermal properties were determined by *Differential Scanning Calorimetry* (DSC) using a Mettler Toledo DSC 1 instrument with a heating and cooling rate of 20 or 10 K/min under nitrogen gas flow (80 mL/min).

Results and discussions

Nanocrystals synthesis and characterization

As prviously described in the first chapter, there are two main protocols adopted to produce PGNCs: grafting-from and grafting-to approach. The first one is a surface intiated growth of a polymer chain from a pre attached initiator. The second approach, on the other hand, consists in the grafting of a preformed and end functionalized polymer to a NCs surface. In order to minimize the anisotropic issues related to the

grafting process we studied a spherical system. Kumar, S. K. et al. explained that "*the "grafting-to" mechanism covers more of the surface of a nanoparticle (NP) than the "grafting-from" analog at the same grafting density. Similarly, the distribution of grafted chains is also narrower in the "grafting-to" case. Finally, we show that the anisotropy of the NP surface coverage by the NP is also smaller in the "grafting-to" situation*."[39] These three facts together imply that the "grafting-to" method produces NPs that are more homogenous and uniformly covered by polymer, which represents the best scenario for our experiments. In our work the grafting-to process is applied to spherical NCs in order to avoid any anisotropic effect. Since the main idea is to create a nanocomposite starting from TiO_2 particles due to their intrinsic properties previously explained in the introduction section, anatase NCs is the most suitable crystal phase, since it is the most stable titanium dioxide polymorph in the range of sizes lower than 30 nm[40]. The synthetic route used is a solvothermal synthesis that produce monodisperse, quasi-spherical anatase NCs. These NCs are stabilized by oleic acid that acts as a capping agent, it can control the crystal growth and at the same time as stibilezes the NCs in organic environments[34].

The NCs have been characterized after being repeatedly washed with ethanol to get rid of the ungrafted OLAC and then dried in a vacuum oven. The size and shape of the NCs was observed by TEM and as reported in the picture Figure 21 they appear as quasi-spherical crystals. Thanks to the analysis of the pictures carried out with ImageJ software, in particular with the particle analyzer plug-in, it has been possible to determine the size of the particles (histogram, Figure 22).

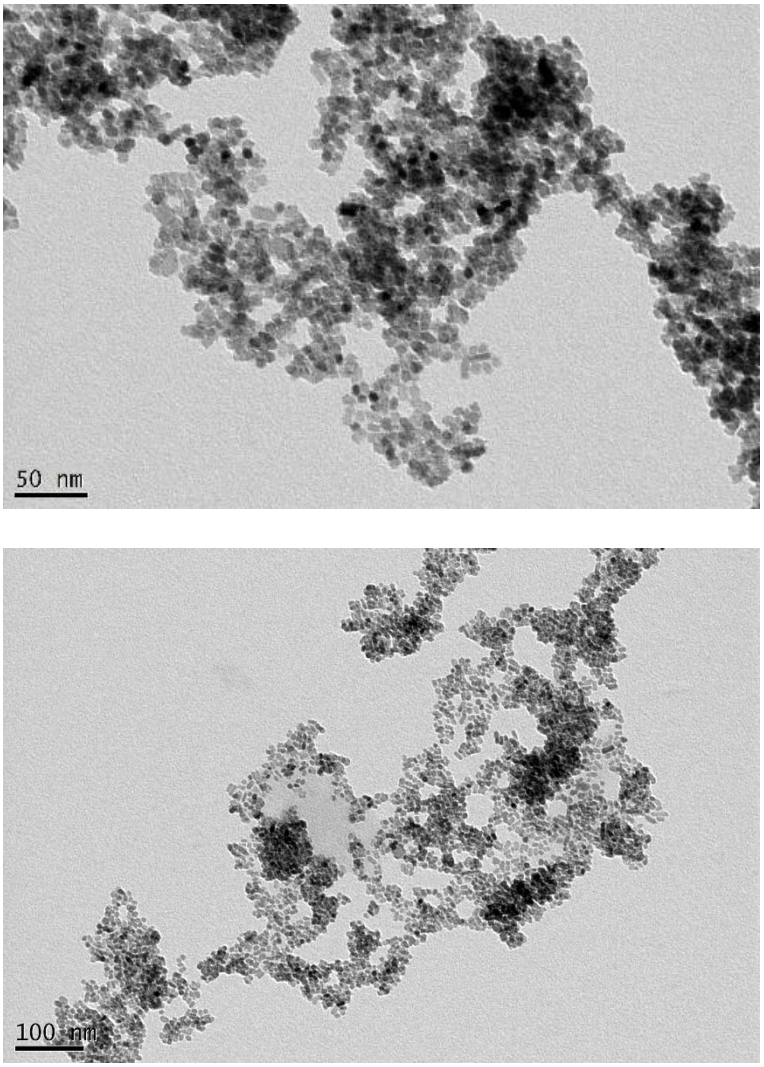

Figure 21 TEM micrographs of anatase nanocrystals covered by oleic acid molecules at different magnitude.

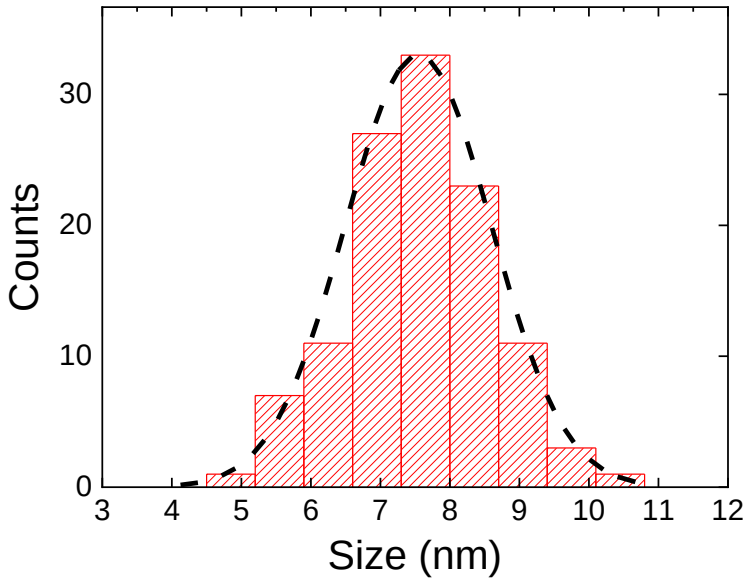

Figure 22 Histograms of the NCs size distribution obtained from TEM micrographs, the dashed line represents the Gaussian fitting of the data.

The XRD pattern (Figure 23) shows that the as prepared particles are anatase nanocrystals. The diffractogram pattern correspond to the simulated one obtained through mercury® software and from literature references. The anatase characteristic diffraction peak at $2\theta = 25.3°$, that corresponds to the (101) face, is observed while the rutile peak at $2\theta = 27.5°$, that corresponds to the (110) face, is absent.

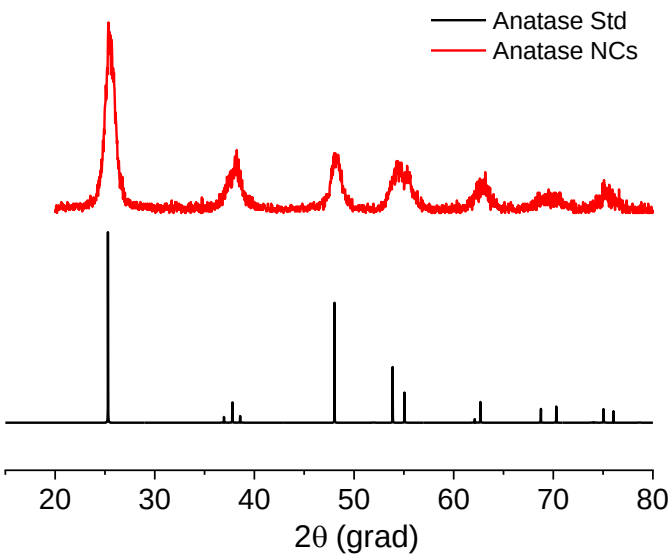

Figure 23 XRD pattern of the anatase NCs prepared by solvothermal approach (up, red line) and anatase bulk standard (bottom, black line).

Moreover, diffractograms of NCs are also influenced by crystal size that causes a broadening in the diffraction lines: the broadening is inversely proportional to crystal size. By analyzing the XRD data, it is possible to estimate the crystal dimensions using Sherrer's formula (eq.12, chapter 2). Eq.1 was used to calculate NCs size as reported in table 1. The raw data obtained by the XRD analysis was analyzed and fitted with a peak analyzer plug in of the Originlab® data analyzer software. The raw data and the fitted functions are reported in the Figure 24.

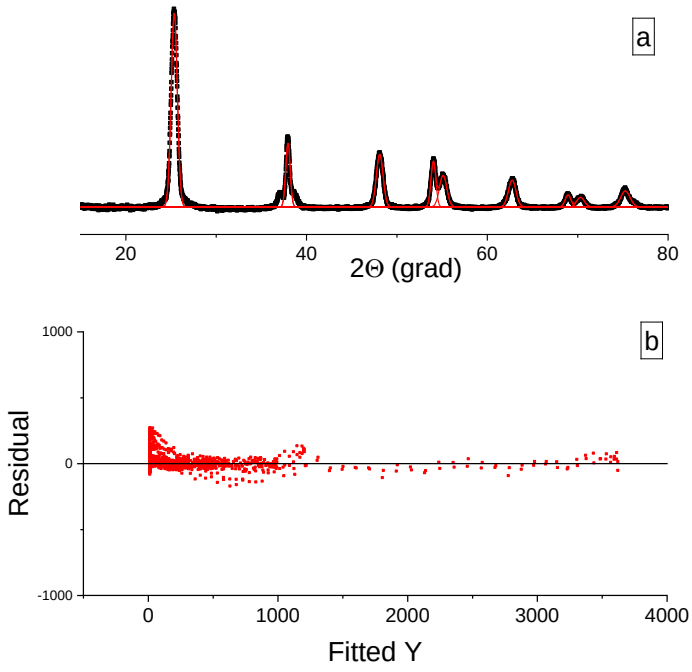

Figure 24 a) Raw XRD data (Black Square) superimposed with the calculated fitted data (Red Line); b) Residual calculated by the fitting process.

From the liine broadening at half the maximum intensity (Full Width at Half Maximum, FWHM) and Θ angle it was possible to calculate the crystalline size with eq.2. The sizes calculated along the different crystallographic directions showed homogeneous distribution along the different directions (Figure 25).

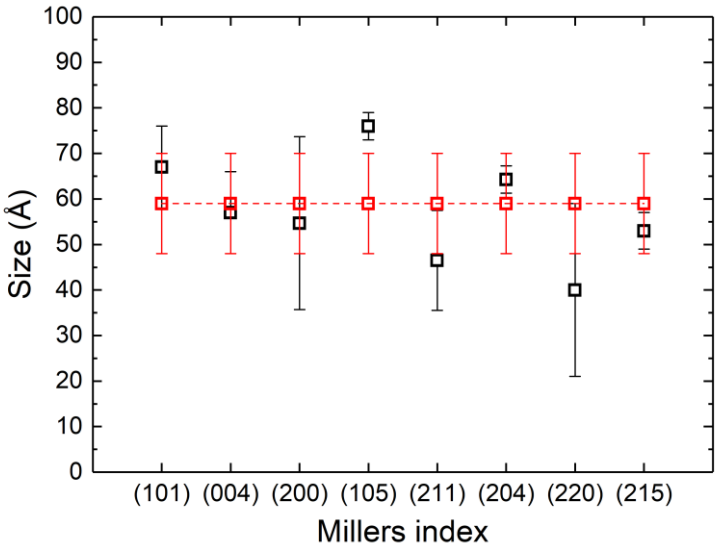

Figure 25 Crystallite size of the anatase NCs, information obtained by XRD analysis: red square represents the mean size with its standard deviation; black square represents the crystallite size along the different crystallographic directions

XRD data confirmed that the NCs have a quasi-spherical shape as firstly suggested by the bidimensional pictures obtained by the TEM. The size has been finally verified through DLS analysis. Size distribution was measured in toluene, DCM and chloroform as solvents, the analyses defined a hydrodynamic diameter of 7.6±1.1 nm. This value refers to a particle covered by a layer of solvated OA (estimated to be 2 nm for a full covered NC[41]). The values obtained with different techniques are consistent (Table 4) and suggest that we are dealing with quasi-spherical anatase NCs. To get all the information required for our next experiments it is necessary the evaluation of the specific surface area (SSA). It is possible to calculate the SSA with the Sauter formula (eq.3)[42]

$$SSA = \frac{K_{sphere}}{\rho \cdot d} \quad (3)$$

Were K representing the shape factor of the NCs, in our case a sphere (K=6); ρ represents the anatase density (4.23 g cm^{-3}) and *d* the represents the estimated diameter. The results obtained from the TEM experimental data are compared with the values obtained from N_2 adsorption at liquid nitrogen temperature and applying the Brunauer-Emmet-Teller analysis (Table 4), a good agreement is evident.

Table 4 Crystal dimensions derived from XRD calculated at (101) peak, TEM micrographs, DLS measurements in water reported with their PDI. Experimental specific surface area (SSA_{exp}) as well as an estimate of surface area based on TEM size and calculated using Sauter equation ($SSA_{predicted}$). ζ-Potential measured in water dispersions. All the data are reported with their standard deviation and refers to the stripped nanocrystal sample.

Sample	XRD nm	TEM nm	DLS nm	PDI	SSA_{exp} m^2g^{-1}	$SSA_{predicted}$ m^2g^{-1}	ζ-Potential mV
Anatase	5.9±0.4	7.6±1.1	12	0.191	174±7	197±28	-27.8±6.5

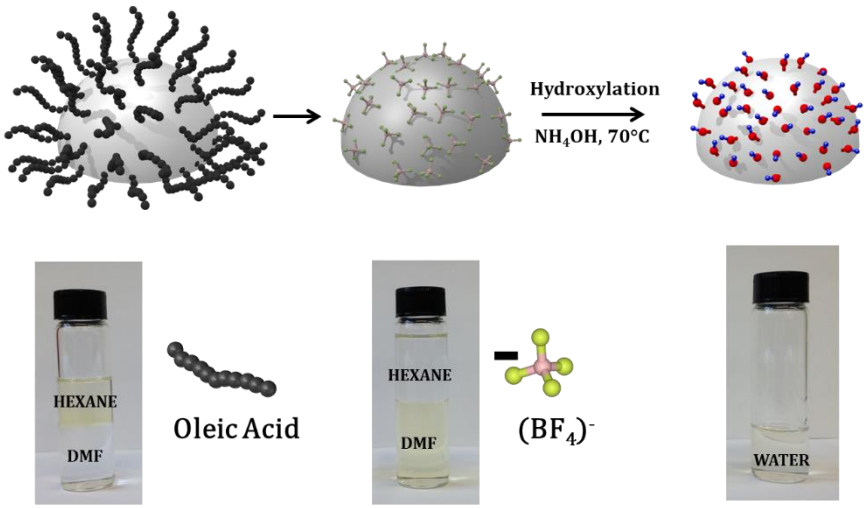

Figure 26 Scheme of the overall ligand stripping process; images of the biphasic solution, at left the particle are covered by OA and are stable in hexane,in the center

is reported the picture of the biphasic solution after ligand exchange process. The particles are covered by BF4- counterion making them more stable in DMF. At the right is reported the picture of the NCs naked dispersed in water.

In order to operate in the simplest and the most ideal conditions, the as prepared NCs were subsequently stripped by a two-step process to give a naked surface that can bind the modified polymer chains (scheme in Figure 26). In order to verify that the stripping process did not affect the size, shape and dispersion of the NCs in solvent, DLS of the NCs in the 2 different stripping stages were performed (Figure 27). As expected the size are not affected by the ligand stripping process and the NCs maintain their own ability to be dispersed and intrinsic characteristics.

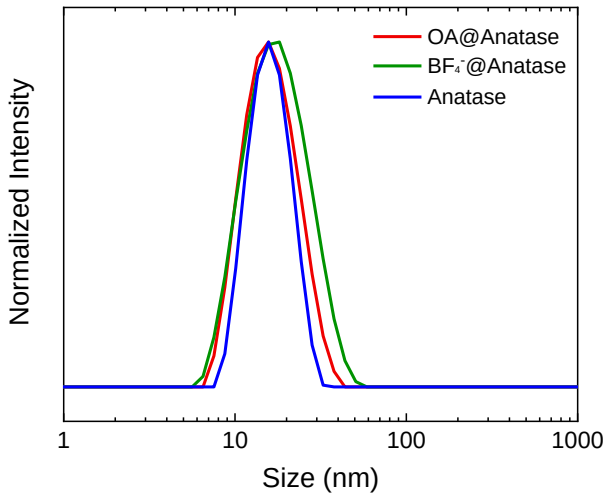

Figure 27 Representation of the DLS study: OA@Anatase in hexane red line; BF_4^- @Anatse in DMF green line and naked anatase in deionized water is represented by blue line

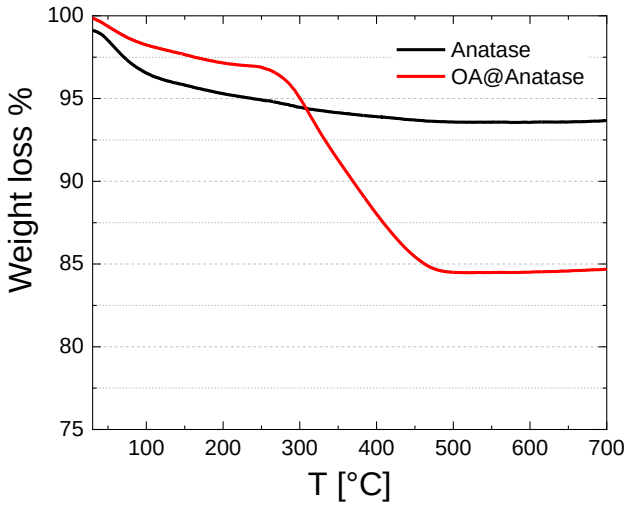

Figure 28 Thermogravimetric analysis of the capped NCs OA@Anatase represented by the red line and the naked NCs represented by the black line

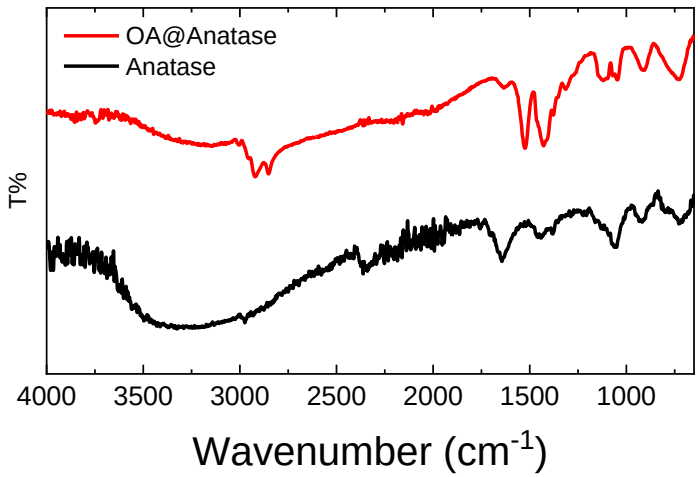

Figure 29 FTIR of the capped NCS OA@Anatase (up, red line); naked NCs of Antase (bottom, black line)

The replacement of OA by inorganic BF^{4-} anions is established by TGA and FTIR. In the IR spectra of the capped particle, reported in Figure 28 and Figure 29, the peaks associated to the aliphatic chain (3000-2750

cm^{-1}) together with the peaks of the antisymmetric and symmetric stretching of the carboxylate group (1520 cm^{-1} and 1410 cm^{-1}) are clearly present. In the stripped NCs spectra the peaks related to the oleic acid aliphatic chain do not appear, while the DMF peak appears (1640 cm^{-1}) due to the fact that DMF acts as a NCs stabilizer and is weakly bonded to the titania surface[35,43]. By comparing the FTIR of capped (top, red line) and stripped (bottom, black line) anatase NCs in Figure 29 we can notice the lack of all adsorptions associated to the oleic acid molecules in the bottom spectrum indicating an effective stripping of the NCs. The TGA analysis of the stripped NCs (Figure 28) shows that between 150 to 600 °C there is no more than 1% of organic material, indicating a fundamentally bare surface except for some absorbed residues that IR identifies as DMF. In order to verify the stability of the colloidal solution prepared with the *naked* nanoparticle a ζ-potential analysis was performed. The value expressed by this analysis indicates the magnitude of electrostatic repulsion between charged particles in a dispersion. For molecules and particles that are small enough, a high absolute zeta potential will thus confer stability, while a low repulsive potential can be overcome by attractive forces resulting in flocculation of the dispersion. From the data collected it appears that the NCs are stable in aqueous solution.

Grafting-to process and characterization

Since our aim was to create a protocol that enables the control over the grafting density and the conformation of a polymer on a spherical surface, we exploited the grafting-to approach in different experimental conditions: anchoring group, molecular weight, solvent, polymer concentration and temperature. All the experiments are depicted in

Table 5, each experiment performed at least three times to verify the reproducibility. The efficacy of the grafting process has been verified through FTIR to get qualitative information and with TGA to get quantitative information. From the infra-red spectroscopy, it is it possible to verify that the polymer is attached on the surface thanks to the comparison between the characteristic vibrational peaks of the mPEO chains and the grafted polymer nanocrystals.

Table 5 List of the experiments conducted for this work, each line corresponds to at least three experiments, all the values corresponds to the arithmetic mean of each experiment with its std. deviation. σ is calculated following eq.5.; Σ is the footprint of a single chain and is calculated following eq.6; Dm corresponds to the mean distance evaluated using eq.7; R_F represents the Flory radius while the conformation is deducted using the method illustrated below in the main text.

Sample	Solvent	N	[mPEO]	T	W_{loss}	σ		Σ		Dm		RF	Conformation
		monomer unit	$mol^{-3}L$		%	chain nm^{-2}	std. err.	nm^2chain^{-1}	std. err.	nm	std. err.	nm	
mPEO_0.5K_OH	Water	11	6.7	25	3.1	0.2206	0.0330	4.53	0.68	2.4	0.36	1.5	MUSHROOM
mPEO_2K_OH	Water	45	6.7	25	5.5	0.1000	0.0020	10.00	0.20	3.6	0.07	3.5	MUSHROOM
mPEO_5K_OH	Water	114	6.7	25	5.4	0.0396	0.0010	25.28	0.64	5.7	0.31	6.0	MUSHROOM
mPEO_10K_OH	Water	227	6.7	25	6.4	0.0238	0.0006	42.09	1.06	7.3	0.18	9.1	BRUSH
mPEO_20K_OH	Water	455	6.7	25	6.7	0.0124	0.0003	80.39	1.94	10.1	0.24	13.8	BRUSH
mPEO_0.5K_COOH	Water	11	6.7	25	3.9	0.2787	0.0093	3.59	0.12	2.1	0.07	1.5	MUSHROOM
mPEO_2K_COOH	Water	45	6.7	25	6.3	0.1157	0.0030	8.64	0.22	3.3	0.21	3.5	MUSHROOM
mPEO_5K_COOH	Water	114	6.7	25	6.4	0.0476	0.0010	21.03	0.44	5.2	0.11	6.0	BRUSH
mPEO_10K_COOH	Water	227	6.7	25	6.8	0.0251	0.0006	39.81	0.95	7.1	0.17	9.1	BRUSH
mPEO_20K_COOH	Water	455	6.7	25	6.7	0.0125	0.0003	80.06	1.92	10.1	0.24	13.8	BRUSH
mPEO_0.5K_POOH	Water	11	6.7	25	6.2	0.4567	0.0230	2.19	0.11	1.7	0.08	1.5	MUSHROOM
mPEO_2K_POOH	Water	45	6.7	25	9.2	0.1747	0.0190	5.72	0.62	2.7	0.29	3.5	BRUSH
mPEO_5K_POOH	Water	114	6.7	25	7.0	0.0518	0.0073	19.29	2.72	5.0	0.70	6.0	BRUSH
mPEO_10K_POOH	Water	227	6.7	25	7.1	0.0265	0.0013	37.75	1.85	6.9	0.34	9.1	BRUSH
mPEO_20K_POOH	Water	455	6.7	25	6.9	0.0127	0.0003	78.74	1.86	10.0	0.24	13.8	BRUSH
mPEO_0.5K_OH	DCM	11	6.7	25	6.1	0.4484	0.0139	2.23	0.07	1.7	0.05	1.5	MUSHROOM
mPEO_2K_OH	DCM	45	6.7	25	6.1	0.1123	0.0020	8.90	0.16	3.4	0.06	3.5	BRUSH
mPEO_5K_OH	DCM	114	6.7	25	6.3	0.0466	0.0010	21.47	0.46	5.2	0.11	6.0	BRUSH
mPEO_10K_OH	DCM	227	6.7	25	6.4	0.0236	0.0010	42.34	1.79	7.3	0.31	9.1	BRUSH

Sample	Solvent	N	[mPEO]	T	W_{loss}	σ		Σ		Dm		R_F	Conformation
		monomer unit	$mol^{-3}L$		%	chain nm^{-2}	std. err.	nm^2chain^{-1}	std. err.	nm	std. err.	nm	
mPEO_20K_OH	DCM	455	6.7	25	7.6	0.0142	0.0003	70.52	1.49	9.5	0.20	13.8	BRUSH
mPEO_0.5K_COOH	DCM	11	6.7	25	8.8	0.6643	0.0200	1.51	0.05	1.4	0.07	1.5	BRUSH
mPEO_2K_COOH	DCM	45	6.7	25	7.8	0.1460	0.0040	6.85	0.19	3.0	0.08	3.5	BRUSH
mPEO_5K_COOH	DCM	114	6.7	25	9.0	0.0681	0.0020	14.69	0.43	4.3	0.13	6.0	BRUSH
mPEO_10K_COOH	DCM	227	6.7	25	8.8	0.0335	0.0007	29.87	0.62	6.2	0.13	9.1	BRUSH
mPEO_20K_COOH	DCM	455	6.7	25	6.7	0.0124	0.0003	80.78	1.96	10.1	0.25	13.8	BRUSH
mPEO_0.5K_POOH	DCM	11	6.7	25	8.2	0.6129	0.0100	1.63	0.03	1.4	0.02	1.5	BRUSH
mPEO_2K_POOH	DCM	45	6.7	25	7.2	0.1345	0.0030	7.43	0.17	3.1	0.07	3.5	BRUSH
mPEO_5K_POOH	DCM	114	6.7	25	7.1	0.0524	0.0010	19.08	0.36	4.9	0.09	6.0	BRUSH
mPEO_10K_POOH	DCM	227	6.7	25	8.6	0.0324	0.0013	30.85	1.24	6.3	0.25	9.1	BRUSH
mPEO_20K_POOH	DCM	455	6.7	25	7.2	0.0134	0.0008	74.57	4.45	9.7	0.58	13.8	BRUSH
mPEO_0.5K_POOH	DCM	11	5.7	50	7.8	0.5867	0.0293	1.70	0.09	1.5	0.07	1.5	MUSHROOM
mPEO_0.5K_POOH	DCM	11	11.5	50	8.8	0.6647	0.0133	1.50	0.03	1.4	0.03	1.5	BRUSH
mPEO_0.5K_POOH	DCM	11	17.2	50	10.8	0.8336	0.0250	1.20	0.04	1.2	0.04	1.5	BRUSH
mPEO_0.5K_POOH	DCM	11	22.9	50	11.5	0.9000	0.0270	1.11	0.03	1.2	0.04	1.5	BRUSH
mPEO_0.5K_COOH	DCM	11	5.5	50	10.2	0.7827	0.0391	1.28	0.06	1.3	0.06	1.5	BRUSH
mPEO_0.5K_COOH	DCM	11	11.0	50	10.1	0.7776	0.0389	1.29	0.06	1.3	0.06	1.5	BRUSH
mPEO_0.5K_COOH	DCM	11	16.5	50	10.1	0.7767	0.0388	1.29	0.06	1.3	0.06	1.5	BRUSH
mPEO_0.5K_COOH	DCM	11	22.0	50	10.3	0.7900	0.0395	1.27	0.06	1.3	0.06	1.5	BRUSH

We reported an example in Figure 30; the green line represents the unfunctionalized mPEO chain where the vibration peak of the OH terminal group is easily detectable at 3300 cm^{-1}; at 2900 cm^{-1} the peak related to the stretching of the CH_2 groups is detected and at 1100 cm^{-1} the C-O bonds vibration peak. The grey area highlights the region of the spectra where the mPEO peaks are found: it is possible to observe that the peaks appears in the grafted samples (in order from top to bottom: POOH yellow line, COOH blue marine line and OH red line), confirming the presence of the polymer chain on the anatase surface, even if the signal sometimes is hardly detectable.

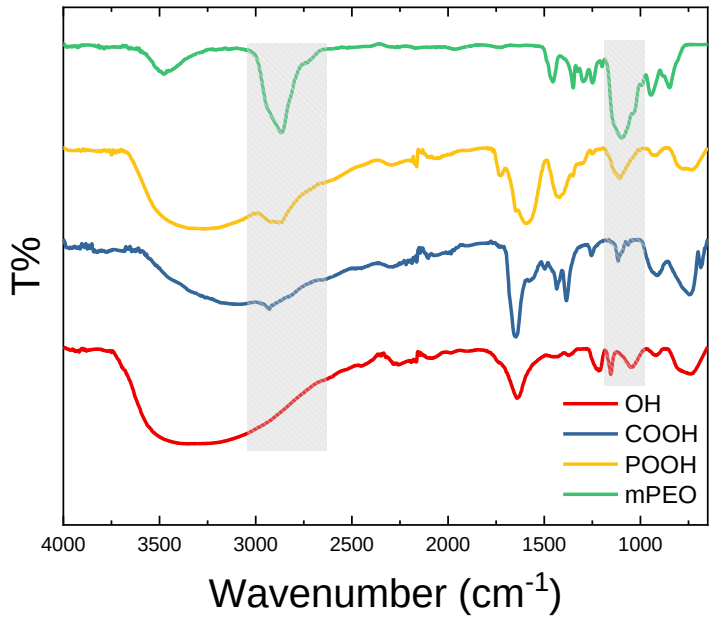

Figure 30 FTIR plotted as function of the transmission percentage of the grafted anatase NCs in same experimental condition with mPEO (Mw̄ 500 $gmol^{-1}$) in order from top to down: mPEO green line, mPEO-POOH yellow line, mPEO-COOH blue marine line and mPEO-OH red line

In order to better understand the grafting process the values of grafting density were calculated. TGA was used to calculate the amount of organic ligand grafted in the NCs surface (Figure 31). The grafted chains are calculated using eq.4

$$\text{chain}_{\text{graft}} = \frac{W_{loss}\%}{(100 - W_{loss}\%)\cdot M\bar{w}_{poly}} \cdot N_a \qquad (4)$$

Were $W_{loss}\%$ represents the weight loss percentage got from the thermogravimetric analysis in the range between 150°-750°C; $M\bar{w}_{poly}$ is the molecular weight of the grafted polymer and N_a is the Avogadro number. Knowing the specific surface area (SSA), it allows to calculate the σ normalized over mass of anatase using eq.5

$$\sigma = \frac{chain_{graft}}{SSA_{BET}} \qquad (5)$$

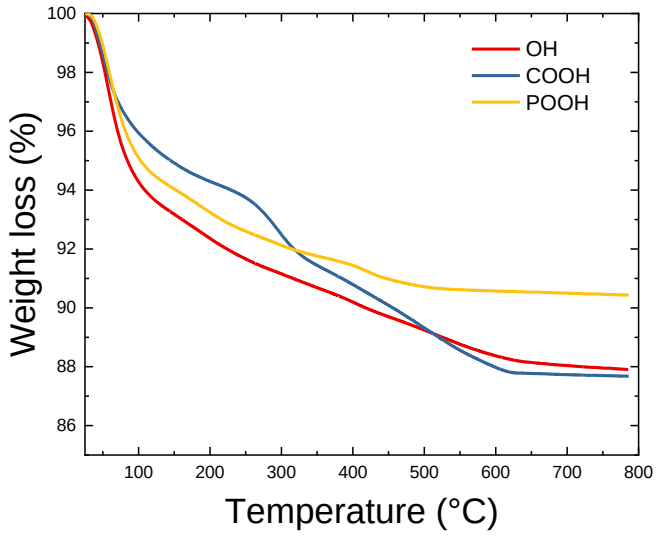

Figure 31 Example of TGA of mPEO (Mw̄ 500gmol^{-1}) functionalized with POOH yellow line, COOH blue marine line and OH red line grafted on anatase NCs.

As previously mentioned in the introduction section, we assume that a single grafted chain acts as a non-interacting rigid sphere tethered on the

surface in a single point (Figure 19). In these conditions it is possible to calculate a theoretical mean distance between two chains represented by the Flory radius (R_F, eq.8), and an experimental mean distance (D_m), deducted by TGA and BET analysis following eq.6.

$$D_m = \sqrt{\frac{4\pi}{\Sigma}} \quad (6)$$

Where Σ represents the footprint of the chain grafted on the surface, this value is experimentally evaluated by eq.7

$$\Sigma = \sigma_{exp}^{-1} \quad (7)$$

Where σ_{exp} is the experimental graft density calculated using eq.4. The Flory radius is defined by eq.8 as follows

$$R_F = aN^{v} \quad (8)$$

Where a represents the monomer length (0.35nm), N the number of monomer units and v is the Flory exponent. This exponent can have different values depending on the conditions, in the ideal condition of a polymer diluted in a good or tetha solvent, v is equal to 0.6. In order to confirm that our system has the overall same behavior, we followed the work of K. Linegar, and using DLS analysis we evaluate the hydrodynamic radius (R_h) and, thanks to the relation $R_h = 0.64\, R_g$, we can calculate the radius of gyration (R_g). We assume that the as calculated R_g is comparable to $R_F/2$ since Flory model describes the size of a polymer dissolved in a good or tetha solvent. The R_g calculated from DLS are reported in Table 6 and plotted in graph at ***Figure 32***. The data are then plotted using an allometric function ($y = ax^b$), is it observed that the experimental data are well fitted by this function and that the resulting constants are (Table 7), within error, in good agreement with the predicted R_F values. We can affirm

that the polymer acts as an ideal random coil dissolved in a good or tetha solvent (b=0.6 as *v*) and that we can use the Flory equation to calculate the theoretical size of our polymer chain for both the solvents used.

Table 6 Results from the DLS analysis conducted at 25°C in water and DCM. $R_F/2$ represents half of the Flory radius and Rg is the radius of gyration extrapolated by the Rh value

		water		DCM	
N	$R_F/2$	Rg	std. dev.	Rg	std. dev.
Monomer unit	nm	nm		nm	
11	0.8	0.9	0.1	0.9	0.1
45	1.7	2.3	0.2	1.5	0.4
114	3.0	4.3	0.3	3.6	0.6
227	4.5	5.0	0.2	5.5	0.4
455	6.9	7.2	0.4	7.3	1.4

Table 7 fitting constant of the allometric function ($y = ax^b$) used to fit the DLS experimental data

Sample	a		b	
	value	std.dev.	value	std.dev.
$R_F/2$	0.175	-	0.600	-
Rg water	0.241	0.0865	0.562	0.045
Rg DCM	0.190	0.0435	0.616	0.045

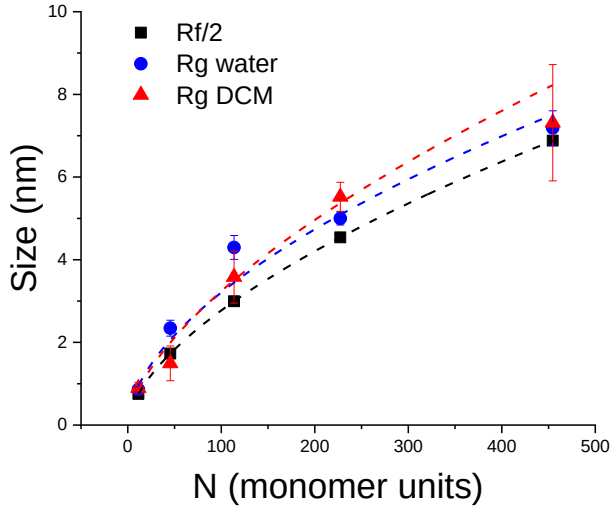

Figure 32 Plot of radius of gyration extimated through DLS analysis as function of the monomer units of the mPEO. The black squarse represent the Flory radius (R_F); the blue circle represents the Rg for polymer dissolved in water and red triangle represent the analysis conducted in DCM. The dashed lines represent the allometric fitting of the experimental points, the fitting function parameters are collected in Table 7.

Once all the parameters are described and calculated it is possible to define the polymer conformational regime: when $D_m<R_F$ the polymer is in the brush like regime, vice versa when $D_m \geq R_F$ the mushroom regime is assumed (Figure 19). All the experiments are reported in Table 5 As reported by Hagar I. Labouta et al.[31] the calculated ratio of the Flory dimension to the average distance between adjacent mPEO chains (R_F/D_m) can be used as an indicator for mPEO conformation: values below 1.0 indicate a mushroom regime, while those above 1.0 indicate brush. As R_F/D_m approaches zero, inter-chain interactions become more and more scarce and areas of bare particle between mPEO chains begin to dominate the particle surface. On the other hand, R_F/D_m values equal to or larger than 2.0 represent denser brush configurations. From the comparison of the experimental data we depicted a map of the different regimes (mushroom, brush, dense brush) as function of R_F/D_m and the monomer units (N) for

both the solvents. First, we tested the behavior of mPEO polymer chain with different molecular weights functionalized with different anchoring groups: hydroxyl, carboxylate and phosphate group (synthesis reported in materials and methods section). The experiments have been done in the same experimental time and temperature conditions, maintaining the polymer molar concentration fixed and using two different solvents. The the reaction was conducted forr 72 hours in order to avoid kinetic effects.

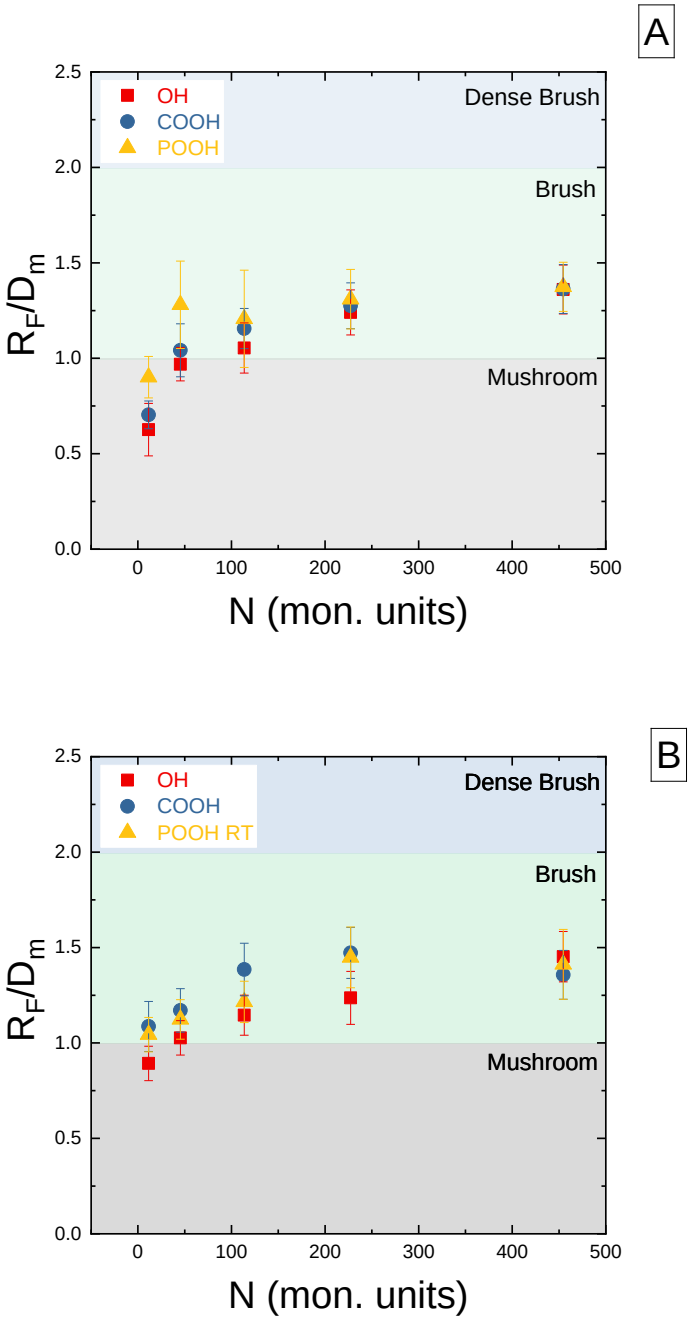

Figure 33 plot ratio R_F/D_m vs N. three sets of samples. A) experiments conducted in deionized water; B) experiments conducted in DCM. For each graph the red square represents OH group; blue marine circle represents COOH group and orange triangles represents POOH group. The areas represent three different thermodynamic conditions:

pale grey represents the mushroom regime; the pale green the brush regime and the pale blue represents the dense brush regime.

The first set of samples was produced in deionized water, while the second one is done in DCM (Figure 33). Comparing the graphs Figure 33 (A, water) and Figure 33 (B, DCM), an effect of the solvent and of the anchoring group on the conformation regime of polymer chains can be appreciated at low molecular weight, while at high molecular weight all the data converge to the same value of R_F/D_m. It is evident that the anchoring group, in certain conditions, plays a key role. It is reported in literature that the best anchoring group for titanium dioxide surfaces are the phosphor end group class of molecules[44–47] (phosphonic acids, phosphoesters, phosphate etc.), followed by carboxylate end groups (maleate, carboxylic acid, anhydride etc.) and hydroxyl groups. In general, all the classes of molecules can bond the highly reactive titanium dioxide nanoparticle surface, because presents several low coordinated titanium sites. We can calculate the number of polymer chains grafted on a single NC (#chains) simply dividing the surface area of a sphere (diameter 7.6 nm) by the footprint of our polymer chains (Σ). If we plot the #chains versus the number of monomer units (N) in a double log axis (Figure 34) it is possible to appreciate and better understand the grafting behavior of the different sets of samples as function of their end groups. Data points can be linearly fitted, the slopes so obtained increase going from mPEO-OH to mPEO-COOH and finally to mPEO-POOH.using water as solvent, On the other hand, if DCM is used the slope of the COOH fitting increases and reaches approximately the same value of the POOH group. These are still higher than the OH ones (COOH≈POOH>OH).

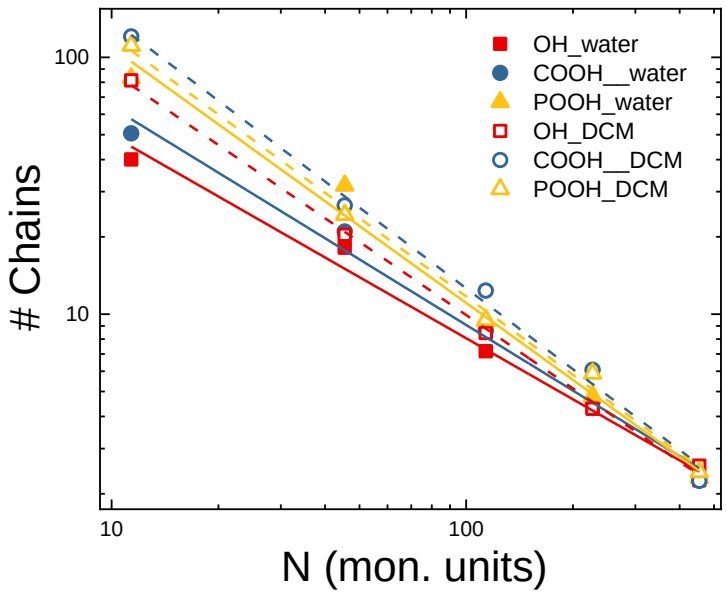

Figure 34 Plot of the #chains versus the number of monomer units (N) using a double log axis. Experiments conducted in deionized water are represented by the solid line and solid symbols; experiments conducted in DCM are represented by dashed lines and hollow symbols. For each graph the red square (solid and hollow) represents OH group; blue marine circle (solid and hollow) represents COOH group and orange triangles (solid and hollow) represents POOH group. The straight lines represent the best linear fitting of the curves.

If we compare the curves obtained for the two different set of experiments and we look at the linear fitting (Figure 34), it is observed that the absolute values of #chains (Table 8) remarkably increases using DCM as solvent (hollow symbols and dashed lines) instead of water (solid symbols and lines).

Table 8 Fitting linear slopes of the grafting density as function of the $M\bar{w}$ for both the solvents and for each sample.

		Slope		Statistics
		Value	**Std. error**	**Adj. R-square**
Water	OH	-0.79	0,05	0,98581
	COOH	-0.84	0,05	0,99276
	POOH	-0.99	0,06	0,98781
DCM	OH	-0,95	0,02	0,99727
	COOH	-1,04	0,05	0,99267
	POOH	-1,01	0,04	0,99293

It is also observed that at high molecular weight there is no evidence of the effect of the solvent or anchoring group. We assume that all these effects are due to multiple factors. Since we are dealing with a three components system (solvent, polymer and NCs) we must consider the interfacial interactions and energy involved. As we depicted and explained in the chapter 1 and as is reported[48,49] there is a strong bond between water molecules and titanium dioxide NCs that can compete with the anchoring group of the polymer chains. DCM is less interacting with the titania surface leaving it uncovered and more accessible to the functional groups of the polymer chains. Another interaction ought to be consideredvis the one between the polymer and the NCs surface. It is known that the polyethylene oxide interacts with the titanium dioxide NCs surface[50,51], minimizing its high surface energy. it should be noted that the polymers used have a chain size comparable or even larger than the anatase NCs. The experimental data shows that at high molecular weight fewer polymer chains are necessary to effectively passivate the anatase surface: it appears that the ethylene oxide monomer units interact with the titanium dioxide surface and lower the high surface energy. The other factor is the interaction of the polymer chain with the solvent. The behavior of a free chain in a solvent has been deeply studied during the years and multiple models and theories have been

developed. As previously mentioned Hansen solubility parameters can be used to estimate the Flory-Huggins interaction parameter, χ between mPEO and selected solvents using eq5:

$$\chi_{12} = \frac{V_m}{RT}\left[\left(\delta_{D.2} - \delta_{D,1}\right)^2 + 0.25\left(\delta_{P,2} - \delta_{P,1}\right)^2 + 0.25\left(\delta_{H,2} - \delta_{H,1}\right)^2\right] \quad (5)$$

Where δ_D, δ_P and δ_H are the contributions of dispersion forces, polar interactions and hydrogen bonds to solubility, respectively, V_m is the molar volume of the solvent, T is temperature and R is the gas constant. The calculated values are listed in Table 9.

Table 9 δ_D, δ_P and δ_H are the contributions of dispersion forces, polar interactions and hydrogen bonds, $\chi_{P\text{-}S}$ represents the Flory-Huggins solubility parameter. In this case evaluated using Hansen solubility parameter

Solvent	δ_{D*}	δ_{P*}	δ_{H*}	$\chi_{P\text{-}S}$
Water	15.6	16	42.3	2.3
Dichloromethane	18	12.3	7.2	0.6

* Handbook of polymer physics

If χ has a value equal to 0, it describes a mixture in the Θ condition, i.e. an athermal mixture. If χ=0.5 we have the so-called theta solvent, and the polymer in the mixtures behaves as unperturbed random coil. For values of χ larger than 0.5 we have a so-called "bad" solvent; for values smaller than 0.5 we have a "good" solvent. It appears from the model that DCM is slightly better solvent than water for polyethylene oxide polymers, is reported in literature that at high dilution they essentially act as Θ solvents[52]. On the other hand we have to consider the complexity of the interaction between water molecules and poly(ethylene oxide) that is not easily summarized in the χ parameter, for example this system is strongly temperature dependent since the PEO tend to phase separate at high temperature. The experimental data show that a grafting reaction is

maximized using solvents that effectively interact with the tethering polymer, a better solvent lowers the entropy of mixing, enabling the chain to access at higher energy conformation, paying less entropic costs.

In order to get a more complete view of the polymer grafting process, a set of reactions was conducted at higher temperature and starting molar concentration. A first attempt was made using mPEO 500 $gmol^{-1}$ functionalized with the phosphate group and grafting it in DCM at reflux temperature, (42°C) constantly increasing the starting molar concentration of the polymer reagent. The sum of these factors should improve the number of chains grafted on a NC, since increasing the temperature enhances the mobility of the mPEO chain, providing the energy necessary to achieve less-favored stretched conformations. Additionally, increasing the concentration of the polymer in solution lead to an improvement of the probability of a chain to stick on to the anatase surface.

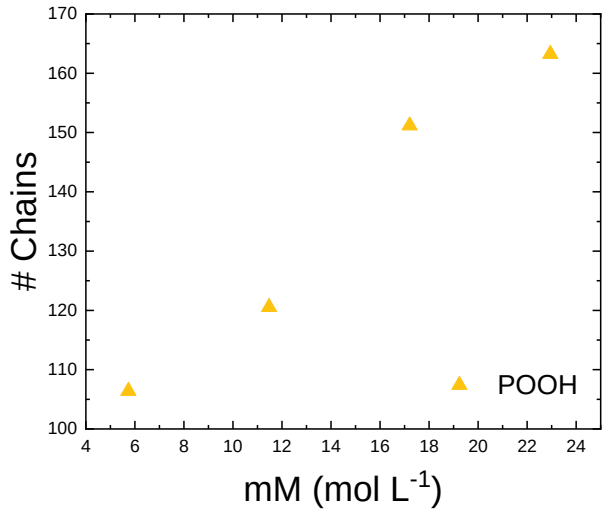

Figure 35 Plotted data of the # chains as function of the starting molar concentration, experiments conducted using phosphate terminated 500 $gmol^{-1}$ mPEO in DCM at 42°C.

In Figure 35, as expected[53], there is a detectable increase of the # chains as the starting concentration of mPEO increases, reaching values that are 65% higher than the starting number of grafted polymers. It is possible to verify the effect of the larger amount of the tethered polymer on the conformation plotting the R_F/D_m as function of the starting molar concentration of the functionalized mPEO (Fig. 19). It is possible to appreciate a shift to higher densities, but still not enough to reach the dense brush regime at this low molecular weight.

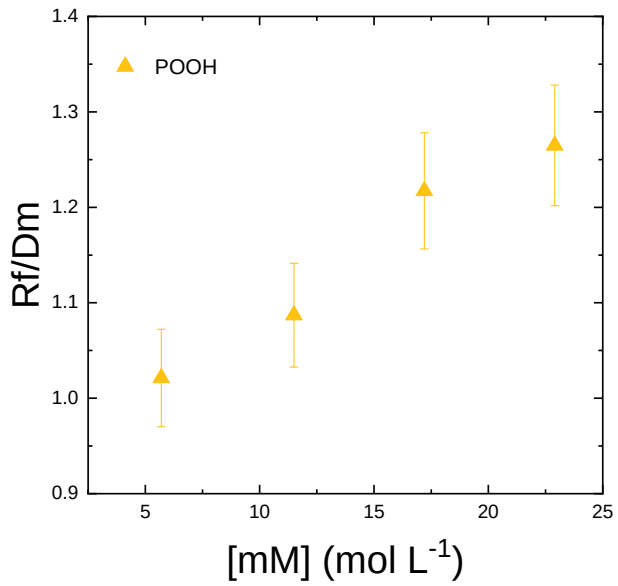

Figure 36 plotR Ratio R_F/D_m vs N. for experiments conducted with phosphate terminated 500 gmol^{-1} mPEO in DCM at 42°C with constantly increased molar concentration of mPEO. (yellow solid triangle.

These results are encouraging since they provide a tool to get more dense polymers grafted on NCs. In order to verify if these considerations are

relevant for other systems, the same set of experiments were done using carboxylic acid end terminated mPEO (results summarized in Figure 37).

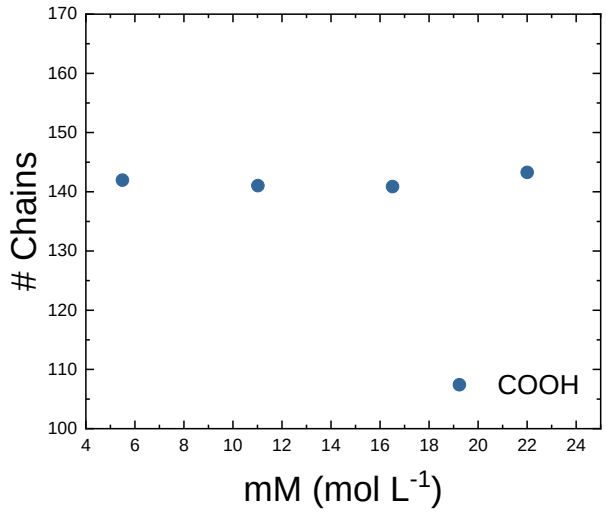

Figure 37 Grafting density as function of the starting molar concentration, experiments conducted using carboxylic acid terminated mPEO in DCM at 42°C.

Data depicted in Figure 20 demonstrate that for COOH terminated PEO neither the increasing amount of polymer concentration nor the increased temperature favors the attachment of the chains on the NCs surface. These results highlight the role of the anchoring group in the economy of the grafting-to process, revealing that the chemistry of the tethering process is more relevant than expected. Using the right chemical reaction, it is possible to modulate the graft densities; many authors exploit this concept to make NCs surface more chemically active, functionalizing the surface with a bifunctional molecule, with one functional moiety being used for grafting on the surface and the another free to react with other compounds that would not spontaneously bind the surface. This approach is found to be useful especially with silica nanoparticles (sylanization process) that are

effectively covered by alcoxysilane groups that bear another reactive group such as primary amines, acrylates and methacrylates, aldehyde etc. that can straightforwardly react with a functionalized polymer[54,55].

NMR Characterization of PGNCs

^{13}C NMR in solution is performed to provide yet another point of view on the behavior of the tethered polymer.NMR is a well established tool for understanding the conformations of polymers in solution. The relative chemical shifts of carbon atom depend on the number and kinds of substituents attached to it. ^{13}C NMR studies of hydrocarbons and their derivatives have established substituent rules which can be used to produce accurate estimates of the observed chemical shifts. For example, γ substituent yields an upfield shift of ca. ppm. This γ effect is due to a gauche arrangement between the observed and substituent carbons. The frequency of such γ gauche arrangements depends on the microstructure of the polymer in the vicinity of the observed carbon. It is possible to evaluate the frequency of γ gauche interactions and the resultant relative ^{13}C chemical shifts from a knowledge of the polymer chain conformational characteristics and the magnitude of the upfield shift produced by each γ gauche interaction. This approach has been successfully applied to predict the ^{13}C NMR chemical shifts expected for the various carbon atoms in different polymer systems. Moreover, the effects of stereosequence, comonomer distribution, and defect structures have all been successfully accounted for, thereby providing detailed microstructural descriptions of these polymers.

In the case of PEO, at given composition and temperature, the partition between the gauche and trans conformations can be predicted by the Karlström model[56–58]. The chemical shift of a theoretical PEO chain for

gauche conformation is estimated to be 71.58 ppm meanwhile for trans chain resonates at 73.83 ppm. When mPEO is dissolved in a good or tetha solvent it can have different conformations, ultimately producing a chemical shift given by the weighted average of those of the two conformers. It is found one single peak whose shift is indicative of the partition between the groups, due to the rapid interconversion between the gauche and trans conformational isomers. The first set of experiments are done on a dispersion of polymer grafted NC (mPEO_0.5K_POOH, σ=0.9 chain nm^2) and free mPEO_0.5K in deuterated water. The second set of experiments are done on a dispersion of polymer grafted NC (mPEO_0.5K_POOH, σ=0.9 chain nm^2) and free mPEO_0.5K in deuterated chloroform. The sample mPEO_0.5K_POOH is characterized by a $R_F/D_m>1$, that describes the brush regime. The first point to stress is that, although the PEO chains are tethered on the surface of TiO_2 NCs, narrow peaks can be collected (Figure 38), this is the case of stable colloid dispersions in the ^{13}C NMR experiment time scale.

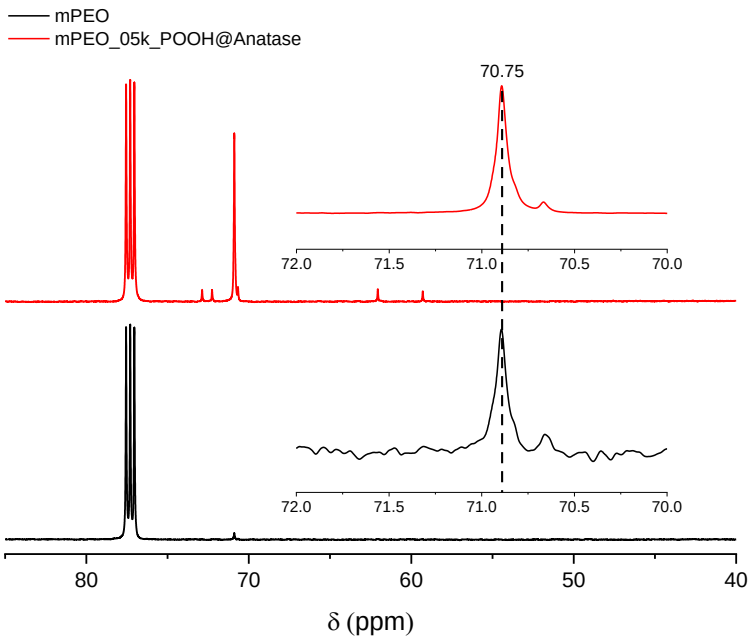

Figure 38 ^{13}C NMR of the mPEO_0.5K_POOH (red line) and free mPEO_0.5K (black line) in deuterated chloroform (A) the internal reference is the deuterated chloroform that is found at 77.2 ppm, while the mPEO chain characteristic peak is found at 70.8 ppm.

This is not trivial, in fact it is well know that large molecules. like proteins, can present broad lines not only for α elices or β sheets portions but also for flexible terminals. In semicrystalline polymers over T_g, the rigid and mobile parts can even be separated by their different lineshape. In fact long correlation times can interfere with the decoupling causing broad lines (the so called motional broadening) and long correlation times can also determine short T_2 values, another origin of broad lines. The information collected by the NMR analysis reported in Figure 39 shows that the chemical shift of the free polymer and the grafted polymer are equal in both solvents. The grafted polymer, in dynamic equilibrium condition, has the same average conformation as the free polymer. That means that, even if the ratio R_F/D_m is higher than 1, the polymer tethered on the surface has an

average conformation closer to the solvated free polymer than to the fully helical conformation that is adopted in the more compact phase of PEO, the crystalline one. at would be expected for a PEO tethered chain in a solvent is a shift of the characterstic peak to higher chemical shifts. It is observed from the NMR analysis that in solution, the tethered polymer and the free polymer adopt, locally, the same avarege conformation. In order to get a more detailed picture of the polymer chains mobility and conformation, further NMR experiments are needed. Like solid state NMR and relaxation time measurements.

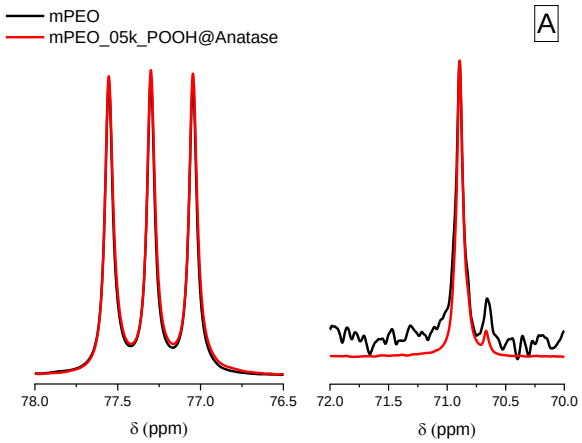

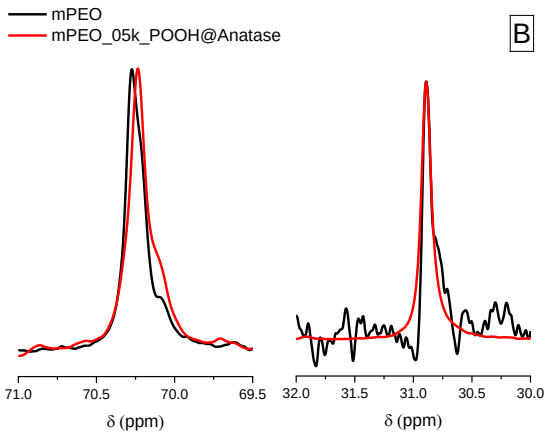

Figure 39 ^{13}C NMR of the mPEO_0.5K_POOH (red line) and free mPEO_0.5K (black line) in deuterated chloroform (A) the internal reference is the deuterated chloroform that is found at 77.2 ppm, while the mPEO chain characteristic peak is found at 70.8 ppm. In deuterated water (B) the internal standard is acetone that is found at 30.9 ppm, while the mPEO chain characteristic peak is found at at 69.4 ppm.

Conclusions

In this chapter we explored and tried to depict a picture of the grafting-to process of mPEO chains on the surface of anatase spherical nanocrystals surface. The polymers have been functionalized with phosphate, carboxylic and hydroxyl end group and tested in a variety of conditions in order to investigate the effect on the graft density. The study was done systematically exploiting the role of the chemical reactivity of the functionalized polymer anchoring group, alongside with the effect of the molecular weight on the graft density in two different solvents. Higher σ are achieved following POOH>COOH>OH using water as solvent. If DCM is used, then the σ is large,r for COOH≈POOH and lower with OH end group. It is also observed that to get even larger graft densities it is necessary to play with the polymers starting concentration and the temperature: higher concentration and temperature leads to a more effective

grafting. It is clear that, since we are dealing with a system composed by three main components, taking control over the polymer-solvent interaction, the polymer-surface reactivity and the solvent-surface interaction allows to tune the density of the tethered polymer chains and thus the conformation. The equilibrium conformation of the polymers on the surface also modulate the grafting reaction. We found a protocol that enables a good control over the grafting process and that can still produce NCs with controlled conformation and graft density, useful for drug delivery systems. At the same time, controlling this process brings to succeed on the drafting of a conformational map, that can possibly help to address the future nanocomposite synthesis.

Reference

(1) Raspa, A.; Marchini, A.; Pugliese, R.; Mauri, M.; Maleki, M.; Vasita, R.; Gelain, F. A Biocompatibility Study of New Nanofibrous Scaffolds for Nervous System Regeneration. *Nanoscale* **2016**, *8* (1), 253–265.

(2) Senapati, S.; Mahanta, A. K.; Kumar, S.; Maiti, P. Controlled Drug Delivery Vehicles for Cancer Treatment and Their Performance. *Signal Transduct. Target. Ther.* **2018**, *3* (1), 7.

(3) Weissleder, R.; Nahrendorf, M.; Pittet, M. J. Imaging Macrophages with Nanoparticles. *Nat. Mater.* **2014**, *13* (2), 125–138.

(4) Chen, H.; Zhang, W.; Zhu, G.; Xie, J.; Chen, X. Rethinking Cancer Nanotheranostics. *Nat. Rev. Mater.* **2017**, *2* (7), 17024.

(5) Li, Y.; Krentz, T. M.; Wang, L.; Benicewicz, B. C.; Schadler, L. S. Ligand Engineering of Polymer Nanocomposites: From the Simple to the Complex. *ACS Appl. Mater. Interfaces* **2014**, *6* (9), 6005–6021.

(6) Karakoti, A. S.; Das, S.; Thevuthasan, S.; Seal, S. PEGylated Inorganic Nanoparticles. *Angew. Chemie - Int. Ed.* **2011**, *50* (9), 1980–1994.

(7) Villa, C.; Campione, M.; Santiago-González, B.; Alessandrini, F.; Erratico, S.; Zucca, I.; Bruzzone, M. G.; Forzenigo, L.; Malatesta, P.; Mauri, M.; et al. Self-Assembled PH-Sensitive Fluoromagnetic Nanotubes as Archetype System for Multimodal Imaging of Brain Cancer. *Adv. Funct. Mater.* **2018**, *28* (19), 1707582.

(8) Bernard, B. K.; Osheroff, M. R.; Hofmann, A.; Mennear, J. H. Toxicology and Carcinogenesis Studies of Dietary Titanium Dioxide-Coated Mica in Male and Female Fischer 344 Rats. *J. Toxicol. Environ. Health* **1990**, *29* (4), 417–429.

(9) Jugan, M. L.; Barillet, S.; Simon-Deckers, A.; Sauvaigo, S.; Douki, T.; Herlin, N.; Carrière, M. Cytotoxic and Genotoxic Impact of TiO 2 Nanoparticles on A549 Cells. *J. Biomed. Nanotechnol.* **2011**, *7* (1), 22–23.

(10) Kubota, Y.; Shuin, T.; Kawasaki, C.; Hosaka, M.; Kitamura, H.; Cai, R.; Sakai, H.; Hashimoto, K.; Fujishima, A. Photokilling of T-24 Human Bladder Cancer Cells with Titanium Dioxide. *Br. J. Cancer* **1994**, *70* (6), 1107–1111.

(11) Kumar, S. K.; Jouault, N.; Benicewicz, B.; Neely, T. Nanocomposites with Polymer Grafted Nanoparticles. *Macromolecules* **2013**, *46* (9), 3199–3214.

(12) Perry, J. L.; Reuter, K. G.; Kai, M. P.; Herlihy, K. P.; Jones, S. W.; Luft, J. C.; Napier, M.; Bear, J. E.; Desimone, J. M. PEGylated PRINT Nanoparticles: The Impact of PEG Density on Protein Binding, Macrophage Association, Biodistribution, and Pharmacokinetics. *Nano Lett.* **2012**, *12* (10), 5304–5310.

(13) Howard, M. D.; Jay, M.; Dziubla, T. D.; Lu, X. PEGylation of Nanocarrier Drug Delivery Systems: State of the Art. *J. Biomed. Nanotechnol.* **2008**, *4* (2), 133–148.

(14) Kotsokechagia, T.; Zaki, N. M.; Syres, K.; Leonardis, P. De; Thomas, A.; Cellesi, F.; Tirelli, N. PEGylation of Nanosubstrates (Titania) with Multifunctional Reagents: At the Crossroads between Nanoparticles and Nanocomposites. *Langmuir* **2012**, *28* (31), 11490–11501.

(15) Oleszczuk, P.; Jośko, I.; Skwarek, E. Surfactants Decrease the Toxicity of

ZnO, TiO2 and Ni Nanoparticles to Daphnia Magna. *Ecotoxicology* **2015**, *24* (9), 1923–1932.

(16) Lin, D.; Ji, J.; Long, Z.; Yang, K.; Wu, F. The Influence of Dissolved and Surface-Bound Humic Acid on the Toxicity of TiO2nanoparticles to Chlorella Sp. *Water Res.* **2012**, *46* (14), 4477–4487.

(17) Jokerst, J. V.; Lobovkina, T.; Zare, R. N.; Gambhir, S. S. Nanoparticle PEGylation for Imaging and Therapy. *Nanomedicine* **2011**, *6* (4), 715–728.

(18) Dang, A.; Hui, C. M.; Ferebee, R.; Kubiak, J.; Li, T.; Matyjaszewski, K.; Bockstaller, M. R. Thermal Properties of Particle Brush Materials: Effect of Polymer Graft Architecture on the Glass Transition Temperature in Polymer-Grafted Colloidal Systems. *Macromol. Symp.* **2013**, *331–332* (1), 9–16.

(19) Barbey, R.; Lavanant, L.; Paripovic, D.; Schüwer, N.; Sugnaux, C.; Tugulu, S.; Klok, H. A. Polymer Brushes via Surface-Initiated Controlled Radical Polymerization: Synthesis, Characterization, Properties, and Applications. *Chem. Rev.* **2009**, *109* (11), 5437–5527.

(20) Bilchak, C. R.; Buenning, E.; Asai, M.; Zhang, K.; Durning, C. J.; Kumar, S. K.; Huang, Y.; Benicewicz, B. C.; Gidley, D. W.; Cheng, S.; et al. Polymer-Grafted Nanoparticle Membranes with Controllable Free Volume. *Macromolecules* **2017**, *50* (18), 7111–7120.

(21) Alexander, S. Adsorption of Chain Molecules with a Polar Head a Scaling Description. *J. Phys.* **1977**, *38* (8), 983–987.

(22) de Gennes, P. G. Polymers at an Interface; a Simplified View. *Adv. Colloid Interface Sci.* **1987**, *27* (3–4), 189–209.

(23) Daoud, M.; Cotton, J. P. Star Shaped Polymers : A Model for the Conformation and Its Concentration Dependence. *J. Phys.* **1982**, *43* (3), 531–538.

(24) Hore, M. J. A.; Ford, J.; Ohno, K.; Composto, R. J.; Hammouda, B. Direct Measurements of Polymer Brush Conformation Using Small-Angle Neutron Scattering (SANS) from Highly Grafted Iron Oxide Nanoparticles in Homopolymer Melts. *Macromolecules* **2013**, *46* (23), 9341–9348.

(25) Dukes, D.; Li, Y.; Lewis, S.; Benicewicz, B.; Schadler, L.; Kumar, S. K. Conformational Transitions of Spherical Polymer Brushes: Synthesis, Characterization, and Theory. *Macromolecules* **2010**, *43* (3), 1564–1570.

(26) Jiao, Y.; Tibbits, A.; Gillman, A.; Hsiao, M.-S.; Buskohl, P.; Drummy, L. F.; Vaia, R. A. Deformation Behavior of Polystyrene-Grafted Nanoparticle Assemblies with Low Grafting Density. *Macromolecules* **2018**, *14*, acs.macromol.8b01524.

(27) Wei, Y.; Xu, Y.; Faraone, A.; Hore, M. J. A. Local Structure and Relaxation Dynamics in the Brush of Polymer-Grafted Silica Nanoparticles. *ACS Macro Lett.* **2018**, *7* (6), 699–704.

(28) Dukes, D.; Li, Y.; Lewis, S.; Benicewicz, B.; Schadler, L.; Kumar, S. K. Conformational Transitions of Spherical Polymer Brushes: Synthesis, Characterization, and Theory. *Macromolecules* **2010**, *43* (3), 1564–1570.

(29) Yang, G.; Kim, K.; Wang, W.; Chen, B.; Mattoussi, H.; Hallinan, D. T. Scaling Laws for Polymer Chains Grafted onto Nanoparticles. *Macromol. Chem. Phys.* **2018**, *219* (8), 1–9.

(30) Dahal, U.; Wang, Z.; Dormidontova, E. E. Hydration of Spherical PEO-Grafted Gold Nanoparticles: Curvature and Grafting Density Effect. *Macromolecules* **2018**, *51* (15), 5950–5961.

(31) Labouta, H. I.; Gomez-Garcia, M. J.; Sarsons, C. D.; Nguyen, T.; Kennard, J.; Ngo, W.; Terefe, K.; Iragorri, N.; Lai, P.; Rinker, K. D.; et al. Surface-Grafted Polyethylene Glycol Conformation Impacts the Transport of PEG-Functionalized Liposomes through a Tumour Extracellular Matrix Model. *RSC Adv.* **2018**, *8* (14), 7697–7708.

(32) Hildebrand, J. Solubility. **1924**.

(33) Mark, H. F.; Atlas, S. H. Principles of Polymer Stability. *Polym. Eng. Sci.* **1965**, *5* (3), 204–207.

(34) Dinh, C. T.; Nguyen, T. D.; Kleitz, F.; Do, T. O. Shape-Controlled Synthesis of Highly Crystalline Titania Nanocrystals. *ACS Nano* **2009**, *3* (11), 3737–3743.

(35) Tawfilas, M.; Mauri, M.; De Trizio, L.; Lorenzi, R.; Simonutti, R. Surface

Characterization of TiO 2 Polymorphic Nanocrystals through H-TD-NMR. *Langmuir* **2018**, *34* (32), 9460–9469.

(36) Zalipsky, S. Functionalized Poly(Ethylene Glycols) for Preparation of Biologically Relevant Conjugates. *Bioconjug. Chem.* **1995**, *6* (2), 150–165.

(37) Lu, C.; Bhatt, L. R.; Jun, H. Y.; Park, S. H.; Chai, K. Y. Carboxyl-Polyethylene Glycol-Phosphoric Acid: A Ligand for Highly Stabilized Iron Oxide Nanoparticles. *J. Mater. Chem.* **2012**, *22* (37), 19806–19811.

(38) Dollimore, D.; Spooner, P.; Turner, A. The Bet Method of Analysis of Gas Adsorption Data and Its Relevance to the Calculation of Surface Areas. *Surf. Technol.* **1976**, *4* (2), 121–160.

(39) Asai, M.; Zhao, D.; Kumar, S. K. Role of Grafting Mechanism on the Polymer Coverage and Self-Assembly of Hairy Nanoparticles. *ACS Nano* **2017**, *11* (7), 7028–7035.

(40) Chen, X.; Mao, S. S. Titanium Dioxide Nanomaterials: Synthesis, Properties, Modifications and Applications. *Chem. Rev.* **2007**, *107* (7), 2891–2959.

(41) Zhang, L.; He, R.; Gu, H. C. Oleic Acid Coating on the Monodisperse Magnetite Nanoparticles. *Appl. Surf. Sci.* **2006**, *253* (5), 2611–2617.

(42) Pacek, A. W.; Man, C. C.; Nienow, A. W. On the Sauter Mean Diameter and Size Distributions in Turbulent Liquid/Liquid Dispersions in a Stirred Vessel. *Chem. Eng. Sci.* **1998**, *53* (11), 2005–2011.

(43) Dong, A.; Ye, X.; Chen, J.; Kang, Y.; Gordon, T.; Kikkawa, J. M.; Murray, C. B. A Generalized Ligand-Exchange Strategy Enabling Sequential Surface Functionalization of Colloidal Nanocrystals. *J. Am. Chem. Soc.* **2011**, *133* (4), 998–1006.

(44) Mutin, P. H.; Guerrero, G.; Vioux, A. Organic-Inorganic Hybrid Materials Based on Organophosphorus Coupling Molecules: From Metal Phosphonates to Surface Modification of Oxides. *Comptes Rendus Chim.* **2003**, *6* (8–10), 1153–1164.

(45) Mutin, P. H.; Guerrero, G.; Vioux, A. Hybrid Materials from Organophosphorus Coupling Molecules. *J. Mater. Chem.* **2005**, *15* (35–36),

3761–3768.

(46) Kim, P.; Jones, S. C.; Hotchkiss, P. J.; Haddock, J. N.; Kippelen, B.; Marder, S. R.; Perry, J. W. Phosphonic Acid-Modified Barium Titanate Polymer Nanocomposites with High Permittivity and Dielectric Strength. *Adv. Mater.* **2007**, *19* (7), 1001–1005.

(47) Queffélec, C.; Petit, M.; Janvier, P.; Knight, D. A.; Bujoli, B. Surface Modification Using Phosphonic Acids and Esters. *Chem. Rev.* **2012**, *112*, 3777–3807.

(48) Levchenko, A. A.; Li, G.; Boerio-Goates, J.; Woodfield, B. F.; Navrotsky, A. TiO2 Stability Landscape: Polymorphism, Surface Energy, and Bound Water Energetics. *Chem. Mater.* **2006**, *18* (26), 6324–6332.

(49) Fazio, G.; Selli, D.; Ferraro, L.; Seifert, G.; Di Valentin, C. Curved TiO2Nanoparticles in Water: Short (Chemical) and Long (Physical) Range Interfacial Effects. *ACS Appl. Mater. Interfaces* **2018**, *10* (35), 29943–29953.

(50) Selli, D.; Valentin, C. Di. Ab Initio Investigation of Polyethylene Glycol Coating of TiO_2 Surfaces. *J. Phys. Chem. C* **2016**, *120* (51), 29190–29201.

(51) Borodin, O.; Smith, G. D.; Bandyopadhyaya, R.; Byutner, O. Molecular Dynamics Study of the Influence of Solid Interfaces on Poly(Ethylene Oxide) Structure and Dynamics. *Macromolecules* **2003**, *36* (20), 7873–7883.

(52) Dinç, C. Ö.; Kibarer, G.; Güner, A. Solubility Profiles of Poly(Ethylene Glycol)/Solvent Systems. II. Comparison of Thermodynamic Parameters from Viscosity Measurements. *J. Appl. Polym. Sci.* **2010**, *117* (2), 1100–1119.

(53) Ma, K.; Zhang, D.; Cong, Y.; Wiesner, U. Elucidating the Mechanism of Silica Nanoparticle PEGylation Processes Using Fluorescence Correlation Spectroscopies. *Chem. Mater.* **2016**, *28* (5), 1537–1545.

(54) Tao, P.; Li, Y.; Rungta, A.; Viswanath, A.; Gao, J.; Benicewicz, B. C.; Siegel, R. W.; Schadler, L. S. TiO2 Nanocomposites with High Refractive Index and Transparency. *J. Mater. Chem.* **2011**, *21* (46), 18623.

(55) Li, C.; Han, J.; Ryu, C. Y.; Benicewicz, B. C. A Versatile Method to Prepare RAFT Agent Anchored Substrates and the Preparation of PMMA Grafted-Nanoparticles. *Macromolecules* **2006**, *39* (9), 3175–3183.

(56) Karlstrom, G. *A New Model for Upper and Lower Critical Solution Temperatures in Poly(Ethy1ene Oxide) Solutions*; 1985; Vol. 89.

(57) Karlstrom, G.; Engkvist, O. Theory of Poly(Ethylene Glycol) in Solution. In *Poly(ethylene glycol). Chemical and biological applications.*; 1997; pp 16–30.

(58) Andersson, M.; Karlström, G. *Conformational Structure of 1,2-Dimethoxyethane in Water and Other Dipolar Solvents, Studied by Quantum Chemical, Reaction Field, and Statistical Mechanical Techniques*; 1985; Vol. 89.

Chapter 4. Grafting-to of Polystyrene on spherical anatase

Introduction

As explained in the previous chapters, the fabrication of nanocomposite materials mainly suffers from the aggregation phenomena of the inorganic filler into the polymer matrix. In order to fabricate materials with improved properties, a better nanoparticle (NP) dispersion is demanded. It is now clear that the interface between a NP and the surrounding polymer matrix plays a critical role in defining the morphology of the polymer grafted nanoparticles (PGN), organization, wetting, chain dynamics, and ultimately many of the properties of a polymer nanocomposite.[1] Thus, the requests to control many aspects of the chains attached to the particle surface have grown over the past few decades, which presents many challenges and opportunities for synthetic polymer chemists. At the same time, the discovery and development of controlled radical polymerization (CRP) methods (atom transfer radical polymerization (ATRP)[2], reversible addition−fragmentation chain transfer (RAFT)[3], macromolecular design via interchange of xanthates (MADIX)[4], and nitroxide-mediated polymerization (NMP)[5] were quickly adapted to take control over polymers tethers to NP surfaces[6]. The challenge to create systems with well controlled molecular weight distribution and graft density (σ) of the tethered polymer chain produced a high number of publications related to the surface modification of different nanocrystals (NC). The general strategy is to graft the inorganic particle surface with a "*coupling agent*" to chemically activate the surface with reactive functionalities[7]. For example,

silica surfaces are reacted with silane coupling agents to create organic surface groups such hydroxyl, amine or carboxylic groups[8]. These can then be reacted with ATRP, RAFT, or NMP compounds that also contain a complementary reacting group[9]. Many efforts have been made to synthesized CRP agents which contain both the controlling agent and surface reactive groups in the same molecule[10,11]. In our contribution we will exploit RAFT polymerization technique to produce well-controlled polymer chain that will be attached to NCs surface through a *grafting-to* method. Two chain transfer agents (CTA) have been designed and synthesized to polymerize polystyrene macro-CTA that were grafted to anatase NCs.

RAFT Polymerization technique

Controlled radical polymerization (CRP) techniques (ATRP, RAFT, NMP) are able to match the useful features of free radical polymerization, such as compatibility with a wide range of monomers and functionalities, relatively mild reaction conditions with a good control over molecular weight distribution, chain architecture, and chain-end functionality. These kinds of polymerization techniques are often mentioned as "living" radical polymerizations (LRP), in order to achieve 'livingness', termination reactions, which are characteristic to radical polymerization processes, need to be reduced. MADIX and RAFT are thought to proceed via the same degenerative transfer mechanism and differ only in the chain transfer agents (CTAs) used. In a free radical polymerization, individual chains are formed, propagate and terminate by radical-radical reactions within 10 s. In an ideal LRP, the birth and growth of all chains should be simultaneous, and no termination occurs. Due to the presence of radicals, the latter condition can

never be fully seen; however, a strategy to reduce all *irreversible* termination reactions negligible was developed at CSIRO in 1998 by Rizzardo and others.[12] Almost simultaneously, a group of researchers in France patented a process they termed *macromolecular design via the interchange of xanthates* (MADIX), which employed xanthates as controlling agents but proceeds by an identical mechanism as the CSIRO-reported RAFT process. Rizzardo's group synthesized organic compounds that can reversibly react with propagating radical species, by reversible chain transfer mechanisms. When that occurs, propagating chains enter a temporarily non-reactive '*dormant'* state. Intermittent switching between the reactive, propagating state and the dormant state ensures that all chains have equal opportunity to grow. Such *'radical regulating'* compounds are thiocarbonylthio-containing molecules with generic structure depicted in Figure 40.

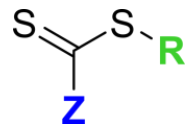

Figure 40 Generic structure of RAFT chain transfer agent (CTA).

The mechanism of RAFT polymerization depends on a series of addition-fragmentation equilibria, as shown in Figure 41. The first step is initiation by radical formation. Thermal initiators are commonly used thanks to their market availability, but photoinitiators are also attracting considerable interest, as they allow 'on-off' polymerization rates and tolerate molecular oxygen.[13,14] Radical-bearing oligomers react with the CTA in a second initialization step. Thanks to the high reactivity of the C=S bond, radical addition is favored over double bond addition, so all CTA is consumed during this step. An equilibrium is established where radical intermediate (**8**) can fragment back to yield the original CTA (**7**) and a propagating

oligomeric radical Pm•, or fragment to yield an oligomeric CTA (**9**) and release a radical re-initiator group R•. R should be a good homolytic leaving group, with a fragmentation rate k_β comparable to initiation rate k_i or fragmentation rate k_{add}. Released radicals subsequently undergo reinitiation and propagation, and growing chains rapidly switch between the propagating state and the dormant CTA end-capped state. Due to the rapid exchange between the two states, the concentration of chain radicals Pm• is lower than the more stabilized compound (**10**). This way, radical-radical termination reactions are suppressed, though not eliminated: combination or disproportion reactions can still occur. *Living* characteristics are imparted only when the molecular weight of the polymer formed is substantially lower than that which might be formed in the absence of a RAFT agent, and the number of polymer molecules with RAFT agent-derived ends far exceeds the number formed as a consequence of termination.

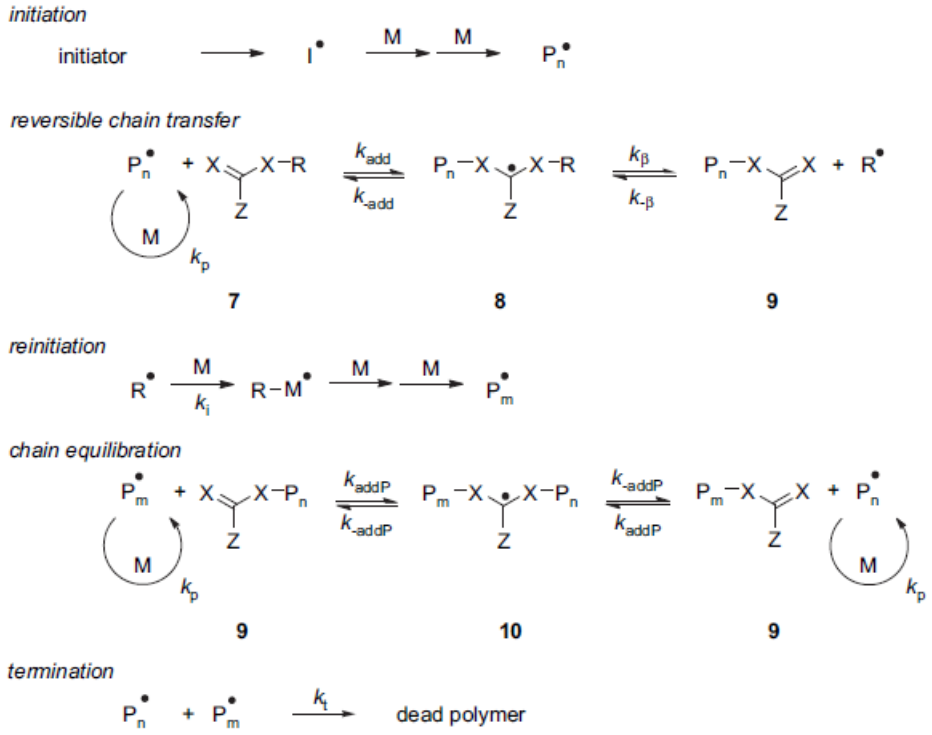

Figure 41 RAFT polymerization mechanism. Reproduced from Boyer, C.; Bulmus, V.; Davis, T. P.; Ladmiral, V.; Liu, J.; Perrier, S. Chem. Rev. 2009, 109, 5402–5436.[15]

It naturally follows that RAFT CTA design is of paramount importance to achieve a good control over polymerization. The R group should possess a better leaving ability than the propagating radical, and should be able to efficiently reinitiate monomers when expelled.[16] A trade-off has to be found between the two features, as they are respectively enhanced and diminished by radical stabilization. The choice of Z group should be guided by its ability to activate the C=S bond towards radical addition and provide little stabilization to adducts (**8**) and (**10**), so that fragmentation is favored. For this reason, Z groups are generally suitable only for specific monomer classes. Particularly active monomers like vinyl acetate (VAc) form (**10**) adducts that are more stable than propagating radicals, so heteroatom-bearing Z groups are necessary to destabilize the adduct and promote

fragmentation[17]. Whereas xanthates and dithiocarbamates are effective in mediating RAFT polymerization of very active monomers, they are unsuitable in controlling the propagation of less activated monomers. Methacrylates feature a higher radical stability and will only add to the CTA if its C=S bond is sufficiently activated; otherwise, fragmentation of adduct (**10**) will be favored, and the concentration of propagating radicals will reach levels where termination reactions are common, as in conventional radical polymerization. Numerous RAFT CTAs have been designed and tested on a great variety of monomers.[18,19] General molecular design guidelines have been proposed by the CSIRO and are shown in Figure 42.

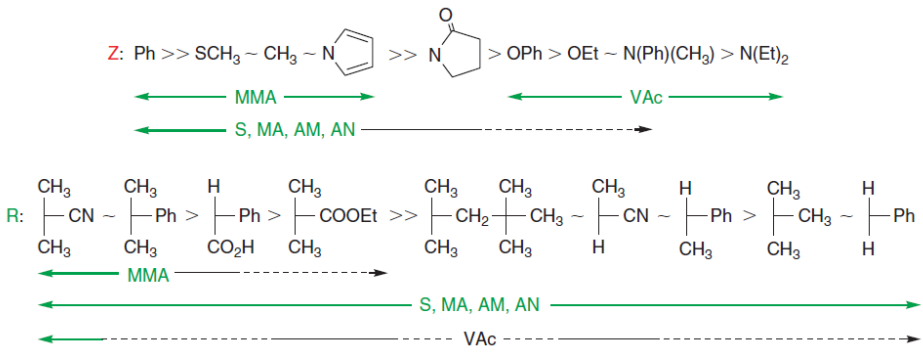

Figure 42 RAFT CTA design guidelines. For Z groups, fragmentation rates increase and addition rates decrease from left to right. For R groups, fragmentation rates decrease from left to right. Dashed lines indicate partial polymerization control. MMA = methyl acrylate, VAc = vinyl acetate, S = styrene, MA = methylacrylate, AM = acrylamide, AN = acrylonitrile. Reproduced from Moad, G.; Rizzardo, A. E.; Thang, S. H. Aust. J. Chem 2005, 58, 379–410.

If the amount of dead polymer is small enough, and chain-end termination with CTA is retained (Figure 42), block copolymers can be synthesized by sequential RAFT polymerization processes (Figure 43). The homopolymer obtained from the first polymerization acts as a macromolecular CTA (macroCTA) for the second polymerization (chain extension) step.

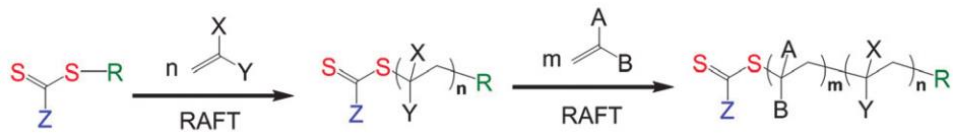

Figure 43 Block copolymer synthesis by sequential RAFT polymerization of two different monomers. Reproduced from: Keddie, D. J. Chem. Soc. Rev. 2014, 43 (2), 496–505.

When chain extension is planned, considerations about the suitability of the Z group must also apply to the second monomer: low activity of the macroCTA during the second step leads to increased copolymer PDI and contamination with homopolymers of the second monomer due to insufficient chain transfer. As for the R group, it is now constituted by the first block (macro-R), so appropriate choice of the R group directly translates to the appropriate choice of the order of monomer addition. Analogously to what was described above, macro-R groups that are more stable in macroradical form possess better leaving group abilities. For this reason, monomers with tertiary propagating radicals (methacrylates, methacrylamides) should be polymerized before less stabilized monomers (acrylates, acrylamides, styrenes), which should in turn be polymerized before more reactive radicals (vinyl esters, vinyl amides) (Figure 44).

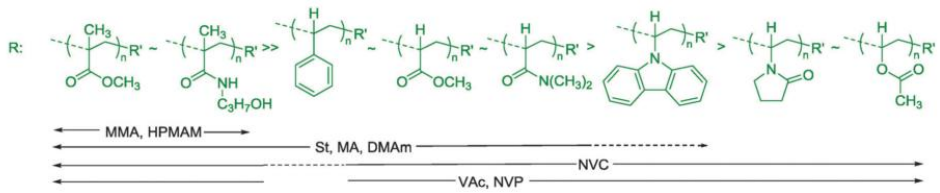

Figure 44 Guidelines for selection of macro-R group for the preparation of block copolymers. Dashed lines indicate partial control over polymerization is achieved. MMA = methyl methacyrlate, HPMAM = N-(2-hydroxypropyl) methacrylamide, St = styrene, DMAm = N,N-dimethylacrylamide, NVC = N-vinylcarbazole, VAc = vinyl acetate, NVP = N-vinylpyrrolidone. Reproduced from: Keddie, D. J. Chem. Soc. Rev. 2014, 43 (2), 496–505.

Surface and Particle Modification via the RAFT Process

Polymer grafting techniques provide a versatile tool to covalently modify the surface of materials. These techniques can be categorized into *grafting-to* and *grafting-from*. In the first technique, the polymer, bearing an appropriate functional group, reacts with the material surfaces to form chemically attached chains. On the other hand, in the *grafting-from* technique, the initiators are initially anchored on the surface and then subsequently used to initiate the polymerization of monomer from the surface. Both the methods have advantages and few drawbacks.

Grafting-to *approach*

The *grafting-to* approach provides a convenient way to modify the surface of materials by utilizing an end-functionalized polymer chain reacting with an appropriately treated substrate. As the grafted chains are pre-formed in this technique, their types and structures can be carefully designed via various polymerization methods. As a versatile CRP technique, RAFT is compatible with almost all of the conventional radical polymerization monomers, which allows for the preparation of a wide range of polymers with well-defined structure. Because RAFT polymerization follows a degenerative chain-transfer mechanism in which thiocarbonylthio compounds act as chain-transfer agents (CTAs), polymers prepared by this technique usually bear dithioester or trithiocarbonate end groups that can be easily reduced to thiols. The high affinity of thiols for the surfaces of metals, in particular gold, makes it possible to modify various metal substrates with well-defined polymer chains prepared via RAFT. Since the engine of the polymerization is the CTA, it can be designed to fulfill both its duties: grow a polymer and attach it to a surface. Although the *grafting-*

to approach provides a convenient way to modify the substrate surface with well-defined RAFT-prepared polymers, the inherent problem associated with this approach is the limitation of surface graft density. The diffusion barrier established by the already-grafted polymer chains makes it difficult for the new polymer chains to access the reactive sites on the substrate. Thus, the amount of the grafted polymer chains was limited, which usually resulted in low grafting densities. However, as mentioned in the previous chapter, this method leads to a more uniform (i.e. isotropic) polymer coverage of the NP surface at low to medium graft densities.

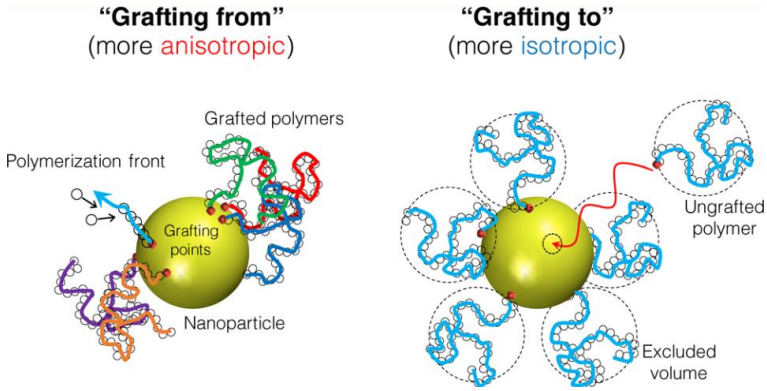

Figure 45 representation of the spatial polymer chain distribution for both the grafting process. Readapted image from reference 20

Thus, at a given grafting density, the *grafting-to* mechanism leads to an enhanced miscibility of the NPs in the matrix (which has the same chemistry as the grafts) and lower propensity to create self-assembled structures. Another important factor is that the dispersity in the number of grafted chains on the NPs is also smaller in the case of *grafting-to* systems, thus leading to better defined materials. This consideration is referred to all the preformed polymers and not only on the RAFT polymerized chains.

Grafting-from *approach*

The immobilization of initiators on the material surfaces can be achieved by various techniques, including chemical reaction, plasma discharge and high-energy irradiation. The subsequent polymerization from these surface-anchored initiators in the presence of free CTA can generate surface-grafted polymer chains with uniform structure and adjustable length. It was found that addition of free initiators was needed to achieve an effective polymerization rate, and increasing the concentration of free initiators produced a thicker polymer layer but decreased the control over the polymerization[20]. A linear increase of film thicknesses with sequential monomer additions was observed, indicating the living characteristics of the grafted polymer chains prepared by this surface-initiated RAFT approach. Both M_n and polydispersity index (PDI) of the homopolymers cleaved from the surface of inorganic substrates were comparable to those of the corresponding free polymers generated in solution, suggesting that the *livingness* characteristics of this kind of polymerization is maintained. However, the disadvantage, which is also derived from the presence of the large amount of ungrafted polymer in the final product, is the requirement of additional isolation and purification procedures after polymerization.

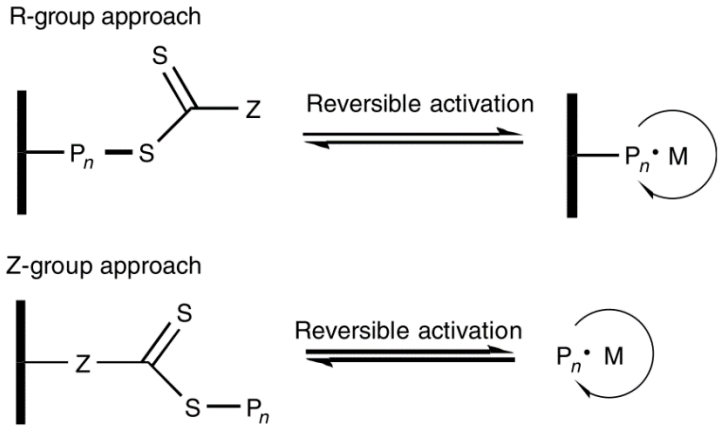

Figure 46 Comparison of R-group and Z-group approaches for surface-initiated RAFT polymerizations. Image readapted from the Handbook of RAFT polymerization[17]

The polymerization is greatly influenced in the case in which the group thiocarbonyl is always close to the surface (Z-approach) or on the terminal of the growing polymer (R-approach) (Figure 46). In the R-group approach, the RAFT agent is attached to the substrate surface via its leaving and reinitiating R group. The solid substrate acts as part of the leaving R group, and thus the propagating radicals are located on the terminal end of the surface-grafted polymer, which eases the growth of grafted polymer chains. In the Z-group approach, the RAFT agent is attached to the surface via its stabilizing Z group. Because the RAFT agent is permanently attached to the surface, this approach resembles a *grafting-to* approach. The polymeric radicals always propagate in solution before they attach to the surface of substrate via the chain-transfer reactions with attached RAFT agents.

Materials and methods

Carbon disulfide (CS_2, 99,9%), dodecanethiol (99.8%), Aliquat® 336 (tricaprylylmethylammonium chloride, 93%). Sodium hydroxide (NaOH), HCl aqueous solution (37% wt/wt), 2-propanol (>99.9%), absolute methanol (>99.9%), dry dimethylformamide (DMF, ≥ 99.9%), acetic acid, hexane (HEX), Oxalyl chloride (OxCl >99%), 2,6-lutidine (98%), Sodium Sulfate (NaSO3, 99.9%), bromotrimethylsilane (TMSBr, 97%). All the reagents were purchased from Sigma-aldrich and used as received. 2.2'-Azobisisobutyronitrile (AIBN) was purified by recrystallization from methanol and further stocked in freezer. Dimethyl (hydroxymethyl)phosphonate was synthesized according to the procedure explained in the chaper#.

Synthetic Methods

The synthesis and characterization of the anatase NCs are the same followed in the previous chapters and were not be discussed.

2-[[(Dodecylthio)thioxomethyl]thio]-2-methylpropanoic acid (DDAT)[21]

In a jacketed reactor with mechanical stirring, 48.07 ml of 1-Dodecanethiol (0.20 mol), 120 ml of acetone and 3.24 g of Aliquot (tricaprylylmethylammonium chloride, 8.0 mmol) were added and cooled to 10 °C under a argon atmosphere. Sodium hydroxide solution 50%, (8.38 ml, 0.21 mol) was added dropwise in 20 min. The color changed to white while the reaction was stirred for 15 min. Then, a solution of 24.54 ml of acetone (0.33 mol) and 12.07 ml of carbon disulfide (0.20 mol) were added dropwise in 20 min, and during this time the color turned red. Twenty minutes later, 24.36 ml of chloroform (0.30 mol) was added, followed by

dropwise addition of 50% sodium hydroxide solution (40 ml, 1.53 mol) over 30 min. The reaction was stirred overnight. 600 mL of distilled water was added at room temperature, followed by 50 mL of concentrated HCl (37%) to acidify the aqueous solution. The reactor was purged with a nitrogen flow during vigorous stirring to help evaporate off acetone. The solid was collected with a Buchner funnel and then dissolved in 600 ml of 2-propanol. The undissolved solid (recognized as *S*,*S*'-bis(1-dodecyl) trithiocarbonate, dimer of DDAT) was filtered off three times. The 2-propanol solution was dried with mechanical vacuum, and the resulting solid was recrystallized from hexane three times. Yield 55% of yellow crystalline solid (**1**); melting point, Tm = 61.15 °C was determined by DSC. FT-IR ATR: 1060 cm-1 C=S groups, 1703 cm-1 C=O groups. ^{1}H NMR ($CDCl^{3}$) δ ppm: 0.90 (t, 3H, -C**H$_3$**), 1.28 (m, 16H, -(C**H$_2$**)$_8$), 1.40 (m, 2H, CH_3-C**H$_2$**-), 1.70 (m, 2H, -S-CH_2-C**H$_2$**-), 1.74 (s, 6H, -C**H$_3$**), 3.37 (t, 2H, -S-C**H$_2$**-), 11.90 (s, 1H, -O**H**).

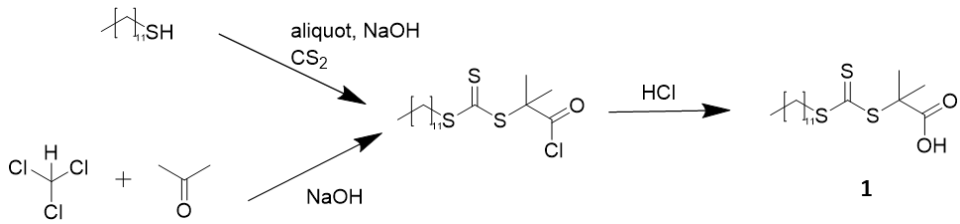

Figure 47 Scheme of the reaction proposed to prepare DDAT.

Propanoic acid, 2-[[(dodecylthio)thioxomethyl]thio]-2-methyl-, (dimethoxyphosphinyl)methyl ester (DDAT-phosphonate)

In a round bottom flask, previously dried and in N_2 atmosphere, are added 13.8 mmol of **1** dissolved in a stock solution of DCM (0.92 mM). Then the mixture is cooled in ice bath and are added dropwise 0.138 mmol of dry DMF and 27.6 mmol of oxalyl chloride (OxCl). The system is maintained

at 0°C for 30 minutes. The solution was slowly brought at room temperature and left react for 24 hours. The solvent and unreacted OxCl is removed via dual low temperature- pressure distillation, and then kept in N_2 atmosphere. The solid formed (**2**) is then dissolved in dry DCM (50 mL) and 15.5 mmol of 2-6 Lutidine are added. Then 27.6 mmol of Dimethyl (hydroxymethyl)phosphonate solution (0.9 mM in dry DCM) are added. The mixture is stirred at room temperature for 24 hours. It is observed the formation of a white precipitate and in an orange solution. The organic salt is removed by filtration and washed twice with DCM. The solvent is then removed by rotary vapor and an intense orange oil is obtained. The oil is diluted in 250 mL of acetic acid and the remaining traces of salts are precipitated and filtered. The acetic acid is evaporated, and the crude product is extracted twice with DCM and acidic water (HCl 1M) and then with brine till the aqueous phase reaches pH 7. The organic layer is then dried over NaSO3 overnight. The DCM is removed by distillation and the obtained product appears as an intense yellow oil. At this stage are still present traces of the unreacted DDAT, purification through silica gel column chromatography with HEX:DCM=1:1 was demanded to obtain the pure yellow solid product (**3)**. ^{1}H NMR ($CDCl_3$) δ ppm: 0.90 (t, 3H, -C**H**$_3$), 1.28 (m, 16H, -(C**H**$_2$)$_8$), 1.40 (m, 2H, CH3-C**H**$_2$-), 1.70 (m, 2H, -S-CH2-C**H**$_2$-), 1.74 (s, 6H, -C**H**$_3$), 3.37 (t, 2H, -S-C**H**$_2$-), 3.81 (d, 6H, OP-(OC**H**$_3$)$_2$); 4.41 (d, 2H, O-C**H**$_2$-P). ^{31}P NMR ($CDCl_3$) δ ppm: 21 (s , O**P**-(OCH_3)$_2$)

Propanoic acid, 2-[[(dodecylthio)thioxomethyl]thio]-2-methyl-, phosphonomethyl ester (DDAT-phosphonic acid)

In a round bottom flask are diluted 1mmol of **3** in 50 mL of dry DCM in N_2 controlled atmosphere. The mixture is then cooled and left at 0 °C while a

solution of 6 mmol of TMSBr (0.01M) is slowly added dropwise. The mixture is left to react at room temperature for 24 hours. The solvent and unreacted OxCl is removed via dual low temperature- pressure distillation, and then kept in N_2 atmosphere. Then are added 200 mL of absolute methanol and the solution is stirred for 24 hours. The solvent was evaporated by vacuum and followed by silica gel column chromatography (1:1 mixture of hexane and DCM) to get DDAT ended with a phosphonic acid moiety (**4**) (98% yield). ^{1}H NMR ($CDCl_3$) δ ppm: 0.90 (t, 3H, -C**H**$_3$), 1.28 (m, 16H, -(C**H**$_2$)$_8$), 1.40 (m, 2H, CH3-C**H**$_2$-), 1.70 (m, 2H, -S-CH2-C**H**$_2$-), 1.74 (s, 6H, -C**H**$_3$), 3.37 (t, 2H, -S-C**H2**-); 4.41 (d, 2H, O-C**H**$_2$-P); 10.27 (s, 2H, OP(O**H**)$_2$).^{31}P NMR ($CDCl_3$) δ ppm: 18 (s , O**P**(OH)$_2$).

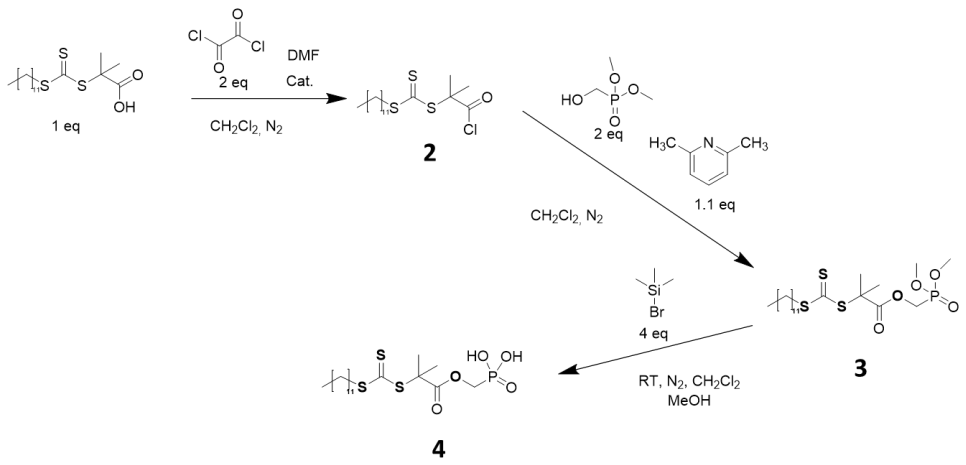

Figure 48 Scheme of the reaction used to prepare DDAT-phosphonic acid.

Macro-PS RAFT polymerization

A typical example of the polymerization method is described here. A defined amount of CTA was dispersed in styrene (0.081 mol). AIBN, dissolved in DMF (0.356mL, 0.01M), was added to the solution, and finally

the mixture was transferred into a dried Schlenk tube. The ratios between species of [monomer]:[CTA]:[initiator] were varied for different experiments. The mixture was degassed by three freeze-pump- thaw cycles, backfilled with nitrogen, and then placed in an oil bath at 110°C. The polymerization solution was quenched in ice bath after a certain amount of time. DCM (30mL) was added to the flask and the solution was poured into methanol (200mL) to precipitate macro-PS, this procedure was done at least three times. The polymer is then dried in vacuum hoven (60°C, overnight) and stocked for the next experiments.

Grafting-to process

The decoration of the anatase NCs is carried using the as prepared Macro-PS chain-ended with the carboxylic acid obtained with DDAT and phosphonic acid obtained with DDAT phosphonic acid.. A precise amount of the as prepared PS functionalized polymer is dissolved in a selected solvent (DMF) and diluted till the solution reaches a molar concentration of 4 mM. The stripped anatase NCs, in form of powder, are added in the solution and the mixture is sonicated for 10 minutes. Once the dispersion became homogenous, the solution is stirred in different experimental conditions. The product is then purified by centrifugation for three times with DCM and dried in vacuum at 60°C overnight.

Characterization methods

Qualitative and quantitative definition of tethered ligand on the NCs surface has been verified with *Attenuated Total Reflection (ATR)-FTIR and Thermogravimetric analysis* (TGA). Fourier transform infrared

characterization was performed using a PerkinElmer Spectrum 100 instrument scanning from 650 to 4000 cm−1 with a resolution of 4 cm−1 for 64 scans. The sample, in the form of powder, is added on the sample holder and directly analyzed over the Si crystal with the Universal ATR (UATR).TGA analysis was carried out with a Mettler Toledo TGA/DSC1 STARe System, at a constant gas flow (50 cm^3 min^1). The thermal profile was the following: 25° C 5 min (air); 25–800° C with a rate 10 C min^{-1} (air).. ^1H, ^{31}P NMR spectra were recorded using a Bruker AMX-500 spectrometer operating at 500 MHz. Molecular weights and molecular weight distributions were determined by Gel Permeation Chromatography (GPC) using a WATER 1515 isocratic HPLC Pump, a WATER 2414 refractive index detector, four Styragel columns (HR2, HR3, HR4, HR5). Samples were dissolved in THF and their chromatograms recorded with a flow of 1.0 ml/min at 35 °C. A calibration with polystyrene standards (Sigma-Aldrich) was used.

Results and discussions

The inorganic NCs used in this contribution are the quasi-spherical anatase NCs used in the previous chapters, synthesis and characterization will not be discussed in this chapter. The theory behind the grafting-to process it is intensively discussed in the previous chapter and will not be discussed in this contribution. The discussion will be focused on the synthesis of PS polymers via RAFT technique and the grafting-to process on anatase NCs

RAFT polymerization

To obtain a controlled molecular weight distribution of PS polymers we explored the RAFT technique. The first step was to produce a CTA able to graft the surface and grow a polymer. Thanks to our previous experiments on mPEO@anatase NCs, we decided to modify our CTA with a phosphonic acid end group to obtain a better coverage of the surface. The selected RAFT agent was synthesized following the synthetic route proposed by John T. Lai and coworkers[21] to produce carboxyl terminated CTA (DDAT).

The as prepared RAFT agents have been used for an investigation of the styrene RAFT polymerization. Four different sets of experiments were conducted at 65°C, with different [monomer]:[CTA]:[initiator]=1000:1:0.1 ratio for each CTAs. Conversion and monomer consumption ($\ln(M_0/M_t)$, where M_0 is the initial monomer concentration and M_t is the monomer concentration at time t)) were defined through 1H NMR analysis of samples collected at a defined reaction time. In Figure 49 are reported the results of these experiments. It is possible to appreciate the controlled nature of RAFT polymerization analyzing the monomer consumption versus time (Figure 49, left Figure 79). A linear relation between monomer consumption and polymerization time was observed for all the experiments, indicating a constant radical concentration during the polymerization. There is a notable difference between the PS growth with the carboxyl-end CTA (PS_C, red symbols) and the phosphonic acid-end CTA (PS_P, black symbols). The polymerization rate is higher in the case of PS_C, probably due to the better leaving ability and effective reinitiation of the R-group functionalized with this group when expelled.

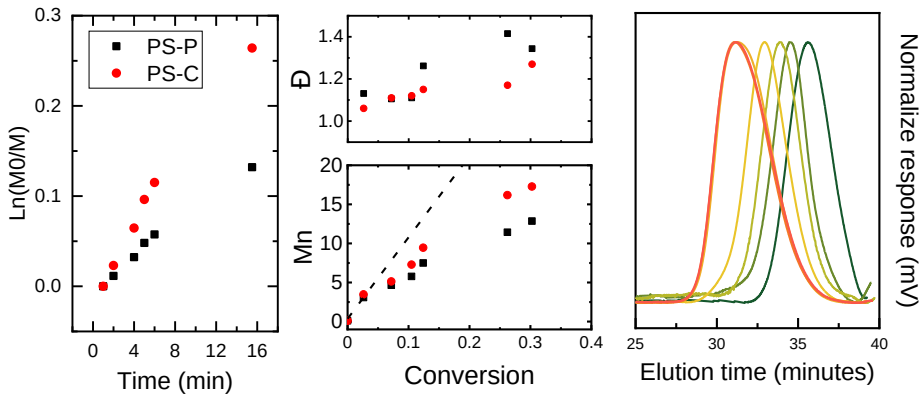

Figure 49 the reaction were carried at 65°C with [monomer]:[CTA]:[initiator]=1000:1:0.1ratios. At the left is reported the monomer consumption vs time graph: Polymerization done using DDAT are PS_C, red symbols; the experiments conducted with the DDAT-phosphonic acid are the PS_P. A the top-center are reported the Đ values as function of the conversion. At the bottom-center are reported the Mn vs conversion, the dash line represents the predicted theoretical Mn values. At the right are reported the GPC curves.

In Figure 49 (bottom center) is reported the molecular weight as function of the conversion, the graph shows the controlled character of styrene RAFT polymerization with this CTAs. These results showed that the number-average molecular weights increased in a linear fashion with monomer conversions, and the measured molecular weights were lower than theoretical molecular weights calculated with eq.1 (dashed line).

$$M_n = \frac{[M]}{[CTA]} \cdot c \cdot M_w(M) + M_w(CTA) \qquad (1)$$

M_n is the theoretical molecular weight; [M] is the monomer concentration; [CTA] is the RAFT agent concentration, c represents the conversion, M_w(M) is the monomer molecular weight and M_w (CTA) the molecular weight of the RAFT agent. At low monomer conversion, the polydispersity index (*Đ*) of the polymers were lower than 1.3, underlining the controlled characteristics of the RAFT technique. At higher monomer conversion the PS_P showed higher *Đ* values, showing a less controlled behavior. This

phenomenon is related to the reaction condition. The experiments were conducted without any solvent in order to rapidly reach high conversion values, but this protocol was affected but few drawbacks. In this case the termination rate was higher than the reinitiation and propagation of the radical, that caused the production of low molecular weight polymers chains.

Grafting-to

Once the best experimental conditions were found, a set of polymers with different molecular weights and tethering group were synthesized (Table 10). Narrow polymer molecular weight distribution is needed to take full control over the grafting process, this was achieved using polymers with $Đ$ <1.3. The grafting-to were conducted in solution using DCM, a solvent that showed the best results in terms of graft density (σ). Moreover, DCM is considered a good solvent for PS[22] (χ<0.5), this allowed us to avoid any side contribution to the tethering process. All the experiments are listed in Table 11, to verify the reproducibility of our data, each result is the average number of at least three experiments.

Table 10 Polymerization of styrene using DDAT (C_PS) and DDAT-phosphonic acid (P_PS).

Sample	[monomer]:[CTA]	Time h	M*n* kg mol^{-1}	M*w* kg mol^{-1}	Đ
P_PS_1	25	48	1.9	2.0	1.06
P_PS_2	100	48	5.9	6.9	1.06
P_PS_3	625	48	47.3	53.6	1.13
P_PS_4	1024	48	78.1	89.2	1.14
C_PS_1	25	36	2.2	2.3	1.08
C_PS_2	100	36	9.9	10.6	1.22
C_PS_3	625	48	61.9	72.3	1.17
C_PS_4	1024	48	78.9	94.2	1.19

Table 11 Grafting-to experiments of the polymer synthesized in Table 10. Each result corresponds to at least three experiments, all the values corresponds to the arithmetic mean of each experiment with its std. deviation. σ is calculated following eq.5.chapter 2; Σ is the footprint of a single chain and is calculated following eq.6 chapter 2; Dm corresponds to the mean distance evaluated using eq.7 chapter 2; R_F represents the Flory radius.

Sample	N monomer unit	W_{loss} %	σ chain nm^{-2}	std. err.	Σ nm^{2}chain^{-1}	std. err.	Dm nm	std. err.	R_F/D_m nm	Conformation
C_PS_1@Ana	19	7,7	0,1482	0,0119	6,7	0,5	2,9	0,2	0,9	Mushroom
C_PS_2@Ana	56	8,2	0,0525	0,0042	19,1	1,5	4,9	0,4	1,1	Brush
C_PS_3@Ana	455	6,7	0,0052	0,0004	192,3	15,4	15,6	1,3	1,2	Brush
C_PS_4@Ana	751	6,5	0,0031	0,0002	324,9	26,0	20,3	1,6	1,3	Brush
P_PS_1@Ana	21	9,0	0,1573	0,0126	6,4	0,5	2,8	0,2	1,0	Mushroom
P_PS_2@Ana	96	9,0	0,0345	0,0028	29,0	2,3	6,1	0,5	1,2	Brush
P_PS_3@Ana	595	8,5	0,0052	0,0004	192,7	15,4	15,7	1,3	1,4	Brush
P_PS_4@Ana	758	12,9	0,0065	0,0005	154,8	12,4	14,0	1,1	1,8	Brush

The success of the grafting process has been verified through FTIR to get qualitative information and with TGA to get quantitative information. From the infra-red spectroscopy, it is it possible to identify the polymer attached on the surface from the comparison of its characteristic vibrational peaks (Figure 50).

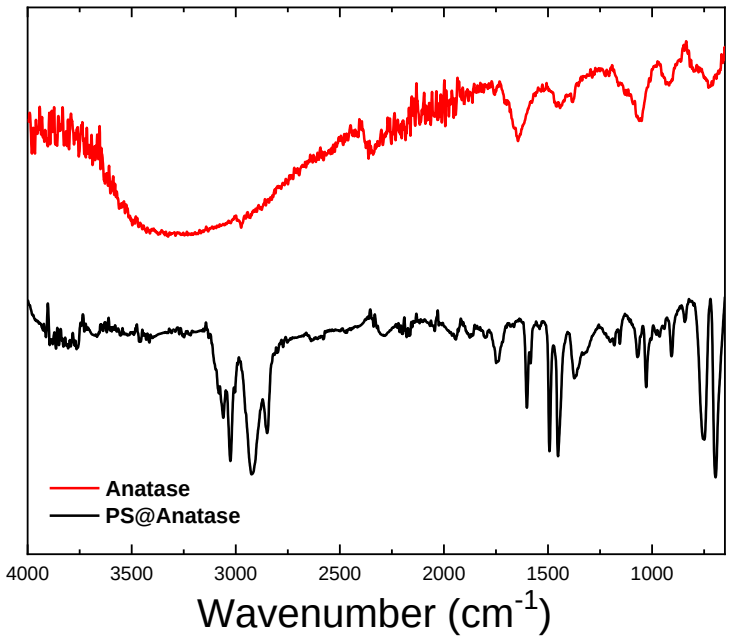

Figure 50 FTIR of the pristine anatase NCs (top, red line); grafted PS@anatase NCs (bottom. Black line).

The vibrational profile of PS@Anatase clearly showed the presence of PS, since the notable peaks are very evident, being in the range of 3000–3100 cm^{-1} the C–H stretching modes and, in the range of 1450–1650 cm^{-1}, the C–C stretching mode due to phenyl rings. TGA analysis, on the other hand, gave the quantitative information needed to understand the magnitude of density reached with this system (Figure 51).

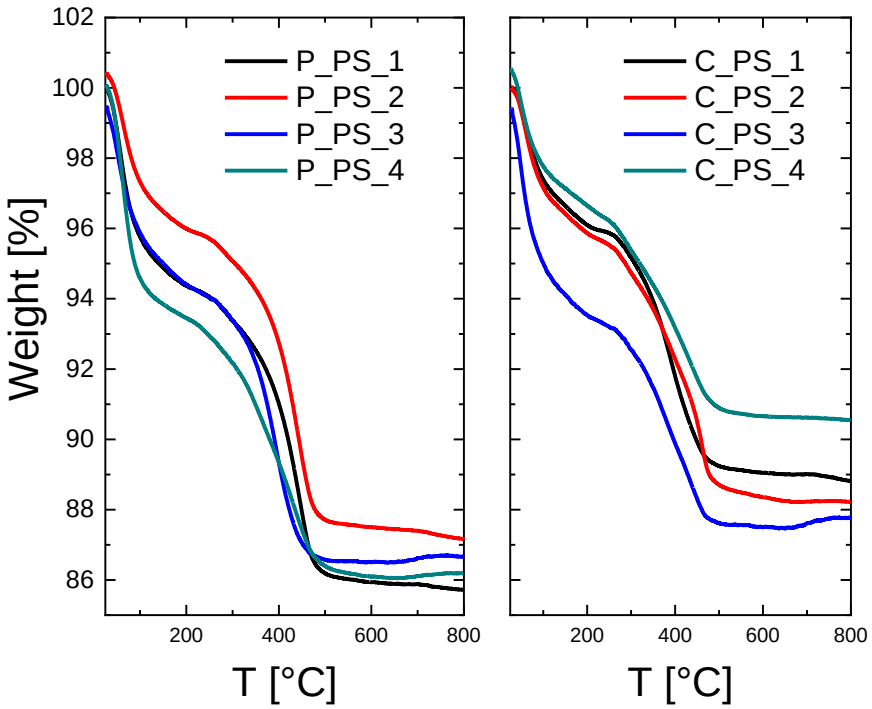

Figure 51 Thermogravimetric analysis of the grafting-to experiments: on the left are represented the TGA data from the experiments conducted using phosphonic acid end polymers. On the right the experiments conducted using carboxylic acid end polymers.

Following the same procedure used in the previous chapter we were able to calculate σ of PS chains (Chapter 2; eq.4 and eq.5) and define a mean distance (D_m, Chapter 2; eq.6). As mentioned in the previous chapter, Hagar I. Labouta et al.[23] proposed that the ratio of the Flory radius and the average distance between adjacent PS chains (R_F/D_m) can be used as an indicator for polymer conformation. In Figure 52 are reported the data collected from the experiments. It is immediately noted that the P_PS chains covers all the *brush* regime, almost reaching the *dense brush* region. On the other hand, the C_PS reaches quickly its limit value, and could not provide a denser system. It is still evident that the anchoring group, in these conditions, plays a key role. It is interesting that, at high monomer units, the surface is able

to adsorb more P_PS chains. The interaction that must be considered is the one between the polymer and the NCs surface. In our case, PS do not strongly interact with the anatase surface, and it can't effectively minimize NCs high surface energy. The only way to lower this energy is to react with the anchoring groups. The phosphonic acid moiety was able to overwhelm the entropic costs due to the stretching of the PS chain during the grafting-to process, making it able to more effectively attach to the "thirsty" surface. On the other hand, the enthalpic gain due to the bond formation between the carboxylic acid group and the anatase surface was not enough to balance the energetic costs involved. We must consider the size of the grafting polymers, in the case of the high molecular weight, the size of the random coil is five times larger than the inorganic substrate.

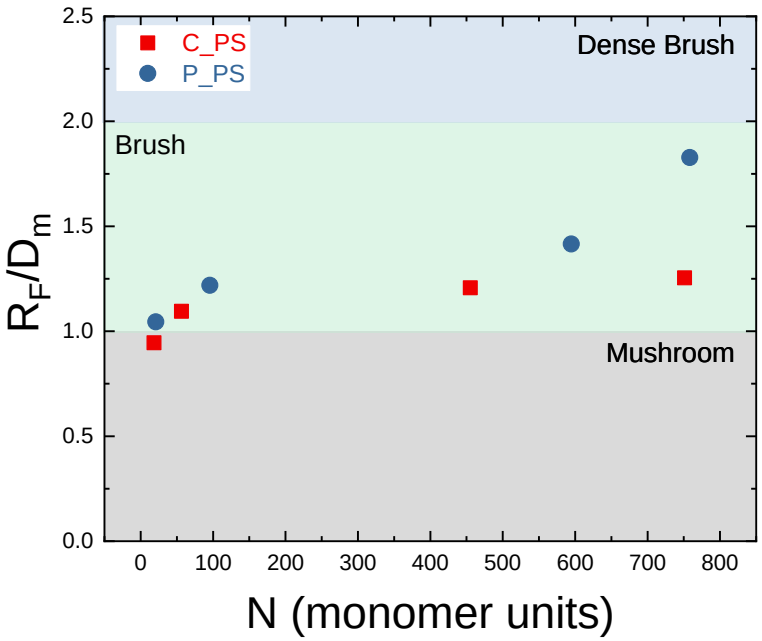

Figure 52 Plot of the R_F/D_m vs N. Experiments conducted in DCM. For each graph the red square represents carboxyl end chain; blue marine circle represents phosphonic acid end chains. For values below 1.0 a mushroom regime is defined, while those above 1.0 indicate brush. As R_F/D_m

approaches zero, inter-chain interactions become more and more scarce and areas of bare particle between mPEO chains begin to dominate the particle surface. On the other hand, R_F/D_m values equal to or larger than 2.0 represent denser brush configurations.

Conclusions

In this chapter we further investigated the contributions involved during the grafting-to process of PS chains on the surface of anatase spherical nanocrystals. The polymers have been synthesized exploiting RAFT techniques that enables us to produce polymers with well-defined narrow molecular weight distributions. The polymerizations were carried using two different CTA designed and synthesized to effectively graft the anatase NCs surface. A set of polymers were produced using a RAFT agent with phosphonic acid R-group, another set was prepared with a carboxylic R-group. The grafting-to experiments highlighted the importance of the interaction between the polymer chain and the surface. In this case we used a polymer and a solvent that did not strongly interact with titanium dioxide surface, leaving room to the end-group to cling on the surface. Even in this case the phosphor-based class of anchoring group showed higher reactivity than the carboxylic acid end moiety. The data obtained from the grafting-to experiments showed, once more, that the parameters that rules the process are the polymer-solvent interaction, the polymer-surface reactivity and the solvent-surface interaction. A clever management of these interfaces can bring to fully control the grafting-to process and thus the conformation of the tethering polymer.

References

(1) Akcora, P.; Liu, H.; Kumar, S. K.; Moll, J.; Li, Y.; Benicewicz, B. C.;

Schadler, L. S.; Acehan, D.; Panagiotopoulos, A. Z.; Pryamitsyn, V.; et al. Anisotropic Self-Assembly of Spherical Polymer-Grafted Nanoparticles. *Nat. Mater.* **2009**, *8* (4), 354–359.

(2) Matyjaszewski, K. Atom Transfer Radical Polymerization (ATRP): Current Status and Future Perspectives. *Macromolecules* **2012**, *45* (10), 4015–4039.

(3) Moad, G.; Chong, Y. K.; Postma, A.; Rizzardo, E.; Thang, S. H. Advances in RAFT Polymerization : The Synthesis of Polymers with Defined End-Groups. 2005.

(4) Perrier, S.; Takolpuckdee, P. Macromolecular Design via Reversible Addition-Fragmentation Chain Transfer (RAFT)/Xanthates (MADIX) Polymerization. *J. Polym. Sci. Part A Polym. Chem.* **2005**, *43* (22), 5347–5393.

(5) Chauvin, F.; Dufils, P.-E.; Gigmes, D.; Guillaneuf, Y.; Marque, S. R. A.; Tordo, P.; Bertin, D. Nitroxide-Mediated Polymerization: The Pivotal Role of the k_d Value of the Initiating Alkoxyamine and the Importance of the Experimental Conditions. *Macromolecules* **2006**, *39* (16), 5238–5250.

(6) Kumar, S. K.; Jouault, N.; Benicewicz, B.; Neely, T. Nanocomposites with Polymer Grafted Nanoparticles. *Macromolecules* **2013**, *46* (9), 3199–3214.

(7) Barbey, R.; Lavanant, L.; Paripovic, D.; Schüwer, N.; Sugnaux, C.; Tugulu, S.; Klok, H. A. Polymer Brushes via Surface-Initiated Controlled Radical Polymerization: Synthesis, Characterization, Properties, and Applications. *Chem. Rev.* **2009**, *109* (11), 5437–5527.

(8) Li, C.; Han, J.; Ryu, C. Y.; Benicewicz, B. C. A Versatile Method to Prepare RAFT Agent Anchored Substrates and the Preparation of PMMA Grafted-Nanoparticles. *Macromolecules* **2006**, *39* (9), 3175–3183.

(9) Wu, L.; Glebe, U.; Böker, A. Surface-Initiated Controlled Radical Polymerizations from Silica Nanoparticles, Gold Nanocrystals, and Bionanoparticles. *Polym. Chem.* **2015**, *6* (29), 5143–5184.

(10) Ohno, K.; Akashi, T.; Huang, Y.; Tsujii, Y. Surface-Initiated Living Radical Polymerization from Narrowly Size-Distributed Silica Nanoparticles of Diameters Less Than 100 Nm. *Macromolecules* **2010**, *43* (21), 8805–8812.

(11) Li, C.; Benicewicz, B. C. Synthesis of Well-Defined Polymer Brushes Grafted onto Silica Nanoparticles via Surface Reversible Addition-Fragmentation Chain Transfer Polymerization. *Macromolecules* **2005**, *38* (14), 5929–5936.

(12) Chiefari, J.; Chong, Y. K.; Ercole, F.; Krstina, J.; Jeffery, J.; T Le, T. P.; A Mayadunne, R. T.; Meijs, G. F.; Moad, C. L.; Moad, G.; et al. Living Free-Radical Polymerization by Reversible Addition-Fragmentation Chain Transfer: The RAFT Process. *Macromolecules* **1998**, *31*, 5559–5562.

(13) Corrigan, N.; Rosli, D.; Warren, J.; Jones, J.; Xu, J.; Boyer, C. Oxygen Tolerance in Living Radical Polymerization: Investigation of Mechanism and Implementation in Continuous Flow Polymerization. *Macromolecules* **2016**, *49* (18), 6779–6789.

(14) Lu, L.; Yang, N.; Cai, Y. Well-Controlled Reversible Addition–fragmentation Chain Transfer Radical Polymerisation under Ultraviolet Radiation at Ambient Temperature{. *Chem. Commun.* **2005**, 5287–5288.

(15) Boyer, C.; Bulmus, V.; Davis, T. P.; Ladmiral, V.; Liu, J.; Perrier, S. Bioapplications of RAFT Polymerization. *Chem. Rev.* **2009**, *109*, 5402–5436.

(16) Chong, (Bill) Y. K.; Krstina, J.; Le, T. P. T.; Moad, G.; Postma, A.; Rizzardo, E.; Thang, S. H. Thiocarbonylthio Compounds [SC(Ph)S−R] in Free Radical Polymerization with Reversible Addition-Fragmentation Chain Transfer (RAFT Polymerization). Role of the Free-Radical Leaving Group (R). *Macromolecules* **2003**, *36* (7), 2256–2272.

(17) Barner-Kowollik, C. *Handbook of RAFT Polymerization*; 2008.

(18) Moad, G.; Rizzardo, A. E.; Thang, S. H. Living Radical Polymerization by the RAFT Process. *Aust. J. Chem* **2005**, *58*, 379–410.

(19) Favier, A.; Charreyre, M.-T. Experimental Requirements for an Efficient Control of Free-Radical Polymerizations via the Reversible Addition-Fragmentation Chain Transfer (RAFT) Process. *Macromol. Rapid Commun.* **2006**, *27* (9), 653–692.

(20) Zhao, Y.; Perrier, S. Reversible Addition-Fragmentation Chain Transfer

Graft Polymerization Mediated by Fumed Silica Supported Chain Transfer Agents. *Macromolecules* **2007**, *40* (25), 9116–9124.

(21) Lai, J. T.; Filla, D.; Shea, R. Functional Polymers from Novel Carboxyl-Terminated Trithiocarbonates as Highly Efficient RAFT Agents. *Am. Chem. Soc. Polym. Prepr. Div. Polym. Chem.* **2002**, *43* (2), 122–123.

(22) Hansen, C. M. Hansen Solubility Parameters: A User's Handbook. **2002**.

(23) Labouta, H. I.; Gomez-Garcia, M. J.; Sarsons, C. D.; Nguyen, T.; Kennard, J.; Ngo, W.; Terefe, K.; Iragorri, N.; Lai, P.; Rinker, K. D.; et al. Surface-Grafted Polyethylene Glycol Conformation Impacts the Transport of PEG-Functionalized Liposomes through a Tumour Extracellular Matrix Model. *RSC Adv.* **2018**, *8* (14), 7697–7708.

Chapter 5. Fabrication of titanium dioxide nanocomposite materials with thermoplastic polyurethane

Introduction

Surface ligand engineering is an effective tool applied for the production of novel polymer nanocomposites, a tantalizing kind of materials that express the properties of inorganic matter within an organic matrix. Many inorganic crystals showed interesting properties when found at the nano size scale. The idea is to bring the inorganic nano filler properties into the polymer matrix and create a new class of materials with enhanced multiple properties. The issue of this objects is the high surface energy that bring to a phase separation in an organic polymer matrix. This phenomenon is driven by the thermodynamics involving both entropic and enthalpic contributions[1,2]. For nanoparticles sufficiently small dispersed in a polymer matrix, the enthalpy of mixing is dominated by van der Walls core-core interaction. In the case of zero enthalpic mismatch, i.e. same chemistry for both grafted polymer and matrix, the NCs dispersion is promoted by the ideal translational entropy, that represents the entropic part associated with the motion of the center of mass of the polymer. This contribution always favors mixing. However, the entropic energy is balanced by excluded volume effects[3]. Moreover, the polymer chains that are close to the NC surface are more tightly packed and presumably their dynamics is slower than in other regions of space. The chain entropic freedom is reduced even more strongly in the volume comprised between two particles. In this case the chains' internal degrees of freedom suffer a substantial reduction and

the chains try to escape from the restricted space. As a result, the particles will be pushed against one another leading to aggregation. The associated force, which is purely entropic, is known as the depletion attraction[3]. The introduction of a thin polymeric layer on the surface of the inorganic nanoparticles (NPs) and nanocrystals (NCs) enables their good dispersion in solvents and matrixes, in which, otherwise, bare particles aggregate and precipitate[3–5]. The surface modification can introduce additional functionalities to the NPs, providing new properties for a wide number of applications. In order to express the intrinsic properties of the NCs they must be well dispersed and distributed in the space. The two main synthetic routes followed to create grafted nanoparticles are the *grafting-to* and *grafting-from* approach. In the *grafting-to* method, a preformed and end functionalized polymer is attached to the surface. The *grafting-to* method has the advantage to be of use but there are some drawbacks. Steric repulsion between polymer chains already attached and a chain diffusing to the surface limits the available graft density[6]. The *grafting-from* method is a surface-initiated polymerization started with an initiator or chain transfer agent. The diffusion of a relatively small monomer to the surface does not suffer from the same steric repulsion as a diffusing polymer chain but lead to a less homogenous polymer layer[7].

Morphology of polymer nanocomposites materials

The main parameters that control the quality of the dispersion and the performance of the final material have been the subject of many scientific works, but finally Kumar S.K. et al. provided a morphology map that helps to navigate into the nanocomposite dispersion and distribution diagram[8]. The main parameters that control the map coordinates are the molecular

weight of the grafted chains and of the polymer matrix (N, P respectively) together with the grafting density (σ), i.e. the number of chains per unit area of the nanoparticle (Figure 53). Looking at the map it is noted that to have homogeneous distribution of single NCs it is needed high molecular weight of the grafted chains (N) and/or high surface coverage (σ) together with polymer matrix with molecular weights (P) lower than that of the grafting chains.

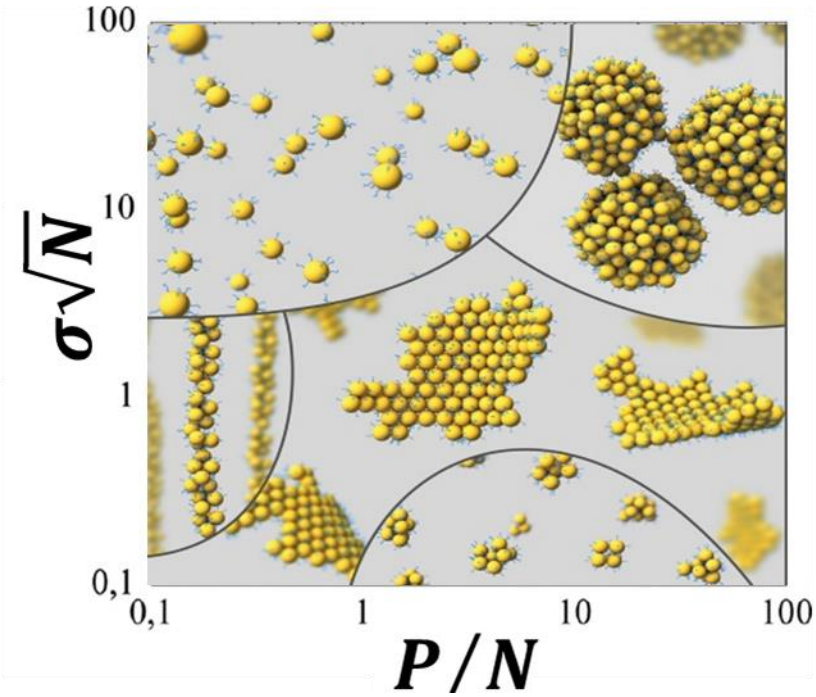

Figure 53 A composite morphology diagram created from all of the available data in the literature: σ√N as a function of P/N. The points, adapted from the literature, are subdivided in different areas coded so that upper left corresponds to well dispersed particles (WD); upper right to phase separated samples (PS); lower left to strings (S); center of the diagram to connected sheets (CS) and lower region to small clusters (SC).

The simpler case is to attach a polymer that has the same chemical structure of the matrix in order to avoid any mixing problems related to the chemistry of the two components. This enthalpic interaction, coupled with the

entropic forces associated with the deformation of the grafted chains, determines the final dispersion state of NPs. For example, at very low graft densities, the insufficient enthalpic screening effect leads to a strong net vdW attraction between particle cores. In this scenario, if the grafted chains are short, the entropic penalty associated with the distortion of brush layers in the region of contact is insignificant compared to the dominant core-core attraction, and the NPs aggregate isotropically into local spherical agglomerates. With increasing grafted chain length, however, the entropic contributions become significant compared to the screened vdW attraction, and a range of anisotropic structures (string-like, sheet-like aggregates) develop[8]. A uniform dispersion state can be obtained by tailoring the delicate balance between the energy gain of particle cores being closer and the entropy penalty of distorting the grafted polymers. For flat substrates it is known that at very low graft densities the polymer chain assumes the "mushroom" structure in the chemically identical polymer matrix. The interface in this case is likely highly entangled between matrix and brush. As the graft density increases, the distance between graft sites becomes smaller than the size of the grafted coils and the mushrooms form a stretched wet-brush layer.[9,10] At even higher graft densities, the conformational entropy losses suffered by the grafted brush chains in order to fully accommodate the matrix chain cannot be compensated by the translational entropy gain of the matrix chain from penetration into the brush layer. Hence, the matrix chains are excluded from the vicinity of the grafted surface, and a "dry brush" is formed. In this case, the matrix and brush are not entangled leading to a mechanically weaker interface. This expulsion or partial brush penetration causes a cross-over from a negative to a positive interfacial energy between the free and the grafted chains (autophobic dewetting). Compared to flat brushes, the effective graft

density of brushes grafted on spherical particles typically decreases with decreasing particle size, leading to a higher degree of interpenetration[11] However, Mean Field models find that positive interfacial energies due to matrix expulsion appear when P > N and graft density (σ) is sufficiently high[11] (Figure 53). More reports predict an exclusion region (analogous to the depletion region in flat brushes), from which free chain ends are excluded, in the vicinity of the NP surface[12–15]. The critical height increases with increasing radius of curvature. The behavior of the exclusion region reflects some aspects of the interaction between spherical brushes with matrix polymers such as the existence of a "dry brush" regime near the NP surface where the solvent cannot swell the brush. A promising approach to control all these effects is to create a double brush layer that could overcome autophobic dewetting between the polymer grafted chains and the chains of the matrix[16]. A bimodal brush is defined as a homopolymer brush with two distinct molecular weight distribution attached to the surface. On the other hand, it is defined a mixed bimodal brush when these chains are also chemically distinct[17]. All these efforts described above to get a homogeneous distribution and dispersion on nanocrystals are crucial for optical applications.

Nanocomposite with high refractive index

Nanocomposite materials found many applications in the optical field due to the intrinsic properties borrowed from the inorganic phase. For example the introduction of quantum dots raise photoluminescence properties into organic matrices[18]. Another important contribution of inorganic fillers is the enhancement of the refractive index (*n*) of the polymer matrix.[19–23]. Transparent materials with high refractive indices are extensively required

for numerous applications, including optical devices, lenses, antireflective coatings, and waveguides. In these applications, synthetic polymers have been employed as optical materials exhibiting excellent formability and tunable chemical and physical properties. However, refractive indices of common polymers are limited to the range from 1.3 to 1.7. For example, TiO_2 is an attractive inorganic component for preparation of hybrid materials because it is a high refractive index crystal (n= 2.5–2.7), it is intensively used in industry and costs production are low[21,23–26]. Many classes of polymers possess different properties, in our contribution we modified the properties of thermoplastic polyurethane matrix. Polyurethanes are a class of handy materials with great potential for use in different applications. This type of polymer can be found in different forms (foam, film etc..) and this eclectic material represents the only class of polymers that display thermoplastic, elastomeric, and thermoset behavior[27]. Their specific mechanical, physical, biological, and chemical properties are attracting significant research attention to tailoring PUs for use in different applications. Enhancement of the properties and performances of PU-based materials may be achieved through a deep transformation of the chemical starting materials, since the characteristics expressed are based on their structure–property relationships.[28]. In order to modify and increase the properties of this interesting material we decided to work on the mechanical and optical properties. In our contribution we dealt with nanocomposite production of a thermoplastic polyurethane-based (TPU) nanocomposite material prepared starting from a mixed double layer system tethered to a rod-like anatase nanocrystal. The presence of high loading of a low dimensional anatase NCs (< 15 nm), grafted with a bimodal layer, into the TPU matrix brought an improvement of the nanocomposite mechanical

properties and the enhancement of the refractive index, maintaining its clearness.

Materials and methods

Titanium(IV) isopropoxide (TTIP, 99.999%), oleic acid (OLAC, 90%), oleyl amine (OLAM, 70%), trimethylamine N-oxide dihydrate ((TMAO, 98%), triethylamine (TEA), phosphoryl chloride ($POCl_3$ >98%) freshly distilled before reactions, tetrahydrofuran (THF >99%) dried with sodium wire and benzophenone and distilled before the reactions start, were purchased from Sigma Aldrich (Merck). Chloroform ($CHCl_3$), diethylether and toluene ($\geq$ 99.9) are eventually dried over calcium chloride and distilled over activated molecular sieves. All solvents used were of analytical grade and purchased from Aldrich. Polyethylene oxide monomethyl ether ($M\overline{w}$= 5000 $gmol^{-1}$) were precipitated twice from ethanol, dried by azeotropic distillation from toluene, and stored in a dry nitrogen atmosphere. Polyurethane thermoplastic used is Estane® AG 8451, produced by Lubrizol. It is a polyether based aliphatic (TPU) specifically formulated to be used as an adhesive interlayer film. AG 8451 is an excellent general-purpose polymer for all optical aliphatic applications.

Synthetic methods

Synthesis of anatase TiO_2 NCs

the synthetic method used is a modified version of the procedure proposed by Raffaella Buonsanti et al.[29]. In a round bottom flask, previously dried, are added 1.5 mol of OLAC. In order to work in an air free environment, OLAC is firstly degassed with three vacuum/nitrogen cycles and further degassed at 120° for 2h the mixture is then cooled down to 90 °C under N_2

flow, when the target temperature is reached 0.011mol of TTIP is added in a single portion. After exactly 5 minutes a solution 2 M of TMAO (0,0367 mol) in water is injected in a single portion. The flask is heated up to 120°C at a ramp rate of ~25 °C/min and then left react under vigorous stirring for 24 hours. The solution turned from a clear pale-yellow mixture to a milky solution. The crude product is then centrifuged, precipitating a white solid constituted by titania NCs covered by oleic acid whose polar terminal group is bound to the surface. The aliphatic portion of oleic acid allows easy dispersal in hexane, an apolar solvent. The particles are precipitated several times in ethanol to remove excess ligands and eventually dispersed in hexane, chloroform or DCM. The obtained NCs, capped with oleic, either used for the fabrication of the nanocomposite films and for the production of mixed double layer grafted NCs.

mPEO-phosphate

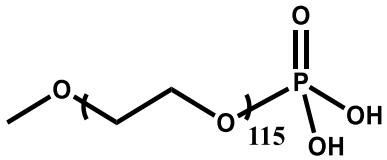

mPEO of $M\overline{w}$= 5000 $gmol^{-1}$ molecular weights is modified following the procedure proposed by Zalipsky[30]. Typically, 0.5 mmol of mPEO is dissolved in dry DCM and added dropwise to a solution of phosphoryl chloride ($POCl_3$, 1.2 eq.) and TEA (2.4 eq.) in ice bath. The reaction is slowly brought to room temperature and the stirred for 24 hours. Then 5 mL of deionized water is slowly added to the mixture and left react for 1 hour. The solvent is dried in vacuum and the crude product is dissolved in DCM and extracted with acidic water (HCl 0.2 mM) and then extracted three times with saturated brine. The organic phase is collected and dried

over $MgSO_3$, filtered and precipitated three times in diethyl ether. ^1H NMR (500 MHz, $CDCl_3$): 4.12 ppm (m, 2H, $CH_2C\mathbf{H_2}$-O-P), δ 3.62 ppm (m, 454H, -$C\mathbf{H_2}C\mathbf{H_2}$- PEO chain), δ 3.34 ppm (s, 3H, -$OC\mathbf{H_3}$), ^{31}P NMR (500 MHz, CDCl3): δ 2.01 ppm (s, 1P, O**P**$(OH)_2$).

Direct exchange process

The grafting reaction is made on the as phosphate modified mPEO. The polymer is dissolved in $CHCl_3$ and the anatase NCs, dispersed in $CHCl_3$, are added in the solution, then the mixture is sonicated for 10 minutes before it is left to react for 16 hours at reflux condition. The product is purified by ultracentrifugation with a mixture of chloroform:diethyl ether 1:2.5 for at least three times (40000 rcf). This process is a direct ligand exchange that provide a mixed bimodal system.

Kinetic study of the exchange process

The study of this process was made on the as phosphate modified mPEO. The amount of mPEO is 0.25 eq respect to the moles of OLAC (1.25 mol) present on the pristine NCs. The polymer is dissolved in $CHCl_3$ and the anatase NCs, dispersed in $CHCl_3$, are added in the solution, then the mixture is sonicated for 10 minutes then is left react for 120 minutes at reflux condition. An amount of the crude solution is withdrawn each 20 minutes and purified as described before the analysis.

Nanocomposite film preparation

The film preparation is made through a solvent casting process. Two sets of samples have been prepared starting from different NCs, the first set

using oleic acid capped anatase (OLAC@Anatase) and the second set with the mixed double layer made of mPEO and oleic acid (mPEO-OLAC@Anatase). In a standard procedure the TPU is dissolved in a certain amount of chloroform in order to reach a concentration of 0.033 g mL^{-1}. A chloroform dispersion 0.1 g mL^{-1} of OLAC@Anatase or of mPEO-OLAC@Anatase, is prepared and then added in a round bottom flask alongside with the dissolved TPU. To the mixture is then added an amount of chloroform to reach 70 mL of total volume. The mixture is then stirred overnight at 40°C. The dispersion is poured in a Petri dish to slowly evaporate the solvent at room temperature, overnight. Once the solvent completely evaporates an optically clear film is obtained and in order to get rid of defects is annealed for 12 hours at 80 °C.

Characterization methods

The hydrodynamic diameter and size distributions of the particles were determined by *Dynamic Light Scattering* (DLS) in deionized water and DCM (0.1 mg mL^{-1}). The measures were recorded at 25 °C on a Malvern Zetasizer equipped with a continuous wave 1 mW He−Ne laser operating at 632.8 nm and an avalanche photodiode detector, Q.E. > 50% at 633 nm, placed at 173° with respect to the incident beam. Reported data are the average of at least three different measurements of the size distribution as the function of the intensity. *Nitrogen adsorption−desorption isotherms* were measured at liquid nitrogen temperature using an ASAP 2010 analyzer (Micro- metrics). The samples were outgassed for 12 h at 473 K. The surface area was calculated using the *Brunauer−Emmet−Teller* (BET) model[31]. For *X-ray* characterization, a D8 Advance powder diffractometer (Bruker) was used with Cu $K\alpha_1$ radiation (λ = 1.5418 Å) and secondary-

beam monochromator. The powder is added on a quartz sample holder and measured. Amount and definition of tethered ligand on the NCs surface has been verified with *Attenuated Total Reflection (ATR)-FTIR and Thermogravimetric analysis* (TGA). Fourier transform infrared characterization was performed using a PerkinElmer Spectrum 100 instrument scanning from 650 to 4000 cm−1 with a resolution of 4 cm−1 for 64 scans. The sample, in the form of powder, is added on the sample holder and directly analyzed over the Si crystal with the Universal ATR (UATR). Thermogravimetric analysis was carried out with Mettler Toledo TGA/DSC1 STARe System, at a constant gas flow (50 cm^3 min^1). The thermal profile was the following: 25° C 5 min (air); 25–800° C with a rate 10 C min^{-1} (air). *Bright field Transmission electron microscopy* (BF-TEM) imaging was performed on a JEOL JEM-1011 microscope equipped with a thermionic gun operating at 100 kV accelerating voltage. For these analyses, the samples were prepared by dropping dilute suspensions of NCs onto carbon-coated 200 mesh copper grids. ^1H, ^{31}P NMR spectra were recorded using a Bruker AMX-500 spectrometer operating at 500 MHz. Solid state ^{13}C NMR and HPDEC NMR experiments were performed at 75.5 MHz on a solid state magic angle spinning Bruker Avance 300 at 25 °C. Spinning rate was set to 10 kHz for both experiments. HPDEC were usually recorded with 2048 scans using a recycle delay of 2 s. Molecular weight distributions and polydispersity indexes were determined by *Gel Permeation Chromatography* (GPC) using a WATER 1515 isocratic HPLC Pump, a WATER 2414 refractive index detector, four Styragel columns (HR2, HR3, HR4, HR5). Samples were dissolved in THF and their chromatograms recorded with a flow of 1.0 ml/min at 35 °C. Thermal properties were determined by *Differential Scanning Calorimetry* (DSC) using a Mettler Toledo DSC 1 instrument with a heating and cooling rate

of 20 or 10 K/min under nitrogen gas flow (80 mL/min). Tensile tests were performed on film slices of dimensions 65 mm long, 15 mm with and 0.25 mm thick using a mechanical testing machine Zwick 1445 with a load cell of 100N. Experiments were carried out at room temperature with a test speed of 500 mm/min and a preload of 0.1 MPa. Tensile strength, elongation at break and elastic modulus have been determined as averages of eight to nine independent drawing experiments performed at the same conditions following the ASTM D882 standard. All the information and values have been obtained with the testXpert II® software. Refractive indices were measured using a prism coupling refractometer Metricon 2010 working at 633 nm with an uncertainty lower than 10^{-3}. We performed 5 measurements in different points of the same sample to check the homogeneity and to evaluate mean value of the refractive index and standard errors.

Results and discussions

To get a highly transparent nanocomposite material with enhanced *n*, few factors must be taken into account. First of all, the inorganic filler must be "*small*". Not all the sizes are suitable due to the Rayleigh scattering law. In fact, intense light scattering occurs with large inorganic domains, due to the *n* mismatch with the organic matrix, determine an opaque appearance of the material. The amount of scattered light can be evaluated by using; as a rule of thumb: scattering can be neglected when the average diameter of the particles is less than 50–60 nm[25]. Furthermore, to achieve complete transparency the filler must be well dispersed and distributed into the polymer matrix. It is necessary because scattering phenomena, that arises from aggregation, brings opacity and lowers the optical quality of the final

material. All these strict requirements are fulfilled by colloidal anatase nanocrystals used in this work. Colloidal synthesis was employed since no extreme work condition are needed, moreover this synthetic route provides a scalable production process. The best crystals suitable for optical applications must be pure and controlled over size distribution. A morphological study was done by TEM micrograph analysis of the as prepared NCs (Figure 54). Thanks to the analysis of the pictures carried out with ImageJ software, in particular with the particle analyzer plug-in, it was possible to determine the size of the particles. The NCs appear as rod shaped NCs (Figure 54).

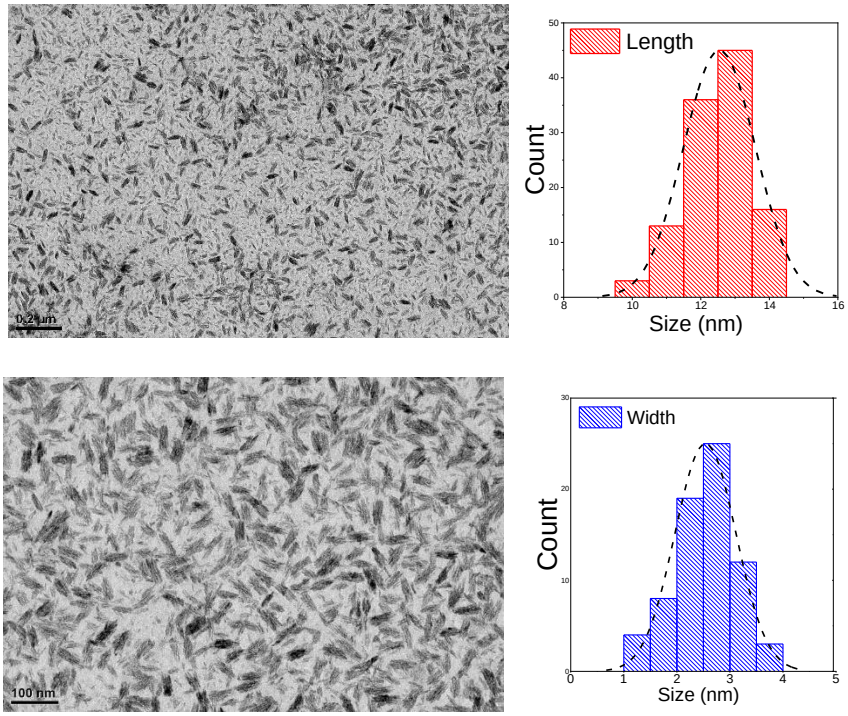

Figure 54 On the left are found the TEM micrographs of the colloidal anatase nanocrystals. On the right are reported the histograms related to the size distribution evaluated through the analysis of TEM pictures. Top-right represents the length size distribution (red pattern); bottom-right represents the width size distribution (blue pattern).

The crystalline phase was defined through the analysis of the XRD diffractogram (Figure 55). The raw data obtained by the XRD analysis was analyzed and fitted with a peak analyzer plug in of the Originlab® data analyzer software. The diffractogram pattern is also simulated through mercury® software for both cases: anatase nanocrystals with 15 nm diameter (Figure 55, blue line) and bulk anatase crystal (Figure 55, red line). The calculated diffractograms and the raw data are then compared, and it is shown that the as prepared particles are pure anatase nanocrystals. The anatase characteristic diffraction peak at $2\theta = 25.3°$, that corresponds to the (101) face, is observed while the rutile peak at $2\theta = 27.5°$, that corresponds to the (110) face, is absent.

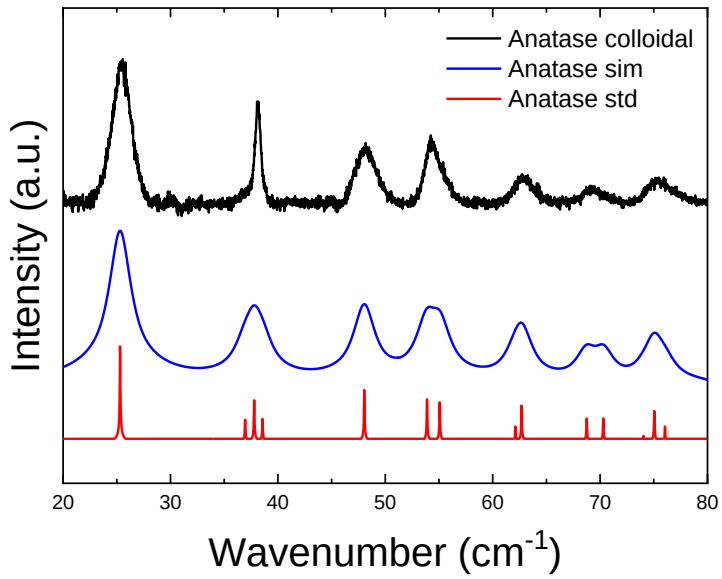

Figure 55 XRD pattern of the anatase colloidal NCs prepared by colloidal approach (up, black line); anatase simulated pattern standard (center, blue line) and anatase bulk standard (bottom, red line).

By analyzing the XRD data, it is possible to estimate the crystal dimensions using the Sherrer's formula (eq.12, chapter 2). Eq.12 was used to calculate

NCs size as reported in Table 12. The size has been finally verified through DLS analysis in chloroform as solvent showed a hydrodynamic diameter of 15.9±1.1 nm. The hydrodynamic diameter refers to a particle covered by a layer of solvated OA (estimated to be 2 nm for a full covered NC[32]). The values obtained with different techniques are consistent (Table 12). To get all the information required for our next experiments it is necessary the evaluation of the specific surface area (SSA). Rod-like NCs specific surface areas are calculated using a simple geometric model as previously reported in Chapter 2. The results are listed in Table 12.

Table 12 Crystal dimensions of OLAC@Anatase derived from XRD calculated at 38.2° (004) peak, TEM micrographs, DLS measure in hexne reported with its PDI. Experimental specific surface area (SSA_{exp}) as well as an estimate of surface area based on TEM size and calculated using Sauter equation ($SSA_{predicted}$).

Sample	XRD	TEM	DLS		SSA_{exp}	$SSA_{predicted}$
	nm	nm	nm	PDI	m^2g^{-1}	m^2g^{-1}
Anatase	10.9±0.4	12.3±1.1	15.9	0.157	200±7	229±32

As mentioned in the synthetic section, the colloidal nanocrystals are capped with OLAC that it is an important and common ligand in the synthesis of many metal oxide nanoparticles. It is quite helpful to stabilize the nanocrystals and improve the dispersity in some organic environments. The presence of OLAC tethered to the NCs surface (OLAC@Anatase) is detected with FTIR analysis. The data reported in Figure 56 show the presence of peaks associated to the aliphatic chain (3000-2750 cm^{-1}) and the peaks of the antisymmetric and symmetric stretching of the carboxylate group (1520 cm^{-1} and 1410 cm^{-1}).

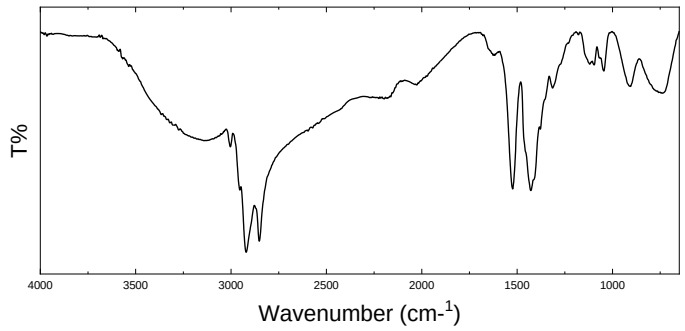

Figure 56 FTIR analysis of the OLAC@Anatase samples

Weight percentage of OLAC is estimated through TGA analysis (Figure 57) and the amount of organic ligand is around 27% of the total weight.

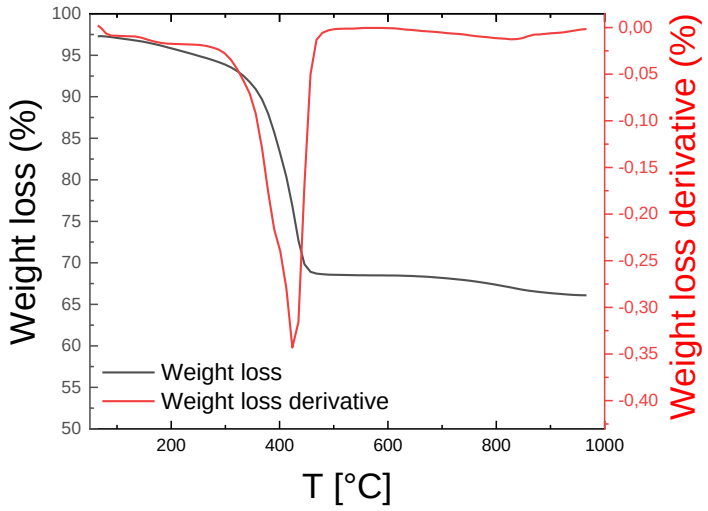

Figure 57 TGA analysis of the OLAC@Anatase NCs (black line) and its first derivative (red line).

The aim of this work is to design a nanosized object that can be effectively dispersed in organic matrices, in particular in TPU matrix. It is important to get a complete picture of the matrix in order to properly engineer the inorganic surface. The weight-average molecular weight of TPU is 58.6 Kg

mol^{-1} with a Đ of 1.84 were obtained by GPC (Figure 58, inset up left). The polymer matrix composition was analyzed using ^{1}H NMR (Figure 58). It is necessary to carefully functionalize the inorganic filler with a compatible ligand, since the chemical interaction between the matrix and the nanocomposite is a relevant aspect that must be taken into account. It is important to identify the chemical composition of the matrix. It should be noted that generally, PUs are often synthesized from the reaction between an isocyanate and polyol molecule in the presence of either a catalyst or ultraviolet light activation. These isocyanate and polyol molecules should necessarily contain two or more isocyanate groups and hydroxyl groups, respectively[33]. There are different kinds of polyols available that can be prepared in laboratories by various ways and generally are polyethers or polyesters. Isocyanates are incorporated into PU synthesis via a hydroxyl-group-containing compound due to their high reactivity[34] and they are usually characterized by the presence of aliphatic or aromatic chains. From the NMR spectrum it is noted that the matrix is mainly made by prepolymers and the polyols: a mixture of polypropylene glycol, polybutanediol, polyoxymethylene and small amount of polyethylene glycol. On the other hand, there is no detectable presence of any aromatic group, suggesting that the main structure of the isocyanates is mainly composed by aliphatic or aliphatic cyclic compounds.

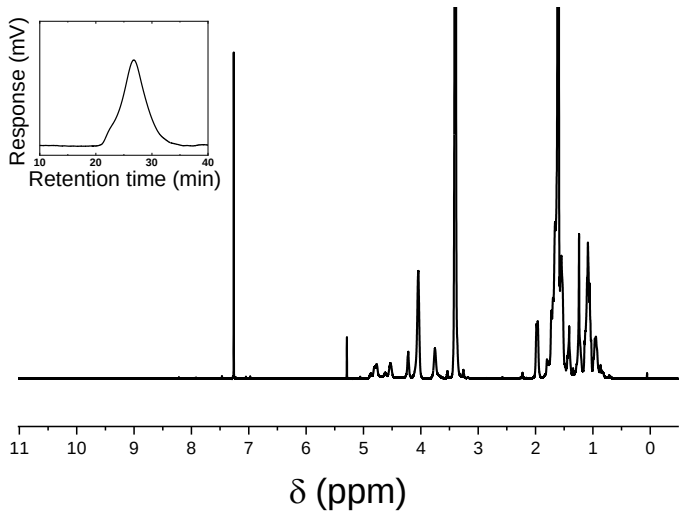

Figure 58 ^{1}H NMR in $CDCL_3$; GPC analysis of AG8451 TPU matrix

The best architecture that effectively allows good dispersion of a nanosized inorganic particle in an organic polymer matrix, is the bimodal brush system. Benicewicz et al.[35] showed in their works that densely grafted short brushes enthalpically screen the core/core attraction, which is especially critical for nanofiller/matrix systems with large surface energy mismatch. On the other hand, sparsely grafted long chains lowers entropic dewetting of high molecular weight polymer matrices. Since the polymer matrix is found to be composed mainly by polyols, and aliphatic chains, poly ethyleneoxide monomethylether (mPEO) and OLAC would be good compatibilizers between the inorganic crystal and this polymer matrix. The NCs will be covered by a mixed double layer: a dense layer made by OLAC that will avoid the core-core interactions and a second layer composed by mPEO, that will enhance the number of entanglements with the matrix. In order to test the behavior of this kind of systems, two sets of samples have

been prepared: one using only oleic acid grafted nanocrystals and a second one with both OLAC and mPEO.

Mixed double layer synthesis and characterization

Fatty acids are common stabilizer that are weakly bonded to inorganic surfaces and are usually replaced with a silane agent and phosphonic acid/phosphate moiety to obtain stronger binding[36,37]. The bimodal systems were obtained with a direct ligand exchange between the OLAC and mPEO functionalized with a phosphate end group. First set of experiments were made to study the kinetic involved in this process and the second set were made in different experimental condition to verify the control over the graft density. The yield of the exchange process has been verified through DLS, FTIR and ^{13}C SS NMR to get qualitative information, while to get quantitative information ^{1}H NMR and TGA were used. From the comparison between the FTIR spectra of OLAC@Anatase with the phosphate mPEO (mPEO_5K) and the mixed double layer (mPEO_5K-OLAC@Anatase) it is possible to detect the characteristic vibrational peaks of the mPEO chains. The sample mPEO_5K-OLAC@Anatase has the vibration peak at 2900 cm^{-1} related to the stretching of the CH_2 groups and at 1100 cm^{-1} the C-O bonds vibration peak. The peaks related to the presence of OLAC are detected (Figure 59 FTIR, right) at 1520 cm^{-1} and 1410 cm^{-1}. The low intensity is due to the fact that the aliphatic chains are screened by the polymer chains.

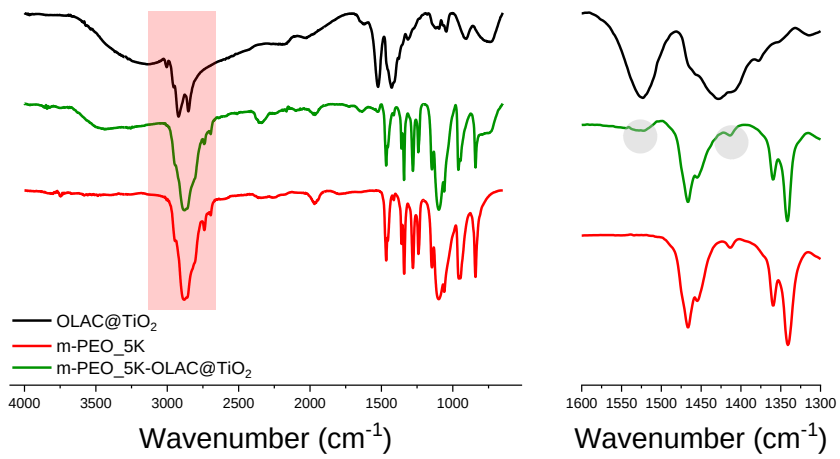

Figure 59 FTIR Top to bottom: OLAC@Anatase black line and grey region; mPEO_5K -OLAC@Anatase green line, mPEO_5K red line and red region.

To get a better picture of the mixed double layer samples a high-power decupling (HP DEC) solid state ^{13}C NMR analyses are performed. This kind of analysis is a powerful tool that enables a better observation of the OLAC grafted on the anatase NCs. The spectra are reported in Figure 60. In the OLAC@Anatase spectrum (Figure 60, black line) is found the peak at 15 ppm related to the methyl end group of the aliphatic chain, in the region between 25 and 38 ppm are found the peaks of the carbons of the aliphatic chains while at 130 ppm is noted the peak related to the carbons of the double bond. The peak at 180 ppm related to the C=O bond is missing due to the low mobility of this group since it is attached on the surface. In the mPEO_5K spectrum (Figure 60, red line) is present 70.2 ppm at the main peak of the carbons that belong to the polymeric chain. The spectra of the mPEO_5K-OLAC@Anatase is the sum of the previously described samples, confirming the presences of both OLAC and mPEO.

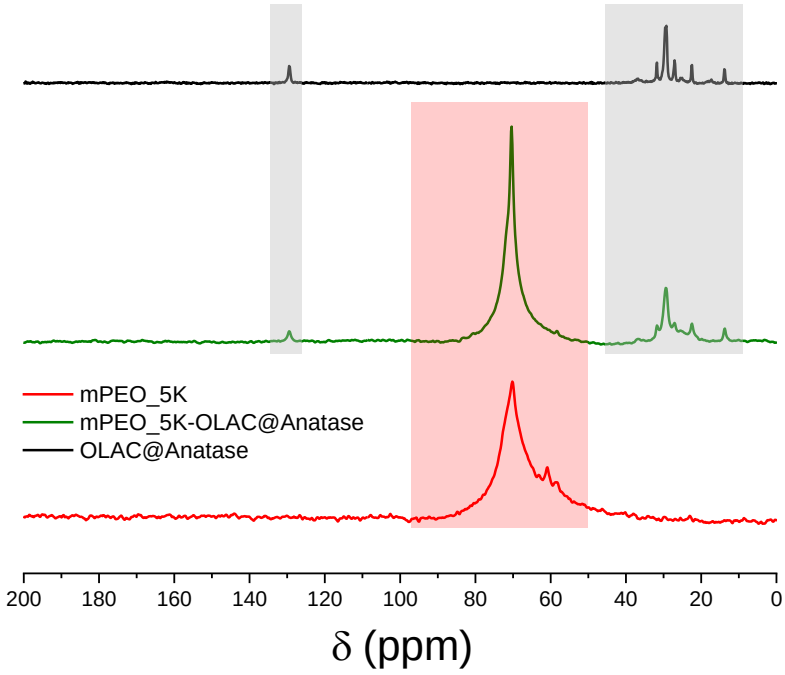

Figure 60 HP DEC ^{13}C MAS NMR, recycle delay 2s and spin rate 10 KHz. Top to bottom: OLAC@Anatase black line and grey region; mPEO_5K -OLAC@Anatase green line, mPEO_5K red line and red region.

DLS measures of the hydrodynamic diameter (d_h) of the pristine NCs and the mixed double layer NCs are reported in Figure 61The d_h of the OLAC grafted NC is 15.9 ± 6 nm with a polydispersity index (PDI) equal to 0.222, while the polymer grafted NC has a d_h 43.8 ± 11 nm with a PDI equal to 0.168. The DLS analysis show an increase of the size of the mPEO-OLAC@Anatase due to the larger dimension of the grafted polymer. The presence of this polymer layer enables a better size distribution and stability highlighted by the lower PDI value.

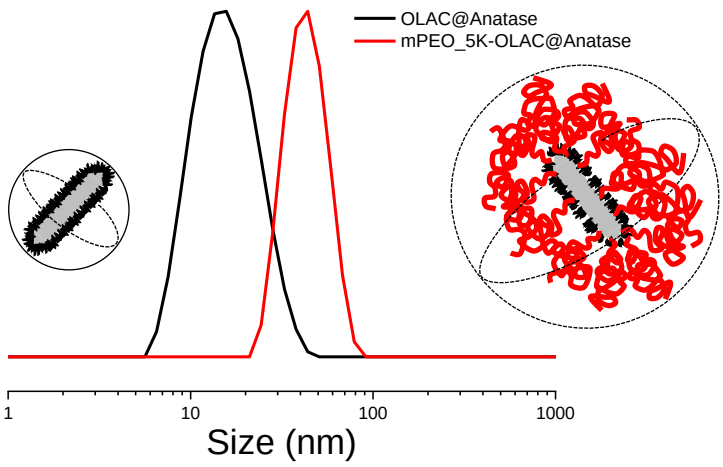

Figure 61 DLS measure in chloroform of the pristine NCs (OLAC@Antase. black line) and the mixed double layer NCs (mPEO_5K-OLAC@Anatase, red line)

TGA and ^{1}H NMR were used to get quantitative information of the experiments conducted, i.e. to define the composition of the as prepares samples. A thermogravimetric analysis of the OLAC@Antase NCs and the mPEO is reported in Figure 62. It is noted that the two curve are described by two different thermal decomposition behavior (Figure 62, top), highlighted by the first derivative plot (Figure 62, bottom). The peak of the first derivative is characteristic for each organic compound and indicates the point of greatest rate of change on the weight loss curve. This is also known as the inflection point. The OLAC has and inflection point around 415°C with a decomposition temperature range between 380°C and 500°C, while the mPEO_5K has an inflection point around 365°C with a decomposition temperature range between 250°C and 380°C.

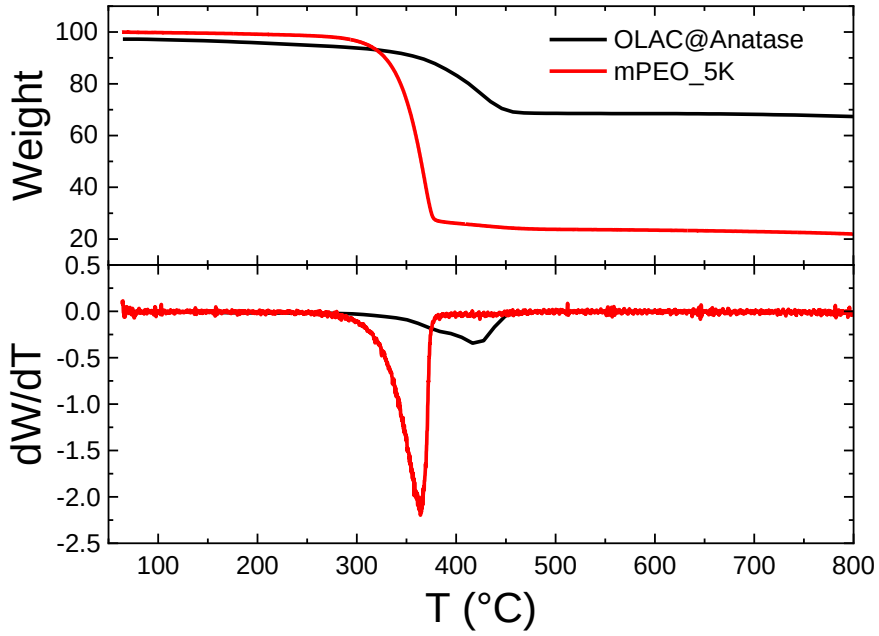

Figure 62 TGA curves of OLAC@anatse (black line) and mPEO_5K (red line) and first derivative of the same samples (lower graph).

The decomposition temperature range of both the chemical compounds are distinguished and allows to define the composition of the mixed double layer samples: the largest decomposition step is attributed to the mPEO and the second step to the OLAC. A kinetic study of the ligand exchange process was made, the experimental protocol is described in the materials and methods section. The weight loss percentage of mPEO and OLAC is defined as described and molar ratio is defined as follows. From the TGA analysis is possible to calculate the total weight loss percentage ($W_{total\ loss}$%) of the organic material attached on the anatase surface. It is possible to calculate the mass amount of the total organic material normalized over 1 gram of NCs (W_N) using eq.9.

$$W_N = \frac{W_{total\ loss}\%}{(100 - W_{total\ loss}\%)\cdot} \cdot \qquad (9)$$

It is then defined the amount of mPEO_5K (m_{mPEO_5K}) and the OLAC (m_{OLAC}) per gram of anatase NC using eq.10 and 11

$$m_{mPEO\_5K} = Wn \cdot W_{mPEO\_5K} \quad (10)$$

$$m_{OLAC} = Wn \cdot W_{OLAC} \quad (11)$$

Where W_{mPEO_5K} is the weight loss percentage of mPEO and W_{OLAC} of OLAC normalized over the total amount of organic content. From the mass value is it possible to calculate the molar fraction (*f*) of mPEO chains and OLAC molecules attached per g of NCs using eq. 12 and 13.

$$f_{mPEO\_5K} = \frac{m_{mPEO\_5K}}{M\bar{w}_{mPEO\_5K}} \cdot \quad (12)$$

$$f_{OLAC} = \frac{m_{OLAC}}{M\bar{w}_{OLAC}} \cdot \quad (13)$$

Where $M\bar{w}$ is the molecular weight of the mPEO or OLAC, Knowing the molar fraction of the chemical species, it is possible to define the graft density of each chemical species using eq.14

$$\sigma = \frac{f}{SSA_{BET}} \cdot N_A \quad (14)$$

where SSA_{BET} is the specific surface area of the anatase NCs and Na is the Avogadro number. All the results are listed in Table 13.

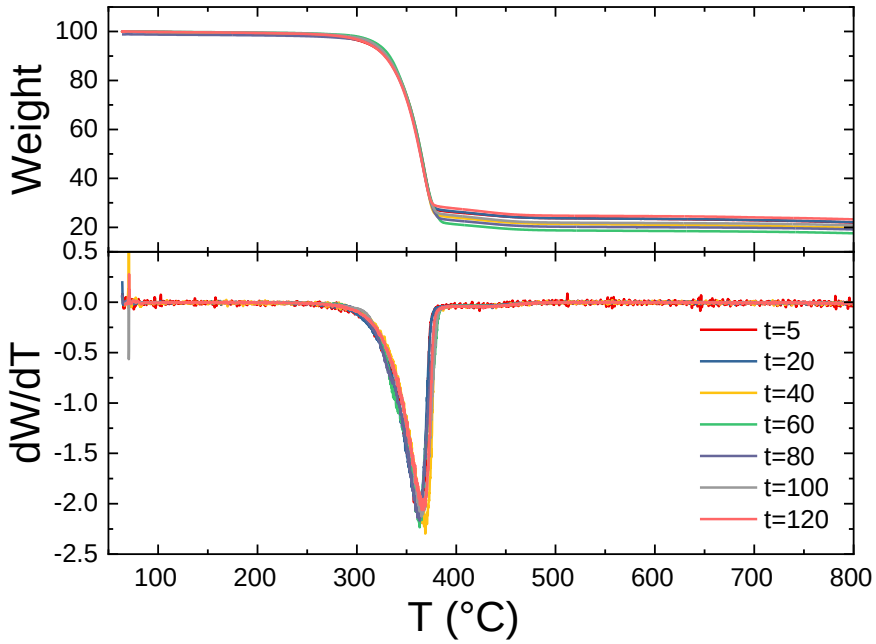

Figure 63 TGA curve (up) and first derivative (bottom) of the samples produced during the kinetic study. Each sample is withdrawn at a certain time after starting reaction.

Table 13 Experimental data of the molar fraction calculated from the TGA analysis. fmPEO_5K molar fraction of the polymer, fOLAC molar fraction of the oleic acid, σmPEO_5K extrapolated graft density of mPEO_5K and σOLAC extrapolated graft density of oleic acid. The reaction was carried starting with mPEO_5K:OLAC = 0.25:1 molar ratio.

Sample	$W_{total\ loss}$ %	f_{mPEO_5K} %	f_{OLAC} %	σ_{mPEO_5K} ch nm^{-2}	σ_{OLAC} ch nm^{-2}
t=5	77.59	0.17	0.83	0.69 0.04	3.26 0.04
t=20	77.55	0.18	0.82	0.70 0.04	3.24 0.04
t=40	79.76	0.19	0.81	0.84 0.04	3.65 0.04
t=60	82.17	0.20	0.80	1.03 0.05	4.22 0.04
t=80	79.46	0.21	0.79	0.92 0.04	3.49 0.04
t=100	78.94	0.23	0.77	0.97 0.04	3.31 0.04
t=120	76.39	0.23	0.77	0.86 0.04	2.83 0.04

On the other hand it is possible to calculate the mPEO_5K-OLAC:OLAC molar ratio through ^{1}H NMR. In Figure 64 is reported an example of a ^{1}H NMR spectrum of a double layer grafted NC. The triplet at 0.88 ppm is attributed to the -CH3 end group of OLAC and the complex signals that lie in the 1.5 – 1.20 ppm region is generated by the protons of the aliphatic chains that do not belong to the two double bonded carbons. At 3.37 ppm is found the triplet attributed to the -CH3 end group of mPEO while the region between 3.9 – 3.4 ppm belongs to the 454 protons of the mPEO chain.

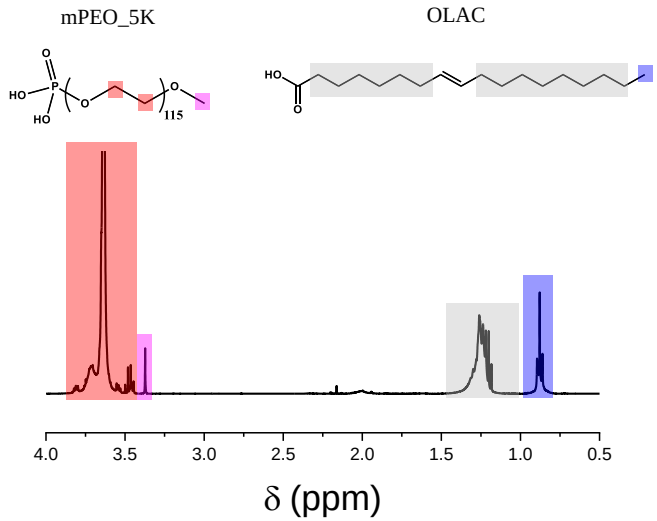

Figure 64 ^{1}H NMR of mPEO_5K-OLAC@Anatase in $CDCl_3$ the mPEO phosphate molecule and the OLAC structure are represented. The spectrum descripition is found within the text.

The molar fraction (*f*) of mPEO_5K OLAC is calculated as follows. The integral of the mPEO protons is used as an internal reference. It is assigned a value of 457, that corresponds to the number of protons of a single mPEO chain. The integral of the OLAC protons in the region between 1.5 and 0.7 ppm divided by the 31 protons of a single OLAC molecule defines the

number of OLAC molecules for each mPEO chain. This number provides the molar ratio between the two population of tethered molecules on anatase surface. The total moles of molecules grafted on the surface are assumed to be equal to the moles of OLAC after the NCs synthesis. This systematic approach was applied for the kinetic study and the data are listed in Table 14 and reported in Figure 65.

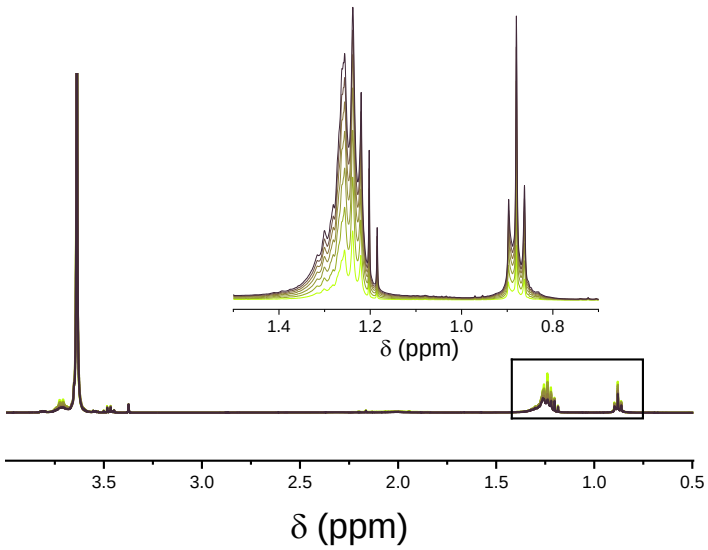

Figure 65 ^{1}HNMR of the mpPEO_5K-OLAC@Anatase at different reaction time. As the time increases the integral of the OLAC (inset graph) decreases. . The reaction was carried starting with mPEO_5K:OLAC = 0.25:1 molar ratio.

Table 14 Experimental data

Sample	f_{mPEO_5K}	f_{OLAC}	σ_{mPEO_5K} **ch nm^{-2}**	σ_{OLAC} **ch nm^{-2}**
t=5	0.16	0.84	0.74 0.04	3.48 0.04
t=20	0.18	0.82	0.75 0.04	3.47 0.04
t=40	0.19	0.81	0.79 0.04	3.43 0.04
t=60	0.20	0.80	0.83 0.05	3.39 0.04
t=80	0.22	0.78	0.88 0.04	3.34 0.04
t=100	0.23	0.77	0.95 0.04	3.26 0.04
t=120	0.24	0.76	0.98 0.04	3.24 0.04

It is shown that the modified mPEO almost completely reacts after 120 min. Moreover, the data obtained by TGA and NMR analysis are consistent and describes with a certain the composition of the as prepared grafted nanocrystals.

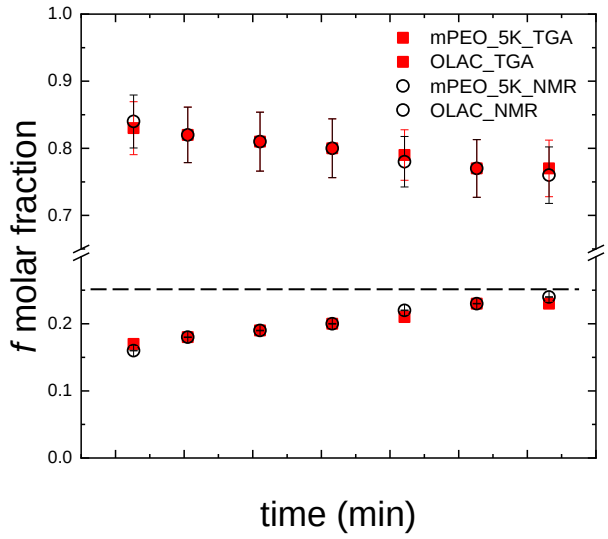

Figure 66 molar fraction (f) vs time plot. Data calculated from TGA analysis is reported with the red squares; molar fractions calculated from NMR analysis are represented by hollow black circles. Dashed line represents the maximum molar fraction that yhe polymer can reach.

TPU based nanocomposite material synthesis and characterization

To test the dispersibility of the mixed double layer NCs (f_{mPEO_5K} : f_{OLAC} = 1:4), a series of TPU based nanocomposite films have been prepared with a solvent casting technique and compared with a set of samples prepared with OLAC@Anatase NCs (Figure 67). All the films appear transparent and slightly colored as the inorganic loading increases. This phenomenon is independent respect to the ligand chemistry, it is related to the size of the filler that produce a Rayleigh scattering effect on the bulk material. The fact

that even the OLAC@Anatase are well dispersed is due to the highly aliphatic content of the TPU used. Not only the graft density and the NCs ligand architecture affect the dispersibility, it must be considered the chemical affinity between the organic matrix and the NCs ligand.

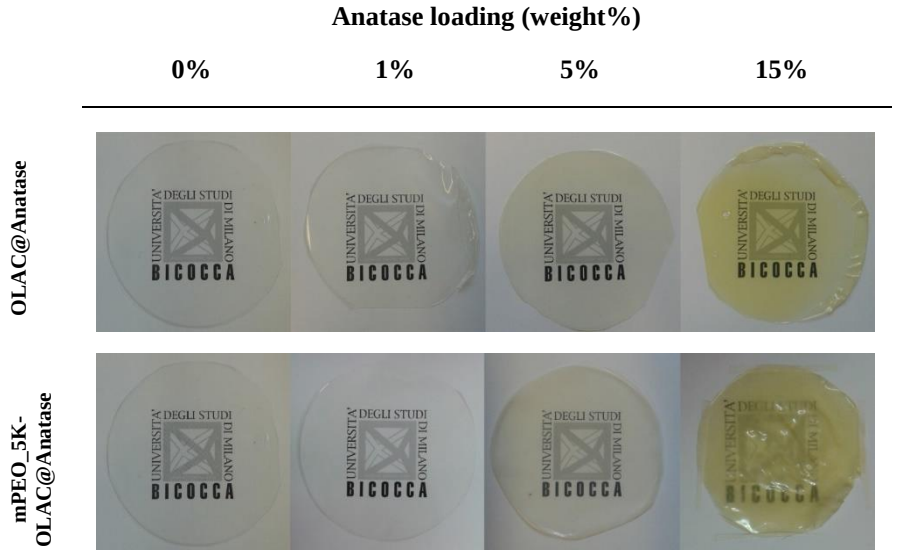

Figure 67 picture of the TPU based nanocomposite material

The films have been synthesized with different loadings of anatase NCs and characterized with TGA to check the correct composition of all the samples. In Figure 68 are reported the thermogravimetric curve of the mPEO_5K-OLAC@Antase. The first derivative of the TGA of the neat TPU presents two main peaks related to the polymer decomposition as the titanium dioxide loading increase. It is noted a decrease of the intensity of TPUs peaks, as the inorganic loading increases, and appear the decomposition peak of the mPEO.

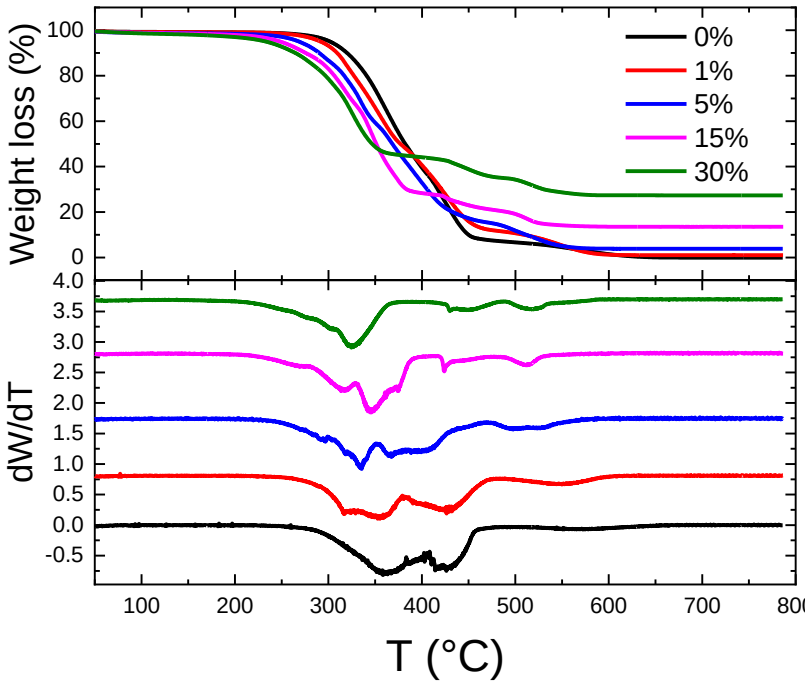

Figure 68 TGA analysis of the mPEO_5K-OLAC@Anatase with increased anatase loading. Upper graph refers to the thermogravimetric curve, lower graph refers to the first derivative of weight loss function of temperature.

Mechanical tests

A series of tensile tests were done to better understand the mechanical behavior of this kind of systems. Neat TPU is used as reference, the films loaded with 50% of titanium dioxide will not be discussed in this section due to impossibility to test them. The results are compared between films prepared from NCs functionalized with a mixed double layer and NCs covered with a single layer of OLAC. Once the films have been annealed and peeled from the glass substrate, they have been cut in 9 slices and characterized. Elastic modulus (*E*) and elongation at break have been determined as averages of nine independent drawing performed at the same

conditions following the ASTM D882 standard. The stress- strain curves are depicted in Figure 69 and the results are listed in Table 15.

Table 15 Tensile test results. The data are averaged from a set of 9 experiments, all the results are reported with their standard deviation. The elastic modulus represents the slope of the linear region. The deformation at break is the ratio between the length of the sample before and during the measure.

	mPEO_5K-OLAC@Anatase				OLAC@Anatase			
TiO_2 weight	**Elastic modulus**		**Deformation at break**		**Elastic modulus**		**Deformation at break**	
%	**MPa**		**%**		**MPa**		**%**	
0	12.4	0.4	412.4	30.4	12.4	0.3	412.4	30.4
1	10.9	0.8	355.8	24	13.3	0.5	339.2	57.7
5	22.7	0.7	262.2	13	16.3	0.7	349.1	48.2
10	31	4	286	18.2				
15	39.8	5.62	290.2	33.4	30.1	1.5	372	76.1
25					76.7	5.7	323.5	51.1
30					152.3	15.6	20	4.1
37.5					223	29.1	18.8	5.6

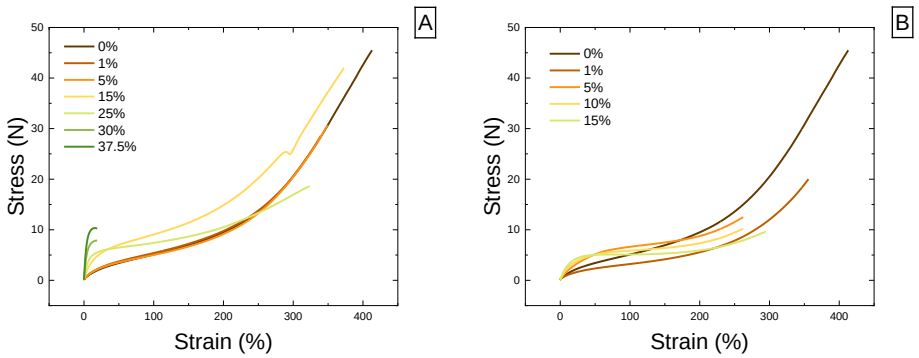

Figure 69 Stress- Strain graphs of the OLAC@Anatase (A, left) and mPEO_5K-OLAC@Anatase (B, right).

Elastic modulus and the deformation at break are plotted as function of the anatase loading (Figure 70). It is observed a general reinforcement of the nanocomposite films respect to the neat one, in terms of elastic modulus. At equal anatase loading, the presence of a double layer with a polymer increases the elastic modulus more than a single layer. As expected, for both

the samples, the elongation at break decreases as the inorganic loading increases. In the case of the mixed double layer nanocomposite the elongation at break is lower than in the single layer samples. This phenomenon is the effect of the presence of a rigid object inside the polymer matrix, that leads to poorer elastic behavior. Moreover, the polymer grafted on the NCs is able to make a higher number of entanglements with the TPU polymer matrix resulting in a reinforced and fragile material.

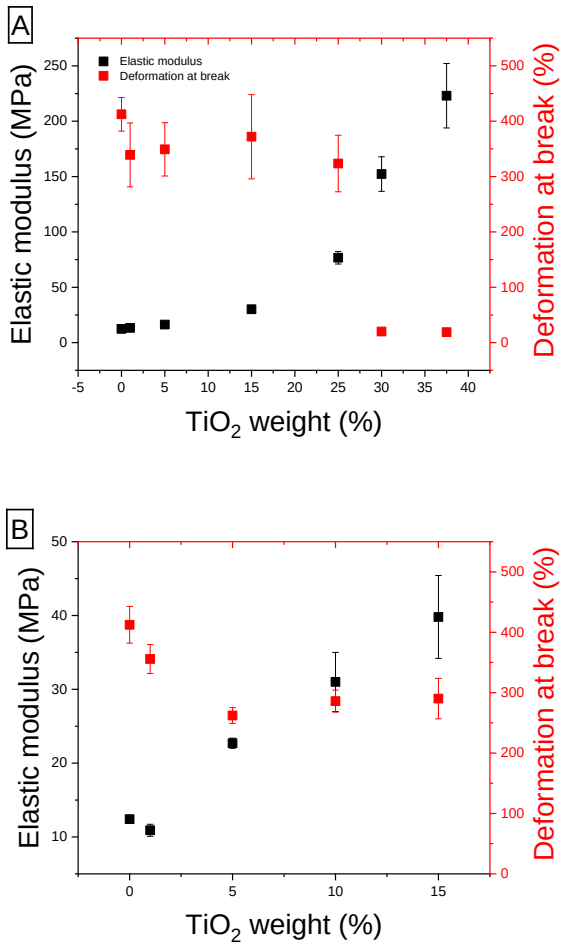

Figure 70 Elastic modulus (black squares) and Deformation at break (red square) as function of the anatase wt% loading. A) results of samples with OLAC@Anatase; B) samples with mPEO_5K-OLAC@Anatase.

Optical properties analysis

The total refractive index of multicomponent material is proportional to the volume fraction of the different components. It is difficult to reach high volume fraction of fillers since higher weight loadings are needed because inorganic systems are generally denser than the polymer matrix. The challenge is to produce a bulk material that is highly loaded with titanium dioxide that maintains its transparency and clearness in all visible spectrum. The transparency is achieved avoiding any aggregation of the inorganic filler, that is possible with a fine tuning of the surface chemistry (Figure 67). In order to calculate the refractive index of our self-standing TPU based nanocomposite material, was used a prism coupling refractometer working at 633 nm. Measurements were performed in different points, five, of the same sample to check the homogeneity In Table 16 and Table 17 are reported the refractive index measured as function of the volume fraction of titanium dioxide for both the samples. The refractive index is theoretically described by eq.15

$$\sum_{i=1}^{n} n_i \cdot \Phi_i \qquad (15)$$

Where n_i represents the refractive index of the i^{th} component and Φ_i represents the volume fraction of the i^{th} component.

Table 16 Refractive index results of the OLAC@Anatase samples. $\Phi_{Anatase}$, Φ_{OLAC} and Φ_{TPU} represents the volume fraction. n represents the refractive index, are reported the theoretical values calculated with eq.15 and the experimental values with their std. dev.

$W_{Anatase}$ %	$\Phi_{Anatase}$ %	Φ_{OLAC} %	Φ_{TPU} %	$n_{theoretical}$	$n_{experimental}$	std dev.
0	0.0	0.0	100.0	1.4962	1.4980	0.0002
1	0.3	0.6	99.1	1.4988	1.5012	0.0002
5	1.4	1.9	96.7	1.5102	1.5087	0.0001
15	4.6	6.7	88.7	1.5409	1.5295	0.0001
25	8.3	12.3	79.5	1.5763	1.5684	0.0006
30	10.9	15.9	73.2	1.6016	1.5906	0.0012
37.5	13.8	20.0	66.3	1.6296	1.6114	0.0002
50	20.6	29.7	49.7	1.6964	1.6533	0.0018

Table 17 Refractive index results of the mPEO_5K-OLAC@Anatase samples. $\Phi_{Anatase}$, Φ_{mPEO_5K}, Φ_{OLAC} and Φ_{TPU} represents the volume fraction. n represents the refractive index, are reported the theoretical values calculated with eq.15 and the experimental values with their std. dev.

$W_{Anatase}$ %	$\Phi_{Anatase}$ %	Φ_{mPEO_5K} %	Φ_{OLAC} %	Φ_{TPU} %	$n_{theoretical}$	$n_{experimental}$	std dev.
0	0	0	0	100	1.4962	1.4980	0.0002
1	0.3	2.5	0.4	96.9	1.4980	1.4979	0.0002
5	1.4	14.0	1.9	82.7	1.5057	1.5082	0.0005
10	1.8	17.6	2.4	78.2	1.5137	1.5126	0.0003
15	4.6	32.1	4.3	59.0	1.5329	1.5300	0.0010

It is noted that the refractive index of the nanocomposite materials is proportionally increasing, from 1.49 to 1.65, as the titanium dioxide volume fraction increases. In Figure 71 is reported the refractive index dependence from the volume fraction of the anatase NCs. The linear dependence of the refractive index in composite materials with filler loading has been reported both from experimental measurements and theoretical calculation. The extrapolated refractive index of the anatase nanocrystals from linear approximation to 100% TiO_2 content was 2.35, which is close to the

reported index of 2.45 for anatase phase TiO_2 nanoparticles at 633 nm wavelength.

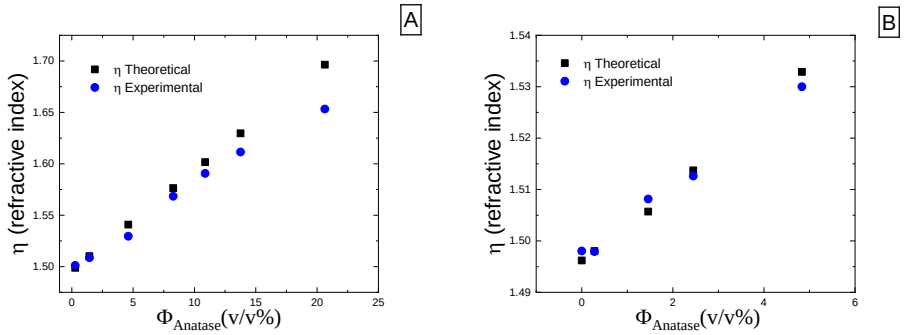

Figure 71 n theoretical (black squares) and experimental (blue circles) as function of anatase volume fraction (Φ). A) results of the OLAC@Anatase in TPU matrix; results of the mPEO_5K-OLAC@Anatase in TPU matrix.

The linear dependence of refractive index was predicted for homogeneously dispersed nanofillers within a matrix. The good linear fitting of the refractive index of TiO_2 nanocomposites, indicates the excellent dispersion of particles is achieved. It is worth mentioning that reaching high transparency only through refractive index matching is very challenging and controlling the dispersion of nanoparticles within the polymer matrix is even more critical[38]. Even with a small refractive index mismatch the transparency degrade rapidly with increased solid loading. Despite the large mismatch of refractive index ($\Delta n \approx 1$) between the titania nanocrystals and the organic polymer, transparent nanocomposites were prepared. The fact that even with singly OLAC layer are produced transparent films is the evidence of the excellent chemical affinity between the highly aliphatic TPU and the as prepared NCs.

Conclusions

In this contribution we prepared a highly loaded TPU based nanocomposite material with a facile and scalable process. The NCs synthesis produce low dimensional anatase NCs capped with OLAC that have been subsequently exchanged with mPEO. The functionalization process was extremely controlled and good control over the mixed double layer composition was achieved. Finally, it was prepared transparent TiO_2 nanocomposites with high refractive index and with improved mechanical properties. The refractive index of the composites increased by 10.4% with 50 wt% loading of TiO_2 fillers, while the film transparency was maintained. The mixed double layer and single layer effectively screen TiO_2 nanoparticles from forming agglomerates with high content of inorganic particles, minimizing transparency loss due to scattering. The grafted particles showed good compatibility with polyurethane thermoplastic and enabled transparent high refractive index TiO_2-TPU nanocomposites. Moreover, the elastic modulus of the as prepared materials increases up to 223 MPa for the sample loaded with 37.5% wt% anatase, respect the 12.4 MPa of neat TPU film. Functionalizing polymer chains onto the surface of high refractive index inorganic nanoparticles is a simple and effective way to achieve excellent dispersion of nanoparticles, even at high loading levels, and to fabricate transparent, high refractive index polymer nanocomposites with improved mechanical properties.

References

(1) Khare, H. S.; Burris, D. L. A Quantitative Method for Measuring Nanocomposite Dispersion. *Polymer (Guildf).* **2010**, *51* (3), 719–729.

(2) Schaefer, D. W.; Justice, R. S. How Nano Are Nanocomposites?

Macromolecules **2007**, *40* (24), 8501–8517.

(3) Li, Y.; Huang, Y.; Krentz, T.; Natarajan, B.; Neely, T.; Schadler, L. S. Polymer Nanocomposite Interfaces: The Hidden Lever for Optimizing Performance in Spherical Nanofilled Polymers. *Interface/Interphase Polym. Nanocomposites* **2016**, 1–69.

(4) Lenart, W. R.; Hore, M. J. A. Structure-Property Relationships of Polymer-Grafted Nanospheres for Designing Advanced Nanocomposites. *Nano-Structures and Nano-Objects* **2017**.

(5) Srivastava, S.; Schaefer, J. L.; Yang, Z.; Tu, Z.; Archer, L. A. 25th Anniversary Article: Polymer-Particle Composites: Phase Stability and Applications in Electrochemical Energy Storage. *Adv. Mater.* **2014**, *26* (2), 201–234.

(6) Ligoure, C.; Leibler, L. Thermodynamics and Kinetics of Grafting End-Functionalized Polymers to an Interface. *J. Phys.* **1990**, *51* (12), 1313–1328.

(7) Asai, M.; Zhao, D.; Kumar, S. K. Role of Grafting Mechanism on the Polymer Coverage and Self-Assembly of Hairy Nanoparticles. *ACS Nano* **2017**, *11* (7), 7028–7035.

(8) Kumar, S. K.; Jouault, N.; Benicewicz, B.; Neely, T. Nanocomposites with Polymer Grafted Nanoparticles. *Macromolecules* **2013**, *46* (9), 3199–3214.

(9) Borukhov, I.; Leibler, L. Enthalpic Stabilization of Brush-Coated Particles in a Polymer Melt. *Macromolecules* **2002**, *35* (13), 5171–5182.

(10) Ferreira, P. G.; Ajdari, A.; Leibler, L. Scaling Law for Entropic Effects at Interfaces between Grafted Layers and Polymer Melts. *Macromolecules* **1998**, *31* (12), 3994–4003.

(11) Trombly, D. M.; Ganesan, V. Curvature Effects upon Interactions of Polymer-Grafted Nanoparticles in Chemically Identical Polymer Matrices. *J. Chem. Phys.* **2010**, *133* (15), 154904.

(12) Wijmans, C. M.; Zhulina, E. B. Polymer Brushes at Curved Surfaces. *Macromolecules* **1993**, *26* (26), 7214–7224.

(13) Wijmans, C. M.; Scheutjens, J. M. H. M.; Zhulina, E. B. Self-Consistent Field Theories for Polymer Brushes. Lattice Calculations and an

Asymptotic Analytical Description. *Macromolecules* **1992**, *25* (10), 2657–2665.

(14) Dan, N.; Tirrell, M. Polymers Tethered to Curved Interfaces. A Self-Consistent-Field Analysis. *Macromolecules* **1992**, *25* (11), 2890–2895.

(15) Dukes, D.; Li, Y.; Lewis, S.; Benicewicz, B.; Schadler, L.; Kumar, S. K. Conformational Transitions of Spherical Polymer Brushes: Synthesis, Characterization, and Theory. *Macromolecules* **2010**, *43* (3), 1564–1570.

(16) Ferreira, P. G.; Ajdari, A.; Leibler, L. Scaling Law for Entropic Effects at Interfaces between Grafted Layers and Polymer Melts. *Macromolecules* **1998**, *31* (12), 3994–4003.

(17) Li, Y.; Tao, P.; Viswanath, A.; Benicewicz, B. C.; Schadler, L. S. Bimodal Surface Ligand Engineering: The Key to Tunable Nanocomposites. *Langmuir* **2013**, *29* (4), 1211–1220.

(18) Meinardi, F.; Colombo, A.; Velizhanin, K. A.; Simonutti, R.; Lorenzon, M.; Beverina, L.; Viswanatha, R.; Klimov, V. I.; Brovelli, S. Large-Area Luminescent Solar Concentrators Based on Stokes-Shift-Engineered Nanocrystals in a Mass-Polymerized PMMA Matrix. *Nat. Photonics* **2014**, *8* (5), 392–399.

(19) Fujita, M.; Idota, N.; Matsukawa, K.; Sugahara, Y. Preparation of Oleyl Phosphate-Modified TiO 2 / Poly (Methyl Methacrylate) Hybrid Thin Films for Investigation of Their Optical Properties. *J. ofNanomaterials* **2015**, *2015*, 1–7.

(20) Colombo, A.; Tassone, F.; Mauri, M.; Salerno, D.; Delaney, J. K.; Palmer, M. R.; Rie, R. D. La; Simonutti, R. Highly Transparent Nanocomposite Films from Water-Based Poly(2-Ethyl-2-Oxazoline)/TiO2 Dispersions. *RSC Adv.* **2012**, *2* (16), 6628.

(21) Nussbaumer, R. J.; Caseri, W. R.; Smith, P.; Tervoort, T. Polymer-TiO2 Nanocomposites: A Route towards Visually Transparent Broadband UV Filters and High Refractive Index Materials. *Macromol. Mater. Eng.* **2003**, *288* (1), 44–49.

(22) Tao, P.; Viswanath, A.; Li, Y.; Siegel, R. W.; Benicewicz, B. C.; Schadler,

L. S. Bulk Transparent Epoxy Nanocomposites Filled with Poly(Glycidyl Methacrylate) Brush-Grafted TiO2 Nanoparticles. *Polym. (United Kingdom)* **2013**, *54* (6), 1639–1646.

(23) Tao, P.; Li, Y.; Rungta, A.; Viswanath, A.; Gao, J.; Benicewicz, B. C.; Siegel, R. W.; Schadler, L. S. TiO2 Nanocomposites with High Refractive Index and Transparency. *J. Mater. Chem.* **2011**, *21* (46), 18623.

(24) Mont, F. W.; Kim, J. K.; Schubert, M. F.; Schubert, E. F.; Siegel, R. W. High-Refractive-Index TiO2-Nanoparticle-Loaded Encapsulants for Light-Emitting Diodes. *J. Appl. Phys.* **2008**, *103* (8), 083120.

(25) Nakayama, N.; Hayashi, T. Preparation and Characterization of TiO2 and Polymer Nanocomposite Films with High Refractive Index. *J. Appl. Polym. Sci.* **2007**, *105* (6), 3662–3672.

(26) Ireni, N. G.; Karuppaiah, M.; Narayan, R.; Raju, K. V. S. N.; Basak, P. TiO2/Poly(Thiourethane-Urethane)-Urea Nanocomposites: Anticorrosion Materials with NIR-Reflectivity and High Refractive Index. *Polym. (United Kingdom)* **2017**, *119*, 142–151.

(27) Engels, H. W.; Pirkl, H. G.; Albers, R.; Albach, R. W.; Krause, J.; Hoffmann, A.; Casselmann, H.; Dormish, J. Polyurethanes: Versatile Materials and Sustainable Problem Solvers for Today's Challenges. *Angew. Chemie - Int. Ed.* **2013**, *52* (36), 9422–9441.

(28) Akindoyo, J. O.; Beg, M. D. H.; Ghazali, S.; Islam, M. R.; Jeyaratnam, N.; Yuvaraj, A. R. Polyurethane Types, Synthesis and Applications-a Review. *RSC Adv.* **2016**, *6* (115), 114453–114482.

(29) Buonsanti, R.; Grillo, V.; Carlino, E.; Giannini, C.; Kipp, T.; Cingolani, R.; Cozzoli, P. D. Nonhydrolytic Synthesis of High-Quality Anisotropically Shaped Brookite TiO2 Nanocrystals. *J. Am. Chem. Soc.* **2008**, *130* (33), 11223–11233.

(30) Zalipsky, S. Functionalized Poly(Ethylene Glycols) for Preparation of Biologically Relevant Conjugates. *Bioconjug. Chem.* **1995**, *6* (2), 150–165.

(31) Dollimore, D.; Spooner, P.; Turner, A. The Bet Method of Analysis of Gas Adsorption Data and Its Relevance to the Calculation of Surface Areas.

Surf. Technol. **1976**, *4* (2), 121–160.

(32) Zhang, L.; He, R.; Gu, H. C. Oleic Acid Coating on the Monodisperse Magnetite Nanoparticles. *Appl. Surf. Sci.* **2006**, *253* (5), 2611–2617.

(33) Akindoyo, J. O.; Beg, M. D. H.; Ghazali, S.; Islam, M. R.; Jeyaratnam, N.; Yuvaraj, A. R. Polyurethane Types, Synthesis and Applications-a Review. *RSC Adv.* **2016**, *6* (115), 114453–114482.

(34) Serrano-Cinca, C.; Fuertes-Callén, Y.; Mar-Molinero, C. Measuring DEA Efficiency in Internet Companies. In *Decision Support Systems*; John Wiley & Sons, Inc: Hoboken, NJ, 2005; Vol. 38, pp 557–573.

(35) Rungta, A.; Natarajan, B.; Neely, T.; Dukes, D.; Schadler, L. S.; Benicewicz, B. C. Grafting Bimodal Polymer Brushes on Nanoparticles Using Controlled Radical Polymerization. *Macromolecules* **2012**, *45* (23), 9303–9311.

(36) Tao, P.; Viswanath, A.; Schadler, L. S.; Benicewicz, B. C.; Siegel, R. W. Preparation and Optical Properties of Indium Tin Oxide/Epoxy Nanocomposites with Polyglycidyl Methacrylate Grafted Nanoparticles. *ACS Appl. Mater. Interfaces* **2011**, *3* (9), 3638–3645.

(37) Akeroyd, N.; Klumperman, B. The Combination of Living Radical Polymerization and Click Chemistry for the Synthesis of Advanced Macromolecular Architectures. *Eur. Polym. J.* **2011**, *47* (6), 1207–1231.

(38) Li, Y.-Q.; Fu, S.-Y.; Yang, Y.; Mai, Y.-W. Facile Synthesis of Highly Transparent Polymer Nanocomposites by Introduction of Core–Shell Structured Nanoparticles. *Chem. Mater.* **2008**, *20* (8), 2637–2643.

Chapter 6. Polymer grafted nanoparticles for gas separation applications

Introduction

New materials in gas separation industrial field are widely used and highly demanded due to their environmental impact and low costs. The separation of different chemical species is usually achieved through thermodynamic means, such as adsorption or distillation processes, which are cost and energy-intensive. In this context membranes are widely employed as gas separator materials and occupy a large market share of gas supply[1]. The membrane gas separation is an old acquaintance in industry and it is growing at a significant rate. Development of higher selectivity and higher permeance membranes would result in faster growth of technologies involved and immediate employment in industry. Membrane separations are cost efficient relative to the current technologies and are characterized by an intrinsic trade-off between high flux and high product purity. A successful example of industrial membrane gas separation system was built by Monsanto in 1979−1980. The systems separated hydrogen from the nitrogen, argon, and methane in the purge gas of an ammonia synthesis plant. Since then, gas separation membranes have found applications in a variety of processes, most importantly nitrogen separation from air, CO_2 from natural gas, and hydrogen from various refinery and petrochemical process streams. In literature are found many reviews and papers reporting the synthesis and evaluation of thousands of new materials[1–4], but more than 90% of current commercial membranes are made from fewer than 10

membrane materials, most of which have been in use for decades. The efforts made to meet the industrial demands are intensive. Different factors must be considered before a new material can be introduced in the gas separation market. One of these is that pure-gas measurements are poor predictors of the performance of industrial membranes. Sometimes permeation properties of thin membranes are very different from thick films. Chemical stability is sometimes an issue, but physical stability is the more common problem. Different approaches were employed to produce more efficient materials. For example, the use of polymers of intrinsic microporosity (PIMs)[5] and thermally rearranged polymers (TR) [6] characterized by an extremely fine nanoporous structure. Another interesting class of materials are the so-called mixed matrix materials (MMM), these are essentially membranes that seek to combine the processability of polymers with the separation properties of molecular sieves and inorganic crystals[4,7,8]. The issue of MMM is the compatibilization of the filler and the polymer matrix that enables the full expression of the final material. It is well-known that MMM systems of nanoparticle (NP) filler dispersed in polymer can substantially increase the mechanical properties of the host polymer and limit chain mobility, reducing physical aging. Both aspects are relevant factors to boost the employment of membranes in industry. R. Bilchak et al.[9] reported a fabrication method that produces nanocomposite materials with well-controlled free volume. This result is surprising as conventional composite theory (e.g., adapted Maxwell model[10–12]) predicts that the permeability decreases with increasing filler volume fraction. The filler acts as a physical barrier, lowering the available free-volume and extending the gas path. It is demonstrated that a membrane composed by polymer grafted nanoparticles are driven to locally self-assemble against the polymer chains that have to

distort to fill the interstices. This competition creates spatial regions of somewhat lower density over a range of polymer graft densities and chain lengths and thus represents a new method for the precise control of the membrane's free volume and hence its transport properties (Figure 72). This is achieved if the polymer chain length and the graft density are extremely controlled. This is possible using controlled polymerization's techniques that allow production of polymers with well-defined chain length, thanks to that, the control over special reorganization of nanoparticles is achieved. This is not possible with wide and scattered molecular weight distribution.

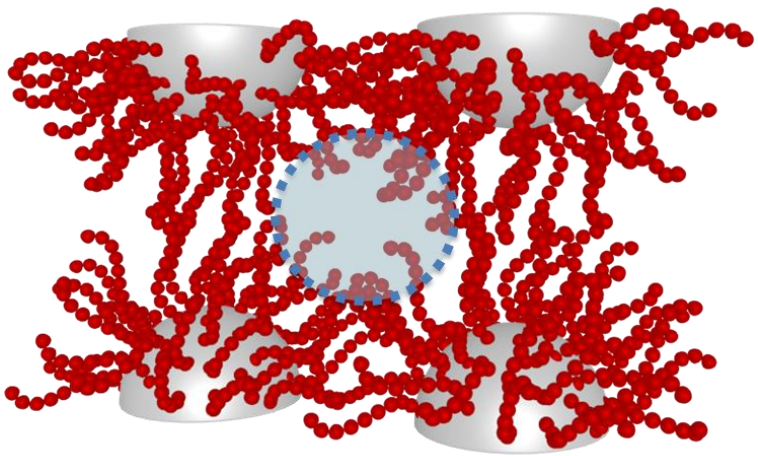

Figure 72 graphic representation of the competition between the rearrangement of the NPs and the polymer chains distortion that creates spatial regions of somewhat lower density over a range of polymer graft densities.

The sum of this properties improves gas permeation properties of polymer membranes. In this promising context it is fitted our contribution. The first part of the chapter will be focused on the *proof of concept* of polymer-grafted nanoparticle membranes with controllable free volume. The second part will exploit this technique to create a new nanocomposite material with both improved permeability and selectivity to CO_2 gas. In order to get a

precise control over free volume it was necessary to use a controlled radical polymerization technique. In our contribution it was applied the *grafting-from* approach using the previously described *Reversible Addition-Fragmentation chain Transfer* (RAFT) polymerization technique.

Fundamentals of membrane gas transport

For a given pair of gases (e.g., O_2/N_2, CO_2/CH_4, H_2/N_2, etc.), the fundamental parameters characterizing membrane separation performance are the permeability coefficient, P_i, and the selectivity, α_{ij}. The permeability coefficient is the product of gas flux and membrane thickness divided by the pressure difference across the membrane. Gas selectivity is the ratio of permeability coefficients of two gases ($\alpha_{ij} = P_i/P_j$), where P_i is the permeability of the more permeable gas and P_j is the permeability of the less permeable gas in the binary pair. Polymers with both high permeability and selectivity are desirable. A rather general tradeoff relation has been recognized between permeability and selectivity: polymers that are more permeable are generally less selective and vice versa[1,3]. On the basis of an extended literature survey[13,14], Robeson quantified this notion by graphing the available data. Robeson plots have been created for other gas pairs of interest. The upper bound lines taken from some of these plots are shown in Figure 73. These upper bound lines are useful in showing the separation performances that can be expected for currently best membrane materials in ideal conditions, and it represents the state of the art of gas separation membrane.

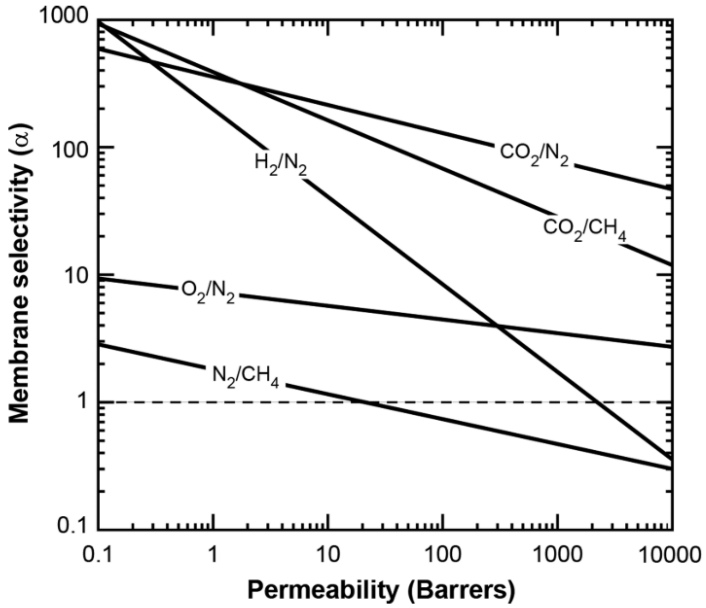

Figure 73 Robeson upper bound plot of a series of gas pairs. Lines are useful in showing the separation performances that can be expected for currently membrane materials in ideal conditions

Materials with the best performance would be in the upper right-hand corner of the graph. Materials with permeability/selectivity combinations above and to the right of the line drawn in this figure are exceptionally rare. These lines were constructed on an empirical basis for many gas pairs using published permeability and selectivity data. The upper bound performance characteristics were best described by eq.1

$$\alpha_{ij} = \beta_{ij}/P_i^{\lambda_{ij}} \qquad (1)$$

which indicates that as the permeability of an upper bound polymer to gas *i*, P_i, increases, selectivity of the polymer for gas *i* over gas *j*, α_{ij}, decreases. Robeson reports values for λ_{ij} and β_{ij} for many common gas pairs[13,14]. The reason for this tradeoff has been widely discussed and the physical

definition of λ_{ij} and β_{ij} have been widely debated. Robeson noted an excellent empirical correlation between λ_{ij} and the difference between the kinetic diameters of the penetrant molecules (d_j-d_i). Two main theories were proposed, both of them reached the same conclusion with two different approaches: solution diffusion model and free volume theory.

Solution-diffusion model

The solution-diffusion model describes successfully gas, vapor, liquid, and ion transport in dense membranes[15]. A basic assumption of this model is that no permanent pores exist in the membrane selective layer, so different chemical species are separated based on their different solubility and diffusivity through the membrane material. Based on this picture, gas molecules dissolve in the high-pressure face of the membrane, diffuse through the membrane down a chemical potential (or concentration) gradient, and finally desorb from the low-pressure face of the membrane. The other assumption of this model is that equilibrium conditions hold between the fluid and the membrane material on both sides of the membrane. A partition coefficient, S_i, (eq.2) also called sorption coefficient, is introduced to relate penetrant concentration in the membrane with the external penetrant partial pressure[4,15]:

$$S_i = \frac{c_{i,0}}{p_{i,0}} = \frac{c_{i,1}}{p_{i,1}} \qquad (2)$$

where $p_{i,0}$ is the penetrant partial pressure at the feed side and $p_{i,l}$ is the corresponding value at the permeate side. The terms $C_{i,0}$ and $C_{i,l}$ represent the penetrant concentration at the feed and permeate face of the membrane, respectively. The permeability of a penetrant, P_i, through the membrane is defined by eq.3

$$P_i = \frac{J_i l}{p_{i,0} - p_{i,1}} \quad (3)$$

where *l* is the membrane thickness. When penetrant diffusion is described by the Fick's law, the following expression holds (eq.4), at steady state, for the penetrant flux, J_i:

$$J_i = D_i S_i \frac{p_{i,0} - p_{i,1}}{l} \quad (4)$$

where Di is the penetrant diffusion coefficient through the membrane material. By comparing eqs 3 and 4, the penetrant permeability can be expressed as the product of penetrant diffusion and solubility coefficient (eq.5)

$$P_{i=} D_i S_i \quad (5)$$

Permeability is an intrinsic material property corresponding to a thickness and pressure normalized permeant flux. Permeability is often expressed in units of barrer, where 1 barrer = 1×10^{-10} cm^3 (STP) cm/(cm^2 s cmHg). The selectivity of a membrane is determined by α_{ij} ,defined as the ratio ofthe gas permeabilities, P_i/P_j. Selectivity can be expressed as (eq.6)

$$\alpha_{ij} = \frac{D_i}{D_j} \frac{S_i}{S_j} \quad (6)$$

The ratio D_i/D_j (related to λ_{ij}) is the ratio of the diffusion coefficients of the two gases and can be viewed as the mobility selectivity, which indicates the relative motion of individual molecules of the two components i and j. The mobility selectivity is proportional to the ratio of the molecular size of the two permeants. The ratio S_i/S_j (related to β_{ij}) is the ratio of the sorption coefficients, which indicates the relative concentration of the components i and j in the membrane material. The sorption of a component increases with

condensability of the component; therefore, the sorption selectivity is proportional to the relative condensability of components i and j. Generally, in conventional glassy polymers, the dominant contribution to selectivity is the ratio of the diffusion coefficients, D_i/D_j, while in rubbery polymers, the dominant contribution is from the ratio of the sorption coefficients, S_i/S_j, The selectivity is an important parameter of a membrane because impacts the energy required to perform a given separation and thus is related to the operating cost of the system.

Free-volume theory

This approach is based on the concept on the volume of the polymer that is not occupied by polymer chains and can therefore be occupied by the diffusing molecules. This volume is defined as free-volume. It is described as a statistical "free volume", the unoccupied volume in a liquid subject to fluctuations in space and time[17]. This kind of free volume is different from static microporosity/nanoporosity, that is described as static voids in the material with well-defined, temporally stable geometric characteristics. The difference between these two quantities comes from the fact that free volume in polymer-based materials often arises from inefficient polymer chain packing coupled to local chain dynamics[5,6]. When a certain unoccupied volume forms close to the diffusing molecule and is large enough to cover it, the molecule can get in it, where it will remain until another favorable polymer chain thermal motion occurs. We can define a total free volume as the sum of all the voids in an amorphous polymer. As mentioned in the previous section, the permeant diffusivity depends on the size of the molecule and on the total volume available[17]. A first theory was made by Cohen and Turnbull that well describes the behavior of small

spherical molecules in long polymer chains[18]. Further Vrentas and Duda[19,20] started from the Cohen-Turnbull theory and developed a model describing diffusion in polymers. In this model it is introduced the concept of jumping unit, which took into account the fact that polymer chain motion occurs stepwise, through the motion of one segment (jumping unit) at a time. The introduction of this concept highlighted the fact that, not only the size of the diffusing molecule, but also the size of the polymer's jumping units defines the diffusion coefficient. The authors did not discuss the energy barrier needed to take a diffusive step needed to jump in a cavity. The single presence of adjacent free volume elements with sufficient size is not enough to explain the diffusion phenomenon[21]. The diffusing molecule needs, in fact, to overcome the attractive forces to take a diffusive step. The contribution of both the phenomena are described in terms of diffusion by a simplified equation introduced by Freeman[22]. The derivatization and formalism of the free volume theory will not be discussed in this chapter, to get a deeper knowledge of the model see references 13-18.

$$D = A_D e^{-\frac{B_D}{f}} \qquad (7)$$

where A_D and B_D can be considered independent of temperature and penetrant concentration. A_D depends on the penetrants's volume and shape, B_D is proportional to the ratio between the volume of penetrant molecule and the minimum volume of the free volume cavities required for the displacement of a polymer jumping unit. B_D is expected to decrease with the size of the penetrant molecules and the chain stiffness[20]. f is the fractional free volume, defined as the ratio between the specific free volume V_F and the macroscopic specific volume V of the polymer:

$$f = \frac{V_F}{V} = \frac{V - V_0}{V} \qquad (8)$$

where the specific free volume $V_F = V - Vo$, i.e. as the difference between the specific volume of the polymer and the specific volume Vo occupied by the polymer chains. In general, free volume in amorphous polymers is higher than glassy polymers. This is explained by analyzing the structure of a polymer above and below its glass transition temperature (T_g). Above T_g, the polymer is in its viscous or rubbery state: polymer chains are relatively free to move, and free volume originates from their imperfect and stressed packing. Below T_g, hole free volume gives a large contribution to the total free volume. Free volume decreases with decreasing temperature until T_g is reached. The cooling process of polymer below its glass transition temperature "freezes" the polymer chains, which can no longer change its conformation freely. Because of the greatly reduced mobility of the polymer chains, the free volume elements are also "frozen" into the polymer matrix: excess free volume elements are therefore trapped in the polymer volume. The magnitude of the free volume in the glassy state depends on how fast the polymer is cooled from the rubbery to the glassy phase[23]. At this point, it is necessary to note that, although the density fluctuations of a glassy polymer are strongly reduced with respect to that of a rubber, they are not completely eliminated. On much longer timescales, free volumes redistribute also in glassy polymers, which reach equilibrium undergoing a densification process (aging process of the polymer) in which the material reaches equilibrium and loses the excess free volume. This process occurs usually in the timescale of weeks to years and depends also on the size and shape of the polymer sample[2,24].

Materials and methods

Dicyclohexylcarbodiimide (DCC, 99%), methacryloyl chloride (98%), 2-mercaptothiazoline (98%), triethylamine (TEA, 98%), ditert-butyl bicarbonate (97%), 4-(dimethylamino)pyridine (DMAP, 99%), were purchased by ACROS and were all used as received without further purification. Aminodiphenylamine (98%) was recrystallized prior to use with ethanol. 2.2'-Azobisisobutyronitrile (AIBN) and dicumyl peroxide (DCP) were purified by recrystallization from methanol and dissolved in dry DMF to make a 10mM solution. DoPAT was purchased from Boron Molecular, Inc. 4- Methyl acrylate (MA, 99%,) were purified by filtration through an activated basic alumina column. Azobis(isobutyronitrile). RAFT agent 2-(dodecylthiocarbonothioylthio)propanoic acid (DoPAT) was purchased from Boron Molecular, Inc. Aminopropyldimethylethoxysilane (95%) purchased from Gelest. Toluene and tetrahydrofuran (THF, HPLC grade) were refluxed over sodium metal for 24 h followed by distillation under argon. N,N-Dimethylformamide (DMF) was treated with 5 Å molecular sieves and distilled under reduced pressure. Dichloromethane (CH_2Cl_2) was dried over calcium hydride and then distilled over 5 Å molecular sieves. Aqueous HF (49%, 0.2 mL) was purchased by ACROS. Deuterated chloroform ($CDCl_3$, 99.9 at. % D) and deuterated methyl sulfoxide (DMSO-d6, 99.9 at. % D) were used as received. Spherical silica nanoparticles (SiO_2) with a diameter of 14 ± 4 nm and declared specific surface area 200 m^2g^{-1} were purchased from Nissan Chemical Co. Fumed silica particles were purchased by Sigma-Aldrich (specific surface area 200 m^2g^{-1}).

Synthetic methods

The polymer grafted nanoparticles were obtained through a *grafting-from* approach using RAFT polymerization technique to grow the polymer chain (Scheme 1, Figure 74).

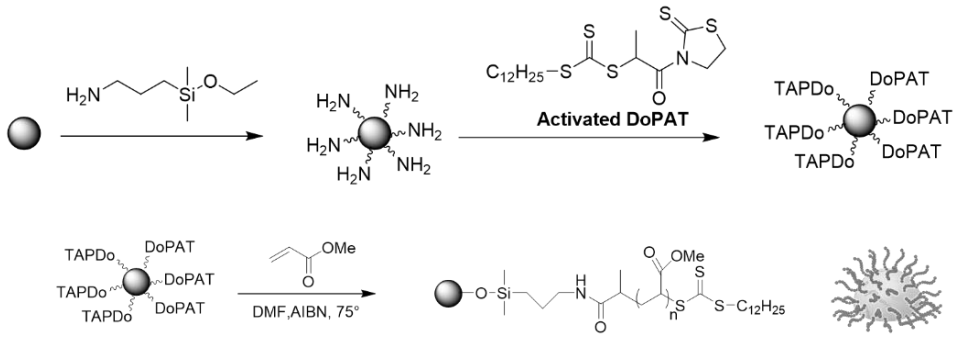

Figure 74 Scheme of the synthetic protocol used for the preparation of PGNs using a grafting-from approach.

DoPAT activation (1)

DoPAT (1.75g, 5mmol) and 2-mercaptothiazoline (0.596 g, 5 mmol) were dissolved in 20mL dry CH_2Cl_2. (Dimethylamino)pyridine (DMAP) (61 mg, 0.50 mmol) was added slowly to the solution. After stirring for 10min at 0°C, dicyclohexylcarbodiimide (DCC) (1.24 g, 6.00 mmol) in 10mL CH_2Cl_2 was added to the solution and stirred at room temperature for 1 hour. After the reaction was completed, the salt was removed by filtration. The solvent was evaporated by vacuum and followed by silica gel column chromatography (5:1 mixture of hexane and ethyl acetate) to get activated DoPAT as yellow oil (2.10g, 93% yield). ^{1}H NMR (300 MHz, CDCl3) δ (ppm): 6.46 (q, 1H), 4.62-4.70 (m, 1 H), 4.42-4.52 (m, 1H), 3.38-3.48 (m, 1H), 3.21-3.34 (m, 3H), 1.51-1.75 (m, 5 H), 1.25 1.42 (m, 18 H), 0.88 (t,

3H,). Elemental analysis: calculated for C19H33NOS5: C, 50.51; H, 7.36; N, 3.10; S, 35.48; found C, 51.31; H, 7.36; N, 3.20; S, 34.46.

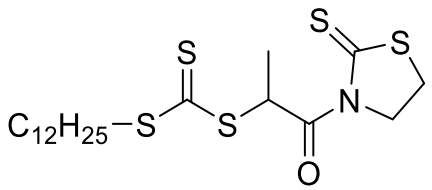

1

Figure 75 Scheme reaction of the activated DoPAT

Silica and Fumed silica functionalization

The functionalization was achieved as follows (Scheme 1), we report an example. Silica nanoparticles (50.0g, 30 wt% in MEK solution) were added to a round bottom flask with 150 mL THF and 3.0 mL 3-aminopropyldimethylethoxysilane. After purging with N_2 for 30min, the solution was refluxed at 75 °C for 5 hours. The solution was then cooled to room temperature and precipitated into large amount of hexane. The amine functional silica nanoparticles were recovered by centrifuge at 5000 rpm for 5 minutes. The dispersion-precipitation process was then repeated two more times. The silica nanoparticles were then dispersed in 150mL dry THF and added to 1.25g activated DoPAT THF (3mL) solution. The solution was stirred overnight and precipitated into a large amount of methanol and re-dispersed in THF. This dispersion-precipitation process was repeated until the supernatant solution was colorless. The nanoparticles were placed in a room temperature vacuum oven to dry. The grafted density of DoPAT@NP was 0.43 chains nm^{-2} and was calculated from UV-Vis experimental data.

N-(4-Anilinophenyl)-methacrylamide (2)

Aminodiphenylamine (0.054 mol, 1 eq.) is added in a 3 neck round bottom flask equipped with a condenser and a drop funnel, the system is purged with nitrogen and the next operation are carefully carried under control atmosphere conditions. Dry methylene chloride (DCM) is added along with the TEA (1.2 eq), the solution is stirred and bubbled with nitrogen for 10 minutes. The mixture is then cooled down with an ice bath and a diluted solution of Methacryloyl chloride in DCM (1.1 eq) is slowly added dropwise. The mixture is left in ice bath for 20 min and then slowly brought to RT and left react for 3 h. The reaction is quenched by the addition of a saturated solution of $NaHCO_3$, the organic layer is collected and washed twice with brine, then is dried over magnesium sulfate overnight. The solution is filtered and dried in vacuum overnight. The product is then recrystallized over toluene (80%) three times. Pale blue product is obtained with 80%yield. ^{1}H NMR (300 MHz, $CDCl_3$ δ (ppm) 7.49 (s, 1H), 7.44 (d, 2H), 7.28-7.20 (m, 2H), 7.09-6.69 (m, 4H), 6.90 (tt, 1H), 5.78 (s, 1H), 5.70 (s, 1H), 5.46-5.40 (m, 1H), 2.07-2.04 (m, 3H).

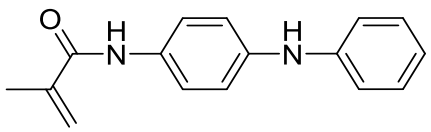

2

Protected N-(4-Anilinophenyl)-methacrylamide

The as prepared monomer (**2**) is then reacted to protect the amine groups. The monomer (0.047 mol, 1 eq) is added in a round bottom flask with the di-tert-butyl carbonate (1.3 eq) and DMAP (0.2 eq) in 70 ml of THF. The solution is then purged with N_2 for 30 minutes and then transferred to a pre-heated oil bath. The atmosphere is maintained in N_2 and the reaction is carried at 90°C for 24h. The solvent is removed under vacuum and the crude

product is then recrystallized over toluene (50%). The product appear as a pale yellow solid, 88% yield. ^{1}H NMR (300 MHz, $CDCl_3$ δ (ppm) 7.49 (s, 1H), 7.44 (d, 2H), 7.28-7.20 (m, 2H), 7.09-6.69 (m, 4H), 6.90 (tt, 1H), 5.78 (s, 1H), 5.70 (s, 1H), 5.46-5.40 (m, 1H), 2.07-2.04 (m, 3H).

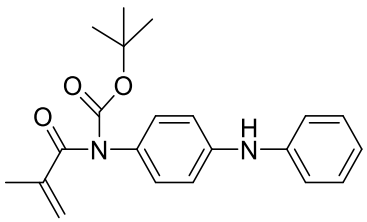

3

PMA RAFT polymerization

A typical example of the polymerization method is described here: DoPAT@NP (0.35g, Σ=0.43 chains nm^{-2}) was dispersed in 14mL DMF and 7.37mL methyl acrylate (0.081 mol). AIBN, dissolved in DMF (0.356mL, 0.01M), was added to the solution, and finally the mixture was transferred into a dried Schlenk flask. The ratios between species of [monomer]: [CTA]:[initiator] were varied for different experiments. The mixture was degassed by three freeze-pump- thaw cycles, backfilled with nitrogen, and then placed in an oil bath at 60 °C. The polymerization solution was quenched in ice water after a certain amount of time. THF (20mL) was added to the flask and the solution was poured into hexanes (120mL) to precipitate PMA grafted nanoparticles. The PMA-grafted silica nanoparticles were recovered by centrifuge at 3000 rpm for 10 min. The nanoparticles were dispersed in 50mL THF and precipitated in 100ml methanol. This dispersion-precipitation process was repeated for other five times. Same procedure was followed for the free polymer.

Cleaving procedure for grafted polymer

Polymer grafted particles (20 mg) were dissolved in 2mL of THF. Aqueous HF (49%, 0.2 mL) was added, and the solution was stirred overnight at room temperature. The solution was poured into a PTFE Petri dish and allowed to stand in a fume hood overnight to evaporate the volatiles. The recollected polymer was then subjected to GPC analyses.

N-(4-Anilinophenyl)-methacrylamide RAFT polymerization

A general example of the polymerization method is described here: DoPAT@NP (0.35g, Σ=0.43 chains nm^{-2}) was dispersed in 14mL dry DMF along with 0.081 mol of N-(4-Anilinophenyl)-methacrylamide. AIBN, dissolved in DMF (0.356mL, 0.01M), was added to the solution, and finally the mixture was transferred into a thermally treated Schlenk flask. The ratios between species of [monomer]: [CTA]:[initiator] were varied for different experiments. The mixture was degassed by three freeze-pump-thaw cycles, backfilled with nitrogen, and then placed in an oil bath at 75 °C. The mixture was quenched in ice bath. The crude product is then purified by ultracentrifugation for 3 times (40000 rcf x 30 min) with a mixture of Water:MeOH = 1:2 to precipitate the polymer grafted nanoparticles. The recovered product is then dried in a vacuum hoven to remove the solvent residues and then analyzed. Same procedure was followed for the free polymer.

Characterization methods

Molecular weights (Mw) and polydispersity indexes (*Đ*) were determined using a Varian 290 LC *gel permeation chromatography* (GPC) with a 390 LC multidetector unit, and three Styragel columns. The columns consisted of HR1, HR3, and HR4 in the effective molecular weight ranges of 100-5000, 500-30000, and 5000-500000, respectively. THF was used as eluent at 30°C and the flow rate was adjusted to 1.0mL/min. Molecular weights were calibrated with poly(styrene) standards obtained from Polymer Laboratories. *Fourier Transform Infra-Red* (FTIR) spectra of the prepared rubber samples were recorded in attenuated total reflectance mode (ATR) using a BioRad Excalibur FTS3000 spectrometer. All measurements were recorded in the scan range of 400 cm^{-1} – 4000 cm^{-1}. The *Transmission Electron Microscopy* (TEM) was performed on a Hitachi H8000 TEM at an accelerating voltage of 200 kV. The samples were prepared by deposition of diluted solution of polymer grafted nanoparticles in DCM, placed on copper grids. The image was acquired in bright field mode using on objective aperture and a XYZ detector. Silica weight fractions (ω) were determined using a Q500 TGA (TA Instruments, 501 New Castle DE, USA) by heating approximately 12-15mg of sample at a rate of 502 10.00°C/min in air to 800°C. UV−vis absorption spectra were recorded on a Shimadzu UV-2450. The hydrodynamic diameter and size distributions of the particles were determined by *Dynamic Light Scattering* (DLS) in deionized water and DCM (0.1 mg mL−1). The measures were recorded at 25 °C on a Malvern Zetasizer equipped with a continuous wave 1 mW He−Ne laser operating at 632.8 nm and an avalanche photodiode detector, Q.E. > 50% at 633 nm, placed at 173° with respect to the incident beam. Reported data are the average of at least three different measurements of the size distribution as the function of the intensity. Transport properties

measurements and free-volume analyses were conducted by the group of Dr. Kumar S.K. (Columbia University, New York, USA), these analyses are reconducted to reference 8.

Results and Discussions

PMA@Fumed silica Nanoparticles

It is reported by many authors that polymer grafted nanoparticles (PGNs) are able to self-assemble in a variety of structures depending on two main factors: the graft density (σ) and the molecular weight (i.e. the chain length)[25–29]. An important factor that drives the self-assembly of this kind of systems is the morphology of grafted nanoparticle. Most of the proposed studies are focused on spherical nanoparticles. As mentioned in the introduction section, PGNs are able to regroup in structures with controlled spatial distribution, thus enhances their permeability properties. During my thesis was used Fumed Silica particles (FS), also known as pyrogenic silica. This kind of material was produced in a flame, consists of microscopic droplets of amorphous silica fused into branched, chainlike, three-dimensional secondary particles which then agglomerate into tertiary particles. Due to its pyrogenic manufacturing process by combustion of silicon tetrachloride in an oxygen-hydrogen flame, fumed silica offers a variety of fascinating properties. since its surface is covered by highly reactive silanol groups which are available for chemical reactions[30].

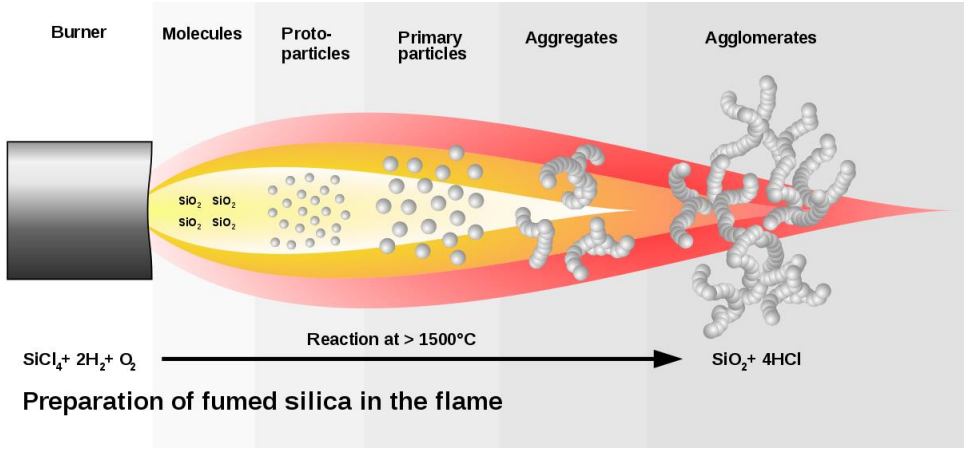

Figure 76 Schematic of the production of fumed silica in which silicon tetrachloride in an oxygen-hydrogen flame is combusted forming an interconnected network of amorphous silica.

The resulting powder has an extremely low bulk density and high surface area. As reported by the TEM pictures in Figure 77 this silica is mainly composed by interconnected silica particles, avoiding any particle regular redistribution.

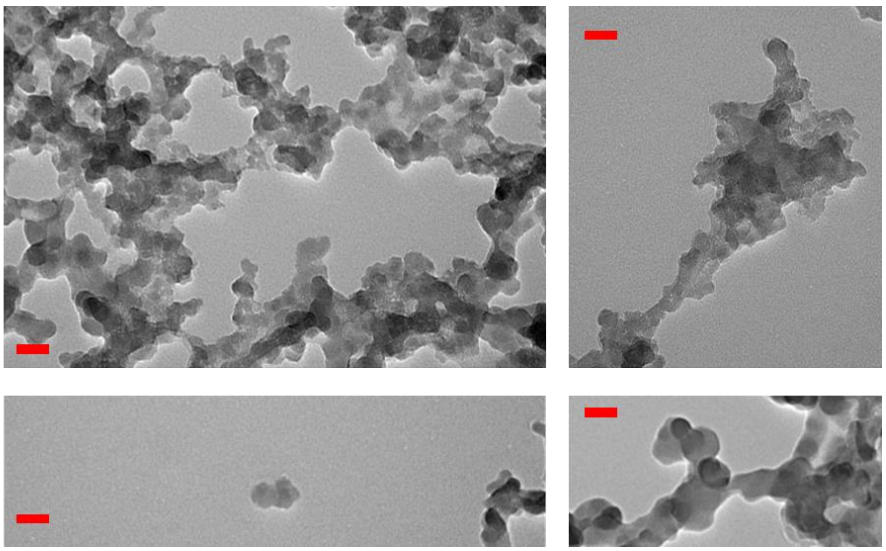

Figure 77 TEM micrographs of FS, red bars corresponds to 50 nm.

The silanol groups found on the surface are reactive species that can be coupled with molecules that carries an alkoxysilane moiety. FS is functionalized using a versatile RAFT agent, DoPAT. This molecule was attached to amino-functionalized FS by direct condensation of mercaptothiazoline-activated DoPAT with the amino groups on the surface (Figure 74). This synthetic route has the advantage of a better control over the grafting chemical reaction. It was shown that a RAFT-silane agent needs a multistep synthesis involving reactions and purifications of intermediates containing methoxysilane groups, which led to an overall low yield of the purified RAFT-silane agent. The instability of methoxy group and the absorption of RAFT-silane agent to silica gel during column chromatography[31] are the main responsible. The selection of the right reaction conditions to attach DoPAT to the amino-functionalized nanoparticles was relevant. Competing reactions or condensation reactions that produced acidic byproducts limited the scope of reactions for the attachment. Attempts to directly prepare the DoPAT anchored silica nanoparticles by reacting the carboxyl group bearing DoPAT and amino group of the modified silica nanoparticles with DCC as the condensation agent failed to yield the desired product. It is well-known that dithioesters are susceptible to aminolysis even under mild conditions. Therefore, the carboxyl group of DoPAT was first activated with 2-mercaptothiazoline. High and low surface density DoPAT anchored silica nanoparticles were thus prepared by the reaction of amino group-functionalized silica nanoparticles and activated DoPAT (Table 18). The experiments were conducted at different RAFT/amine molar ratios and reaction time to control the graft density. The yellow DoPAT@FS were dispersed in THF and analyzed using UV-Vis spectroscopy (Figure 78). The evaluation of the

chain density was done using a calibration curve constructed from standard solutions of free DoPAT in THF.

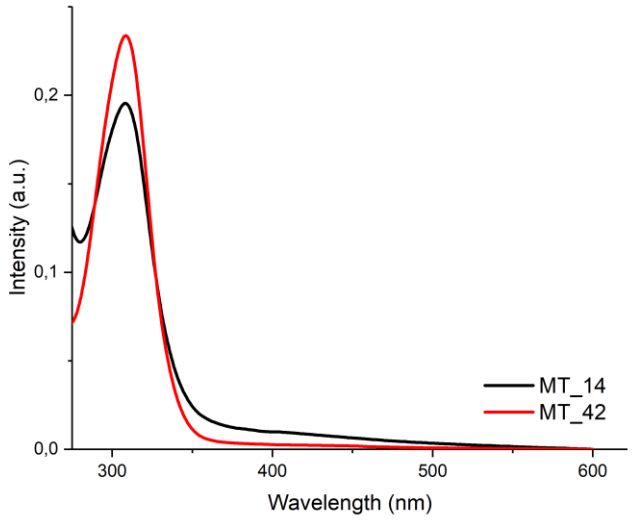

Figure 78 UV-Vis analysis of FS functionalized with activated DOPAT. The peak related to the RAFT agent absorption is due to the trithiocarbonyl group that absorbs at 308 nm-.

Table 18 Results of the grafting reaction at different RAFT/amino molar ratios and time. All the reactions were carried at the same temperature and concentrations of FS nanoparticles.

Sample	RAFT/amino	Time	σ
	mol/mol	hour	Chain nm^{-2}
MT_14	0.13	5	0.45
MT_17	0.22	16	0.45
MT_20	0.22	5	0.22
MT_27	0.09	16	0.12
MT_41	0.05	16	0.10

The as prepared samples have been subsequently used for the surface-initiated polymerizations. A kinetic study of the PMA RAFT polymerization has been done on the free and grafted polymer. The study was made at fixed [monomer]: [CTA]:[initiator] = 2300:1:0.1 ratio and the reaction temperature was set at 75°C. Once the polymerization starts, a

certain amount of crude product was recovered and immediately cooled in ice bath to quench the polymerization and to be subsequently analyzed. The polymer conversion was monitored through ^{1}H NMR analysis using 1-3-5 trioxane as internal standard. Molecular weight and polydispersity index were collected from GPC analysis. It is possible to see the living radical characteristics of RAFT polymerization analyzing the monomer consumption ($\ln(M_0/M_t)$, where M_0 is the initial monomer concentration and M_t is the monomer concentration at time t)) versus time (Figure 8). A linear relationship between monomer consumption and polymerization time was observed for the freePMA, indicating a constant radical concentration during the polymerization. In the case of the surface-initiated polymerization, it is observed a longer induction period and linear monomer consumption. The overall polymerization rate is higher in the PMA@FS case. This phenomenon is consistent with the results reported in literature[32–34], which could be ascribed to the "localized high RAFT agent concentration" effect.

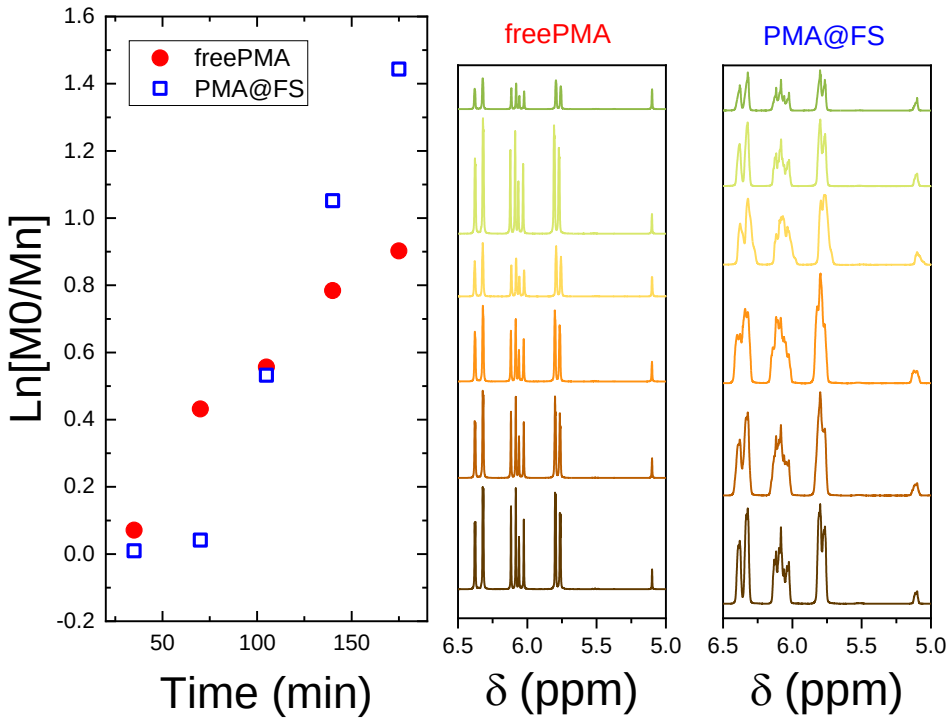

Figure 79 Left: plot of the monomer consumption ($ln(M_0/M_t)$, where M_0 is the initial monomer concentration and M_t is the monomer concentration at time t)) versus time. Red circles represent the freePMA; hollow blue squares represent the PMA@FS. Right boxes are the ^1H NMR experiments: δ(ppm) 5.1 is found the peak related to 1-3-5 trioxane protons used as internal standard, between 5.5 - 6.5 ppm are found the peaks related to the monomer. Spectra of samples withdrawn at different times (increasing time from bottom to top).

In Figure 9 is reported the molecular weight as function of the conversion, the graph shows the controlled character of methyl acrylate RAFT polymerization. These results showed that the number-average molecular weights increased in a linear fashion with monomer conversions, and the measured molecular weights determined by SEC calibrated with PMMA standards were close to theoretical molecular weights (dashed line, eq.9), which indicated a very high efficiency of the anchored DoPT throughout the polymerization.

$$M_n = \frac{[M]}{[CTA]} \cdot c \cdot M_w(M) + M_w(CTA) \qquad (9)$$

M_n is the theoretical molecular weight; [M] is the monomer concentration; [CTA] is the RAFT agent concentration, c represents the conversion, M_w(M) is the monomer molecular weight and M_w (CTA) the molecular weight of the RAFT agent.

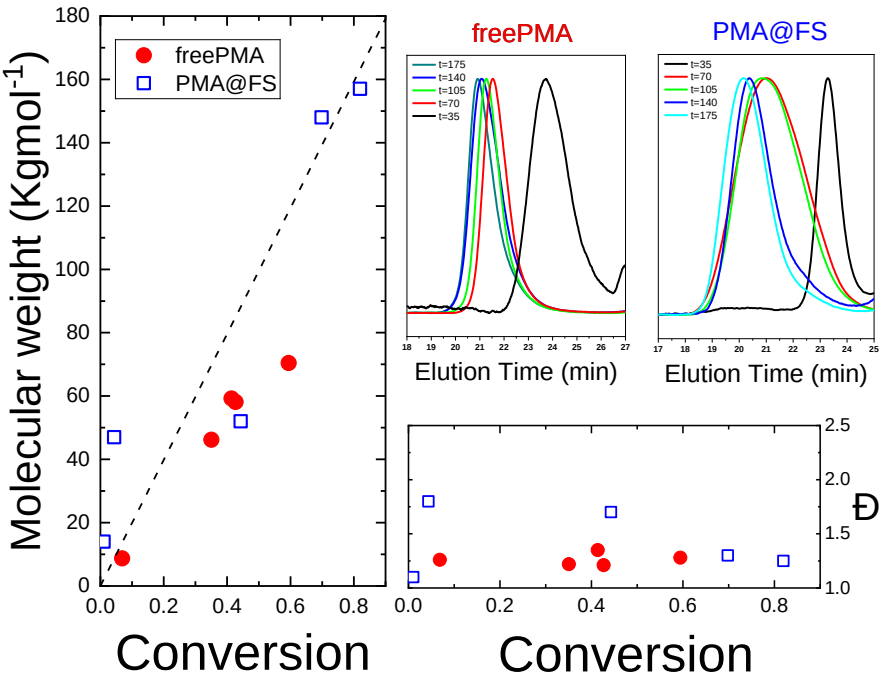

Figure 80 On the left is depicted the molecular weight vs conversion plot, red circles represent the freePMA; hollow blue squares represent the PMA@FS, dashed line represent the theoretical molecular weight calculated with eq.9. Up-right boxes are the GPC chromatograms of free PMA and the cleaved PMA@FS. Bottom right are reported the polydispersity indices vs conversion of the free PMA and PMA@FS.

In a RAFT-mediated graft polymerization, a very effective surface migration of the graft radical can occur via successive degenerative (exchange) chain transfer reactions if the surface density of the dormant (potentially active) graft chain is high enough. This effective surface

migration improves the rate of the polymer growth. Experimental data are consistent with this theory, in fact free PMA can't reach the conversion values reached by PMA@FS. At the same time, however, the surface migration allows the graft radicals to undergo bimolecular termination at an unusually high rate, especially when σ is large, which broadens the chain length distribution. This phenomenon is highlighted by the GPC analyses reported in Figure 80. The PMA@FS samples have broader peaks, expressed by higher *Đ* values, at intermediate times.

A set of samples have been prepared in order to get a variety of molecular weights ant graft density of PMA on FS, the experiments are reported in Table 19.

Table 19 Experiments conducted in dry DMF, with FS particles grafted with σ 0.45 chain nm^{-2}. Molecular weight (Mn) and polydispersity obtained from GPC analysis of the cleaved polymer. M:CTA represents the molar ratio between the monomer and the Raft agent; CTA:I is the molar ratio between the CTA and the initiator.

Sample	*M:CTA*	*CTA:I*	*T* *°C*	*Time* *h*	*Mn* *kgmol^{-1}*	*Đ*
MT_6	1000	0.1	60	4	24.5	1.17
MT_7	1000	0.2	110	16	72	1.19
MT_21	6500	0.1	60	4	-	-
MT_22	2500	0.1	60	10	-	-
MT_25	6500	0.1	60	24	151	1.34
MT_26	2500	0.1	60	24	122.8	1.53
MT_31	2500	0.1	60	48	-	-
MT_32	6500	0.1	60	24	148.4	1.40
MT_36	2500	0.1	60	48	133.8	1.27
MT_37	6500	0.1	60	24	84	1.21
MT_43	4500	0.1	75	12	103	1.80
MT_44	2300	0.1	75	12	167	1.32
MT_45	2300	0.1	75	3.5	80	1.30
MT_45	2300	0.1	75	1	15	1.10

PMA@FS with different molecular weights have been synthesized, high M_n values with low *Đ* (151 Kgmol^{-1}, 1.34) were reached. The gas

permeation properties (Figure 81) of the samples were analyzed by the group of Dr. Kumar S.K at the Columbia University of New York; all the measures follow the procedure reported in reference 8.

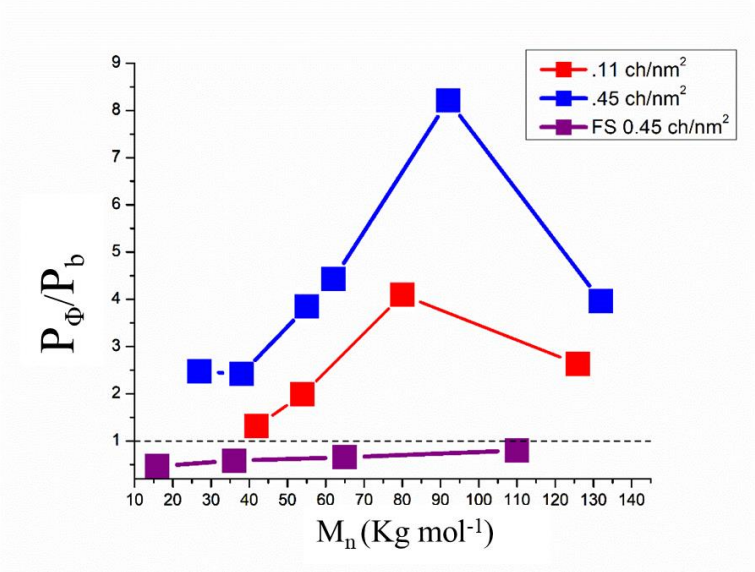

Figure 81 ***P_ϕ/P_b, of CO_2 vs polymer molecular weight Mn. Are reported the data reported by Bilchack et al. for spherical silica nanoparticles (diameter ≈14nm) grafted with 0.45 chain nm^{-2} (bleu square), and 0.11 chain nm^{-2} (red square) PMA. FS grafted with 0.45 chain nm^{-2} PMA of different Mn is represented by purple square. Dash line represents the neat PMA permeability***

In Figure 81 are summarized the relative permeability, P_ϕ/P_b, of CO_2. where P_ϕ and P_b are the permeabilities of the composite and neat polymer, respectively, PMA@FS results are compared with data reported in literature[9]. Nanosized spherical nanoparticles show a range of M_n where is noted an improvement of the gas permeability properties. Tuning the graft density brings a further enhancement of the relative permeability to CO_2. It is observed that the FS particles, even if covered with PMA polymer chains, acts as a physical gas barrier lowering the overall permeability of the nanocomposite material. The main difference between the two system is the spatial distribution of the particles. To better understand this phenomenon, it is necessary to analyze the morphology of the dispersions through TEM

analysis (Figure 82). It is evident that the PMA@FS are not able to self-assemble in ordered systems with controlled spatial distribution. The peculiarity of the FS particle can't provide the desired control over the permeability properties. This evidence confirms that the nature of the permeability improvements of nanocomposite materials, is ruled by the fine control over the free volume; that is obtained tuning the graft density and polymer chain length.

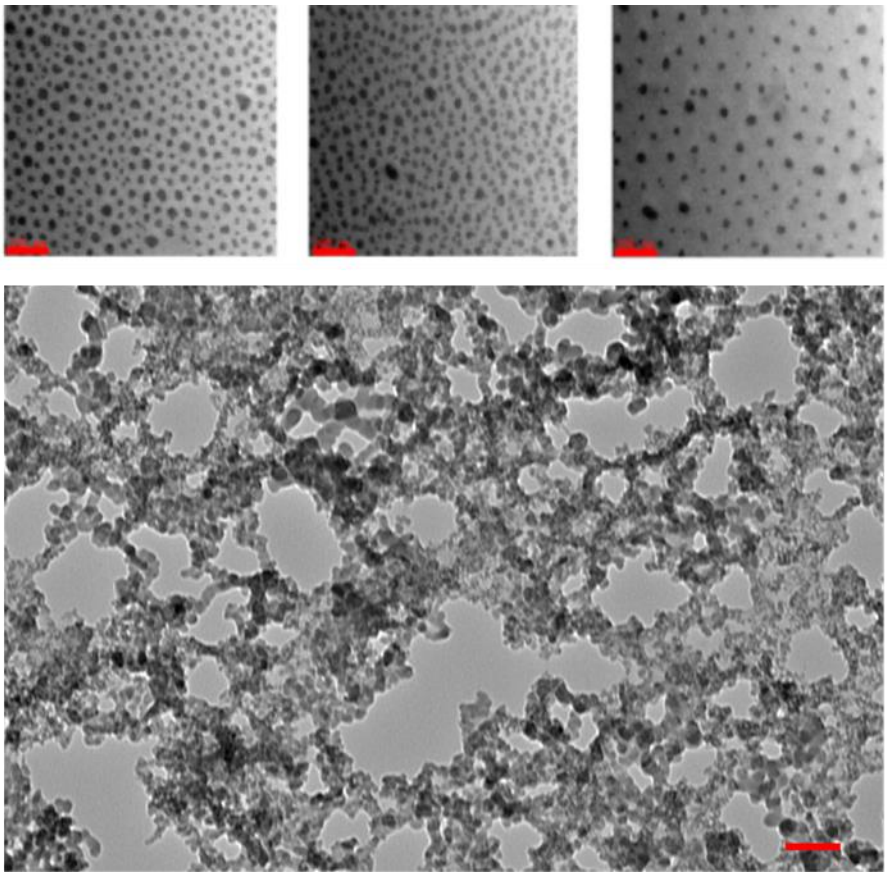

Figure 82 TEM micrographs of (top) silica nanoparticles (diameter ≈14nm) with 0.45 chain nm^{-2} with increasing molecular weight (78, 90, 135 Kg mol^{-1} respectively from left to right. Picture of PMA@FS with 0.45 chain nm^{-2} and 68 Kg mol^{-1} Mn (bottom). The red bars correspond to 100 nm.

Polymehacrylamide-oligoaniline side chain nanocomposite materials

To get improved polymeric membrane in gas permeation fields, as it was demonstrated in the previous section, it is possible to follow a synthetic route that provides well-defined PGNs able to self-assemble in a controlled fashion. These encouraging results open to a variety of nanocomposite materials based on polymers with specific properties. It is possible to enhance both the permeability and selectivity using a "smart" monomer and choosing it by its chemical characteristics. For example, fluorinated polymers in general showed interesting performances in several of the listed gas pairs in the Robeson work[14,35]. In the class of stiff chain polymers, the liquid crystal polyesters possess good permeation and selectivity to several gas mixtures[14,35]. Another interesting class of polymers is represented by polyaniline (PANI). These systems are mainly used for their conductivity properties, but few authors reported experiments proving good separation performances for CO_2/CH_4[36–39]. The aniline polymers generally have controllable electrical conductivity, environmental stability, and interesting redox properties associated with the chain nitrogen. They have been extensively studied for their unique characteristics and potential applications in electrical devices, such as polymer electrodes and sensors[40]. Matsumoto K. showed in his work[36] that CO_2 permeability of PANI was increased by the formation of a quinonediimine unit with the oxidation. The increase of permeability with oxidation resulted from the increase of diffusivity, which was attributable to morphological variation, i.e. free volume, by the increase of a quinonediimine unit. The oxidation it is obtained through controlled doping and redoping of the PANI film.

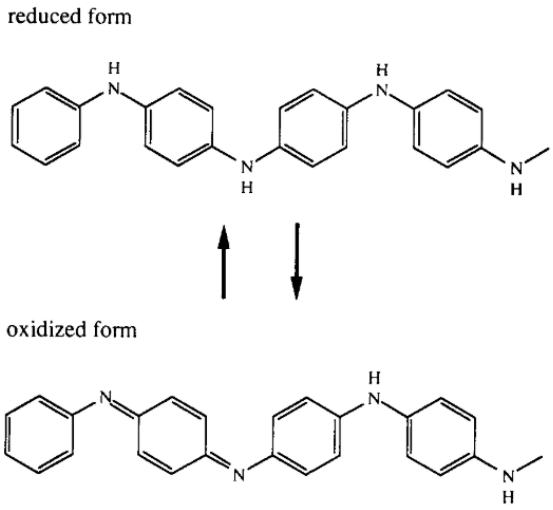

Figure 83 the unit sequence of as-cast PA is mainly composed of a p-phenylenediamine. This form is changed to another unit sequence, which is composed of both a quinonediimine and a p-phenylenediamine, by oxidation.

Polyaniline are generally polymerized through cyclic voltammetry, a tricky polymerization. In general, the polyaniline polymers are difficult to handle due to their low solubility in the main organic solvents. It is possible to mimic this polymer with a side chain on a handier acrylate or methacrylate monomer[41]. This kind of monomers, polymerized by radical methods, showed that their electrochemical nature is maintained. Since the Robeson works[14,35] points to doped polyanilines as interesting materials for gas separations, the electrochemistry implies that, for example, acrylate oligoaniline side-chain polymers are also dopable in a similar fashion. This kind of convenient monomer can be polymerized through controlled radical polymerization techniques. These lends to produce a nanocomposite material with controlled graft density and chain lengths, which are trademarks of the previous investigations. In this perspective it is set this contribution, many efforts were made to synthesize a monomer that can mimic the aniline behavior and that could possibly be polymerized through surface-initiated RAFT polymerization. A N-(4-Anilinophenyl)-

methacrylamide was synthesized. RAFT agents generally possess a thiocarbonylthio group like xanthates (or dithiocarbonates), dithiocarbamates, trithiocarbonates and dithioesters. Thiocarbonylthio agents have demonstrated themselves to be tolerant to a large number of chemicals and experimental conditions, however thiocarbonylthio group could be cleaved by few classes of organic compounds. Particularly problematic are amines, specifically primary and secondary amines. Just as thiocarbonylthio species are susceptible to hydrolysis, they are also prone to aminolysis. Indeed, dithioesters are well known to react with primary and secondary aliphatic amines at much faster rates than esters yielding thioamides and thiols. In the realms of RAFT chemistry this is harmful and, for example, precludes the direct polymerization of monomers with such functional groups[42]. The monomer synthesized in this work is a methacrylamide with a diphenilaniline side chain, this group contains an amine that could possibly cleave the trithiocarbonyl group present in DoPAT agent. A polymerization was done with the N-(4-Anilinophenyl)-methacrylamide, but no polymer was obtained. This is an evidence of the lability of the trithiocarbonyl group. The amine group was protected by a BOC moiety in order to prevent the aminolysis of our polymerization engine. NMR analyses of the monomer and the protected one were done. It is noted that the reaction took place between the t-BOC group and the amide group, instead of the amine (Figure 84). The amine group showed no reactivity and it was decided to go further and use the protected monomer for the next experiments.

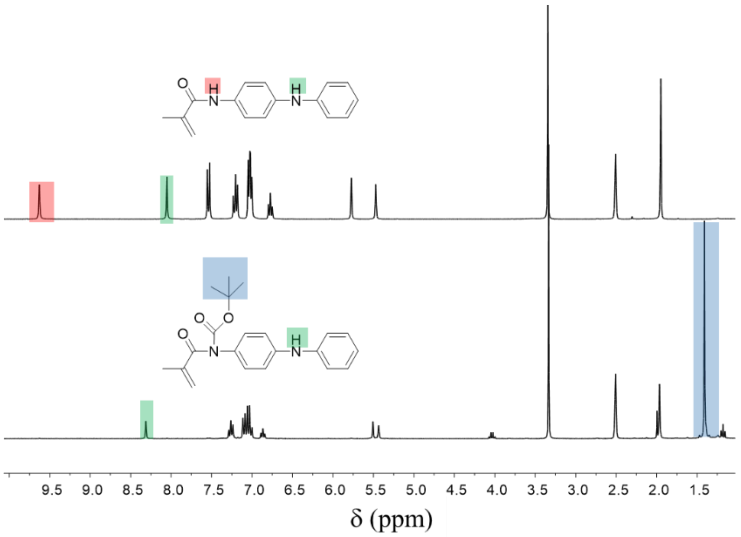

Figure 84 ^{1}H NMR in DMSO-d6. Top: N-(4-Anilinophenyl)-methacrylamide monomer at 9.67 ppm is found the signal of the amide proton (red square); at 8.05 ppm it is fund the proton of the diphenilanilie group (green square), between 7.75-6.5 lead the aromatic proton of the side chain; between 6.0-5.4 ppm are found the double bond protons. Bottom: protected-N-(4-Anilinophenyl)-methacrylamide. The proton related to the amine group disappears confirming that the reaction took place between the t-BOC and the amide group; the nine protons of the t-BOC protecting group are found at 1.41 ppm (blue rectangle).

A series of silica nanoparticles samples were grafted with activated DoPAT with different graft densities using the same approach previously reported. The next surface-initiated polymerization experiments were conducted using silica nanoparticles with 0.1 chain nm^{-2}. A kinetic study of the free and the graft polymerization was done in order to find the best experimental condition to get a complete picture of the polymerization process. The graphs of the monomer consumption versus time and the conversion as function of time are reported in Figure 14. It is noted that the free polymer has no induction time, while the surface-initiated polymerization starts after five hours. Moreover, monomer conversions of both the systems are lower than 25% after 24 hours. This is probably due to its hindrance, that does not allow a good diffusion to the active RAFT agents. The polymers obtained from the free polymerizations were soluble in THF, making them suitable

for GPC analysis. The *Đ* of the as prepared polymers were low, reporting good control over the molecular weight distribution (Table 20).

Table 20 Results of the free polymerization conducted in dry DMF at 70°C for 48h using AIBN as initiator.

Sample	M:T	T:I	Mn Kgmol-1	Đ
MT_12	100	0.1	69.8	1.23
MT_18	100	0.1	72.1	1.16
MT_54	1000	0.23	170	1.32

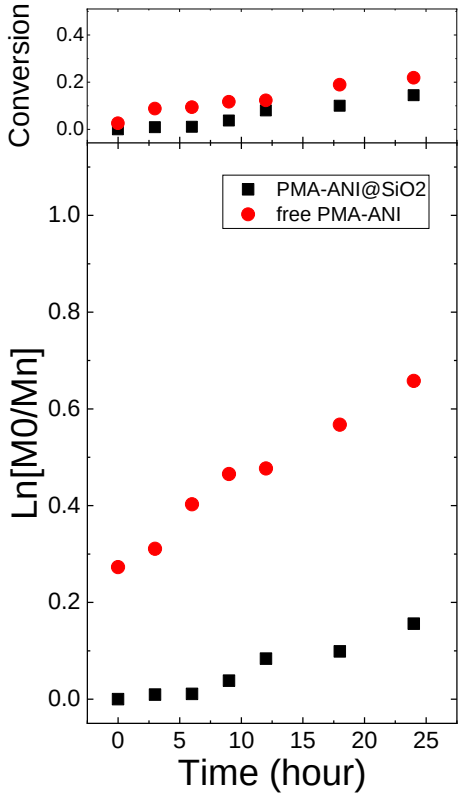

Figure 85 Conversion vs Time (top) analysis of the free PMA-ANI (red circles) and PMA-ANI@SiO_2 (black square). Monomer consumption, expressed as ln($[M_0]/M_t$]), vs time (bottom).

Unfortunately, it was not possible to recover the grafted polymer since the product of this reaction was not soluble in THF, that is not suitable for GPC analysis. TGA analysis was used instead to get the information about

molecular weight of these samples. It was possible to calculate the amount of RAFT agent from TGA analysis using eq.10, knowing the graft density of the starting nanoparticles

$$mol_{RAFT} = \sigma\,(1 - W_{loss}) \cdot 10^{-6} \qquad (10)$$

Where W_{loss} represents the absolute weight loss value calculated from TGA analysis. From the mol_{RAFT} it was possible to calculate the normalized average molecular weight of the grafted polymer using eq.11

$$M_w = \frac{W_{loss}}{mol_{RAFT}} \qquad (11)$$

Table 21 list of results from the surface initiated polymerization of PMA-ANI using dry DMF; all the reactions were carried for 48 hours. The reactions were conducted with different M:T and T:I ratios. AIBN and DCP were used as initiator. Mw is calculated using eq.11.

Sample	**M:T**	**T:I**	**T**	**Initiator**	**M*w***
			°C		**Kgmol^{-1}**
MT_56	100	0.10	70	AIBN	4.4
MT_57	100	0.10	70	AIBN	3.0
MT_61	100	0.10	70	AIBN	1.7
MT_62	200	0.10	70	AIBN	1.9
MT_64	100	0.10	115	DCP	1.6
MT_67	1000	0.10	70	AIBN	2.8
MT_72	100	0.10	70	AIBN	2.3
MT_73	100	0.10	70	AIBN	2.1
MT_74	2300	0.23	115	DCP	14.0
MT_75	200	0.10	70	AIBN	1.7
MT_78	1000	0.20	115	AIBN	4.0
MT_79	2000	0.20	115	DCP	5.7
MT_80	500	0.20	115	DCP	4.9
MT_82	1000	0.20	115	DCP	2.1
MT_85	2000	0.23	115	DCP	28.6

A first set of reactions was conducted at 70°C using 0.1 T:I ratio, a second set was carried with higher M:T ratios and higher temperature. As it is shown in Table 21 the M_w of these first experiments were very low. To get a longer polymer chain from the surface was necessary to increase the reaction temperature to 115°C with higher T:I ratio. AIBN has a half life lower than 1h at 80°C, that it is not suitable for polymerizations conducted at higher temperature. On the other hand, DCP half life at 115°C is about 10 hours, that is preferred for RAFT polymerizations. The best results were obtained in severe experimental condition: it was needed a greater amount of monomer and initiator, besides the polymerization did not occur with less than five *freeze-pump-thaw* cycles. The difficult synthesis of this polymer it is probably related to the instability of the formed radical during the first stage of the polymerization. Moreover, the hindrance of this monomer makes this process even more difficult. However, after several experiments were found the right conditions to prepare PGNs suitable for gas permeation tests. The most promising sample (MT_85, Table 21) with 28.6 Kg mol^{-1} and σ = 0.1 chain nm^{-2} was analyzed by TEM microscopy. The pictures of the particles grafted with only the RAFT agent showed aggregation, while with PGNs no aggregation occurs (Figure 86).

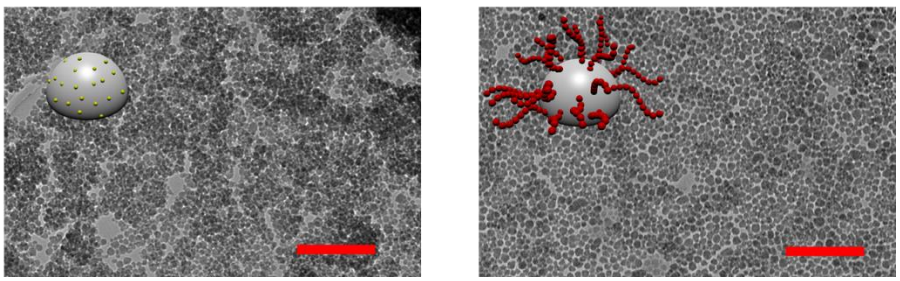

Figure 86 TEM micrographs (left) of the silica nanoparticles covered with σ 0.1 chain nm^{-2} RAFT agent (right); PGNs with PMA-ANI 28.6 Kg mol^{-1}. Red bars represent 200 nm scale.

To get an idea of the gas permeability and selectivity properties of this particular sample, it was sent to the group of Dr. Kumar S.K., that performed a first screening on its properties. Permeability and selectivity measures of the doped PGNs showed that the permeability to CO_2 is increased 100 times while selectivity was increased 1.2 times compared to simple polyaniline membranes. The combination of the intrinsic selectivity properties of polyaniline and the application of the synthetic protocol proposed by Bilchak et al.[9] produced an interesting PGNs polymeric membrane that found its location above the revisited Robeson upper bound[13] (Figure 87).

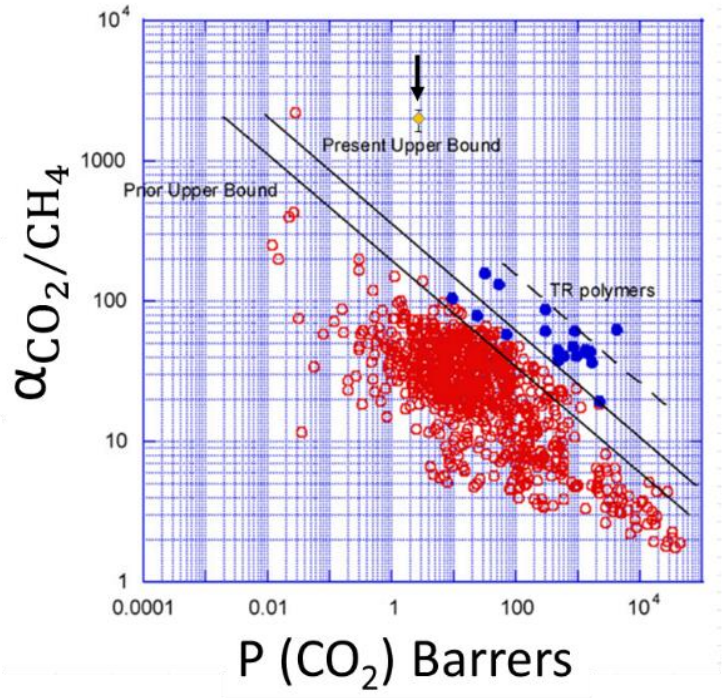

Figure 87 Revisited Robesn upper bound graph in which is reported the PGNs with PMA-ANI side chain 28.6 Kg mol^{-1} and σ 0.1 chain nm$^{-2.}$

Conclusions

In this contribution we observed that the chemical grafting of polymer chains to inert NPs is a novel design platform for advanced polymeric membranes. This material platform provides accurate tuning of gas permeabilities and selectivity through the polymer graft characteristics. Moreover, the morphology and size of the nanoparticles assumes an important role. In fact, fumed silica particles are not able to reorganize in a controlled way, thus no improvement of the gas properties are detected. Statistical free volume is directly manipulated by the grafts and the inorganic substrate, as observed in previous works[9]. While the performance improvements found for these polymer-grafted NP membranes are significant, there are other glassy polymers even better suited for particular separations. In this perspective it was synthesized a methacrylamide diphenilanilene monomer that could mimic the behavior of polyaniline. This monomer was suited to be polymerized through RAFT technique, that provided the desired control on the polymer growth. A set of samples were prepared and characterized, It was shown that the combination of the intrinsic selectivity properties of polyaniline and the application of the preparation proposed by Bilchak et al.[9] produced an interesting PGNs polymeric membrane that is located above the revisited Robeson upper bound[13]. It must be taken into account that nanocomposite membranes possess better mechanical properties and they can face better aging problems of simple polymer membranes. This work opens to a series of new membranes made by PGNs with new functional monomers that will exceed the Robeson limit.

References

(1) Baker, R. W.; Lokhandwala, K. Natural Gas Processing with Membranes: An Overview. *Ind. Eng. Chem. Res.* **2008**, *47* (7), 2109–2121.

(2) Baker, R. W.; Low, B. T. Gas Separation Membrane Materials: A Perspective. *Macromolecules* **2014**, *47* (20), 6999–7013.

(3) Lin, H.; Freeman, B. D. Materials Selection Guidelines for Membranes That Remove $CO_2$from Gas Mixtures. *J. Mol. Struct.* **2005**, *739* (1–3), 57–74.

(4) Galizia, M.; Chi, W. S.; Smith, Z. P.; Merkel, T. C.; Baker, R. W.; Freeman, B. D. 50th Anniversary Perspective: Polymers and Mixed Matrix Membranes for Gas and Vapor Separation: A Review and Prospective Opportunities. *Macromolecules* **2017**, *50* (20), 7809–7843.

(5) Budd, P. M.; Msayib, K. J.; Tattershall, C. E.; Ghanem, B. S.; Reynolds, K. J.; McKeown, N. B.; Fritsch, D. Gas Separation Membranes from Polymers of Intrinsic Microporosity. *J. Memb. Sci.* **2005**, *251* (1–2), 263–269.

(6) Park, H. B.; Han, S. H.; Jung, C. H.; Lee, Y. M.; Hill, A. J. Thermally Rearranged (TR) Polymer Membranes for CO2 Separation. *J. Memb. Sci.* **2010**, *359* (1–2), 11–24.

(7) Chung, T.-S.; Jiang, L. Y.; Li, Y.; Kulprathipanja, S. Mixed Matrix Membranes (MMMs) Comprising Organic Polymers with Dispersed Inorganic Fillers for Gas Separation. *Prog. Polym. Sci.* **2007**, *32* (4), 483–507.

(8) Bastani, D.; Esmaeili, N.; Asadollahi, M. Polymeric Mixed Matrix Membranes Containing Zeolites as a Filler for Gas Separation Applications: A Review. *J. Ind. Eng. Chem.* **2013**, *19* (2), 375–393.

(9) Bilchak, C. R.; Buenning, E.; Asai, M.; Zhang, K.; Durning, C. J.; Kumar, S. K.; Huang, Y.; Benicewicz, B. C.; Gidley, D. W.; Cheng, S.; et al. Polymer-Grafted Nanoparticle Membranes with Controllable Free Volume. *Macromolecules* **2017**, *50* (18), 7111–7120.

(10) Maxwell, J. C. *Treatise on Electricity and Magnetism.*; Dover Pubns, 2007.

(11) Shimekit, B.; Mukhtar, H. Gas Permeation Models in Mixed Matrix

Membranes. In *2011 National Postgraduate Conference*; IEEE, 2011; pp 1–5.

(12) Gonzo, E. E.; Parentis, M. L.; Gottifredi, J. C. Estimating Models for Predicting Effective Permeability of Mixed Matrix Membranes. *J. Memb. Sci.* **2006**, *277*, 46–54.

(13) Robeson, L. M. The Upper Bound Revisited. *J. Memb. Sci.* **2008**, *320* (1–2), 390–400.

(14) Robeson, L. M. Correlation of Separation Factor versus Permeability for Polymeric Membranes. *J. Memb. Sci.* **1991**, *62* (2), 165–185.

(15) Wijmans, J. G.; Baker, R. W. The Solution-Diffusion Model: A Review. *J. Memb. Sci.* **1995**, *107* (1–2), 1–21.

(16) Sperling, L. H. *Introduction to Physical Polymer Science*; John Wiley & Sons, Inc.: Hoboken, NJ, USA, 2005.

(17) Ramesh, N.; Davis, P. K.; Zielinski, J. M.; Danner, R. P.; Duda, J. L. Application of Free-Volume Theory to Self Diffusion of Solvents in Polymers below the Glass Transition Temperature: A Review. *J. Polym. Sci. Part B Polym. Phys.* **2011**, *49* (23), 1629–1644.

(18) Cohen, M. H.; Turnbull, D. Molecular Transport in Liquids and Glasses. *J. Chem. Phys.* **1959**, *31* (5), 1164–1169.

(19) Vrentas, J. S.; Vrentas, C. M. Solvent Self-Diffusion in Rubbery Polymer-Solvent Systems. *Macromolecules* **1994**, *27* (17), 4684–4690.

(20) Vrentas, J. S.; Duda, J. L. Diffusion in Polymer—solvent Systems. I. Reexamination of the Free-Volume Theory. *J. Polym. Sci. Polym. Phys. Ed.* **1977**, *15* (3), 403–416.

(21) Macedo, P. B.; Litovitz, T. A. On the Relative Roles of Free Volume and Activation Energy in the Viscosity of Liquids. *J. Chem. Phys.* **1965**, *42* (1), 245–256.

(22) Freeman, B. D. Basis of Permeability/Selectivity Tradeoff Relations in Polymeric Gas Separation Membranes. *Macromolecules* **1999**, *32* (2), 375–380.

(23) Ganesh, K.; Nagarajan, R.; Duda, J. L. Rate of Gas Transport in Glassy

Polymers: A Free Volume Based Predictive Model. *Ind. Eng. Chem. Res.* **1992**, *31* (3), 746–755.

(24) Rittigstein, P.; Torkelson, J. M. Polymer-Nanoparticle Interfacial Interactions in Polymer Nanocomposites: Confinement Effects on Glass Transition Temperature and Suppression of Physical Aging. *J. Polym. Sci. Part B Polym. Phys.* **2006**, *44* (20), 2935–2943.

(25) Kumar, S. K.; Jouault, N.; Benicewicz, B.; Neely, T. Nanocomposites with Polymer Grafted Nanoparticles. *Macromolecules* **2013**, *46* (9), 3199–3214.

(26) Sunday, D.; Ilavsky, J.; Green, D. L. A Phase Diagram for Polymer-Grafted Nanoparticles in Homopolymer Matrices. *Macromolecules* **2012**, *45* (9), 4007–4011.

(27) Akcora, P.; Liu, H.; Kumar, S. K.; Moll, J.; Li, Y.; Benicewicz, B. C.; Schadler, L. S.; Acehan, D.; Panagiotopoulos, A. Z.; Pryamitsyn, V.; et al. Anisotropic Self-Assembly of Spherical Polymer-Grafted Nanoparticles. *Nat. Mater.* **2009**, *8* (4), 354–359.

(28) Chevigny, C.; Dalmas, F.; Di Cola, E.; Gigmes, D.; Bertin, D.; Boué, F.; Jestin, J. Polymer-Grafted-Nanoparticles Nanocomposites: Dispersion, Grafted Chain Conformation, and Rheological Behavior. *Macromolecules* **2011**, *44* (1), 122–133.

(29) Maguire, J. F. Polymer Nanocomposites With Prescribed Morphology : Going Beyond Nanoparticle- Filled Polymers (Preprint). *Chem. Mater.* **2007**, *19*, 2736–2751.

(30) Barthel, H.; Rsch, L.; Weis, J. Fumed Silica - Production, Properties, and Applications. In *Organosilicon Chemistry Set*; Wiley-VCH Verlag GmbH: Weinheim, Germany; pp 761–778.

(31) Li, C.; Benicewicz, B. C. Synthesis of Well-Defined Polymer Brushes Grafted onto Silica Nanoparticles via Surface Reversible Addition-Fragmentation Chain Transfer Polymerization. *Macromolecules* **2005**, *38* (14), 5929–5936.

(32) Ohno, K.; Ma, Y.; Huang, Y.; Mori, C.; Yahata, Y.; Tsujii, Y.; Maschmeyer, T.; Moraes, J.; Perrier, S. Surface-Initiated Reversible Addition-

Fragmentation Chain Transfer (RAFT) Polymerization from Fine Particles Functionalized with Trithiocarbonates. *Macromolecules* **2011**, *44* (22), 8944–8953.

(33) Zhao, Y.; Perrier, S. Reversible Addition-Fragmentation Chain Transfer Graft Polymerization Mediated by Fumed Silica Supported Chain Transfer Agents. *Macromolecules* **2007**, *40* (25), 9116–9124.

(34) Li, C.; Han, J.; Ryu, C. Y.; Benicewicz, B. C. A Versatile Method to Prepare RAFT Agent Anchored Substrates and the Preparation of PMMA Grafted-Nanoparticles. *Macromolecules* **2006**, *39* (9), 3175–3183.

(35) Robeson, L. M. The Upper Bound Revisited. *J. Memb. Sci.* **2008**, *320* (1–2), 390–400.

(36) Hachisuka, H.; Ohara, T.; Ikeda, K. -I; Matsumoto, K. Gas Permeation Property of Polyaniline Films. *J. Appl. Polym. Sci.* **1995**, *56* (11), 1479–1485.

(37) Illing, G.; Hellgardt, K.; Schonert, M.; Wakeman, R. J.; Jungbauer, A. Towards Ultrathin Polyaniline Films for Gas Separation. *J. Memb. Sci.* **2005**, *253* (1–2), 199–208.

(38) Gupta, Y.; Hellgardt, K.; Wakeman, R. J. Enhanced Permeability of Polyaniline Based Nano-Membranes for Gas Separation. *J. Memb. Sci.* **2006**, *282* (1–2), 60–70.

(39) Sairam, M.; Nataraj, S. K.; Aminabhavi, T. M.; Roy, S.; Madhusoodana, C. D. Polyaniline Membranes for Separation and Purification of Gases, Liquids, and Electrolyte Solutions. *Sep. Purif. Rev.* **2006**, *35* (4), 249–283.

(40) Wang, P.; Tan, K. L.; Zhang, F.; Kang, E. T.; Neoh, K. G. Synthesis and Characterization of Poly (Ethylene Glycol)-Grafted Polyaniline. *Chem. Mater.* **2001**, *13* (10), 581–587.

(41) Chen, R.; Benicewicz, B. C. Synthesis and Characterization of Polymers with Oligoaniline Side Chains; 2003; pp 126–139.

(42) Barner-Kowollik, C. *Handbook of RAFT Polymerization*; 2008.

Conclusions

Fabrication of nanocomposite materials involves multistep process; it starts with the nanocrystals synthesis, passes through the fine tuning and functionalization of the filler surface to finally get to the nanocomposite bulk material production. In this work we covered all these steps facing problems and limits of each process with the purpose to find new solutions and synthetic protocols. Nanocrystals synthesis is followed by many issues related to the definition of them properties (crystal phase, shape, size etc.). We found that TD-NMR can be an additional technique useful to understand NCs properties. Taking advantage of the interaction between water molecules and titanium dioxide NCs, it is possible to use water NMR relaxation as probe. Titanium dioxide NCs of different crystal phase were prepared and characterized. We demonstrated that if we correlate the proton transverse relaxation times (T_2) as the function of the concentration and the specific surface area ($\delta_p \cdot C_m$) it is possible to identify the crystal phase of titanium dioxide NCs. Once the inorganic nanofillers are prepared it is convenient, and sometimes necessary, to mimic the environment in which they are eventually placed. For biological application it is important to cover the NCs surface with biomolecules like proteins, DNA or biocompatible polymers. In this work we studied the grafting-to approach of end functionalized mPEO chains on anatase NCs. mPEO is a well-known and established biocompatible polymer used in drug delivery systems. Titanium dioxide NCs on the other hand are common inorganic compounds used in cosmetic products like for example sun screen cream. We developed a protocol that provide a good control over the grafting process and that can still produce NCs with controlled conformation and graft density, important aspects in drug delivery systems. At the same time, controlling this process

brings to succeed on the drafting of a conformational map, that can possibly help to address the future nanocomposite synthesis. The purpose of this thesis was to create and develop nanocomposite materials, we further explore the *grafting-to* of end-chain functionalized polyethylene oxide, producing a synthetic protocol to create well defined PGNs. In these conditions we were able to realize that to tune the density of the tethered polymer chains and thus, the conformation it is necessary to control polymer-solvent interaction, the polymer-surface reactivity and the solvent-surface interaction allows. The ability to control PGNs characteristics through experimental conditions, stimulated us to develop a polymer-based nanocomposite material starting from a mixed bimodal layer grafted nanoparticle. This system provided a dispersion of NCs in TPU polymer matrix such that we were able to produce a material with a high loading of anatase NCs, maintaining the transparency of the final material. Plus, we obtained a material with improved optical properties and higher elastic modulus. On the other hand, applying a controlled polymerization technique, leads to a better control over NCs dispersion in polymer matrix. In this direction our experiments were driven. RAFT polymerization has been used as a tool to functionalize and control the chain length of the grafted polymer. A set of experiments were done applying the grafting-to method on anatase NCs of polystyrene chain, growth exploiting RAFT polymerization. Following the same protocol used for the previously studied mPEO, we were able to control the process and the characteristics of the nanocomposite material. We observed that the mechanical properties of a PGNC depends on the conformation of the attached chains. Lastly,it was observed that the fine tuning of PGNs characteristics contribute to dominate spatial distribution in polymer matrix, that arises in enhanced gas permeability properties. The definition of the density and the length of

polymer chains tethered to spherical NPs offer the ability to take advantage on the free volume formation in a nanocomposite material. Thus, we were able to fabricate a new membrane exploiting this property, by using a *smarter* polymer. It was selected and developed a monomer with a preferred selectivity to CO_2 inspired by polyaniline membranes. This monomer was designed to be polymerized via RAFT polymerization using the *grafting-from* approach. With this method it was prepared a PGNs membrane with enhanced gas permeability and selectivity to CO_2, a threat and a resource.